Katharina Maria Golder

The Materials Gap in the Fischer-Tropsch Synthesis

MODEL STUDIES ON Co(0001) AND Co($10\bar{1}15$) BY SCANNING TUNNELING MICROSCOPY AND GAS CHROMATOGRAPHY

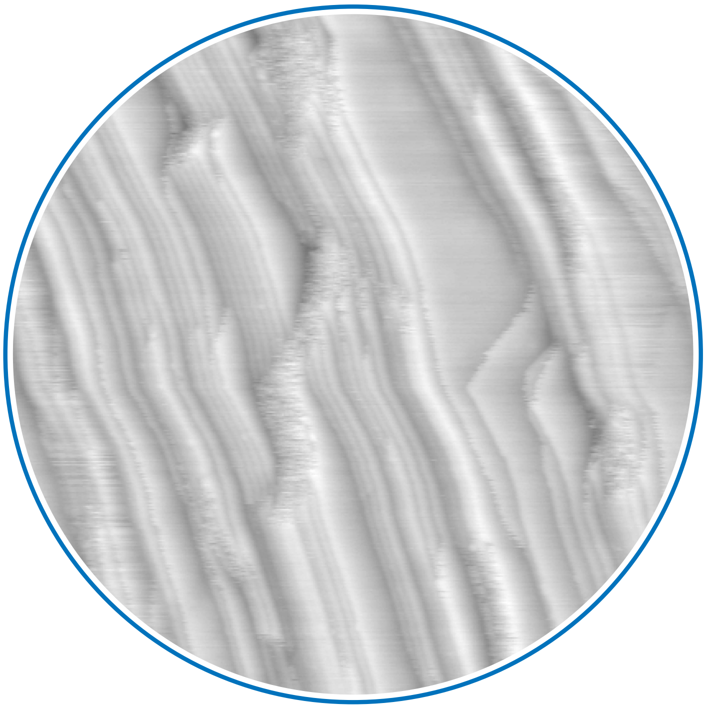

Dissertation
Physical Chemistry

Munich 2022

Dissertation zur Erlangung des Doktorgrades
der Fakultät für Chemie und Pharmazie
der Ludwig-Maximilians-Universität München

The Materials Gap in the Fischer-Tropsch Synthesis

–

Model Studies on Co(0001) and Co($10\bar{1}15$) by Scanning Tunneling Microscopy and Gas Chromatography

Katharina Maria Golder
(geb. Durner)

aus

Augsburg, Deutschland

2022

Erklärung

Diese Dissertation wurde im Sinne von § 7 der Promotionsordnung vom 28. November 2011 von Herrn Prof. Dr. Joost Wintterlin betreut.

Eidesstattliche Versicherung

Diese Dissertation wurde eigenständig und ohne unerlaubte Hilfe erarbeitet.

München, 30.08.2022

Katharina Golder

Dissertation eingereicht am:	30.08.2022
1. Gutachter:	Prof. Dr. Joost Wintterlin
2. Gutachter:	Prof. Dr. Sebastian Günther
Mündliche Prüfung am:	11.10.2022

Every great and deep difficulty bears in itself its own solution.
It forces us to change our thinking in order to find it.
[Niels Bohr (1919)]

Table of Contents

List of Publications

This thesis includes the following three publications, listed in chronological order. They are reprinted in the chapters 3.4 (**2**), 4.1 (**1**) and 4.2.1 (**3**).

1. **The active sites of a working Fischer-Tropsch catalyst revealed by operando scanning tunnelling microscopy**
   B. Böller, K. M. Durner, J. Wintterlin
   Nat. Catal. **2019**, *2*, 1027–1034.

   Contributions by K. M. Golder: modifying and testing the first version of the GC, assisting GC and XPS measurements, performing the STM study of the sputtered Co(0001) crystal in vacuum

2. **A highly sensitive gas chromatograph for in situ and operando experiments on catalytic reactions**
   K. M. Golder, B. Böller, G. Stienen, J. Sickerling, J. Wintterlin
   Rev. Sci. Instrum. **2021**, *92*, 124103.

   Contributions by K. M. Golder: modifying and testing the first version of the GC, performing calibration measurements, performing all experiments and analyses, preparing the images, writing the manuscript

3. ***In Situ/Operando* STM of the Fischer-Tropsch Synthesis on a Co($10\bar{1}15$) Surface – A Study to Bridge the Materials Gap between Single-Crystal Models and Supported Catalysts**
   K. M. Golder, J. Wintterlin
   ACS Catal. **2022**, *12*, 7199–7209.

   Contributions by K. M. Golder: performing all experiments and analyses, preparing the images, screening and analyzing the literature data of supported nanoparticles, writing the manuscript

Additional Publication:

4. **Lithium tin sulfide – a high-refractive-index 2D material for humidity-responsive Photonic Crystals**
   K. Szendrei-Temesi, O. Sanchez-Sobrado, S. Betzler, K. M. Durner, T. Holzmann, B.V. Lotsch
   Adv. Funct. Mater. **2018**, *28*, 1705740.

CHAPTER 1

Introduction

More than 90 vol% of the chemicals worldwide are produced by means of heterogeneous catalysts.[1] Catalysts increase the reaction rates by lowering the activation barrier, e.g., due to the stabilization of a reactive transition state, without being expended.[2] By definition, heterogeneous catalysts are present in a phase different from that of the reactants. Typically, they are solid materials like metal nanoparticles stabilized by relatively inert support materials and the reactants are present in the gas or liquid phase.[3] As the reaction takes place at an interface, the surface structure of the catalyst is significant for its performance. Usually, specific active sites play a critical role. Active sites are formed by a certain fraction of atoms on the catalytic surface, e.g., some defect, at which a key step of the reaction takes place.[4] The knowledge about active sites is thus crucial for the understanding of catalytic reactions. However, the identification of active sites is an enormous challenge as the catalytic surface may undergo dynamic structural transformations, so that active sites may only exist under reaction conditions. An *ex situ* analysis of a surface of a catalyst may therefore not provide information about the active sites, creating the necessity of analyzing the surface under working conditions.[5] To correlate this information with the activity, one ideally has to measure the catalytic turnover in the same experiment. These so-called *operando* measurements can reveal insights into the mechanism of a catalyzed reaction but the analysis of surfaces at high temperatures and pressures drives the analytical methods to their physical limits.

As most surface sensitive methods, e.g., X-ray photoelectron spectroscopy (XPS) or low-energy electron diffraction (LEED), are based on the detection of electrons, vacuum conditions below ~1×10^{-4} mbar are needed because of the inelastic mean free path of the electrons in the gas phase. In order to control the coverage of adsorbates on the surface, experiments in surface science are usually performed under ultra-high vacuum (UHV) conditions.[6] In contrast, industrial catalytic processes operate at pressure of several bar.[7] The difference in pressures of more than 10 orders of magnitudes is termed “pressure gap”.[2] To get insight into the mechanisms of industrially catalyzed reactions, it is necessary to perform studies at similar conditions. During the last decades, great efforts have been undertaken to overcome these pressure limitations. For example, near-ambient pressure XPS has been be realized by separating the sample cell and the electron analyzer by differential pumping or ultrathin membranes.[5,8] However, XPS has so far been restricted to pressures of a few mbar.

One of the few surface methods that has no general pressure limitations is scanning tunneling microscopy (STM).[8,9] In this method, electrons tunnel between the sample and a tip, which are separated by a few nanometers, so that only a few gas molecules are present in this gap. The tunneling currents can therefore be measured at arbitrary pressure. Various solutions for high-pressure scanning tunneling microscope (HP-STM) setups have already been developed.[9] For example, the group in Leiden[10] operates a small reactor cell in which only the tip of the STM is exposed to the gas phase in the reactor. The groups in Berkeley and Aarhus use high-pressure cells, housing the complete STM setups, and attached UHV chambers for sample preparation or further surface analysis.[11–13] The HP-STM setup used in the present work also consists of two chambers, one for *ex situ* analysis in UHV and the other for catalytic experiments with the STM.[14] Despite the principal possibility of operating an STM at elevated pressures, *operando* measurements are not easy. One challenge for *operando* STM measurements is to achieve stable atomic resolution under reaction conditions, typically at elevated temperatures. At the same time, one has to be able to measure the formation rates of products. Because of the relatively large volume of the chamber that houses the STM and the small catalytic surface, product concentrations are generally low. Hence, a sensitive detection of the reaction products is required. If successful, the combination of STM with activity measurements has the potential of identifying the active sites of a catalytic reaction.

One of the most complicated heterogeneous catalyzed reactions for which the nature of the active sites is still under debate is the Fischer-Tropsch synthesis (FTS). Patented in 1925 by Fischer and Tropsch,[15] the synthesis of long hydrocarbons from CO and hydrogen is becoming increasingly important as it allows for the production of liquid fuels. Rising crude oil prices and the climate crisis draw attention to synthetic alternatives for gasoline or diesel. Based on synthesis gas (syngas), a mixture of CO and H_2, valuable middle distillates and lubricants can be produced.[16,17] Depending on the conditions and the catalyst,[18,19] syngas is mainly converted to saturated and unsaturated hydrocarbons:

$$n\,\mathrm{CO} + 2\,n\,\mathrm{H_2} \xrightarrow{\text{cat.}} \mathrm{C}_n\mathrm{H}_{2n} + n\,\mathrm{H_2O} \qquad \text{(olefins)}$$

$$n\,\mathrm{CO} + (2\mathrm{n}+1)\,\mathrm{H_2} \xrightarrow{\text{cat.}} \mathrm{C}_n\mathrm{H}_{2n+2} + n\,\mathrm{H_2O} \qquad \text{(paraffins)}$$ [20]

As in most plants the syngas comes from natural gas, the process is part of the more modern gas to liquid (GtL) technology, but the coal to liquid (CtL) process is still applied in industry.[16,19,21,22] As syngas can also be obtained from renewable sources, the FTS gained increasing interest in the last years. In the power to liquid (PtL) process, H_2 is produced by the electrolysis of water and CO by the inverse watergas-shift reaction from CO_2.[19,23] Also biomass can be converted to syngas for the FTS (biomass to liquid, BtL).[18,24–27] Pilot plants, using biomass and wind power, showed that sustainable liquid fuel production is possible.[28,29]

In the present, in commercial FTS, multitubular fixed bed and slurry reactors are applied in the so-called low-temperature Fischer-Tropsch (FT) process. Temperatures in the industrial plants are between 220 and 240 °C and pressures between 20 and 45 bar, with H_2:CO-ratios of 1.7 – 2.15.[16,30,31] Mostly, iron or cobalt-based catalysts are used.[17,19,21,32] The transition metals Ru > Fe > Co > Rh > Ni > Ir > Pt > Pd, ordered according to the average molecular weights of the produced hydrocarbons, are active FT catalysts.[33] Due to their high costs, the 4d and 5d metals of this row are not used in industry and Ni is avoided because of its high selectivity towards the undesirable product CH_4.[16] This leaves Fe and Co as actual FT catalyst. Compared to iron, cobalt catalysts are more resistant to deactivation, and their activity at high conversions is higher. Moreover, the higher water-gas shift (WGS: $CO + H_2O \rightleftharpoons CO_2 + H_2$) activity on iron catalysts leads to an enhanced formation of the undesired byproduct CO_2.[16,19] The conversion of CO and the production of additional H_2 by the WGS reaction alters the H_2:CO ratio and affects the FT performance of the catalyst. For this reason, cobalt catalysts are preferred in the industrial GtL process compared to iron-based catalysts, despite their higher costs. Commercial FT catalysts consist of cobalt nanoparticles, usually dispersed on oxide supports like Al_2O_3 or SiO_2. Furthermore, it is common to modify the support by structural promoters, e.g., with oxides of Zr, La or Si. Promoters like Pt, Ru, or Re are added to facilitate reduction of the starting material of the catalyst.[17,25,32,34,35] This thesis focuses on the FTS on bare cobalt.

While industrial catalysts are usually highly complex systems, surface science works with well-defined surfaces. This approach is based on the expectation that clearer information about the surface processes is obtained on single crystals.[2,36,37] For FTS, Co(0001) single crystals and a few other orientations has been used as model systems for catalysts.[38–42] Although it is assumed that general aspects of the reaction mechanism can be captured on single crystals, there are some characteristics of supported catalysts which cannot be reproduced, e.g., the fact that nanoparticles display several facets or the interaction with the supporting material. The difference in shape and composition between surface science systems and industrial catalysts is called “materials gap”.

Figure 1.1 shows a comparison of the Co(0001) surface and a Co nanoparticle. Bulk Co has a hexagonal close-packed (hcp) structure, and most surface science studies have used single crystals with the (0001) orientation. In contrast to bulk Co, the cobalt nanoparticles of the industrial catalyst are mainly face-centered cubic (fcc)[43] and display rounded-off, cubo-octahedral shapes.[44,45] While the Co(0001) model only provides one densely packed surface with few steps, the fcc nanoparticles contain several facets, are rich in defects, and display a high step density.[44,45]

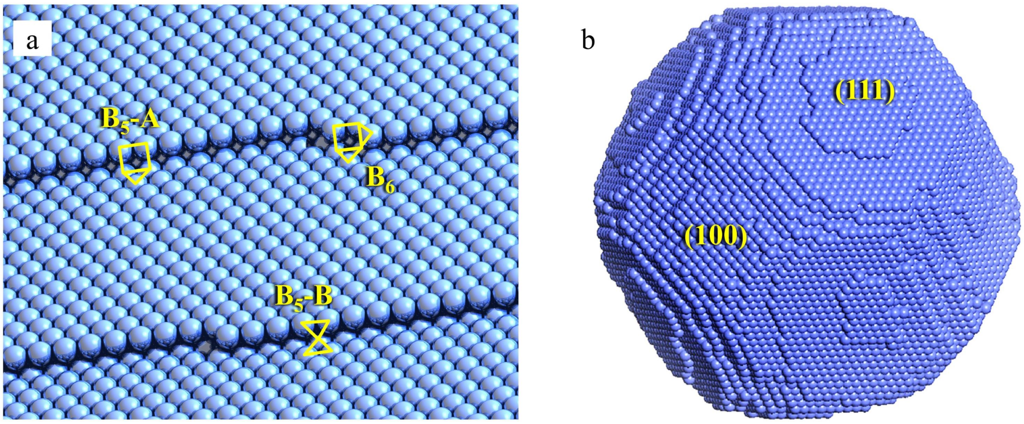

Figure 1.1: Models of the catalytic surfaces used in FTS. (a) shows the hcp (0001) surface of a single crystal and (b) a model of a fcc nanoparticle [(b) was adapted from ref. [44], with permission from Elsevier]. The different step (B_5-A and B_5-B) and kink (B_6) sites which exist on the densely packed surface (a) and the exposed facets of the nanoparticles (b) are indicated.

Whether the activity of the Co FTS catalyst is sensitive to the surface structure is under debate. While experiments on single crystals indicate that the activity is independent of the facets,[39] nanoparticles show a distinct size-dependent activity. The catalytic activity steeply increases with increasing particle sizes up to a diameter of approximately 8 nm and then levels off and remains constant for a wide range of particle sizes.[46] Due to the wide range in which the activity is independent of the particle diameter, the reaction has previously been assumed to be structure-independent which is not the case according to the more recent literature.[16,47] As this thesis deals with the question of how the surface structure is related to the catalytic performance, chapter 4 discusses activity-vs-particle size rates for FTS in detail.

As a surface polymerization reaction, the FTS can be divided into three major reaction steps: reaction initiation, chain growth and reaction chain termination.[48] Details of the mechanism are not understood. Mainly two different mechanisms concerning the chain growth are discussed – the carbide mechanism[49] and the CO insertion mechanism.[50] The key issue is how a single C unit becomes inserted into a growing hydrocarbon chain. According to the carbide mechanism, a C atom is formed by the initial cleavage of the C-O bond of an adsorbed CO molecule. The C atom is partially hydrogenated to give an adsorbed CH_x moiety, which is incorporated into the growing chain. In the CO insertion mechanism, the chain growth is divided into two steps. After direct or hydrogen assisted dissociation of CO and formation of a CH_x moiety, a further CO molecule or partially hydrogenated intermediate (CHO or CHOH) becomes inserted into the CH_3 surface bond. In the second step, the C-O bond of the inserted unit is cleaved, and the C atom in the chain is hydrogenated. Insertion, bond cleavage, and hydrogenation are then repeated. Depending on the chain termination step, both mechanisms can explain the formation of paraffins (hydrogen addition) and olefins (CH cleavage), whereas oxygenates must be the result of the CO insertion mechanism or formed by a combination of both mechanisms.[31,48]

Common to both mechanistic proposals is the initial cleavage of the C-O bond of the adsorbed CO. Most likely, this step is rate-limiting in the FT synthesis. Quantum chemical data show that this step is very sensitive to the site structure. The calculated activation barrier for the dissociation of CO on a step site, 1.20 to 1.61 eV, is significantly lower compared to that on the flat surface (2.28 – 3.80 eV).[48,51] Consequently, the whole reaction should be structure sensitive. In this picture, step edge sites are the active sites of the FTS.[51,52] There are a few *in situ* STM studies of FT synthesis[41,53–56] but none of them determined correlations of possible active sites and activity. The broad range where the catalytic activity is independent of particle size has been explained by a roughening or dynamic surface reconstruction of the Co surface during the reaction.[42,57,58] There are also density functional theory (DFT) calculations claiming that the formation of nano islands and clusters, which are responsible for the surface roughening, is driven by the presence of adsorbed C atoms formed by the reaction.[53,59,60] However, the present work does not show any roughening of the Co(0001) surface under reaction conditions.[61] It seems that an alternative explanation for the plateau in the activity-vs-particle size function is needed.

This thesis focuses on the aim of bridging the materials gap between single-crystal and nanoparticle FTS catalysts by means of *operando* STM studies. In order to achieve this goal, the existing STM setup had to be extended by a highly sensitive gas chromatograph. To answer the question of whether single crystals can serve as models for industrial catalysts, a Co($10\bar{1}15$) crystal, which has a step density similar to that of industrially applied nanoparticle catalysts, was investigated.

The structure of this thesis is as follows. Chapter 2 describes the HP-STM setup, the samples, and the procedure of the measurements. It also introduces the analytical methods and the data evaluation procedure. In chapter 3, experimental improvements which were achieved in this thesis are described. To examine the problem of Ni deposition, a reactor setup was developed for testing experiments. The results are presented in section 3.1. Another problem, connected with the glass fibers used for sample heating by an IR laser in the STM chamber is investigated in section 3.2. The following section 3.3 describes the temperature calibration of the Co samples.

For the performance of *operando* STM experiments, a new analytical device for activity measurements was needed. Details of the customized gas chromatograph (GC) setup as well as its performance and calibration are described in the article “A highly sensitive gas chromatograph for *in situ* and *operando* experiments on catalytic reactions” (section 3.4). Based on the altered setup, new insights into the mechanism of the FT synthesis were possible. The experimental results of two *operando* studies on Co(0001) and Co($10\bar{1}15$) single crystals are presented in chapter 4 in the published articles “The active sites of a working Fischer–Tropsch catalyst revealed by operando scanning tunnelling microscopy” and “*In Situ/Operando* STM of the Fischer-Tropsch Synthesis on a Co($10\bar{1}15$) Surface – A Study to Bridge the Materials Gap between Single-Crystal Models and Supported Catalysts”. Both studies treat the structure sensitivity of the catalytic activity of Co single crystals during FTS. The first study reveals correlations between step density and catalytic activity; the second bridges the materials gap between Co single crystals and supported nanoparticles.

CHAPTER 2

Setup and Methods

2.1 High-Pressure STM Chamber

The *operando* Fischer-Tropsch experiments in this thesis were performed at an existing high-pressure scanning tunneling microscope system (high-pressure STM, HP-STM). The basic setup was developed by Rößler and Wintterlin (see ref. [14]) and expanded by Böcklein[62] and Böller[63]. During this thesis, a new analytical method – a customized gas chromatograph – was attached to the STM chamber. With the extended setup *operando* STM measurements can be performed at pressures up to 950 mbar at temperatures up to 240 °C.

A schematic of the setup is depicted in Figure 2.1. It combines a conventional ultra-high vacuum (UHV) chamber (here called preparation chamber) and an additional chamber, which serves as catalytic reactor and houses the STM (STM chamber or STM cell). Using a transfer rod, samples can be transferred between the two chambers without breaking vacuum. The gas inlet, attached to the STM chamber, was mainly designed and installed by B. Böller[63]. With this system, syngas between ~100 and 950 mbar can be fed into the STM cell. The UHV components are linked by means of ConFlat (CF) flanges, the gas inlet and the connection to the GC is based on Swagelok-fittings. More details about the setup and the sample preparation are given in the following.

2.1.1 Preparation Chamber

The preparation chamber is a typical UHV chamber, which was used for sample preparation before reaction experiments as well as for *ex situ* analysis afterwards. The pump unit I (see Figure 2.1), consisting of a turbomolecular pump and a rotary vane pump with attached zeolite trap as well as a combined ion and titanium sublimation pump provides a base pressure of approximately 8×10^{-11} mbar. The pressure is measured with an ionization gauge. The position of the sample for preparation or analytical purpose can be adjusted by a manipulator. It is equipped with a tungsten filament for sample heating and S-type thermocouple contacts for temperature measurement of

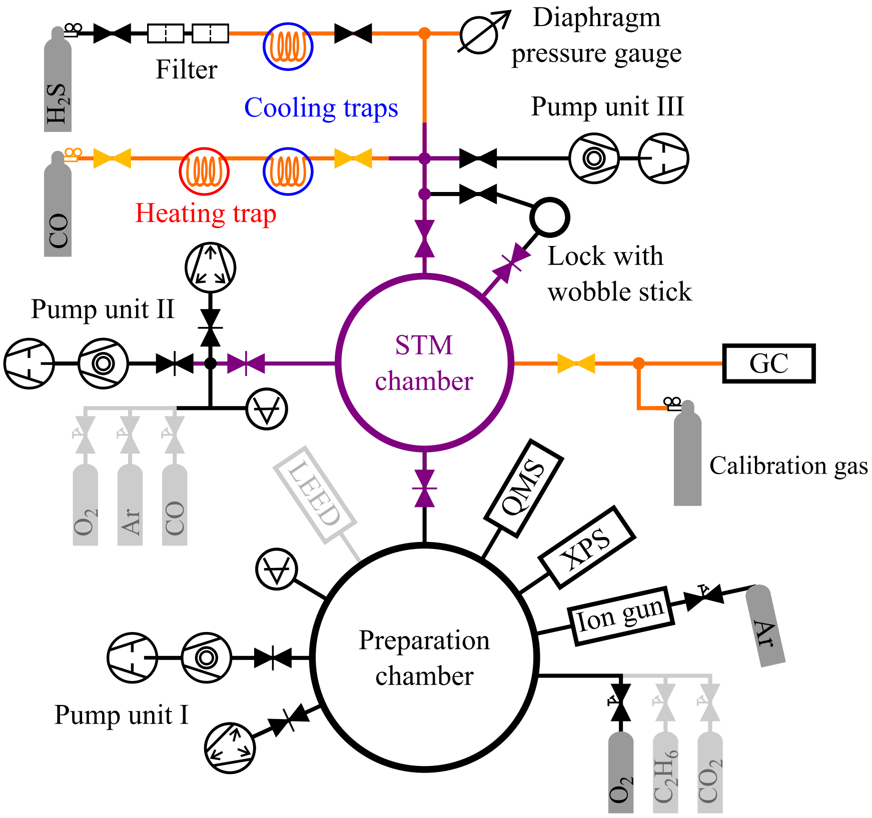

Figure 2.1: Scheme of the HP-STM setup. The STM chamber is connected to the preparation chamber by a transfer rod. Si-coated components are displayed purple, copper pipes orange, brass valves yellow and stainless steel components black. Parts which have not been used in this work are displayed in light grey.

the sample by a meter providing room temperature correction. A PID (proportional-integral-differential) controller is used to hold the desired sample temperature. By means of a wobble stick, samples can be transferred from the manipulator to the transfer rod or to the sample magazine in the preparation chamber. Samples were cleaned by Ar^+ ion sputtering (ISE 10 sputter ion source, Omicron), oxidation and annealing. The gases O_2 (purity 99.995 Vol %, Linde) and Ar (purity 99.999 Vol %, Messer-Grießheim) are dosed from minicans by leak valves into the preparation chamber. A quadrupole mass spectrometer (QMS, Prisma QMS 200 M2, Pfeiffer-Vacuum) was used for residual gas analysis as well as for leak detection. Due to its insufficient detection limit, catalytic activity measurements of the FT synthesis cannot be performed by means of QMS. For this purpose, a new custom gas chromatograph was attached to the STM cell. The low-energy electron diffraction (LEED) unit was not used in this thesis. Control of sample cleanliness as well as *ex situ* surface analysis were performed by XPS. The chamber is equipped with a monochromatic Al K_α ($h\nu = 1486.6\,\text{eV}$) X-ray source (XM 1000 MKII, Omicron) and a hemispherical energy analyzer (Phoibos 100, Specs, work function = 4.9 eV) equipped with five channeltrons for electron detection. During this thesis, the X-ray anode had to be replaced because of a crack at the surface. After installing a new anode and baking the chamber, monochromator and sample position were calibrated by means of a Ag(111) crystal [E_B(Ag 3d$_{5/2}$) = 368.3 eV].

2.1.2 STM Chamber and Gas Supply

The STM chamber is a small UHV chamber with a volume of approximately 1.8 L. It houses the STM head and the copper stack with fittings for the sample holder. A second wobble stick is used to grab the sample holder at the transfer rod and transfer it to the STM. The wobble stick is mounted to a tube that can be sealed from the STM cell by a gate valve and serves as load-lock to transfer samples into/out of the setup without breaking the vacuum. The STM chamber is connected to a separate pump unit II (Figure 2.1) and ion gauge, which can be sealed off from the STM chamber by a gate valve. Additional gate valves to the preparation chamber and the wobble stick are closed when the STM cell is filled with syngas by means of the gas supply. STM measurements can be performed between vacuum conditions (base pressure ~3×10^{-9} mbar) and a pressure of 950 mbar. Further increase in pressure is currently not possible as the system is not designed for internal overpressure. Therefore, the reaction pressure is currently limited to ambient pressure (~950 mbar in Munich). An additional pump unit III is used to evacuate the STM chamber after high-pressure experiments to a pressure lower than 1×10^{-5} mbar before reopening the gate valve to the pump unit II and transferring the sample to the UHV chamber. A diaphragm pressure gauge (CDG020D, Inficon), located in the gas inlet pipes is used to measure pressures between 10 and 1000 mbar. Nearly all components of the STM chamber that are in contact to syngas were coated by amorphous silicon (SilcoGuard 100, Silcotek GmbH) to avoid the formation of nickel carbonyls. Problems with Ni contaminants arose when the syngas pressure was increased during the studies by B. Böller. In order to avoid Ni containing components, all commercial electrical and thermocouple feedthroughs were replaced by home-built versions and stainless steel components were replaced by components made from other metals, such as Al, Mo or Ta. Details are described in the thesis of B. Böller, reference [63]. For the gas inlet, copper pipes as well as brass valves and fittings are used to avoid contamination with Ni. The reactant gases are fed through filters and traps to avoid contamination of the sample by the gases. The H_2 pipe is equipped with an inline water filter (MicroTorr MC1-904FV, $H_2O, O_2, CO, CO_2 < 0.1$ ppb, Saes Gasproducts) and an S-filter (MicroTorr MC50-403F; volatile acids, organics, refractory compounds < 1 ppt; volatile bases < 5 ppt; metals < 1 ppb; Saes Gasproducts), followed by a liquid nitrogen trap. The CO pipe is equipped with a heating trap (Cu pipe loop filled with molecular sieve, operating temperature ~300 °C) and a liquid nitrogen cooling trap. Both cooling traps consist of a loop of Cu pipe, filled with molecular sieve, in a dewar containing liquid N_2.

The STM head is of the beetle-type. It can be placed on the sample holder by means of a lifting frame. The STM chamber with magnified STM head is shown in Figure 2.2. The STM head consists of four piezo tubes glued to an anodized Al disc. The outer three piezo tubes serve as the legs of the beetle to the ends of which ruby balls are glued (the feet of the beetle) on which it stands on the sample holder. Scanning is performed by means of the central piezo, holding the tip, which consists of an etched Pt/Ir wire (80/20, 0.25 mm). Due to the inclined planes of the sample holder, the tip can be approached to the sample surface by applying tangential voltages to the outer piezos so that the beetle rotates in a stick-slip motion. By applying voltages in x or y directions, the beetle moves in a stick-slip motion parallel to the surface. The sample holder rests on a stack of Cu plates, which are separated by viton loops for vibrational decoupling. In the framework of the present experiments, all Cu plates were cleaned by grinding and polishing to remove possible Ni depositions. A clamp, made of a thermocouple pair at the mounting assembly on the Cu stack, makes contact to the thermocouple on the sample when the sample holder is inserted into the mounting assembly.

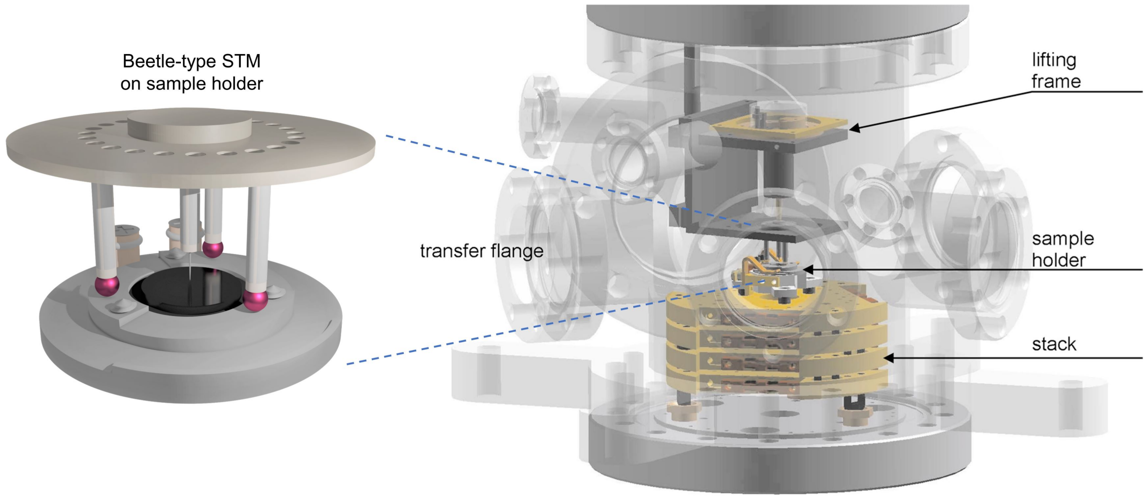

Figure 2.2: Scheme of STM cell (right) including Cu stack, sample holder and lifting frame (reprinted from ref. [14], with the permission of AIP Publishing). The beetle type STM on a sample holder is magnified on the left hand side.

The sample within the STM chamber can be heated by means of an IR diode laser (LDD 50/LIMO32-S1779, LIMO GmbH) providing light with a wavelength of 808 nm at a maximum power of 32 W. The light is coupled into the chamber by means of a glass fiber and illuminates the back of the sample. A detailed description of the glass fiber setup is given in section 3.2 where the degradation problem of glass fibers is investigated.

For analysis of the catalytic activity of the samples, a specially designed GC was attached to the STM cell. The setup is described in detail in section 3.4. Due to problems with Ni contamination during experiments, GC measurements, shown in chapter 4, were also performed in a simplified setup without installed STM, as it is a possible source of Ni deposited on its surfaces in previous experiments. In this configuration, the STM was de-installed and replaced by a blind flange and the Cu stack was replaced by a flange with a simplified mounting assembly and feedthroughs for the glass fiber and the thermocouple. Because all commercial electrical feedthroughs contain Ni or Ni alloys, versions with glued-in contacts were built.

2.1.3 Samples

The FT experiments of this thesis were performed with a Co(0001) sample (MaTeck, 99.99 %), a Co(10$\bar{1}$15) sample (MaTeck, 99.99 %) and a Au(111) sample (MaTeck, 99.999 %) for measurements of the blank activity. In order to measure the sample temperature by means of a thermocouple at the sample and nevertheless be able to transfer the sample from the preparation chamber to the STM cell, a special sample holder is used. A scheme of the sample/sample holder setup is depicted in Figure 2.3.

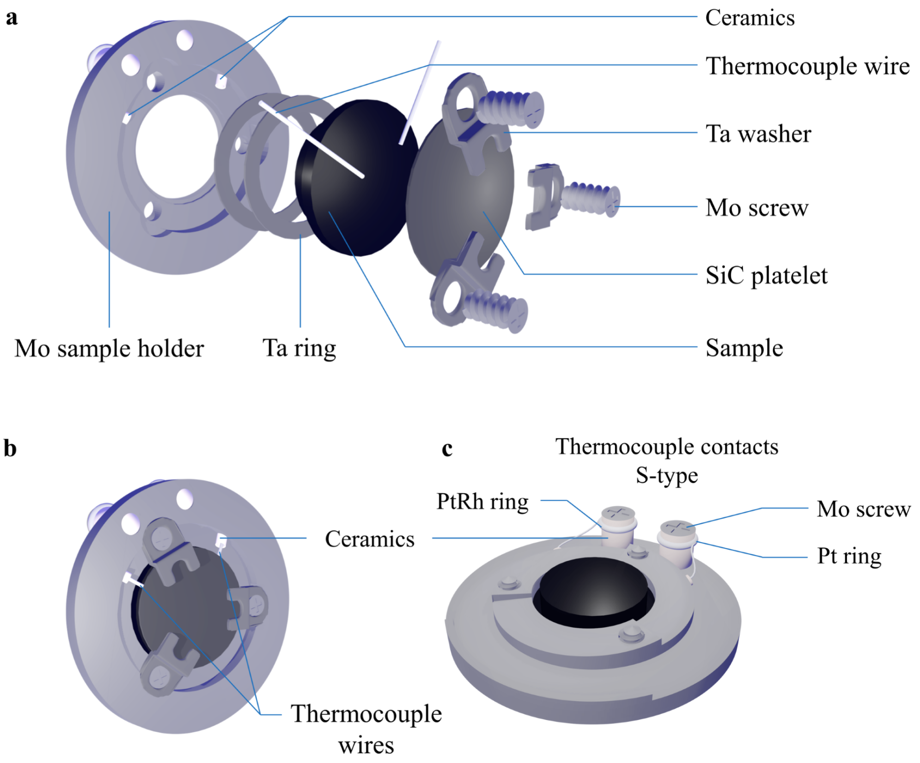

Figure 2.3: Scheme of the sample setup. (a) The sample is inserted from the back into the Mo sample holder and fixed by means of a SiC platelet and Ta washers/Mo screws. Ta rings allow to adjust the crystal height. (b) Back view of the complete sample setup with sandwiched thermocouple wires in between sample and SiC platelet. (c) Top view of a complete sample setup with mounted S-type thermocouple contacts for temperature measurements.

The sample holder is made of Mo and provides three inclined, polished planes which are used for the coarse approach of the beetle. The samples are hat-shaped single crystals (bottom diameter: 7 mm, top diameter: 5 mm, height: 1.8 mm). The surface was polished by the manufacturer down to a residual roughness of $< 0.03\,\mu\mathrm{m}$ for the Co(0001) sample and $< 0.01\,\mu\mathrm{m}$ for the Co($10\bar{1}15$) sample and an accuracy of the orientation of $< 0.1°$. Using the rim of the hat-shaped samples, the crystals are mounted in an opening in the center of the sample holder [see Figure 2.3 (a)]. A sandwich, consisting of a sample and a SiC platelet at the bottom is mounted to the holder by means of three Ta washers and Mo screws. The SiC platelet serves as absorber of the laser light used for heating; the metallic samples were too reflective. To adjust the correct distance between the sample surface and the STM tip, Ta rings can be placed between the sample holder and the crystal. The temperature is measured by means of an S-type thermocouple mounted to the sample holder. Pt and PtRh wires (0.05 mm) are sandwiched between the crystal and the SiC platelet and fed through ceramic tubes to the front side of the sample holder, where they are spot-welded to sleeves of ∅ 0.5 mm Pt/PtRh wires mounted to Al_2O_3 insulation tubes [see Figure 2.3 (b) and (c)]. The tubes are fixed by means of Mo screws at the rim of the sample holder. The Pt/PtRh sleeves make contact to corresponding fittings at the manipulator of the preparation chamber as well as at the mounting assembly in the STM chamber when the sample holder is inserted into the respective fittings. The sample temperatures are measured by means of meters with integrated room temperature correction. A problem with this configuration was that the temperature measured with the thermocouple clamped between the backside of the sample and the SiC platelet considerably differed from the temperature of the frontside, as was found out in later experiments. For this reason, calibration experiments with additional thermocouple wires were performed. The results are discussed in section 3.3.

2.1.4 Sample Preparation

The samples were cleaned by alternating sputtering and annealing cycles of variable duration in the preparation chamber. All crystals were sputtered by means of the ion source, operated at $7{\times}10^{-7}$ mbar Ar at an acceleration voltage of 985 V and 10 mA emission current. Because of the hcp-to-fcc phase transition of Co around 422 °C,[64,65] the samples were never heated to temperatures above 360 °C to avoid any damage to the crystallinity. The Au crystal, which was used for reference measurements, was treated in the same way as the Co samples and was also annealed at 350 °C for reasons of comparability. Due to the low temperature, flat hillocks were detected in the STM images of the Co($10\bar{1}15$) as well as of the Co(0001) crystal. They were caused by incorporated Ar atoms into the Co lattice from sputtering and could not be completely removed at the low annealing temperature. During preparation, the surfaces were regularly analyzed by XPS to check for residual contaminants. When large amounts of carbidic carbon were present, these were removed by oxidizing the crystal for 5 min at 350 °C at $5{\times}10^{-8}$ mbar and subsequent sputtering. As the Co($10\bar{1}15$) crystal had not been used in experiments before, it had to be prepared for several weeks before it could be used for FT experiments. After concluding the initial preparation, a single sputtering and annealing cycle was enough to clean the surface from contaminants from the former experiment.

2.1.5 Experimental Procedure

For a typical *operando* FT experiment, presented in section 4.2.1, the crystal was first sputtered for 15 min in the preparation chamber. During the last 5 min of the sputtering, the sample was heated to 350 °C. Once a temperature of 350 °C was reached, sputtering was stopped and the crystal was annealed at 350 °C for ~12 min. XPS analysis of the C 1s and O 1s regions was performed to ensure cleanliness of the surface. For the experiments aiming at an enhanced step density of the Co(0001) sample, the crystal was sputtered again for 10 min. Subsequent to the preparation and surface analysis in the preparation chamber, the crystal was transferred to the STM chamber.

Depending on the experiment – STM or GC –, the beetle of the STM was placed on the sample or not. STM and GC analysis were not performed simultaneously but in separate experiments for practical reasons. Because of the manual operation of a valve between the STM chamber and the GC, it would have been necessary to interrupt the scanning process for every GC measurement in order not to damage the tip or cause vibrations by touching the valve. Hence, scanning at the same position for more than 1 h would not have been possible, as GC samples were taken regularly every hour. Furthermore, it would not have been possible to switch off the pump of the GC during STM measurements. For both types of experiments, the valves to the load-lock and the pump unit II were closed before 320 mbar CO were led in through the heating and cooling trap into the STM cell. The H_2 was led in through the other cold trap until a pressure of 920 mbar was reached. As the gas atmosphere heats up during experiments, this reduced pressure was chosen to prevent internal overpressure; it corresponds to ~950 mbar at elevated temperatures. Once the final pressure was reached, the pipes of the gas dosing systems were evacuated by means of pump unit III (Figure 2.1). In the STM experiments, first some images were recorded at room temperature, after which the sample was heated to 220 °C[1] by means of the laser. In the GC experiments, first a gas sample of the syngas was injected into the GC to determine the amount

---

[1] This value corresponds to the temperature measured at the bottom of the crystal. The calibration procedure and resulting temperatures at the surface are discussed in detail in section 3.3.

of impurities in the syngas at room temperature. Then the laser was turned on, and every hour a gas sample was extracted for analysis by the GC.

Once an STM or GC experiment ended (usually after 6 h), the laser was turned off and the sample was cooled down in the gas atmosphere to a temperature below 65 °C before evacuating the chamber via the pump unit III. When a pressure of 1×10^{-7} mbar was reached, the sample was transferred to the preparation chamber and analyzed by means of XPS.

2.2 X-Ray Photoelectron Spectroscopy

X-ray photoelectron spectroscopy (XPS) was used for surface chemical analysis during preparation and after reaction experiments at the HP-STM. The Au-coated Si wafers, used in the test reactor for nickel deposition (see section 3.1), were analyzed in another vacuum chamber (called XPS chamber in the following). XPS is a surface-sensitive technique because the mean-free path of the photoelectrons, created by the soft X-ray radiation, is only a few atomic layers.[6] Because standard XPS, as applied here, requires vacuum, the composition of the surface layers could only be analyzed *ex situ*, after finishing an elevated-pressure reaction experiment. The technique is shortly described below.

The illumination of a sample by soft X-rays of a given energy $h\nu$ leads to the emission of photoelectrons from its surface. Their kinetic energy (E_{kin}) in vacuum is given by $h\nu - E_B - e\phi_S$, where E_B corresponds to the binding energy of the orbital from which the electron originates and $e\phi_S$ is the work function of the sample. Connecting the sample electrically to the analyzer leads to an alignment of the Fermi levels E_F, which creates an electrical field between the sample and the analyzer. The kinetic energy of the electrons in the analyzer is therefore related to the work function $e\phi_A$ of the analyzer:[6,67]

$$E_B = h\nu - E_{kin} - e\phi_A \tag{2.2.1}$$

A scheme of the corresponding energy levels is shown in Figure 2.4. As the binding energies are specific for each orbital, every element shows a unique set of E_B. This fact allows one to determine the elemental composition at the sample surface. Figure 2.5 shows a survey scan of the clean Co(0001) crystal that has been used for the Fischer-Tropsch experiments. The sharp peaks arise from photoelectrons of specific orbitals. In general, the p, d and f levels show spin-orbit splitting, resulting in more than one peak per orbital, namely $2p_{1/2}$ and $2p_{3/2}$ peaks in the XP spectra of Co. The splitting of the 3p level is not resolved in the Co survey spectra. Due to inelastic energy loss,

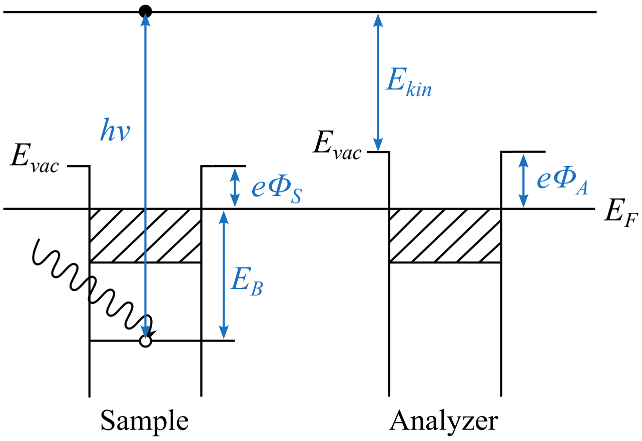

Figure 2.4: Schematic of the energy levels of solid surfaces that play a role in XPS according to ref. [66]. An X-ray photon with energy $h\nu$ causes an electron with binding energy E_B to exit from its core level. The emitted photoelectron has to overcome the work function of the sample $e\phi_S$ to reach the hypothetical vacuum level E_{vac}. Due to the same Fermi levels E_F of sample and analyzer, the E_B of the emitted photoelectron can be determined by measuring its kinetic engergy E_{kin} in respect to the work function of the analyzer $e\phi_A$ and the energy of the X-rays $h\nu$.

the background in the spectra rises towards higher binding energies. Auger lines (here LMM series) are the result of the Auger process. It describes the filling of the inner orbital vacancy, created by the emission of the first electron, by a second electron from a higher orbital and the simultaneous emission of a third electron, which carries off the excess energy.[67]

Changes in the chemical environment of elements may result in different oxidation states which change the binding energy of the involved orbitals. For this reason, also the chemical state of the adsorbates on the sample surface can be analyzed.[67] As a consequence, XPS allows one to distinguish, e.g., graphitic carbon and carbon originating from adsorbed CO molecules.

In the present experiments, monochromatic Al K_α ($h\nu = 1486.6\,\text{eV}$) radiation (measurements at the HP-STM setup) and non-monochromatic Mg K_α ($h\nu = 1253.6\,\text{eV}$) X-rays (measurements at the XPS chamber) were used. The monochromator narrows the line width of the X-ray and in this way the peaks in the photoelectron spectra, and it avoids satellite peaks originating from the $K_{\alpha3,4}$ radiation.[6] Concentric hemispherical analyzers served as analyzers and channeltrons as detectors of the photoelectrons. The work function of the analyzer at the HP-STM setup (4.9 eV) and at the XPS chamber (5.15 eV) had been determined in former works. In both setups, a constant pass energy was used (HP-STM: 10 eV, XPS chamber: 22.4 eV). In this operation mode, the emitted photoelectrons are accelerated or decelerated to a certain energy by means of a varying retarding potential between the sample and the entrance slit of the

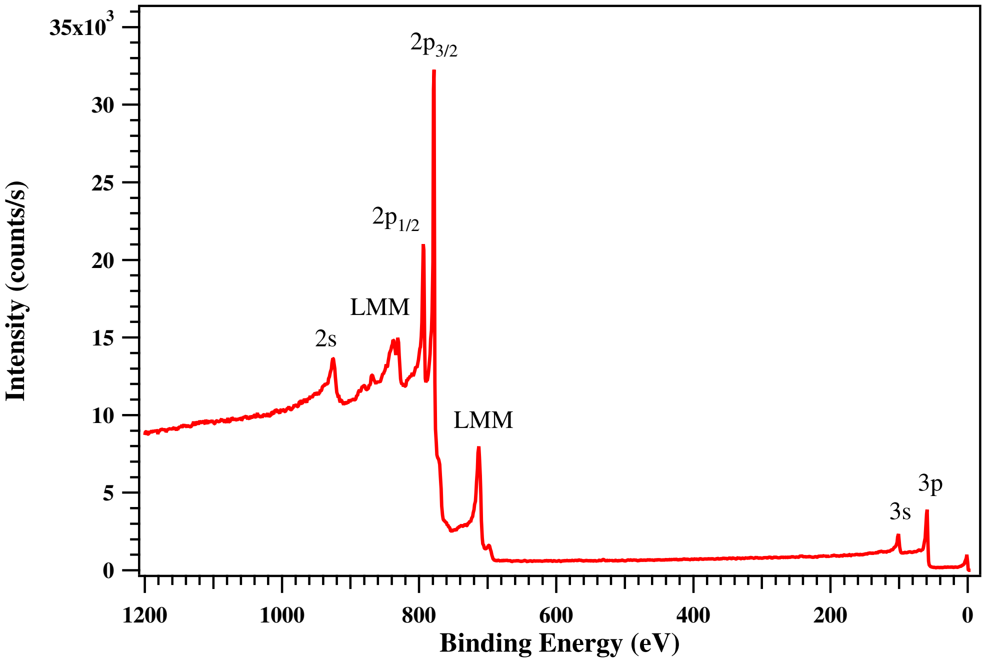

Figure 2.5: Survey XPS scan of the prepared Co(0001) surface. Besides the 2s, 2p, 3s and 3p peaks, also Auger LMM peaks are visible. The $2p_{3/2}$ peak shows the highest intensity.

analyzer. As a result, only electrons of a specific kinetic energy can pass the analyzer.

In addition to qualitative information about the elemental composition of a surface, XPS also provides a quantitative analysis. It is based on the fact that the signal intensity is proportional to the amount of detected photoelectrons. The proportionality factor depends on the energy of the photoelectrons and the orbitals from which they originate. The general expression for the signal intensity I_X of an XPS peak X is given by Equation 2.2.2[6] if the entrance aperture of the spectrometer is small and the sample is uniformly illuminated:

$$I_X = \sigma_X \cdot D \cdot L_X(\gamma) \cdot J_0 \cdot N_X \cdot \lambda_M(E_X)\cos(\theta) \cdot T \qquad (2.2.2)$$

σ_X is the photoionization cross section, D the detection efficiency of the electron spectrometer, $L_X(\gamma)$ the angular asymmetry of the emitted intensity with respect to the angle γ between the direction of incidence and detection, J_0 is the flux of primary photons on the sample surface, T is the transmission of the electron analyzer and N_X is the density of atoms X. $\lambda_M(E_X)\cos(\theta)$ determines the depth resolution due to the escape depth $\lambda_M(E_X)$ of the photoelectrons (inelastic mean free path within the metal M), where θ is the angle between the surface normal and the direction of electron detection. All XPS measurements within this work were performed with $\theta = 0$.

For the cross sections σ_X, tabulated values from ref. [68] were taken. The values are functions of the radiation energy and the orbitals. Due to the constant pass energy, D is constant and cancels when only relative peak intensities are analyzed. As the illumination is constant, the same holds for J_0.[6] $L_X(\gamma)$ and T have to be calculated.

The angular asymmetry factor $L_X(\gamma)$ is given by Equation 2.2.3:[6,69]

$$L_X(\gamma) = 1 + \frac{1}{2}\beta_A \cdot (\frac{3}{2}\sin^2\gamma - 1) \tag{2.2.3}$$

The values for β_A depend on the subshell and the atomic number and were extracted from the literature.[69] The value for γ is given by the geometry of the setup (HP-STM: 66°;[62] XPS chamber: 75°[70]).

The energy dependence of T for the XPS chamber was determined experimentally[71] and is given by Equation 2.2.4:

$$T(E_{kin}/\mathrm{eV}) = 102 \cdot E_{kin}^{-0.636} \tag{2.2.4}$$

E_{kin} is the kinetic energy of the emitted photoelectrons. Due to the lens setup in front of the analyzer of the HP-STM setup, its T is constant[72] and cancels for relative peak intensities.

For the present studies, two different quantification methods were used. Measurements at the HP-STM setup usually showed adsorbate layers on Co below one monolayer (ML). In this case, for the calculation of the coverages it was assumed that adsorbates are only present at the surface without any depth distribution in the substrate. As a result, the impact of damping can be ignored and damping only affects the deeper layers of the bulk material. Relative peak intensities I of the adsorbates referred to those of the metal substrate M lead to the surface coverage $\theta(X)$ of an adsorbate species X [% ML].

$$\theta(X)\ [\%\,\mathrm{ML}] = \frac{I_X}{I_M} \cdot \frac{\sigma_M}{\sigma_X} \cdot \frac{L_M}{L_X} \cdot \frac{T(E_{kin,M})}{T(E_{kin,X})} \cdot \Lambda_M \cdot 100 \tag{2.2.5}$$

The amount of detected atomic layers of the metal Λ_M can be calculated by means of the spacing of the metal d_M and the inelastic mean free path (IMFP) $\lambda_M(E_X)$ of photoelectrons within the metal:[63]

$$\Lambda_M = \left(1 - e^{\frac{-d_M}{\lambda_M(E_X)}}\right)^{-1} \tag{2.2.6}$$

d_M of Co(0001) is equal to 2.03 Å and the energy dependent values for the IMFP were calculated by means of the NIST Database[73] based on the data of Tanuma et al.[74].

If the adsorbate coverage exceeds one monolayer, its damping effect can no longer be ignored. As the spatial distribution is usually unknown in this case, for simplicity a uniform distribution of the elements within the analyzed area was assumed. The amount $\chi(X)$ of each element or species X can then be calculated as a ratio [atom %] in the sample. For simplicity, the number of detected layers Λ was calculated assuming the same layer distance as in the bare metal substrate.[63]

$$\chi(X)\ [\text{atom}\,\%] = \frac{N_X}{\sum_i N_i} \cdot 100 = \frac{\frac{I(X)}{\sigma_X \cdot L_X \cdot \Lambda_X \cdot T(E_{kin,X})}}{\sum_i \frac{I(i)}{\sigma_i \cdot L_i \cdot \Lambda_i \cdot T(E_{kin,i})}} \cdot 100 \tag{2.2.7}$$

All parameter values used for quantification calculations are listed in Table B.1 on page 99 and Table B.2 on page 99.

The signal intensities I and binding energies E_B were evaluated by means of the IGOR Pro software.[75] The fit routine was developed by Sebastian Günther. It uses a convolution of Gaussian and Doniach-Šunjić[76] functions as fit functions and a linear baseline correction. For more details see ref. [62]. The fit functions were adjusted using the method of least squares. Variable parameters were the E_B value, the Gaussian as well as the Lorentzian broadening, the asymmetry parameter, and the signal intensity and background slope.

At the HP-STM setup, XP spectra of the Co 2p, C 1s and O 1s peak were recorded before each experiment and additionally of the Ni 2p and S 2p peaks after the reaction experiments, i.e., *ex situ*. Due to an overlap of the Co $2p_{3/2}$ and an Auger Co-LMM peak, the Co $2p_{1/2}$ peak was used for the analysis of the Co substrate instead of the more intense Co $2p_{3/2}$ peak. For quantification purposes, the intensity was multiplied by 3 to obtain the intensity of the total Co 2p peak, which uses the intensity ratio of the spin-orbit-split p doublet. Furthermore, after each experiment, survey scans were measured to exclude further contaminants. Due to the necessity to perform the XPS analysis *ex situ*, the significance with respect to the coverages of the surface species in the high-pressure experiments is limited as the coverage may change during pumping down to UHV. However, major chemical changes, for example a surface oxidation, should be detectable. Furthermore, the amount of non-gaseous contaminants, namely S or Ni, should not change during evacuating the chamber.

The analysis of samples from the test reactor for nickel deposition (see section 3.1) was even more limited. As the samples had to be transferred to the XPS chamber through air, the carbon and oxygen species detected afterwards may not be the same as during the experiment. On the other hand, as the Ni content was the crucial point in these experiments, the contamination by the transport through air has no negative effect on the results. XP spectra of the Au 4f, C 1s, O 1s, Ni 2p, and S 2p peaks were measured in order to analyze the surface composition.

2.3 Scanning Tunneling Microscopy

In this thesis, scanning tunneling microscopy (STM) was used in *operando* experiments using the HP-STM setup to image the catalytic surface under reaction conditions with atomic resolution. In this section, the basics of imaging by means of STM are explained.

In an STM measurement, a metal tip scans over a conducting surface at a distance of ~1 nm. A constant voltage (tunneling voltage, V_t) that is applied between sample and tip results in a small current (tunneling current, I_t) based on the quantum mechanical tunneling effect. A scheme of the potential barrier between sample and tip is shown in Figure 2.6. Here, a negative tunneling voltage is applied to the sample, resulting in relative shift of the two Fermi levels E_F by eV_t. Electrons tunnel from occupied states of one electrode into empty states of the other, where only states in the energy window eV_t contribute to the current.[77] In the case shown, electrons tunnel from the occupied states of the sample into the empty ones of the tip, resulting in a filled state image. If the sign of V_t is inverted, the Fermi levels shift and electrons tunnel from the tip to the sample (empty states image).

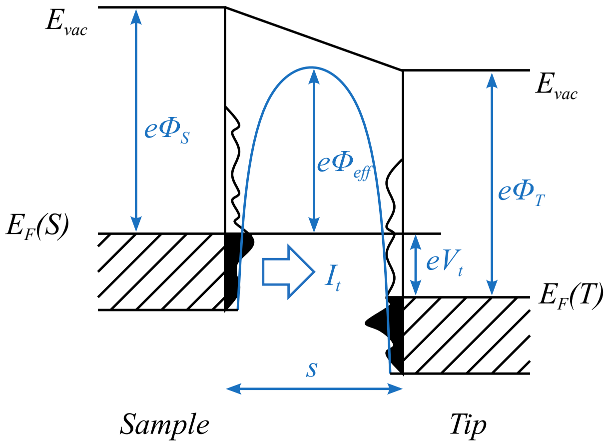

Figure 2.6: Schematic of potential barrier between sample and tip in scanning tunneling microscopy according to ref. [77] and [78]. In this case, where a negative bias (eV_t) is applied to the sample, electrons tunnel from occupied electronic states (local density of states, $LDOS$) of the sample to the unoccupied ones of the tip. This flux can be measured as the tunneling current I_t. $e\phi$ represent the work functions and s the distance between sample and tip. $e\phi_{eff}$ is the effective tunneling barrier.

During scanning, the tip position is accurately controlled by piezoelectric drives. They scan the tip in the two lateral, x and y directions, while a feedback circuit constantly adjusts the tip height (displacement in z-direction), to keep the tunneling current constant.[79] As a result, the tip follows the morphology of the sample surface resulting in a 3D topographic picture of the sample. This mode is called constant-current mode. Another possibility is to measure in constant-height mode in which the height of the tip is kept constant, while the variation of the tunneling current is used for imaging.[77]

The tunneling current strongly depends on the distance between sample and tip, the barrier width s, but also on the electronic states of the sample. It is proportional to the applied voltage, the local density of states at the Fermi level $LDOS(E_F)$ and decays exponentially with the distance between sample and tip s:[79]

$$I_t \propto V_t \cdot LDOS(E_F) \cdot e^{-2\kappa s} \tag{2.3.1}$$

where the decay length κ is equal to:

$$\kappa = \frac{\sqrt{2m_e(e\phi_{eff})}}{\hbar} \tag{2.3.2}$$

m_e is the electron mass, $\hbar$ the reduced Planck constant and $e\phi_{eff} \approx {}^1\!/\!_2(e\phi_S + e\phi_T)$ the effective tunneling barrier – the mean barrier height. As a consequence, an STM image is a superposition of the electronic structure and the topography. As a result of the image potentials, the corners of the rectangular barrier are rounded off. Furthermore, the barrier thickness and height are reduced (see Figure 2.6).[78]

The STM setup used in this thesis, including the beetle-type STM head, has been described in detail above (see section 2.1.2). Images presented in chapter 4 were recorded at various pressures applying different tunneling voltages and currents as indicated in the respective image captions. It has to be noted that all tunneling currents given in section 4.1 display the wrong sign. In the present experiments, all images were recorded in the constant-current mode. The STM results were processed by the IGOR Pro software[75] for plane and line noise correction and for adaptation of contrast.

2.4 Gas Chromatography

Gas chromatography was the basis for the *operando* experiments in this thesis. A customized setup was introduced to meet the requirements for the detection of the products in the FT experiments. After tests and alterations of the new gas chromatograph (GC) at the flow reactor during the master thesis of the author, the GC was attached to the HP-STM setup during the work for this thesis. As the subsequent tests and calibration procedure are an essential experimental part of this thesis, the setup is described in detail in section 3.4. Here, a brief overview of the data handling is given. This section describes how the signals of the flame ionization detectors (FIDs) of the GC are converted to activity data, expressed in terms of turnover frequencies (TOFs).

After separation of the individual FT products in the column, the hydrocarbons are ionized in the flame of the FID. The mass flux as a function of time results in a chromatogram, the output signal of the GC. An example of a chromatogram recorded after 6 h of a FT experiment is shown in Figure 2.7.

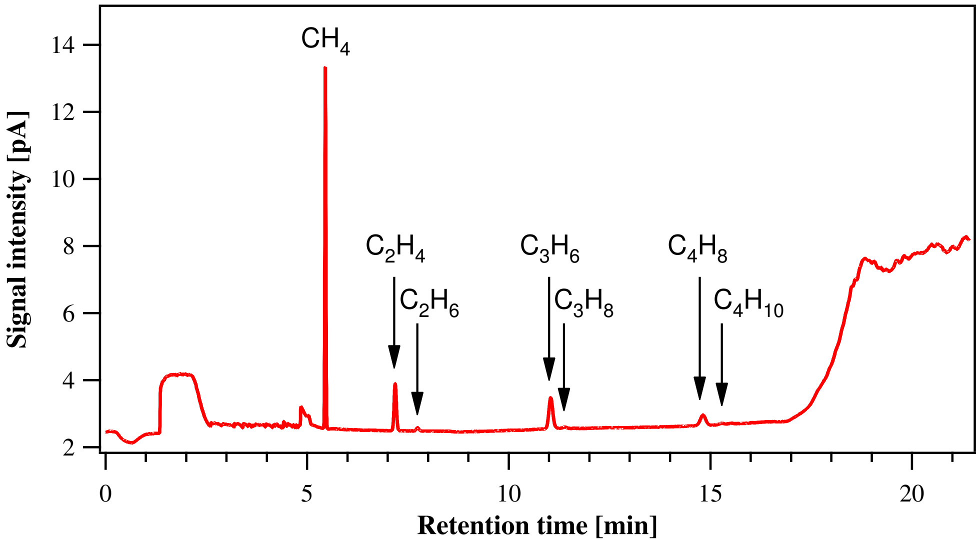

Figure 2.7: Chromatogram of channel II of a Fischer-Tropsch experiment after 6 h. The peaks of methane, ethylene, ethane, propylene, propane, butylene and butane are indicated. Conditions: H_2:CO = 2:1, total pressure 950 mbar, sample surface temperature ~210 °C, Co(0001) sample.

The initial, broad signals result from the matrix of H_2 and CO (till ~5.3 min). The following sharp peaks are caused by the hydrocarbons methane, ethylene, ethane, propylene, propane, butylene and butane. The rise in baseline, starting at ~18 min, is attributed to the rising oven temperature which causes some bleeding of the stationary phase of the column.

The detected signal intensities (in pA) are converted to concentrations in parts per billion (ppb) by the CHROMELEON 7.2 software (Thermo Fisher). This conversion requires calibration measurements that define the integral value for each component. The calibration was done during this thesis by means of a gas mixture (Air Liquide, 150 bar) containing the following components: ~10 ppm of methane, ethane, ethylene, propane, propylene, and butane in a mixture of H_2 and CO (2:1). The concentration of this mixture was stepwise reduced over four orders of magnitude, from 10 ppm to 1 ppb. A detailed description of the calibration procedure is included in Appendix C.5.

Based on the calibration, the software converts the detected signal intensity to the amounts in ppb for every species.

During a typical 6 h FT experiment, a gas sample was taken every hour for GC analysis. Together with the measurement before the sample was heated, seven data sets were recorded in a typical experiment. The evolution of the individual hydrocarbon species with time is shown in Figure 2.8.

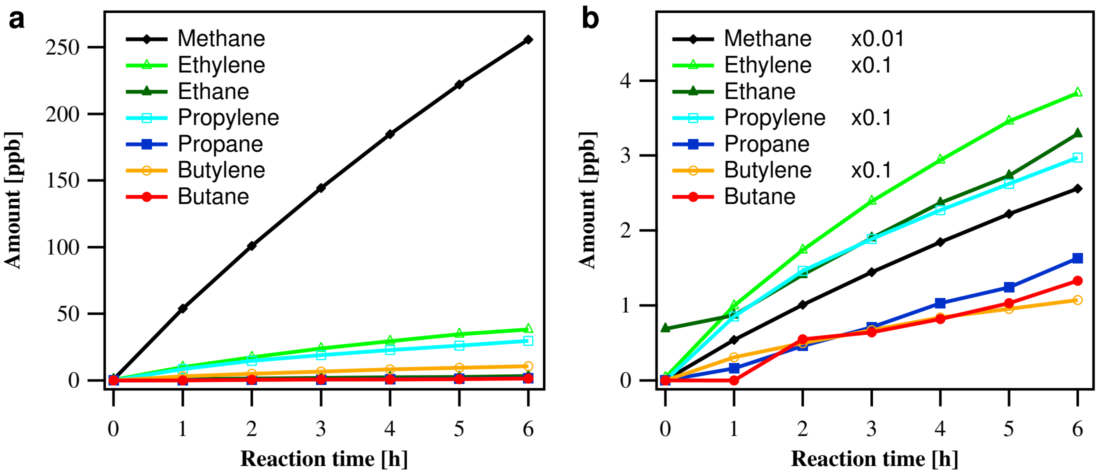

Figure 2.8: Development of the individual hydrocarbon concentrations during a FT experiment. For better visualization of the less concentrated hydrocarbon species, the methane and olefin signal intensities were multiplied by the factor indicated in (b). Conditions: H_2:CO = 2:1, total pressure 950 mbar, sample surface temperature ~210 °C, Co(0001) sample.

The product concentration within the STM cell rises due to the batch mode of the experiment. For visualization of low concentrations, (b) shows the data of (a) at an enhanced amplification. Figure 2.8 (b) shows that except ethane no hydrocarbons are present in the STM cell before heating the Co catalyst ($t = 0$). The increased initial concentration of ethane is a result of impurities in the used H_2. Despite the upstream cooling trap, a complete elimination of impurities was usually not possible and methane and/or ethane were regularly detected in the snygas. As for the evaluation of the activity only differences between two data points in a time series are used, residual contaminants do not influence the results.

Based on the thus detected product concentrations, the catalytic activity of the samples was determined. The activity is expressed as a product formation rate (turnover frequency, TOF). In theory, TOFs should be referred to the number of active sites but due to the lack of knowledge about the density of active sites, TOFs are usually expressed as areal rates.[80] As a consequence, TOFs are given in numbers of produced molecules N_{C_n} for each species C_n per time t divided by the number of surface atoms

N_{surf}:

$$\text{TOF}(C_n) = \frac{\Delta N_{C_n}}{\Delta t \cdot N_{surf}} \tag{2.4.1}$$

In this thesis, TOFs were calculated using the concentrations c detected by GC. The product concentration changes Δc were converted to changes of product particle numbers ΔN_{C_n} by using the pressure p, volume V, and temperature T of the reaction gas in the STM cell, according to:

$$\text{TOF}(C_n) = \Delta c \cdot \frac{1}{\Delta t} \cdot \frac{p \cdot V \cdot \mathrm{N_A}}{\mathrm{R} \cdot T} \cdot \frac{1}{N_{surf}} \tag{2.4.2}$$

The extraction of a gas sample leads to a lower pressure which was taken into account by a p reduction factor of 5.5 mbar per measurement. Due to the unknown number of active sites, the density of Co surface atoms of the Co(0001) surface ($\rho_{\mathrm{Co,surf}} = 1.837 \times 10^{19}\,\mathrm{m}^{-2}$) and the macroscopic size of the crystal surface ($A = 19.6 \times 10^{-6}\,\mathrm{m}^2$) were used to calculate the number of Co surface atoms $N_{surf} = A \cdot \rho_{Co,surf}$.

All TOFs presented in this thesis, independently of the crystal, are values per Co surface atom of the ideal hcp surface per second:

$$\text{TOF}(C_n) = \frac{\Delta N_{C_n}}{\Delta t} \cdot \frac{1}{A \cdot \rho_{\mathrm{Co,surf}}} \tag{2.4.3}$$

As an example, the TOFs of the individual product species of the experiment of Figure 2.8 are shown in Figure 2.9. One can see a trend that was generally observed for the Co(0001) crystal, a decrease of the olefinic TOFs with time indicating some deactivation processes on the catalytic surface. Paraffinic TOFs stay rather constant or even increase slightly but due to their small amounts, which are at the detection limit, the reliability of these data is limited.

In addition to product-based TOFs for each hydrocarbon species, the consumption rate of CO was calculated. This CO-based TOF was assumed to be equal to the overall activity in an experiment. The CO-based TOFs were calculated by multiplying the individual TOFs of each hydrocarbon species by the corresponding number of carbon atoms and adding up:

$$\text{TOF(CO)} = \sum_n \text{TOF}(\mathrm{C}_n) \cdot n \tag{2.4.4}$$

In the example experiment, the CO-based TOF after 6 h is equal to $1.99 \times 10^{-3}\,\mathrm{s}^{-1}$. The evolution with time is also displayed in Figure 2.8 (pinkish curve).

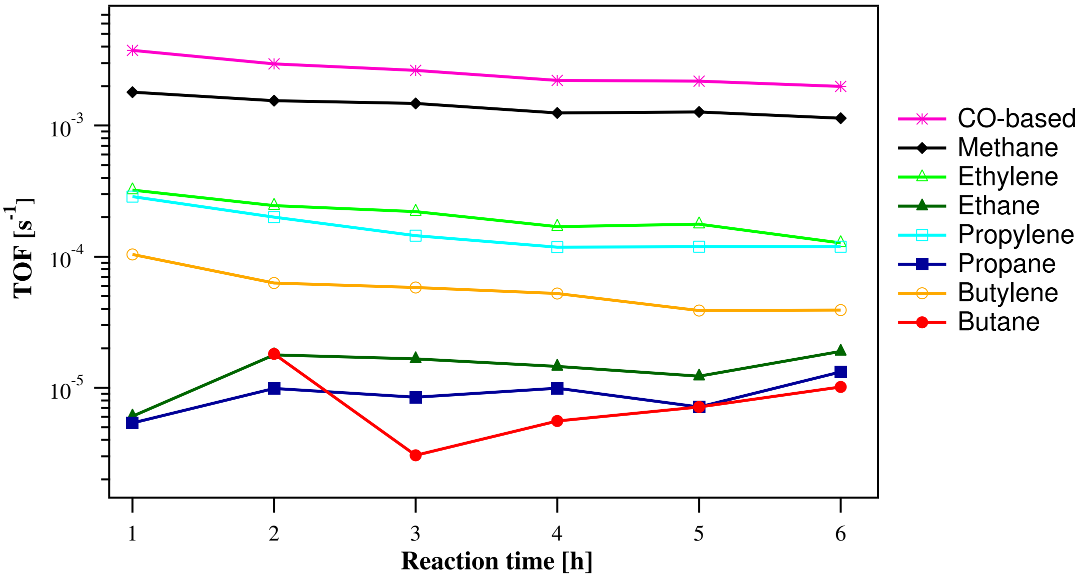

Figure 2.9: Development of product- and CO-based TOFs within a FT experiment of 6 h. Conditions: H_2:CO = 2:1, total pressure 950 mbar, sample surface temperature ~210 °C, Co(0001) sample.

2.5 Scanning Electron Microscopy

A major experimental problem in this work was the decomposition of the glass fiber used for sample heating by the IR laser. To obtain information about possible reasons, the damaged end of the fibers were investigated by means of scanning electron microscopy (SEM) (see section 3.2). The measurements were performed by Dr. Steffen Schmidt (group of Prof. Thomas Bein) on a Helios NanoLab G3 UC (FEI) electron microscope (Fisher Scientific). All images shown were generated by secondary electrons at an operation voltage of 3 kV. Due to their insulating character, all fibers were sputtered with carbon before performing the measurements in a CCU-010 HV carbon coater (safematic).

In addition to the characterization of the surface structure of the fibers, also their chemical composition was analyzed. This was done by means of energy dispersive X-ray spectroscopy (EDX) at operation voltages of 3 and 5 kV. An X-Max^N 80 EDX detector (Oxford Instruments) was used to detect contaminants on the glass fiber surface. Such measurements were also performed to analyze the metal films that partially covered the insulation ceramics of the thermocouple after extended experiments.

CHAPTER 3

Experimental

High-pressure surface science experiments lead to several challenges, including the materials used for the setup as well as the purity of the gases. Materials must not show any catalytic activity during high-pressure experiments. In addition, they have to be chemically stable in the gas atmosphere. Furthermore, they should be mechanically stable and should not outgas. To illustrate the conflict of material properties, the example of aluminum is described in the following. In one set of experiments, an Al sample holder, instead of the standard Mo holders, was used.

As Mo shows a small FT activity, an Al sample holder was tested in order to further reduce blank activity during FT experiments. Al does not show any catalytic activity in FT synthesis and is resistant to syngas. However, pure Al is too soft and ductile to be used for mechanical components, and standard Al is alloyed with small amounts of other metals including zinc. This fact caused serious problems during sample preparation. During annealing of the sample, zinc evaporated from the alloy and contaminated the sample and the preparation chamber. Standard Al cannot be used for experiments in UHV for components that are to be heated. A pure Al sample holder could not be machined due to its ductility.

Also the resistance of the materials to the used gases is important. One major challenge of performing high-pressure experiments in the dissertation of B. Böller[63] was the formation of nickel tetracarbonyl. Reactions of Ni containing components with the high-pressure CO gas phase led to contamination of the sample by Ni. In addition, with raising reaction pressures the purity of used gases became crucial. Even traces of impurities, especially sulfur, in the ppb range contaminated the sample.

This chapter deals with experimental challenges which were met in this thesis. Some problems are related to materials, some to gas purity. But also special requirements for the experimental setup are described. The following sections mainly show experimental improvements, which are not described in the included publications. Although it was achieved to reduce the problems of Ni and S contamination of the samples during the thesis of B. Böller, they were still present. For this reason, considerable efforts were undertaken in the present work to identify the source of nickel deposition on the samples. In the first section (section 3.1) of this chapter, a specially constructed test reactor setup for examining nickel deposition as well as its performance are described.

Another problem that occurred at the increased experimental pressures, was that the glass fibers, used for heating of the crystals by an IR laser, were damaged during the reactions and were finally destroyed on a much shorter time scale than in previous experiments at lower pressures. Section 3.2 investigates reasons why the glass fibers were damaged and presents a solution that let to an enhanced life time.

Another challenge, which was faced in this thesis, concerned the question of how the two Co single crystals could be compared in a quantitative way. During the experiments with the Co($10\bar{1}15$) sample, it turned out that its catalytic activity could not directly be compared to that of the Co(0001) crystal which had been used in former experiments. It became apparent that the temperatures at the crystal surface differed from each other, despite the equal design of the holders as well as the equal experimental conditions. For this reason, temperature calibration measurements were performed with both crystals. These experiments are described in section 3.3.

An central part of this thesis was to put into operation a customized GC to solve the detection problem of low concentrated FT products. The last section 3.4 of this chapter describes the setup, which was attached to the HP-STM setup during this work, in the publication “A highly sensitive gas chromatograph for *in situ/operando* experiments on catalytic reactions”. The calibration and modifications of the oven program were an essential experimental part of this work and are also part of this section.

3.1 Test Reactor for Nickel Deposition

As mentioned above, raising the syngas pressure in the STM chamber was accompanied by a contamination of the sample surface by nickel and sulfur. Introducing heating and cooling traps as well as coating most of the stainless steel components in the STM cell with amorphous Si reduced these problems, as described in the thesis by B. Böller (ref. [63]). Nevertheless, after ~6 h FT experiments at ~1 bar, Ni was still detected on the sample surface by *ex situ* XPS.

The transfer of Ni to the Co samples takes place through the gas phase. This process happens by the reaction of Ni with CO to give gaseous nickel tetracarbonyl $Ni(CO)_4$:[81]

$$\mathrm{Ni\,(s)} + 4\,\mathrm{CO}\ \mathrm{(g)} \rightleftharpoons \mathrm{Ni(CO)_4(g)}$$

This transport reaction is known as Langer-Mond process and is even industrially used for the refining of nickel.[82] The exothermic formation of $Ni(CO)_4$ takes place at temperatures between 75 and 125 °C,[83,84] whereas the decomposition is favored at higher temperatures (>180 °C).[82] As a consequence, Ni in a CO-containing atmosphere is transported from zones of lower to zones of higher temperatures. In the HP-STM cell, the chamber walls as well as the STM components are areas of low temperatures (somewhat above room temperature) whereas the Co crystal at the reaction temperature of ~220 °C is the hottest part of the system. Consequently, nickel tetracarbonyl is transported from setup components that contain Ni – stainless steel parts are a possible source – to the sample and decomposes to give metallic Ni. Although extensive efforts were undertaken to remove all Ni containing components of the STM cell or coat most stainless steel parts by amorphous Si, there are some components which could not be replaced or coated, such as the shield of the cable to the STM tip. Whether CO can actually react with the Ni content of stainless steel has been examined in a few studies.[85–87] It was found that carbonyl formation was strongly reduced when stainless steel with high Cr contents was used, but also that it could not be completely suppressed. For the FT experiments this would be a major problem, because Ni coverages on the sample of the order of a monolayer would strongly alter the system.

For this reason, a new setup for tracing the origin of Ni was constructed. The aim was to test stainless steel components with regard to their reactivity towards syngas and to find out whether the stainless steel components in the STM chamber may be the source of the remaining Ni impurities. The next sections describe the test reactor (section 3.1.1), the experimental procedure (section 3.1.3), and the results of Ni transport experiments (section 3.1.4).

3.1.1 Experimental Setup

The test reactor was designed such that it could simulate the FT experiments in the STM cell. The setup is shown in Figure 3.1. Basically, it consisted of a glass reactor into which various materials as possible Ni sources could be placed. A sample mounted to a heatable holder served as target. Further components were two pipes with needle valves (NV1 and NV2) and shut-off valves (V1 and V2) for the CO and H_2 supply, a rotary vane pump with adsorption trap, and a Baratron (Type 121A, 1000 mbar, MKS) for pressure control. A hot trap after the pressurized CO gas cylinder was installed to avoid contamination from the gas itself. To prevent the formation of Ni carbonyl at other components of the setup than the materials placed into the reactor, mainly brass (valves) and aluminum components and a glass reactor (length = 101 cm, diameter = 16 mm) were used. In the scheme, the materials are indicated by color.

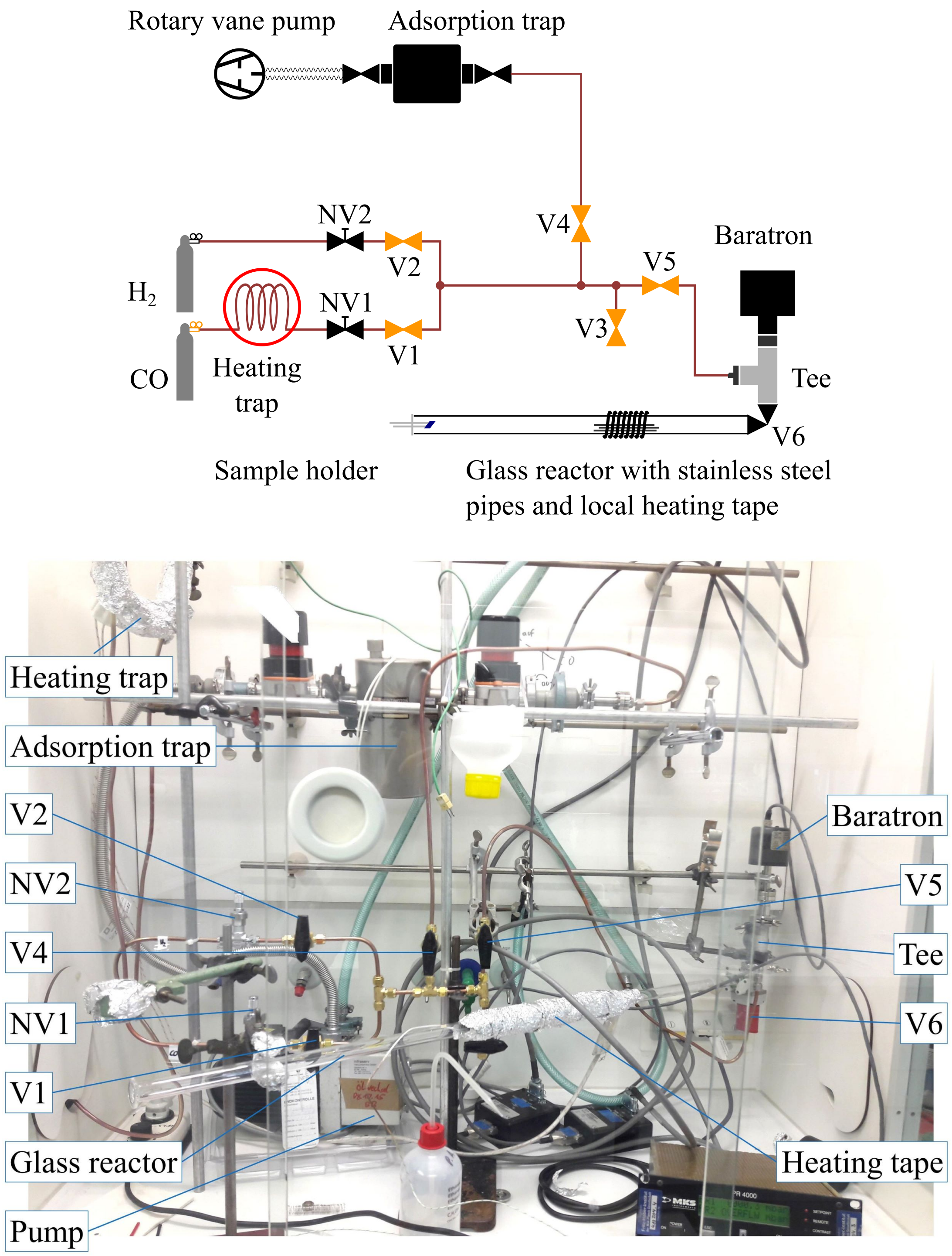

Figure 3.1: Test reactor for the Ni transportation experiments. The system contains a heating trap, needle valves (NV), shut-off valves (V), an aluminium T-piece, a Baratron, and the glass reactor including sample and heating tape. The setup was evacuated through a zeolite trap by a rotary vane pump. The gas pipes (6 mm) were made of copper, orange valves are brass valves, black components were made of stainless steel, and gray ones are aluminum components.

Black components contained stainless steel parts, orange valves were made of brass and light gray components consisted of aluminum. Copper pipes (6 mm) were used. As the Baratron contained Ni alloy (Inconel) membranes, an angle valve (V6, AVC 016 SA, Pfeiffer Vacuum) was mounted between the pressure sensor and the glass reactor, which was closed after filling the reactor with syngas. Thus, the syngas had no contact to the Baratron during the experiments. A heating tape around the glass reactor at the position of the inserted materials was used to adjust the temperature of the possible Ni source.

As target sample for the deposition of Ni served a Au-coated Si wafer (~1x1 cm^2, prepared by the group of Prof. Thomas Bein). Au was chosen because it is more noble than Co so that less complications with contamination from the contact with air were expected during sample transfer to the XPS chamber after the experiments. The self-built sample holder is shown in Figure 3.2 (a).

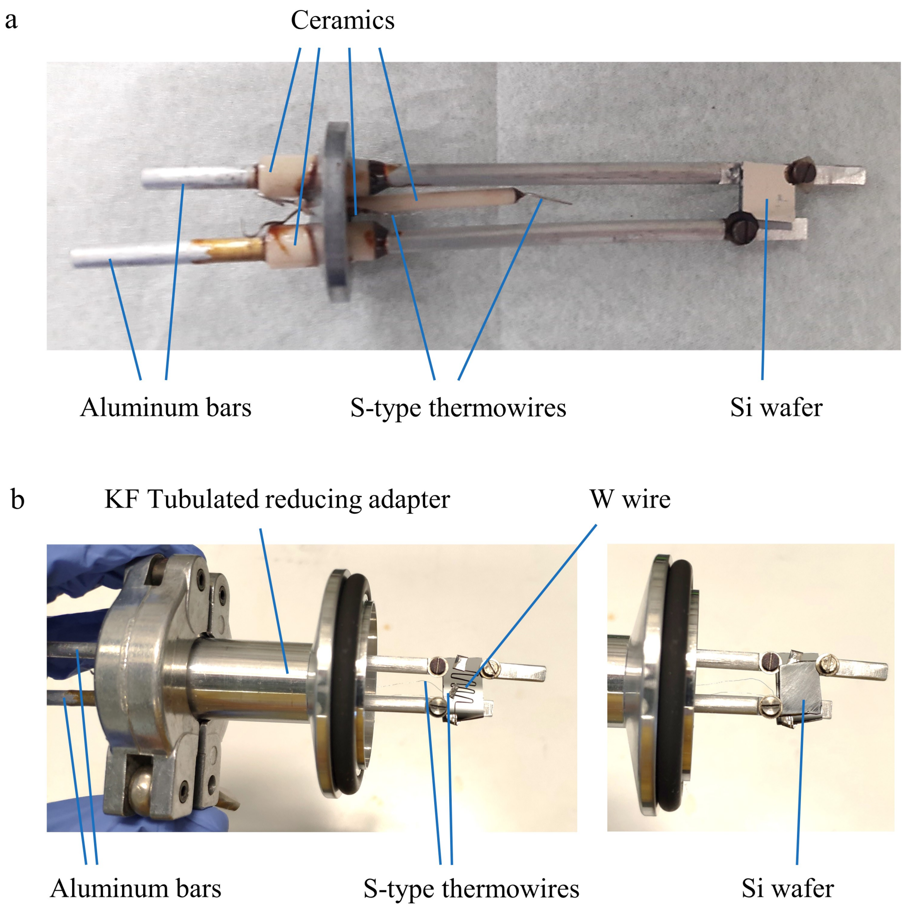

Figure 3.2: Sample holder for the test reactor. It consisted of two aluminium bars, glued to an Al blind flange (KF-16) which were used to heat and fix the sample. The temperature was measured by two Pt/PtRh thermowires between the Si wafers. (a) shows the original version, (b) the modification. For more constant heating, a winded W wire was placed between two Si wafers. The sample wafer was mounted above this sandwich (not shown) with thermocouple wires clamped between.

It consisted of two insulated Al bars with flat ends at which the samples were mounted. The samples were sandwiches, consisting of the Au-coated wafer, a second, uncoated wafer and S-type thermocouple wires clamped between the two wafers. Applying a voltage to the two Al bars enabled resistance heating of the wafers. During the first experiments, it became apparent that stable heating of the wafers was not possible. The most likely reason is the fact that the conductance of Si increased with temperature, so that at a given voltage the deposited heat increased, leading to a self-amplification effect. As a result, the temperatures fluctuated strongly and the Al bars got too hot which resulted in the decomposition of the epoxy used to glue the bars to the insulation ceramics.

To solve this problem, an alternative sample heating setup was built [Figure 3.2 (b)]. A winded W wire was placed between two Si wafers and fixed by means of Ta loops. The Au-coated sample was placed above this sandwich of two Si wafers, with thermocouple wires clamped between, and fixed by means of Mo screws.

First experiments were performed with syngas and stainless steel pieces as possible Ni sources in the glass tube of the reactor. After Ni could not be detected on the wafer, a Ni wire was placed in the glass reactor in addition to the stainless steel pieces. However, still Ni was not detected. It was suspected that the gas diffusion length was too short to reach the sample in the relatively long glass tube.

The setup was therefore modified (see Figure 3.3). The glass reactor was replaced by an Al 4-way cross and a straight connector to provide a more compact structure to reduce the pathways for diffusion. A water cooling pipe prevented heating of the straight connector to which the sample holder was mounted. Due to the cooling pipe, the decomposition of nickel tetracarbonyl should be favored on the Si wafer, the single hot place within the reaction volume. To enhance the formation of carbonyl on the inserted material, the 4-way cross was heated by a heating tape.

In addition to the reactor design, it was also possible that the lack of a catalyst may have caused the absence of Ni on the wafer. It is known that sulfides strongly increase the formation rate of $Ni(CO)_4$.[88–90] Greiner et al. suggest that the promotion effect of adsorbed sulfur is the result of a weakening of the bond strengths of Ni and CO to the surface.[90] The decreased binding energy of CO may suppress the dissociation of CO, which prevents the surface from forming a carbidic C layer which inhibits Ni carbonyl formation. As an alternative explanation, the formation of a reactive γ-NiS phase has been discussed.[88] A contamination of the Co(0001) crystal with sulfur has also been observed in the experiments of B. Böller.[63] To investigate possible effects of sulfur, a gas pipe for H_2S was integrated into the setup. Previous experiments with

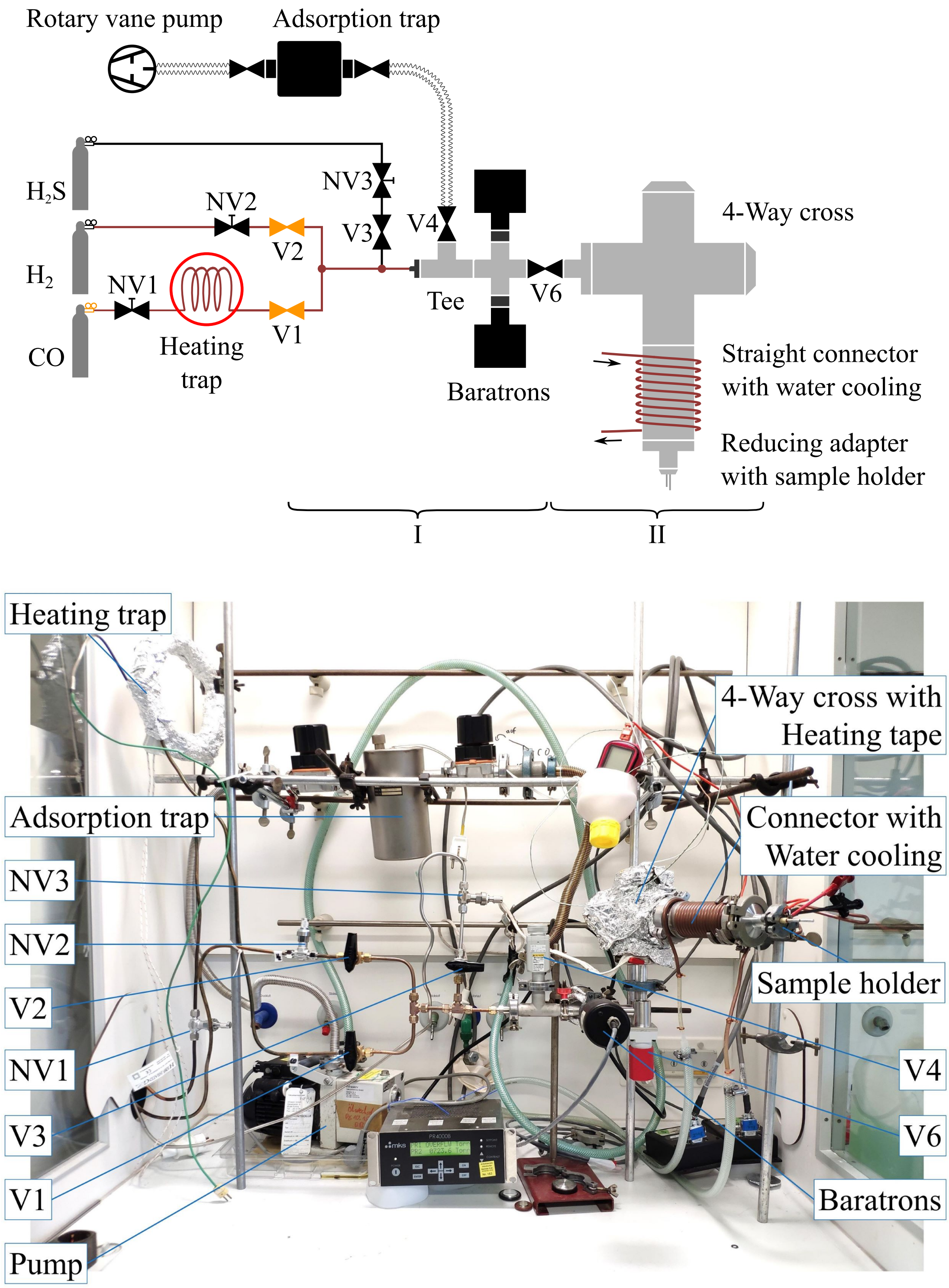

Figure 3.3: Test reactor for Ni transportation experiments after modifications. The setup was expanded by an H_2S pipe and a second Baratron. The glass reactor was replaced by an Al 4-way cross and a KF 40 connector with water cooling pipes.

H_2S showed that optimal partial pressures for the gas phase transport reaction of Ni were in the range of 0.3 – 3 mbar H_2S.[91] As the sulfur content in the H_2 used for experiments in the STM cell was very low as a result of the filters, it was tried to keep the amount of sulfur in the test reactor as low as possible. Assuming that less than 1 mbar H_2S was needed for successful $Ni(CO)_4$ formation, this pressure could not be measured as it was below the detection limit of the two installed Baratrons (Type 121AA, 100 Torr and 5000 Torr, MKS). To solve this problem, the setup contained two volumes (I and II). By filling the first part (smaller volume) with H_2S gas with closed V6 under pressure control and then expanding this volume into the second part (5-fold larger volume), the concentration of the gas could be kept below the detection limit of the Baratrons.

3.1.2 Applied Nickel Sources

For experiments with the initial setup (see Figure 3.1), pieces of stainless steel pipes were placed in the glass reactor. These pipes (diameter: 6 mm, total length: 84.5 m, Sandvik 5R75) are used for all vacuum applications in the group. According to the manufacterer, its nominal chemical composition is: $C < 0.05\,\%$, $Ti \geq 5 \cdot C$, Si 0.5 %, Mn 1.3 %, Cr 17 %, Ni 12 % and Mo 2.1 %.[92] Furthermore, a pure Ni wire (diameter = 0.5 mm, length = 2 m) was used for testing purpose in both setups. In addition, a Ni sheet (~7x10 cm) was placed in the modified setup (see Figure 3.3) to provide a sufficiently large Ni source.

3.1.3 Experimental Procedure

The Ni deposition tests were performed with a total pressure of 940 mbar to prevent over-pressure within the reaction chamber and to simulate the conditions of the experiments in the STM cell. After mounting the Au-coated wafer on the Al bars, the sample holder was installed and the Al bars were connected to a voltage source. The apparatus was evacuated and the temperature of the heating trap was adjusted to 300 °C. After introducing CO (~310 mbar) through V1, the valve was closed and the reactor was filled with H_2 up to 940 mbar. The pressure during filling was precisely adjusted by the needle valves (NV1 and NV2). After the desired pressure was reached, the angle valve (V6) next to the glass reactor was closed to separate the syngas from the Baratron. Subsequently, the gas pipes were evacuated and the wafer was heated to ~220 °C. The wafer temperature was monitored by the S-type thermocouple. In some experiments, the reactor was locally heated at the position of the inserted material to ~75 °C by means of a heating tape. The temperature was controlled by an external K-type thermocouple. After 15.5 – 97 h, the setup was evacuated, ventilated and the Au-coated wafer was detached from the sample holder. For surface analysis, the wafer was transferred to the XPS chamber.

For experiments with H_2S, the angle valve V6 remained closed during the filling of the smaller volume (part I) with H_2S. By means of NV3 and additional pumping through V4, a pressure of ~2.6 mbar was adjusted. The H_2S was then diluted by a factor of ~5 by opening V6 to expand the gas into the reaction volume (part II). Then, like in the experiments described above, CO (~310 mbar) was introduced and then H_2 to a total pressure of ~940 mbar. Before heating the wafers, V6 was closed. In the same way as in the above experiments, the wafer was finally analyzed by XPS. After cleaning by sputtering, the wafer was used for the next experiment. After experiments that let to high amounts of Ni, the Al bars were cleaned by grinding to prevent Ni transport from the sample holder to the wafer.

3.1.4 Experimental Results

Figure 3.4 shows XP spectra of a Au-coated wafer before a transport experiment. The peak energies are listed in Table 3.1.

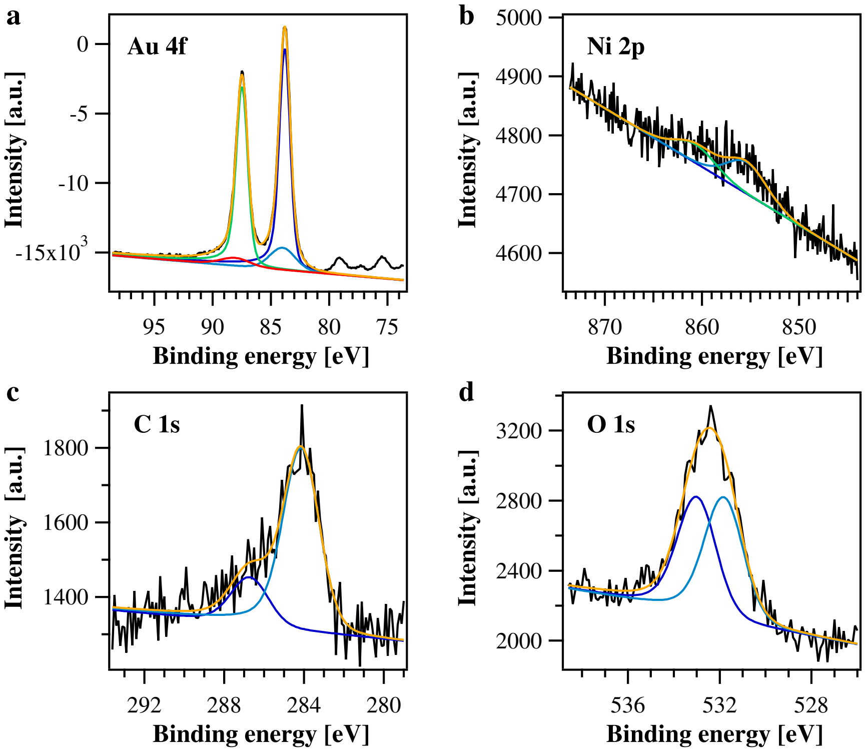

Figure 3.4: XPS analysis of a fresh gold-coated Si wafer. The results are listed in Table 3.1.

The Au surface [E_B (Au $4f_{7/2}$) = 83.8 eV] was covered with carbon and oxidic species which originated from the unavoidable original air contact. The main C 1s peak (284.1 eV) can be attributed to graphite.[67,93–95] The second C 1s peak (286.7 eV) may

Table 3.1: XPS results from spectra of a new gold coated Si wafer, shown in Figure 3.4.

Peak	**Au 4f**		**Ni 2p**		**C 1s**		**O 1s**	
Sample	E_B [eV]	Amount [%]	E_B [eV]	Amount [%]	E_B [eV]	Amount [%]	E_B [eV]	Amount [%]
reference	83.8	52.0	852.0	1.1	284.1	21.7	531.2	9.9
					286.7	5.8	533.0	9.4

originate from a superposition of contributions from C-OH or C-S components,[96] and chemisorbed CO/CO_2 species.[97] Also the O 1s signal (531.2 eV) is in the range of hydroxides and CO[98,99] but also oxidized aluminum shows signals in this range.[100,101] An Al 2s peak (120.4 eV) (not shown) originated from the oxidized aluminum[102] sample holder used for XPS measurements. The O 1s peak with a E_B of 533.0 eV is due to H_2O.[100] A minimal peak was detected in the range of elemental Ni[103] [E_B (Ni $2p_{3/2}$) = 852.6 eV]. This signal did not change in the first experiments with the original setup. An explanation for the lack of Ni transportation might be the length of the reactor cell. As the formation of nickel tetracarbonyl is slow,[90] the diffusion pathway from the Ni source to the Au-coated wafer may have been too long on the time scale of the experiments. Another possibility is that an oxide layer on the Ni wire prevented the formation of Ni tetracarbonyl.[89,104]

After these negative results, the setup was redesigned and H_2S was added, as described above. After an experiment with ~0.5 mbar H_2S in addition to the syngas and a Ni sheet as Ni source, the Au-coated Si wafer had a different appearance. Its surface looked tarnished gray compared to the shiny dark original state. The XP spectra (Figure 3.5) showed a clear Ni peak (852.6 eV). Whether elemental Ni or NiS were the dominant surface state cannot be said, as the two E_Bs are too close to be distinguished.[103,105] The broad Ni $2p_{3/2}$ peak at 855.0 eV and the shake up peak at 860.0 eV arise from $NiO/Ni(OH)_2$.[103] A distinct S $2p_{3/2}$ peak at 161.6 eV[105] indicates sulfur in sulfidic form. The interpretations of the C 1s and O 1s peaks are as above. For the amounts see Table 3.2.

After the first successful Ni transport reaction, blank experiments without any Ni containing materials still showed Ni in the XPS analysis. Obviously, some Ni covered the internal surfaces of the reactor from the preceding experiment. It was then tried to remove this Ni by repeated blank experiments. These experiments were performed under syngas with and without additional H_2S and at a wafer temperature of ~215 °C. The total time exceeded 300 h, but the Ni coverage was only reduced from 13 to 5 % (Figure 3.6 and Table 3.2).

Even after replacing the Si wafers and grinding the Al bars, Ni was still present after

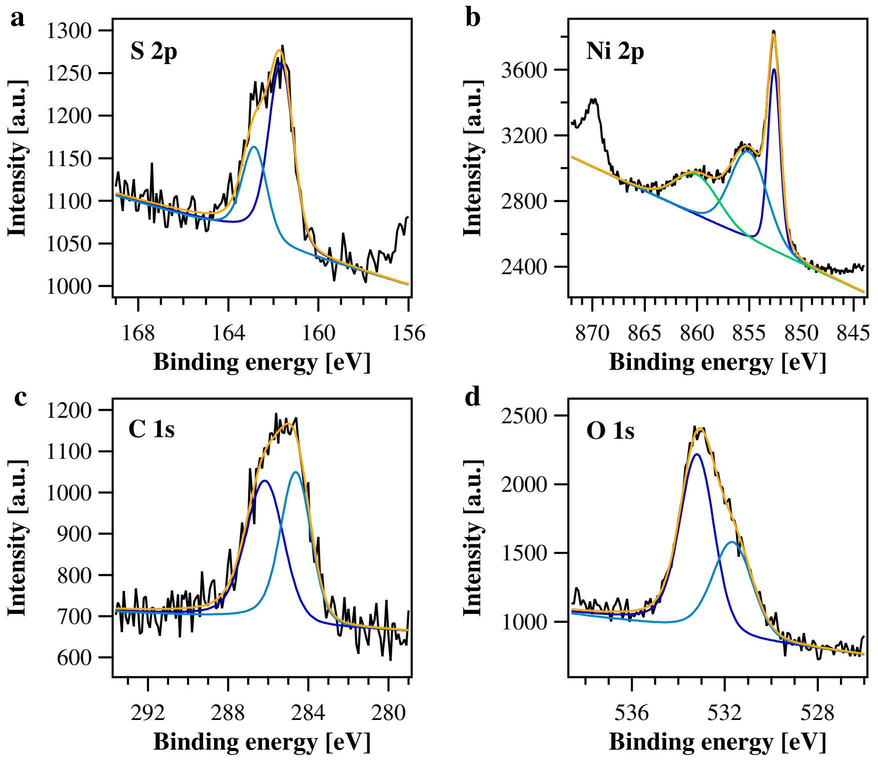

Figure 3.5: XP spectra recorded after an experiment with a Ni sheet. The corresponding peak data are listed in Table 3.2. Conditions: Ni sheet and Ni wire, heating tape ~75 °C, 967 mbar syngas, H_2:CO = 2:1, 0.5 mbar H_2S, wafer temperature ~210 °C, reaction time ~16 h.

experiments with syngas with and without additional H_2S. Further experiments with syngas of a total duration of more than 200 h and grinding of the sample holder finally resulted in the XP spectra shown in Figure 3.7. The amounts are listed in Table 3.2. It is clearly visible that a further reduction of the Ni 2p signal was possible. The final amount of Ni was 1 % only, which is in the range of the signal of the pristine Au-coated Si wafer.

Table 3.2: XPS results from experiments performed in the test reactor.

Peak	**S 2p**		**Ni 2p**		**C 1s**		**O 1s**	
	E_B	Amount	E_B	Amount	E_B	Amount	E_B	Amount
Sample	[eV]	[%]	[eV]	[%]	[eV]	[%]	[eV]	[%]
Ni sheet	161.6	6.5	852.6	14.7	284.6	15.2	531.6	10.7
Figure 3.5					286.1	16.9	533.2	17.3
Blank exp.	161.4	1.6	852.4	7.3	284.3	18.1	530.7	2.1
Figure 3.6					286.1	7.0	532.4	18.9
Blank exp.	161.0	0.4	852.4	1.8	283.8	16.3	531.2	3.7
Figure 3.7					285.9	8.3	532.9	14.0

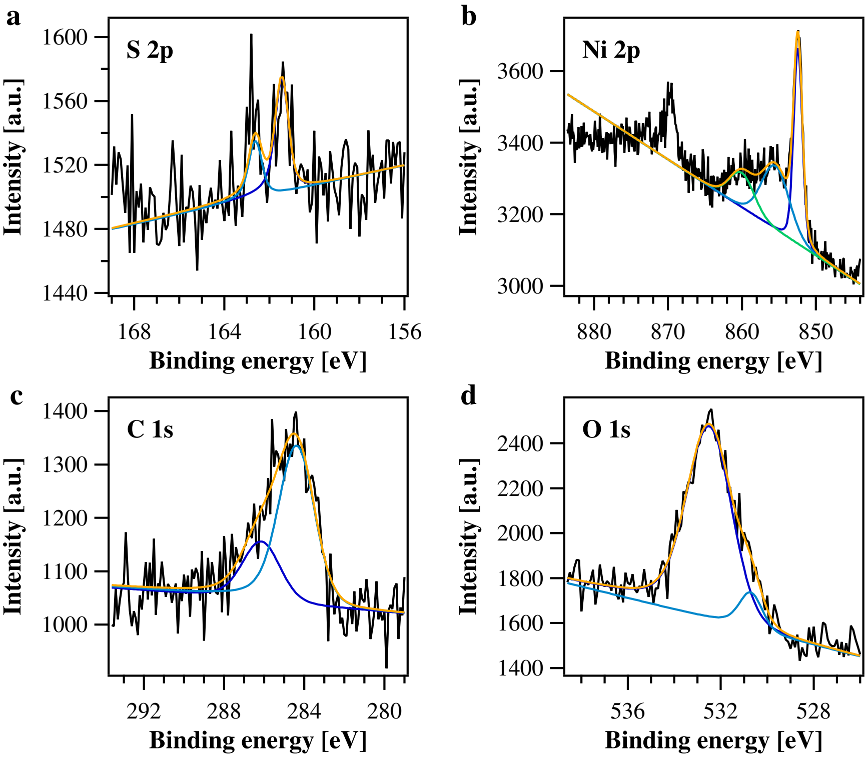

Figure 3.6: XP spectra after several blank experiments with syngas, showing a depletion of Ni. The results are listed in Table 3.2. Conditions: 963 mbar syngas, H_2:CO = 2:1, 0.2 mbar H_2S, wafer temperature ~220 °C, reaction time ~17.5 h.

In conclusion, these experiments show that not necessarily an extra Ni source is needed to deposit Ni in experiments with syngas. After the initial distribution of Ni in the reactor, it took many hours to deplete it again. The fact that grinding of the sample holder, a component that gets hot during these experiment, did not solve the problem indicates that Ni deposited also in colder parts of the setup and could be a Ni source in subsequent experiments. It has to be concluded that the remaining Ni in the HP-STM setup is not necessarily based on a remaining Ni source, such as uncoated stainless steel parts, but may be the result of Ni deposited in former experiments, e.g., when a K-type thermocouple had still been used. Hence, a redistribution process may be the reason for the remaining Ni. As the chamber is regularly exposed to air for repairs and modifications, this may introduce some sulfur, as an S signal is always detected by XPS after contact to the atmosphere.[63] Thus, a catalyst for the formation of nickel tetracarbonyl is available, so that Ni can be transported to the sample, the hottest part in the chamber. The possibility to remove the remaining Ni by extended treatments with syngas has been demonstrated, but it was also shown that this is extremely time-consuming. As experiments in the HP-STM chamber cannot be performed without supervision, similar reaction times as in the test reactor cannot practically be applied. To make use of the results of these experiments, the Cu-stack

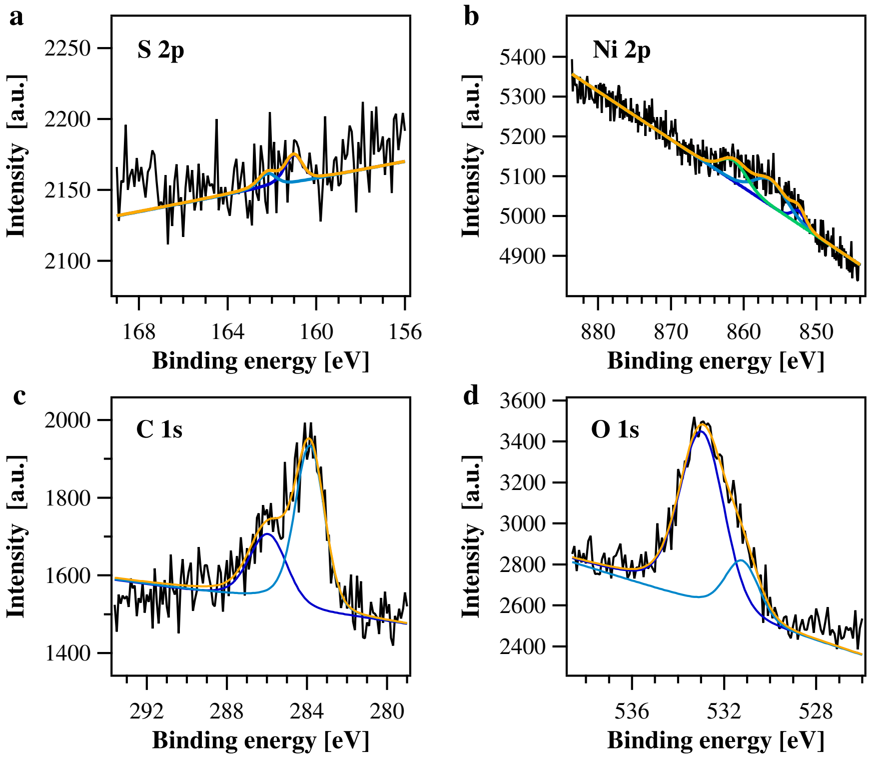

Figure 3.7: XP spectra of a Au-coated wafer after prolonged blank experiments. The results are listed in Table 3.2. Conditions: heating tape ~75 °C, 967 mbar syngas, H_2:CO = 2:1, 0.2 mbar H_2S, wafer temperature ~210 °C, reaction time ~19 h.

of the STM as well as the Mo sample holders and other transferable components were polished to reduce possible Ni deposits. However, up to this point Ni was still detected after FT experiments.

Experiments at the HP-STM revealed a possible additional source of Ni. The Al oxide ceramics of the mounting assembly of thermocouples are annealed with a gas flame before mounting, in order to remove contaminants. It turned out that the material of the wire (stainless steel or Pt), on which the ceramics are held during flame annealing, and even the material of the tweezers used to handle the ceramics let to massive differences in the contamination by Ni. To minimize the Ni contamination of these ceramics, only Ni-free tools should be used in the future, e.g., a Pt-wire for annealing and Ta tweezers for handling.

3.2 Stability of the Glass Fibers

As described in section 2.1, the sample in the STM cell is heated by means of a diode laser. The laser light is coupled into the chamber by a glass fiber. However, when the syngas pressure in FT experiments was raised to 950 mbar, a massive problem occured, which had not been known from UHV experiments before. The front end of the glass fiber decomposed after only few experiments, which led to anomalous heating behavior and a high blank activity. This section describes the investigations which were performed to solve this problem and it presents a solution that led to strongly enhanced glass fiber lifetimes.

3.2.1 Glass Fiber Setup

The IR light of the laser is coupled into the STM cell through an optical fiber. A scheme of the original glass fiber design is shown in Figure 3.8.

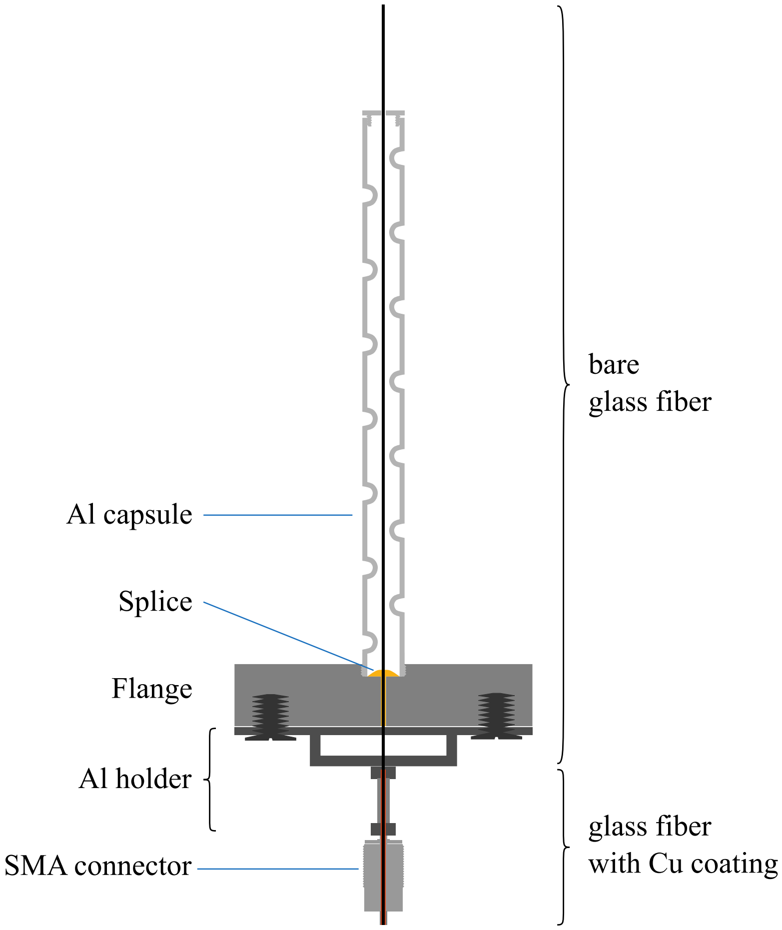

Figure 3.8: Scheme of the glass fiber setup for sample heating in the STM chamber.

The fiber is held on a CF-16 flange and Al holder at which it is mounted to the STM cell. It is connected to a fiber-optic cable by means of the SMA connector. The fiber has a SiO_2 core (600 µm) and a cladding that is doped with F. In the original version, the Cu-alloy coating had already been removed by the manufacturer (art photonics) because it led to leaks in earlier UHV experiments. The bare glass fiber was glued in the flange by means of an epoxy glue (EpoTek 353ND, FOP) which led to a leak-tight connection. An Al capsule fixes the fiber in place. The distal end is cut at an angle of 8 ° by the manufacturer to prevent back reflection of the light, and the surface is polished. The fiber is mounted such that the SiC platelet at the backside of the sample, that serves as absorber, is illuminated.

3.2.2 Fiber Degradation

In the work of B. Böller and also in this thesis, the optical fiber had to be replaced many times. An indicator that the fiber was defect was when blank experiments showed anomalous high product amounts, and, in particular, unusually high amounts of acetylene, which was not detected in normal FT experiments. In extreme cases, the laser power had to be raised to hold the usual sample temperature indicating that only a reduced fraction of the light reached the sample. Visual inspections of the glass fibers after such problems showed massive degradations of the distal end. Figure 3.9 depicts a selection of optical fibers which showed anomalous behavior in the FT experiments. In contrast to a new fiber (a), fibers which produced enhanced amounts of CH_4 and acetylene showed a film that appeared metallic under magnifying glass but looked blackened when viewed with the naked eye (b+c). In extreme cases, the distal end of the fibers had disappeared (d–f). The ends looked like bare glass and no polished end could be seen any longer. The length of the fibers was measurably shorter as a result of the evaporation or spalling of the end. Due to the altered length and the changed geometry, the exiting light not only illuminated the SiC absorber disc but also the Mo sample holder. Experiments with a Mo platelet instead of SiC showed the production of acetylene, indicating that the acetylene production is indeed linked to Mo.[63] It appears that at elevated syngas pressures chemical processes happened at the front end of the glass fiber that precipitated material on the polished surface. The partially blocked light heated this material, further enhancing these processes, so that a self-amplifying temperature increase finally destroyed the fiber.

3.2.3 Temperature Measurements

In order to understand this behavior of the optical fibers, a number of control experiments were performed. Fist, attempts were made to measure the gas temperature close to the end of a fiber. For this purpose, a Ag wire (length = 7 cm, diameter = 0.25 mm) was mounted by means of two ceramics which were fixed on the Al capsule by Ta plates [see Figure 3.10 (a+b)]. The Ag wire was placed approximately at the end of the glass fiber at a distance of ~2 mm. An S-type thermocouple was fixed at the

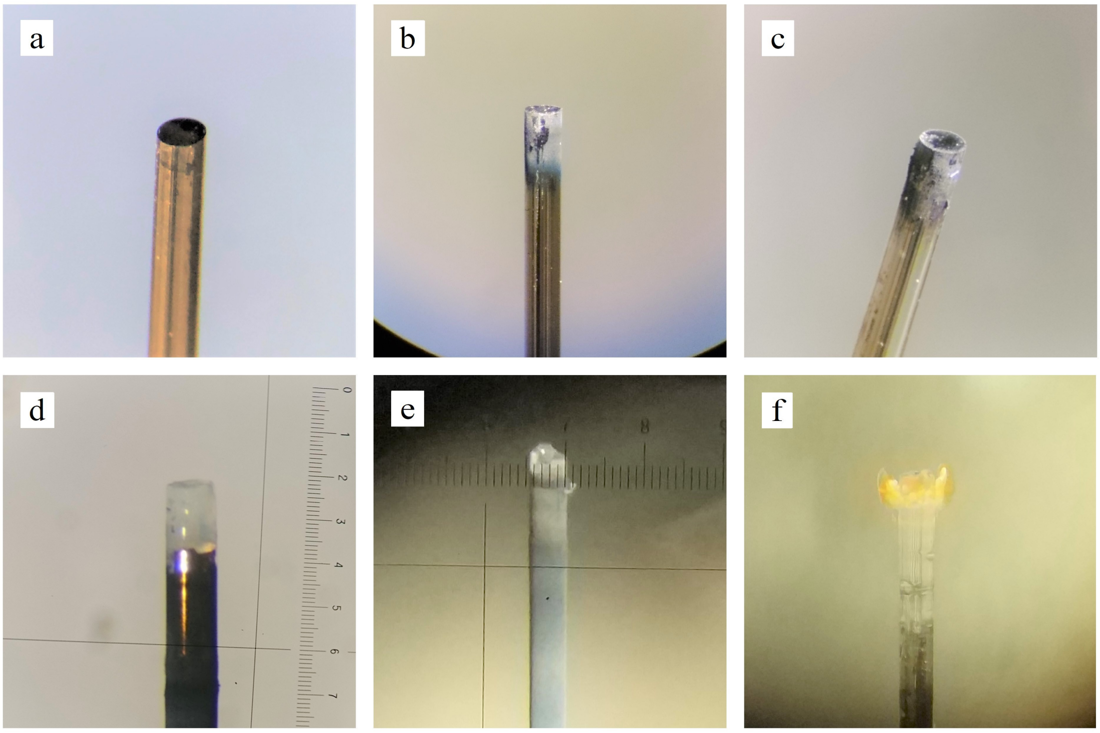

Figure 3.9: Ends of glass fibers which were used for sample heating by means of an IR Laser: (a) new glass fiber with polished end, (b+c) glass fiber the end of which appeared blackened. This fiber produced anomalously high turnover rates, (d–f) in extreme cases parts of the fiber seem to have evaporated. With such fibers, acetylene formation was detected in FT experiments. Pictures (e) and (f) were taken by Bernhard Böller and are displayed in his thesis.[63]

Ag wire. These measurements were performed with a damaged fiber that had shown increased blank turnovers and acetylene in GC measurements.

The tests in 925 mbar syngas and with a laser power of 23 A, parameters at which the sample temperature would approximately be 220 °C, showed a temperature of the Ag wire of ~120 °C. This temperature is too low for spontaneous reactions between CO and H_2 and seems insufficient to explain the high turnover numbers. At such low temperatures, the formation of hydrocarbons from syngas without catalyst would require a different energy source, e.g., electrical discharge, which can be ruled out.[106,107]

In a second set of measurements, it was attempted to measure the temperature of the fiber. For comparison reasons, thermocouple wires were wound around a damaged and a new glass fiber. A Ag(111) single crystal was used as sample. The glass fibers with attached thermocouples are displayed in Figure 3.10 (c+d). The measured temperatures are listed in Table 3.3. These temperatures are approximate values only, as it was not waited until constant values were reached. Nevertheless, these measurements show that the temperature of the damaged glass fiber at a given laser power was significantly higher than the temperature of the new fiber. While the temperature of the new fiber

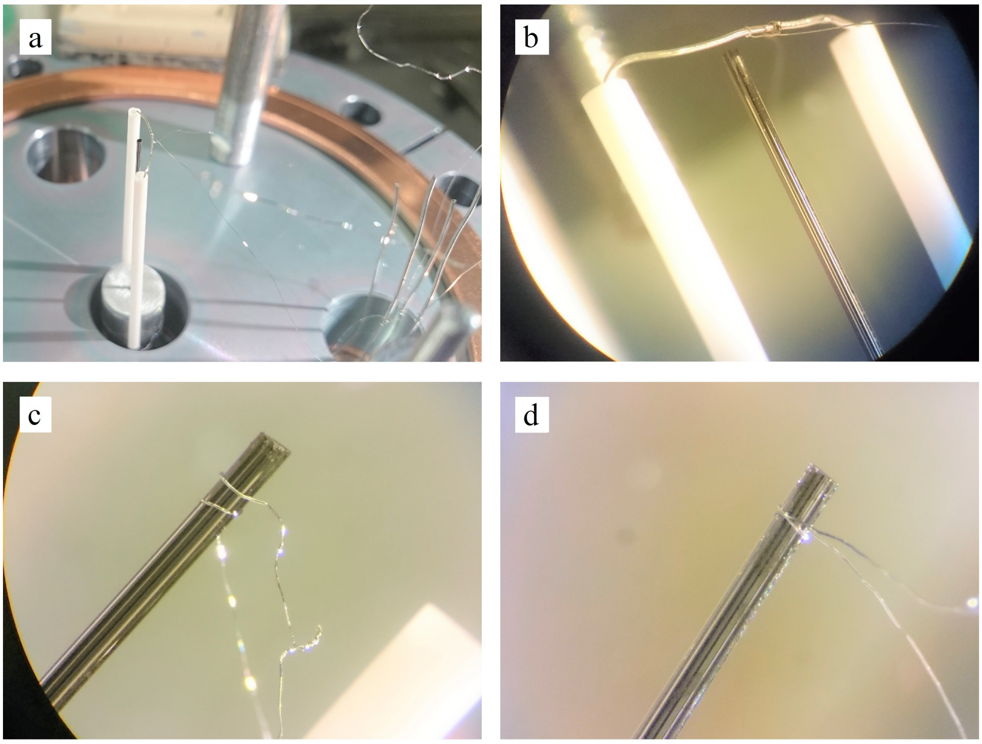

Figure 3.10: Pictures of the thermocouple setup for measurements of the gas phase and glass fiber temperatures: (a) and (b) show the setup for measurements of the gas temperature next to the end of a damaged glass fiber. (c+d) display glass fibers with S-type thermocouple wires winded round the tip of the fibers for temperatures measurements. (c) corresponds to a damaged tip, which produced too high blank turnovers and (d) shows a new glass fiber.

Table 3.3: Measured temperatures of a damaged and a new glass fiber depending on the applied laser power.

	Laser power [A]	**Temperature [°C]** broken glass fiber	new glass fiber
vacuum	9	220	
	9.4		156
	10.0	320	176
	11	380	
	11.5		240
syngas, 1 bar	20		64
	24	164	
	25		65
	30	200	

did not exceed 65 °C, the damaged glass fiber heated up to 200 °C in syngas. Further measurements under FT conditions showed that enhanced blank turnover rates always corresponded to elevated temperatures of the glass fiber.

3.2.4 Surface Analysis

To further understand the heating behavior of the glass fibers, SEM data were taken. The surface of the polished end of three glass fibers is shown in Figure 3.11. Images (a–c) were taken from an optical fiber the end of which looked black and which produced high turnover rates including acetylene. The fiber shown in images (d–f) looked unchanged when viewed with the naked eye but produced enhanced product concentrations and acetylene as well. Images (g–h) depict a new glass fiber which has not been used in an experiment. It is clearly visible that the front surfaces of the damaged fibers have changed compared to the new one. While the new fiber looks smooth, the damaged fibers show defects which look as if they have been molten. These defects are centers where the emitting light is scattered. It therefore no longer forms a well-defined spot on the SiC disc but also illuminates the Mo holder. This may explain the enhanced turnover rates, mainly of CH_4, and the formation of acetylene. Moreover, these defects should represent centers at which the temperature is locally higher and thus form nuclei at which a larger-scale damage of the fiber starts.

To find possible reasons for the degradation of the glass fibers, EDX measurements were performed at the front surfaces as well as on the shafts next to the edge. A selection of analyzed areas is shown in Figure 3.12 and the detected elements are listed in Table 3.4. The measurements on the damaged fibers showed minimal amounts of Al (b) and Mo (e_2) at some defects on the front surface, but also areas without any contaminants (a, e_1, f_1, f_2). On most parts of the front surfaces, no impurities could be detected. The shafts next to the edges of the front surfaces of the damaged fibers (c, d, g, h) showed Ni and S contamination as well as Al, Pt and Ca. While Al and Pt might result from the contact with the Al capsule and the thermocouple wire for temperature measurements, respectively, Ni and S must have been transported through the gas phase. EDX results of the new fiber showed no contamination by any metal but some fibers at the shaft with high F content. These may be leftovers from the Teflon (tetrafluoroethylene) tape, which is usually used by the manufacturer for transportation of the optical fibers. The presence of F in (h), (l) and (m) is due to the F in the cladding of the glass fiber. It has been concluded that the EDX measurements did not reveal any clear reasons for the glass fiber degradation. Since neither Ni nor S could be found on the front surface, they are probably not responsible for the degradation of the fibers but secondary results of the elevated temperatures of the damaged fibers. As has been shown in section 3.1, $Ni(CO)_4$ forms in the presence of sulfur and decomposes at temperatures above 180 °C.

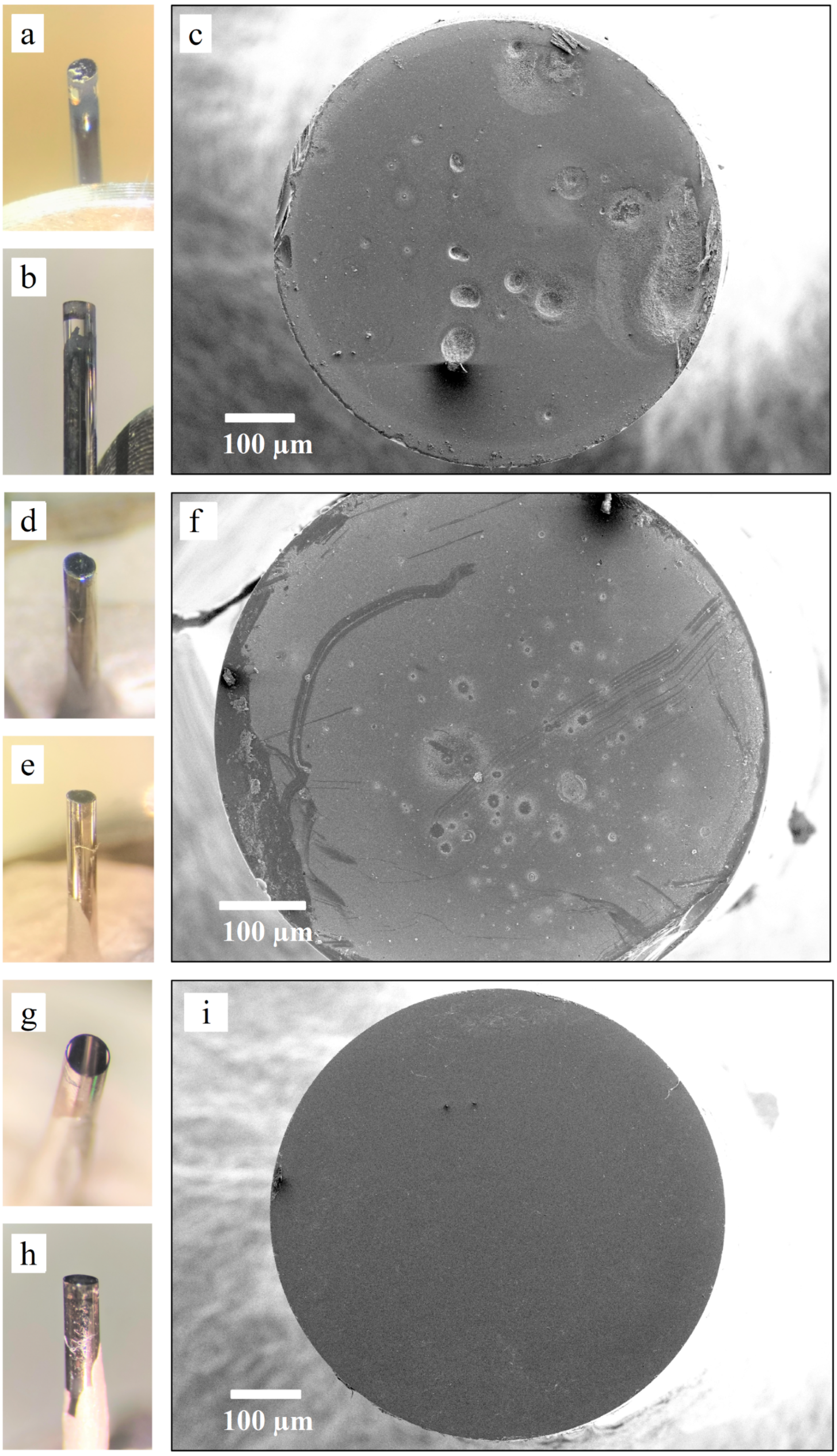

Figure 3.11: SEM images of the distal end of glass fibers: (a–c) glass fiber with blackened end that showed too high turnovers and acetylene with blank samples, (d–f) glass fiber which looked unchanged when viewed with the naked eye but produced high turnover rates and acetylene with blank samples, (g–i) new glass fiber with polished end.[a]

---

[a] The images on the left were taken after the SEM measurements. For this reason the Ag lacquer for fixation on the SEM sample holder can be seen.

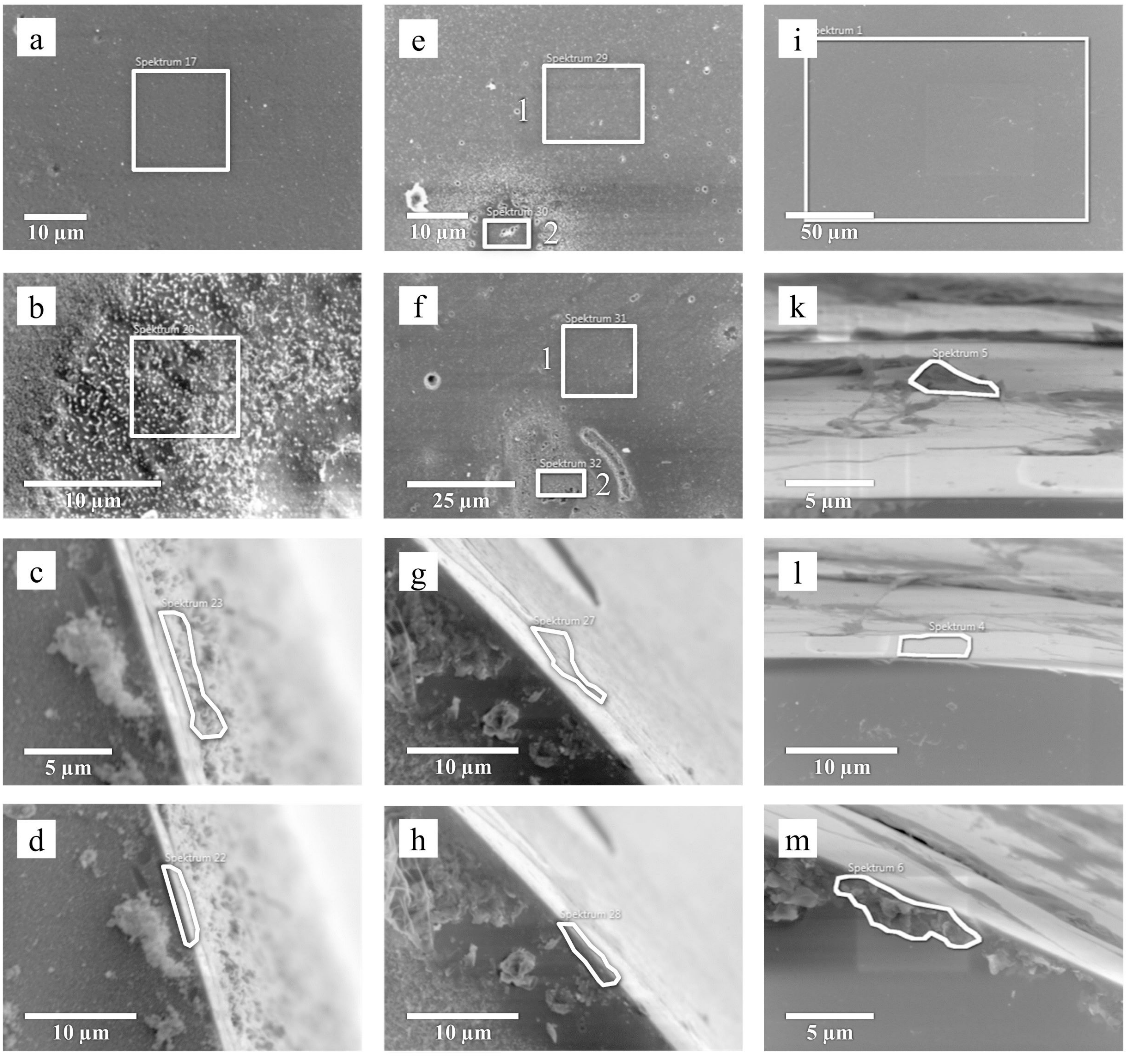

Figure 3.12: Surface areas used for EDX analysis of glass fiber ends: (a–d) glass fiber the end of which looked black and which produced too high turnover numbers and acetylene with blank samples, (e–h) glass fiber the end of which looked unchanged to the naked eye but produced too high turnover and acetylene with blank samples, (i–m) new glass fiber with polished end. Images (b) and (f) were taken with an acceleration voltage of 3 kV. All other measurements were performed with an acceleration voltage of 5 kV. The corresponding EDX results are listed in Table 3.4.

Table 3.4: EDX results corresponding to Figure 3.12: (a–d) correspond to a glass fiber the end of which looked black and which produced too high turnovers and acetylene with blank samples, (e–h) to a glass fiber which looked unchanged to the naked eye but produced too high turnovers and acetylene with blank samples, (i–m) to a new glass fiber with polished end.

Element	**Atom %**						
	a	**b**	**c**	**d**	**e_1**	**e_2**	**f_1**
O	65.62	63.22	66.35		63.11	62.54	62.5
F							
Al		7.56	0.20				
Si	34.38	29.22	31.16	17.37	36.89	36.07	37.5
S				6.05			
Ni			2.29	76.58			
Mo						1.39	

Element	**Atom %**						
	f_2	**g**	**h**	**i**	**k**	**l**	**m**
O	59.88	69.29	64.61	64.7	14.91	64.04	62.83
F			1.89		76.45	3.35	4.30
Al		0.74	2.54				
Si	40.12	25.26	26.41	35.3	8.64	32.60	32.87
S		2.05					
Ca			3.94				
Ni		1.85	0.62				
Pt		0.81					

3.2.5 Discussion and Solution

To sum up, the damaged glass fibers became hot in syngas atmospheres and displayed changes in the surface morphology of the polished front surface. EDX showed Ni and S at the edges of the shafts, but not on the front surface, making it unlikely that the deposition of Ni initiated the degradation. One alternative explanation for the decomposition is coking at the front surface. Coke deposition is known from industrial hydrocarbon cracking processes, where it has to be burnt to regenerate the catalyst.[108] The endothermic decomposition of methane to carbon and hydrogen is also an unwanted side reaction of the steam reforming process for industrial H_2 production, which takes place at temperatures above 500 °C.[109,110]

$$\mathrm{CH_4} \rightleftharpoons \mathrm{C} + 2\,\mathrm{H_2} \qquad \Delta H^{\circ}_{298} = 74.6\,\mathrm{kJ\,mol^{-1}}\text{[110]}$$

The heat of decomposition increases with the chain length of the hydrocarbons from $84.7\,\mathrm{kJ\,mol^{-1}}$ (ethane) to $126.2\,\mathrm{kJ\,mol^{-1}}$ (butane) for paraffins and from $-52.3\,\mathrm{kJ\,mol^{-1}}$ (ethylene) to $0.1\,\mathrm{kJ\,mol^{-1}}$ (1-butene) for olefins.[111] Hence, olefins, the main products under the conditions of the experiments, may already decompose at relatively low temperatures. Although the temperature at the front surface is not directly known, it is probably higher than at the edges, where temperatures around 200 °C were measured. Defects may even be sites where the temperature is locally higher. It is therefore not unlikely that the temperature was high enough for a self-amplifying coking process. As the insulating glass fibers had to be coated with carbon for SEM measurements, EDX does not provide information about possible carbon deposits on the fibers.

It is also possible that traces of Ni on the front surfaces of the fibers, which were below the detection limit of EDX, catalyzed the decomposition of methane. Ni is the active component in the industrial steam reforming process of methane, known to be suffered by deactivation due to the complete decomposition of methane into carbon and hydrogen.[110,112]

The most likely explanation is therefore that hydrocarbons decomposed at the fiber's front surfaces during FT experiments. The deposited carbon was heated by the laser light, further enhancing the coke formation at the front surface. Starting at defects, the temperature became so high that structural changes of the front surfaces occurred by melting or spalling of smaller areas. The light was then no longer focused on the SiC platelet but illuminated the Mo sample holder or other parts of the setup. This led to high blank turnovers and acetylene production.

Based on the idea that a self-amplifying temperature increase is the problem, a glass fiber with an aluminum coating up to the front surface was used (see Figure 3.13).

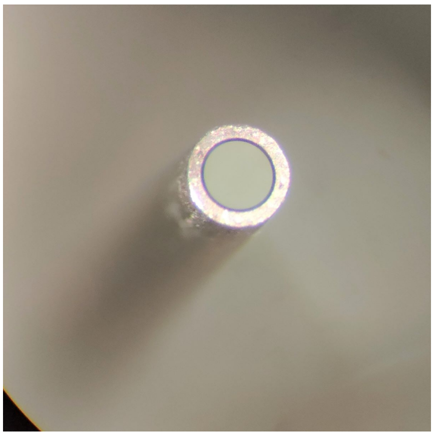

Figure 3.13: New glass fiber with aluminum coating, front view.

As specified by the manufacturer, the metal coating provides effective heat dissipation. As aluminum is not active in the FT synthesis, an enhanced temperature along the shaft of the glass fiber does not constitute a problem for usage under reaction conditions. Blank experiments with a Au(111) sample showed an order of magnitude lower activities than FT experiments on Co(0001), which also rules out any significant contribution of the glass fiber. Similar temperature measurements as described above (see Figure 3.10 c+d) showed fiber temperatures around 50 °C at a laser power of ~21 A, a typical value to heat the sample to the usual temperatures of ~220 °C. Within 6 h, the typical duration of a reaction experiment, the temperature of the glass fiber rose to ~70 °C. So far, the Al coated fiber has not shown any of the problems met with uncoated glass fibers although it has been used in more experiments than any of the bare glass fibers before. All experiments shown in section 4.2 were performed with the same new Al-coated glass fiber. This fact confirms the idea that heat accumulation at the distal end of the glass fiber induced the structural changes of the front surfaces. However, it must be said that the coating with Al only solved the problems in the FT experiments at 950 mbar. In UHV experiments, the efficient thermal conduction damaged the epoxy glue used to hold the fiber in the flange. Obviously, the heat from the fiber is absorbed by the gas phase in high-pressure experiments. Further improvement in the future could be to clamp a Cu braid to the fiber, which could take up the heat during experiments in UHV.

3.3 Temperature Calibration of Co(0001) and Co(10$\bar{1}$15) Surfaces

Another problem which occurred in the experiments was the exact measurement of the surface temperature of the single-crystal samples. The problem became obvious when the crystals were remounted or when the thermocouple setup was changed, after which the activities were strongly altered although the temperatures measured at the backsides of the sample were the same. One aim of this thesis was to correlate the surface morphology and catalytic activity of two different samples, the Co(0001) and the stepped Co(10$\bar{1}$15) crystal. For these measurements, the same experimental conditions, especially the temperatures, were crucial. For meaningful correlations between the surface morphology and the catalytic activity, it was therefore important to ensure that temperatures were the same for both crystals. As a consequence, one experimental challenge in this thesis was the accurate measurement of the sample temperature. This section describes the temperature calibration procedure used for the measurements in section 4.2.1.

3.3.1 Calibration Setup

In the normal sample setup, the temperature is measured by means of an S-type thermocouple fixed at the backside of the hat-shaped crystal (see Figure 2.3 in section 2.1). However, it was found in an experiment after the thermocouple ceramics had been replaced that, despite the setup, the sample and the laser power were identical, the temperatures were different from those before. It was therefore regarded as essential to directly measure the temperatures at the surface. Additional S-type thermocouple wires were spot-welded on the frontsides of the hat-shaped crystals. Pictures of the sample holder setup are shown in Figure 3.14.

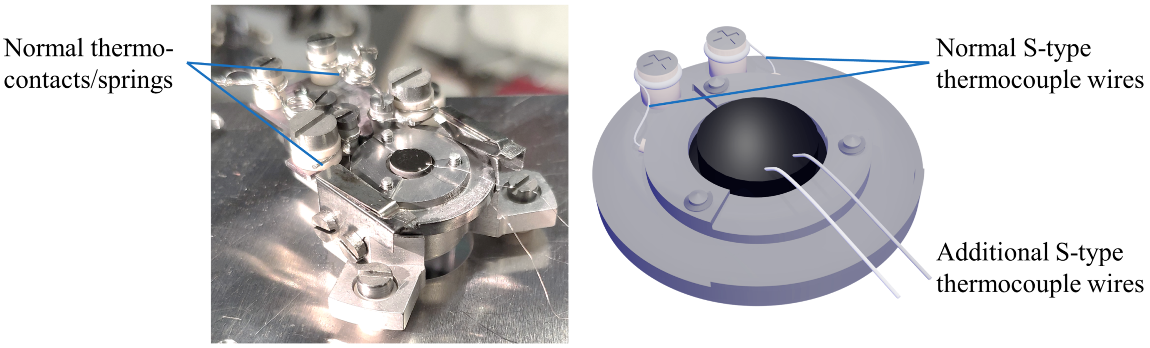

Figure 3.14: Sample setup for temperature calibration measurements. S-type thermocouple wires were fixed directly on the surface of the Co crystals in addition to the normal thermocouple contacts at the backside of the crystal.

To exclude effects of the sample mounting, that may lead to a modified thermal contact to the holder, the Co($10\bar{1}15$) crystal was not reassembled between the calibration measurements of the old and new ceramics. Only the ceramics, holding the thermocouple wires, were replaced and the thin thermocouple wires were reused by spot-welding them to the contacts of the thermocouple clamps.

3.3.2 Calibration Procedure

With the additional thermocouple wires in place, the sample holder could no longer be transferred to the preparation chamber. For this reason, the Co surface could not be prepared prior to the calibration and no activity measurements were performed. After pumping to ~1×10^{-8} mbar, the STM cell was filled with syngas at the same concentration as used in the FT experiments (H_2:CO = 2:1, 950 mbar). The temperatures at the backsides as well as on the frontsides were measured as a function of the laser power. In order not to contaminate the unprepared crystal by long heating, the temperatures were read 5 min after changing the laser power which does not correspond to thermal equilibrium. However, this was done for all measurements exactly in the same way, so that the values are comparable to each other.

3.3.3 Calibration Curves and Discussion

The resulting calibration curves are displayed in Figure 3.15. The filled symbols correspond to the temperatures measured at the surface, the empty symbols belong to the temperatures measured at the normal thermocouple position between the backside and the SiC disc. It is clearly visible that a higher laser power was needed for the Co(0001) crystal (red circles) than for the Co($10\bar{1}15$) crystal (blue and green triangles) to reach the same surface temperature. This is contrary to expectations, as both sample holders are identical and the same laser power for the same temperatures was expected. One explanation for the divergent heating behavior may be the Ta rings between the single crystals and the sample holders. These spacer rings adjust the heights of the samples with respect to the tunneling tip (the beetle STM can only travel a height difference in the order of 0.1 mm). For the Co(0001) sample four such rings were required, for the Co($10\bar{1}15$) sample only two. This difference might cause different temperature gradients between the samples and the sample holders. It also leads to slightly different distances to the glass fiber tip. Another explanation is that the position of the glass fiber was not exactly the same, as the Al capsule was integrated only after the first calibration measurements. Both crystals have in common that the temperatures at the surfaces were higher than at the backsides. This appears counterintuitive as the samples are illuminated from the backside. However, there is a temperature gradient from the backsides across the Ta spacer rings to the sample

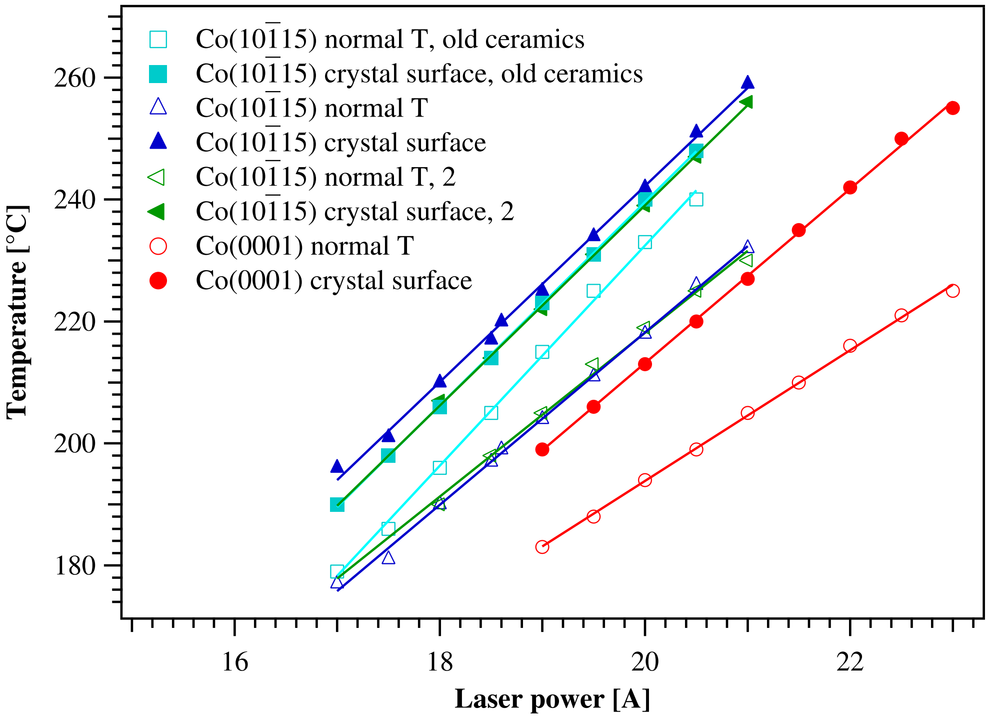

Figure 3.15: Plot of the temperatures of the Co(0001) and Co(10$\bar{1}$15) crystal. The temperatures measured by means of the normal thermocouple setup are displayed with empty symbols, the temperatures at the crystal surfaces are shown with filled symbols. Squares correspond to the Co(10$\bar{1}$15) crystal with the old thermocouple ceramics, the data displayed by triangles are the result of a measurement with the Co(10$\bar{1}$15) crystal with a new set of thermocouple ceramics. This measurement was repeated to validate reproducibility. Circles represent the temperatures of the Co(0001) crystal.

holders. The thermocouple wires are mounted at the outer rims of the samples, which is in contact with the spacers, and may therefore be slightly colder than the frontsides of the samples.

According to Figure 3.15, the normally measured temperatures at the backside also varied when the thermocouple ceramics were changed. While new ceramics (dark blue and green triangles) resulted in nearly parallel slopes of the temperature curves, old ceramics (light blue squares) that were partially covered by a visible metal film led to a steeper slope of the curve. EDX measurements showed that the metallic coatings on the ceramics and the thermocouple wires were mainly Mo. The obvious reason is the preparation procedure of the samples during which the sputtering also affects the Mo holder. The reason for the divergences in temperature might be changes of the thermoelectric voltages due to alloying of the Pt/PtRh wires with Mo. Pt is known to be particularly susceptible to contamination resulting in changes of its thermoelectric sensitivity.[113–115] In particular, the thin thermocouple wires connecting the backsides of the samples with the contacts of the thermocouple clamps at the frontsides of the holders may be susceptible to contamination. Their low diameters make them more vulnerable to contamination effects than the thicker wires of the thermocouple clamps. Several alloys of the Mo-Pt system are known[116–119] but whether they form at the relatively low temperatures applied here is unknown. However, some solid diffusion of Mo into the Pt wires may take place during annealing (350 °C) or FT reactions (220 °C). One also has to consider the long time scales; in some cases the thermocouples have been in use for several years. By means of the calibration measurements, these uncertainties were adjusted.

Apart from the offset in laser power, the measurements of Co(0001) and Co(10$\bar{1}$15) (both with new ceramics) show comparable differences between the surface and the backside temperatures. The reproducibility of the temperature measurements was tested by repetition of the measurement with the Co(10$\bar{1}$15) crystal (new ceramics) after repeated adjustments of the glass fiber and after replacing the ceramics. For this purpose new thermocouple wires were spot-welded to the crystal surface. According to Figure 3.15, apart from a minimal deviation of the surface temperature, the measurements show the same results.

To conclude, the temperature calibration measurements show that the deposited metal films on the ceramics, used to mount the thermocouple wires, influenced the temperature at the crystal surface. As a result, accurate calibrations of the surface temperatures were needed for the comparison of the two samples. For the experiments shown in section 4.2.1, the sample had to be transferred between the preparation chamber and the reaction cell, so that only the temperatures measured at the backsides were available. In order to select a certain frontside temperature, the calibration curves of Figure 3.15 were used. For a surface temperature of ~228 °C, the Co(0001) sample was heated to a temperature of ~205 °C measured at the backside, whereas the Co(10$\bar{1}$15) crystal was heated to a backside temperature of ~220 °C.

Further experiments showed that the relation between the surface temperature and backside temperature also changed when the crystal was re-mounted, or when the position of the glass fiber was adjusted. To safely exclude that the differences between TOFs of the Co(0001) and Co(10$\bar{1}$15) single crystals were determined by different temperatures, the sample setup was modified and the thermocouple wires at the backsides were removed and replaced by thermocouples directly spot-welded to the crystal surfaces.

3.4 Installation of a Customized GC

For the *operando* FT experiments at the HP-STM setup, a new method to determine the catalytic activity was needed. The relatively large volume of the STM cell in addition to the small catalytically active crystal surface, compared to a sample of a typical supported catalyst, result in very low concentrations of hydrocarbon products. According to an estimate by B. Böller,[63] the concentration of C_4-hydrocarbons, after 1 h reaction at 1 bar syngas and a sample temperature of 220 °C, was expected to be in the lower ppb range. The QMS, which is attached to the HP-STM setup, does not provide the sensitivity for these low concentrations. Furthermore, the fragmentation patterns of the different hydrocarbons strongly overlap in the mass spectra, which makes them extremely complicated to distinguish. Figure 3.16 displays the superposition of mass spectra (tabulated data) for methane, ethane, ethylene, propane, propylene, butane, α-butylene, and isobutylene. The individual spectra are shown in Appendix D.

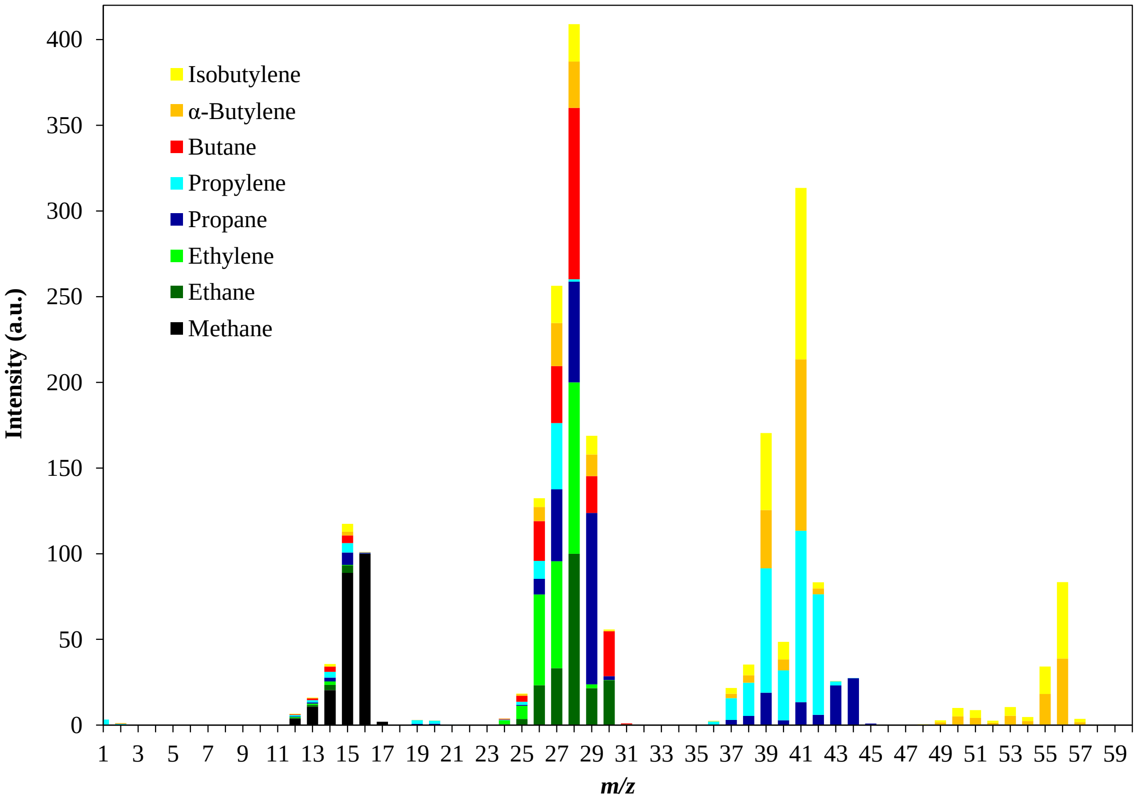

Figure 3.16: Sum of mass spectra of methane, ethane, ethylene, propane, propylene, butane, α-butylene and isobutylene. The individual mass spectra were taken from the NIST database[120] and are shown in Appendix D.

It is clearly visible that, for example, ethane, ethylene, propane and butane all show large signal intensities at $m/z = 28$, so that this strong signal cannot be used to identify individual components in the product mixture. More importantly, the CO of the syngas matrix has the same m/z value and completely overwhelms the signal. Furthermore, due to fragmentation, smaller fragments of long hydrocarbons have higher intensities than longer ones. For example, propylene and butylene have the highest peak at $m/z = 41$ despite their different chain lengths. Thus, other fragments with lower intensities have to be used to distinguish these hydrocarbons. Theoretically, for FT experiments masses with lower output signals could be used for product quantification, but the sensitivity of the QMS was insufficient to analyze longer hydrocarbons than C_2.

A technique, which can distinguish different kinds of hydrocarbons is gas chromatography. The different chain lengths result in different interactions with the column which cause individual retention times. For more details concerning the working principle of gas chromatography, see section 2.4. However, the sensitivity of common gas chromatographs (GCs) is not sufficient for concentrations in the ppb range. Beside the sensitivity, another challenge had to be overcome. The reaction pressure in the STM cell is usually below the working pressure of the GC of 1 bar and, as experiments are performed in batch mode, only small amounts of gas sample can be extracted. Standard GC setups could therefore not be used. In cooperation with S+H Analytik GmbH, a GC setup was developed that meets the requirements for the FT experiments in the HP-STM cell. It had been tested and modified at a separate reactor prior to this thesis. In the framework of the present work, the GC was attached to the HP-STM setup, tested, and calibrated. A new micropacked column was mounted, and serial dilution measurements were performed for calibration purposes. Details of the calibration procedure are given in Appendix C.5.

Furthermore, the oven program was optimized to ensure a better distinction of C_4 compounds from the rising background towards higher retention times. With the new parameters, the quantification of butane was possible. An additional aim was a better separation of propane and propene for a more reliable quantification. For details of the previous and optimized oven programs see Appendix C.4. Data in this chapter as well as in section 4.1 were recorded with the previous oven program, whereas for the study in section 4.2, the optimized oven program was used. All GC setting are listed in Appendix C.

In the following, the GC setup is described by the publication “A highly sensitive gas chromatograph for *in situ* and *operando* experiments on catalytic reactions”,[121] published in *Reviews of Scientific Instruments.* It presents the setup and its performance and describes the automated gas sampling and injection unit in detail. Key points of the publication are:

- Using a new automated gas sampling and injection unit, gas samples can be injected at pressures below 1 bar. This is achieved by a buffer volume that is filled with gas samples from the STM reactor at a reduced pressure, followed by a compression to the injection pressure of 1000 mbar by means of He. Tests showed that intermixing of the gas sample and He can be neglected. Due to the design, only small fractions of the reaction gas are abstracted from the total sample volume in the STM cell.

- The gas sampling and injection unit is attached to a modified standard gas chromatograph including two channels with FIDs and He carrier gas supply.

- Due to the small concentration of hydrocarbons within the gas sample, a comparatively large sample volume (~5 mL) is needed to meet the detection limits. To avoid peak broadening resulting from this volume, a cryo trap at the head of one of the two columns concentrates the hydrocarbons in the sample volume and provides focused peaks. The other channel, a standard configuration, is used for comparison; it has a smaller sample loop, showing much less sensitivity compared to the cryo channel. All shown experiments are based on measurements with the cryo channel.

- Calibration measurements with a custom-made calibration gas mixture, containing ~10 ppm of C_1–C_4 hydrocarbons, show a good linearity over four orders of magnitude between 1 ppb and 10 ppm.

- FT experiments on a Co(0001) catalyst at pressures of 200 mbar and 950 mbar demonstrate the high performance of the setup. With the installed micropacked column in addition to the capillary columns, separation of all product peaks – short paraffins and olefins C_1 to C_4 – from the synthesis gas (H_2:CO) was achieved.

- Experiments with low concentrations of propane revealed a detection limit for short hydrocarbons of 0.4 ppb. The limit for quantification is 1.3 ppb. Hence, TOFs of the order of $1\times10^{-5}\,s^{-1}$ can be measured.

The article "A highly sensitive gas chromatograph for *in situ* and *operando* experiments on catalytic reactions" published in *Review of Scientific Instruments* is reproduced from *Rev. Sci. Instrum.* **92**, 124103 (2021), with the permission of AIP Publishing.

Review of
Scientific Instruments
ARTICLE
scitation.org/journal/rsi

A highly sensitive gas chromatograph for *in situ* and *operando* experiments on catalytic reactions

Cite as: Rev. Sci. Instrum. **92**, 124103 (2021); doi: 10.1063/5.0068021
Submitted: 22 August 2021 • Accepted: 20 November 2021 •
Published Online: 9 December 2021

View Online Export Citation CrossMark

Katharina M. Golder,[1] Bernhard Böller,[1] Günter Stienen,[2] Joern Sickerling,[2] and Joost Wintterlin[1,a)]

AFFILIATIONS

[1] Department Chemie, Ludwig-Maximilians-Universität München, 80377 Munich, Germany
[2] S+H Analytik GmbH, 41066 Mönchengladbach, Germany

[a)] Author to whom correspondence should be addressed: wintterlin@cup.uni-muenchen.de

ABSTRACT

We describe an automated gas sampling and injection unit for a gas chromatograph (GC). It has specially been designed for low concentrations of products formed in catalytic *in situ* and *operando* experiments when slow reactions on single crystal models are investigated. The unit makes use of a buffer volume that is filled with gas samples from the reactor at a reduced pressure. The gas samples are then compressed by He to the injection pressure of 1000 mbar and pushed into two sample loops of the GC, without major intermixing with He. With an additional cryo trap at one of the GC column heads, the design aims at concentrating the gas samples and focusing the peaks. The performance is characterized by experiments on the Fischer–Tropsch synthesis, using H_2/CO mixtures (syngas) at 200 and 950 mbar and a Co(0001) single crystal sample as model catalyst. Chromatograms recorded during the reaction display sharp, well separated peaks of saturated and unsaturated C_1 to C_4 hydrocarbons formed by the reaction, whereas the syngas matrix only gives moderate signals that can be well separated from the product peaks. Detection and quantification limits of 0.4 and 1.3 ppb, respectively, have been achieved and turnover numbers as low as 10^{-5} s^{-1} could be measured. The system can be combined with all known analysis techniques used in *in situ* and *operando* experiments.

INTRODUCTION

In situ and *operando* experiments can provide direct information on the state of an active heterogeneous catalyst under the conditions of the reaction.[1,2] We here use the terms *in situ* and *operando* for experiments in which a catalyst is analyzed in a reaction gas mixture under pressure and temperature conditions that approach those in the respective industrial process, and in which, at the same time or at least in the same reactor and under the same conditions, the catalytic turnover is measured. When a surface-sensitive technique is applied, the activity of the catalyst can be correlated with the surface structure and the chemical species adsorbed on its surface. Experiments are challenging, but for powder catalysts, techniques such as diffuse reflectance infrared Fourier transform spectroscopy (DRIFTS) and transmission electron microscopy (TEM) have successfully been combined with turnover measurements.[3,4]

In situ/*operando* experiments on single-crystals, utilizing their defined surface structures, can, in principle, provide even clearer correlations. However, the experiments become more difficult, too. The problem, which equally exists for experiments on powder samples, is then not only the presence of the gas phase, which makes a surface analysis more difficult than in vacuum. Surface techniques that can be applied at elevated pressures also exist for single crystals, in particular, sum frequency generation (SFG),[5] polarization modulation reflection absorption infrared spectroscopy (PM-RAIRS),[6,7] near-ambient pressure x-ray photoelectron spectroscopy (NAP-XPS),[8–10] surface x-ray diffraction (SXRD),[11] and scanning tunneling microscopy (STM).[12,13] However, a single crystal has a several orders of magnitude smaller surface than a typical powder catalyst sample so that the catalytic turnover is lower by a comparable factor. Moreover, the reactors are often relatively large because they have to house components of the respective analysis technique. The concentration of products becomes an issue. For fast reactions such as the oxidation of CO, this is usually uncritical, and there are several *in situ*/*operando* studies in which the CO_2 formed on single crystals of Pt and other active metals could readily be detected by quadrupole mass spectrometry (QMS).[14–17] QMS has also been utilized in a number of investigations of other fast reactions,[10] and in some PM-RAIRS and NAP-XPS studies, products could also be detected by the respective IR and XPS gas phase signals.[18,19] However, for slow, kinetically demanding reactions, product detection can become a massive problem, and there are only few *in situ*/*operando* investigations of such reactions on single crystals where QMS could be used.[20]

We faced an extreme detection problem in *in situ*/*operando* STM experiments on the Fischer–Tropsch synthesis of hydrocarbons from H_2/CO mixtures (syngas). The experiments were performed in a chamber of 1.8 l at syngas pressures between 10 mbar and ~1 bar, using a Co(0001) single crystal (~220 °C) as catalyst.[21–23] The main product under these conditions, methane, could be detected by QMS at a reasonable signal-to-noise ratio. However, for the higher hydrocarbons, which are more relevant for the industrial process but are formed in much lower amounts, this was no longer the case. For example, the concentration of butane, after a 1 h batch experiment at 200 mbar syngas at 220 °C, was only of the order of 1 ppb (parts per billion). It proved impossible to detect longer hydrocarbons than C_2 by QMS in these experiments.

An alternative to QMS is gas chromatography (GC). GC has been used in PM-RAIRS and SFG studies in a few cases,[5,24] and because of its high sensitivity, it would, in principle, also be suitable for slow reactions. The sensitivity for low concentrations of hydrocarbons has been demonstrated in investigations of atmospheric air, in which traces of less than 1 ppb, even down to 1 ppt (parts per trillion), of hydrocarbons could be detected.[25–28] However, these measurements have been performed with large gas samples of the order of 1 l (at 1 bar), which is prohibitive for the experiments considered here. To keep the conditions in the reactor unchanged, gas samples no larger than a few milliliters should be extracted.

The second difficulty with GC is that *in situ*/*operando* experiments on single crystals are mostly performed at somewhat lower pressures than 1 bar, typically between several mbar and several 100 mbar. The reduced pressures mainly result from the constrictions from the respective surface analytical technique, but usually there are some further practical limits. The reduced pressures are in conflict with the working pressure of a GC of ≥1 bar required for injecting a gas sample into the separation column. In some studies, a fill-up gas, He or Ar, has been used in the reactor chamber to increase the pressure to this value.[29,30] However, for the extremely low concentrations considered here, the volume of the sample loop of the GC, in order to collect enough product material, would have to be increased to compensate for the dilution by a fill-up gas. The increased injection time would lead to broadened and distorted peaks.

We here describe an automated gas sampling and injection system for a GC that solves these problems. We have previously shown that the surface structure of a cobalt single crystal resolved by STM could be correlated with the Fischer–Tropsch activity determined by GC.[23] Here, we give a detailed description of the GC system that has been constructed to enable these measurements, and we characterize its performance by means of data from the Fischer–Tropsch reaction. The system would also be suitable for combined experiments with other enhanced-pressure analysis techniques and for other slow catalytic reactions.

OVERALL EXPERIMENT

Figure 1 shows the components of the overall experiment, i.e., the reaction chamber, the gas sampling and injection unit, the GC, and the cryogenic nitrogen unit. The reaction chamber with the beetle-type STM and the attached ultra-high vacuum (UHV) chamber (not shown) have been described previously.[31] All our *in situ*/*operando* experiments have been performed in this chamber. Pressures between 10^{-10} and 1000 mbar can be adjusted, and the sample is heated by light from an infrared laser coupled into the chamber by a glass fiber. The Fischer–Tropsch experiments we discuss here were carried out with a Co(0001) single crystal as model catalyst, applying H_2:CO = 2:1 syngas mixtures at total pressures of 200 and 950 mbar, and at sample temperatures of ~220 °C. Under these conditions, the Fischer–Tropsch synthesis

$$(2n + 1)H_2 + nCO \rightarrow C_nH_{2n+2} + nH_2O$$

mainly produces hydrocarbons with n = 1–4.[23,32] Because of the relatively large volume of the STM chamber and the low turnover numbers (TONs), the analysis problem consists of detecting low concentrations of light hydrocarbons in a large matrix of H_2 and CO. (We here use the acronym TON instead of TOF so that in this GC context, one might not get confused with time-of-flight mass spectrometry.)

The special gas sampling and injection unit is described in detail below. The GC itself is a modified standard gas analyzer trace 1310 (Thermo Fisher). It has two channels, each with its own sample loop, six-port valve for injection, carrier gas supply column, and flame ionization detector (FID). He (99.999%) serves as carrier gas. To further reduce impurities and minimize baseline fluctuations, the He gas is additionally passed through a filter (Helium Purifier, VIVI Metronics). Gas samples are simultaneously injected into both channels, and He flows of 10 ml min^{-1} (channel I) and 5 ml min^{-1} (channel II) are applied.

Channel I is a standard configuration. It is equipped with a small sample loop (250 μl) and two capillary columns in series (30 m TracePlot TG-BOND Q+ 0.53 mm ID, 20 μm dF, Thermo Fisher). This column type was chosen because of its reliable separation of

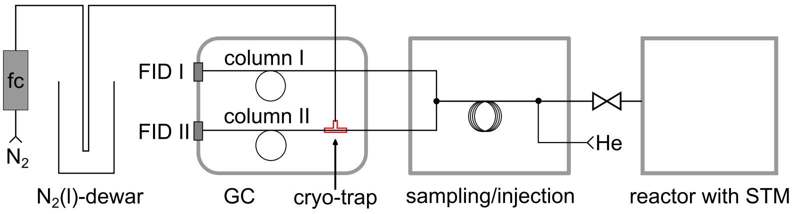

FIG. 1. Block diagram of the overall experiment. The components from right to left are the STM chamber, the gas sampling and injection unit, the gas chromatograph with its two analysis channels and the cryo trap on one channel, and the cryogenic N_2 supply with gas flow controller (fc) and liquid N_2 Dewar.

ethane and ethylene, and the relatively long capillary ensures good separation of the various species, even when they are present in higher amounts. In test measurements, this channel was suitable for concentrations of CH_4 of ≥500 ppb and of C_2 and higher hydrocarbons of ≥65 ppb. The quality of the spectra was unchanged up to the highest tested concentrations of C_1 to C_4 hydrocarbons of 10 ppm.

Channel II is configured for the very low hydrocarbon concentrations formed in the experiments considered here. It is equipped with a large sample loop (5.4 ml) to collect sufficient material, and it uses a micro-packed column (2 m HayeSep Q80/100, Restek GmbH) followed by a capillary column (30 m TracePlot TG-BOND Q+, 0.53 mm ID, 20 μm dF, Thermo Fisher). Approximately 10 cm downstream from the head of the micro-packed column, a cryo-trap is mounted (MicroJet cryo-trap MJT 1035E, Frontier Lab). Cryo-trapping is an efficient way of concentrating analytes in dilute gas samples and focusing the peaks in the chromatograms.[33–35] In the present setup, cryo-trapping is realized by feeding dried nitrogen gas (7 l min^{-1}) through a thermal exchange coil in a liquid nitrogen Dewar to the MicroJet tube before and during injection of a gas sample. The MicroJet tube cools a ~3 cm long segment of the micropacked column. The idea is that the hydrocarbons in the gas sample become trapped in the cooled column part during injection, whereas H_2 and CO from the matrix, because of their lower boiling temperatures, are much less affected. After injection of a gas sample, the cooling is turned off and the GC oven program starts heating the columns and the cryo-trap. The micro-packed column was more efficient for trapping than the capillary column, probably because of the enhanced adsorption on the densely-packed adsorbent. Most of the separation happens in the capillary column downstream.

FIDs are used for both channels because of their sensitivity for hydrocarbons.[36–38] At the same time, they are almost insensitive to H_2 and CO so that the signals are not overwhelmed by the components of the syngas matrix. N_2 serves as make-up gas. Chromeleon 7.2 software (Thermo Fisher) is used for controlling the injection and for data recording and analysis.

GAS SAMPLING AND INJECTION UNIT

Figure 2 shows the specially designed gas sampling and injection unit. It is based on the idea of extracting gas samples from the STM chamber at a preset, reduced pressure into a buffer volume, and then to compress the gas in this buffer volume such that it fills the two sample loops of the GC at a pressure of 1000 mbar. In this way, the sample loops are loaded with concentrated gas samples at the pressure required for injection.

The main parts of the unit (Fig. 2) are the buffer loop, the valves [NV (FITOK GmbH), MV2, MV3 (Parker Hannifin GmbH)] for filling the buffer loop with gas samples and feeding in He for compression, and a precision membrane pressure sensor (Keller AG). Further components are the sample loops of the two GC channels, two six-port valves (6-PV I and II, VICI Valco Instruments Co.) and their connections to the He carrier gas, a rotary pump for evacuation of the line, and a solenoid valve [MV1 (Gems Sensors and Controls)] for disconnecting the pump. The unit is controlled by a Labview/National Instruments system.

An automated GC measurement is started when the cryogenic N_2 transfer line has reached a temperature of ≤−194 °C. Then, the solenoid-valve MV1 closes to stop the evacuation of the system, and the valve MV2 opens (the needle valve NV is in a fixed, partially open position) to let gas from the STM chamber flow into the evacuated buffer loop and the two sample loops. The sensor monitors the pressure, and when a preset value has been reached (80 mbar for the experiments shown below), a window comparator closes the magnetic valve MV2 to stop the sampling. The role of the needle valve NV is to reduce the gas flow so that the time for filling is prolonged to ~10 s. In this way, pressure gradients during filling are largely avoided, and the valve control, which has a limited response time, can work properly. After the MV2 has closed, the magnetic valve MV3 opens to introduce He. The He gas compresses the gas in the buffer loop into the two sample loops, until the sensor records a pressure of 1000 mbar.

When 1000 mbar have been reached, the window comparator closes the MV3, the six-port valves switch to their injection positions, and a GC analysis cycle is started. At the same time, the MV1 opens (and is kept open until the next measurement) to re-evacuate the sample loops and the buffer volume by the rotary pump. After 3 min, the six-port valves switch back to their loading positions (Fig. 2). 4.5 min after the injection, the GC oven program starts increasing the temperature at a rate of 25 °C min^{-1} from an initial value of 35 °C to a final value of 200 °C, holds the temperature at 200 °C for 1 min, and then stops the heating.

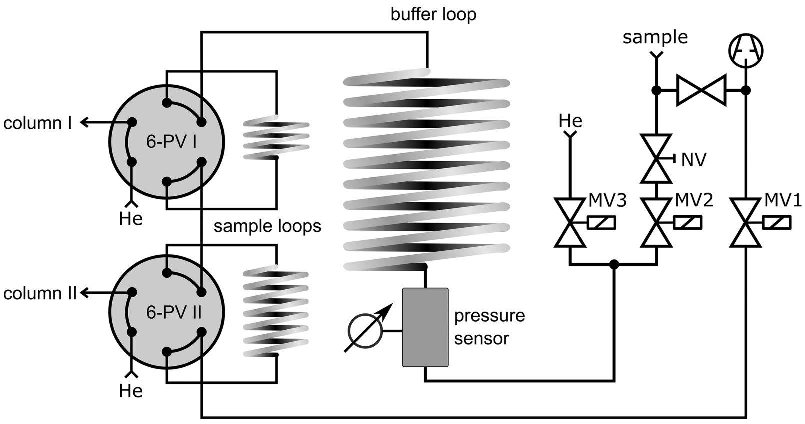

FIG. 2. Schematic of the automated gas sampling and injection unit. Gas samples from the STM chamber are fed through a needle valve (NV) and a solenoid-valve (MV2) to the buffer loop and the two sample loops. A sensor records the pressure during filling. When a preset pressure of 80 mbar has been reached, the filling is stopped and He is fed through the solenoid-valve MV3, compressing the gas into the two sample loops. At 1000 mbar, the two six-port valves (6-PV I and II) simultaneously switch to their injection positions.

80 mbar was chosen for the filling pressure of the buffer loop because it is lower than the pressure in the STM chamber in the experiments (200 and 950 mbar). As long as this condition is fulfilled, the system works independently of the pressure in the STM chamber, a flexibility that can be used, e.g., for investigations of pressure-dependent TONs.

The volume of the buffer loop (76.3 ml), the largest part of the sampling and injection unit (total volume 87.6 ml), was chosen such that, after filling at 80 mbar and compression, a gas sample (6.3 ml at 1000 mbar) completely fills the two sample loops (0.25 and 5.4 ml). Losses to dead volumes are low. The second consideration has been to keep the gas samples small. At the chosen volume and pressure, the extracted molar fractions per GC run are 1.9% and 0.4% of the gas in the STM chamber in the 200 and 950 mbar experiments, respectively. The conditions in the STM chamber are thus largely unchanged.

For the compression step it is, of course, essential that the gas sample does not significantly mix with He. Mixing could happen by interdiffusion. To estimate the extent, we use the diffusion constant of $D = 0.69\ \mathrm{cm}^2\ \mathrm{s}^{-1}$ that has been measured for methane in He at 1 bar and 298 K.[39] With this value, the interface between the gas sample and He (which, after compression, is close to the end of the buffer loop) has broadened to roughly 7 cm after the time for compression (35 s), a reasonably small value with respect to the length of the buffer loop (4 m). Initially, when the pressure in the buffer loop is 80 mbar, the diffusion constant is higher and the broadening is faster, but this should largely be compensated when the interface is compressed during the influx of He.

Intermixing could also happen by turbulence. To assess whether this plays a role, we estimate the Reynolds number, taking into account that the compression almost entirely takes place in the buffer loop. With the tube dimensions of the buffer loop (length 4 m and inner diameter 4.93 mm) and the time for compression (35 s), and using the fact that the tube initially contains 80 mbar syngas (simplified to pure H_2), a Reynolds number of ~1 is calculated. At the end of the compression, when the tube contains 1000 mbar He, the Reynolds number has increased to ~10. Hence, even when massive errors are taken into account, these numbers are far below the critical range of 2300–4000, above which the flow would become turbulent. The flow during filling is laminar and turbulence-induced mixing should not occur.

To determine the extent of intermixing experimentally, a modification of the setup in Fig. 2 was used. It contained a smaller buffer loop (~8.5 ml), and the pressure sensor (volume 3–4 ml) was mounted downstream of the two sample loops. A gas sample was taken at 80 mbar and compressed to 1000 mbar, a GC was recorded, and this was repeated with filling pressures of 160, 240, and 320 mbar. At 80 mbar, the GC (channel II) only showed minor signals from CH_4, ethylene, and ethane because the gas sample (~1.5 ml after compression in this configuration) had almost completely been pushed into the downstream pressure sensor, and the sample loops only contained He. At 160 and 240 mbar, the signals were somewhat higher, but at 320 mbar, the hydrocarbon signals suddenly increased strongly because, at this point, the sample loop of channel II had started to fill. In the complete absence of intermixing, the signals at the lower pressures would have been zero. For the standard filling pressure of 80 mbar, the signals were 0.4% of the extrapolated signals from a fully loaded sample loop (channel II). This value can be seen as the error caused by intermixing.

PERFORMANCE

Figure 3 displays the general shape of the chromatograms recorded during the Fischer–Tropsch experiments. Channel I (black trace) shows a peak from CH_4, a second, hardly visible peak from C_2H_4, and a third peak from C_3H_8 (visible in the enhanced inset). Channel II (red trace) shows distinct peaks from CH_4, C_2H_4, C_2H_6, C_3H_6, C_3H_8, C_4H_8, and C_4H_{10}. (The peaks from the saturated molecules appear at the right sides of the unsaturated molecules.) The scalings are the same, showing that the peak intensities of the cryo-trapped channel are significantly higher than those of the standard channel. The saturated C_2 and C_3 hydrocarbons, which, under the conditions of the experiment, are formed in lower amounts than the unsaturated molecules and both saturated and unsaturated C_4 hydrocarbons are only detected on the cryo-trapped channel. This enhanced sensitivity of channel II is not paid for by wider peaks in the chromatograms, despite a volume ratio of more than 20 of the two sample loops. The peaks on channel II are equally sharp as on channel I, and also the saturated and unsaturated hydrocarbons are well-separated, a result of the focusing effect of the cryo trap.

The broad initial signals at retention times between 2.0 and 2.4 min (channel I) and between 1.5 and 5.5 min (channel II) are attributed to the H_2/CO syngas matrix. For channel II, efforts have been made to minimize the overlap of the first hydrocarbon peak (CH_4) with the matrix signal by varying the cooling time and the parameters of the oven program. Considering the high partial pressure ratio of the syngas and the hydrocarbon products, the resulting interference of matrix signals with the hydrocarbon peaks is satisfactorily low, a result of the use of FIDs. The increasing baseline after 10 min is caused by some bleeding of the stationary phase of the columns toward higher oven temperatures.

It is obvious that the performance of the cryo-trapped channel II is much better than that of channel I, and in the following,

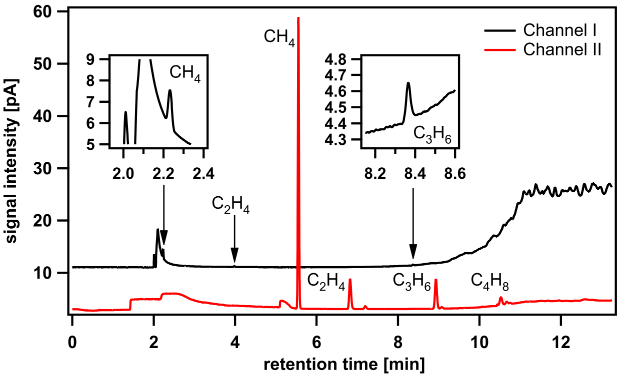

FIG. 3. Two simultaneously recorded chromatograms, showing the different sensitivities of channel I (black) and of the cryo-trapped channel II (red). The chromatograms were recorded after a 6 h Fischer–Tropsch experiment in the STM chamber, performed with a H_2:CO = 2:1 syngas mixture at a total pressure of 200 mbar. A Co(0001) single crystal served as model catalysts, and the sample temperature was 220 °C.

TABLE I. Linearity of the chromatograms. $\bar{x}$: Peak area/concentration ratios, normalized by the peak area/concentration ratio of the 10 ppm mixture of the calibration gas, averaged over five consecutive measurements. σ: Standard deviations.

	10 ppm		1 ppm		100 ppb		10 ppb		1 ppb	
	$\bar{x}$	σ	$\bar{x}$	σ	$\bar{x}$	σ	$\bar{x}$	σ	$\bar{x}$	σ
CH_4	1.00	0.001	0.98	0.001	1.10	0.004	1.17	0.023	2.99	0.233
C_2H_4	1.00	0.001	0.97	0.001	0.96	0.005	1.00	0.023	1.07	0.063
C_2H_6	1.00	0.002	0.98	0.001	1.03	0.004	1.04	0.008	1.03	0.059
C_3H_6	1.00	0.004	0.97	0.001	0.92	0.005	1.07	0.026	1.19	0.029
C_3H_8	1.00	0.002	0.97	0.000	0.98	0.005	0.98	0.021	0.94	0.048
C_4H_{10}	1.00	0.002	0.97	0.001	0.92	0.002	1.02	0.025	1.14	0.106

we only discuss data from channel II. Moreover, all quantifications are made with these data. (The reason for installing a channel without cryo trap has been that, initially, it had not been clear whether CH_4, because of its lower boiling temperature, could quantitatively be cryo-trapped like the higher hydrocarbons. However, it turned out that this was unproblematic, and CH_4 could equally be quantified on channel II.) In the first weeks of operation, the retention times showed some shifts, probably caused by degradation and compression effects in the micro-packed column that reduced the He flow. This problem was solved by adjusting the pressure of the He carrier gas.

For quantification of the chromatograms, a custom-made calibration gas was used (Air Liquide, 150 bar). It contained ~10 ppm of most of the relevant hydrocarbons in a 2:1 mixture of H_2 and CO (9.67 ± 0.19 ppm CH_4, 9.58 ± 0.19 ppm C_2H_4, 9.49 ± 0.19 ppm C_2H_6, 9.45 ± 0.19 ppm C_3H_6, 9.60 ± 0.19 ppm C_3H_8, 9.50 ± 0.19 ppm C_4H_{10}, 30.91 ± 0.62% CO, and the rest is H_2).

The calibration gas was also used for determining the linearity of the system. For the undiluted case, the calibration gas was directly fed into the sampling and injection unit. Dilutions were prepared in the STM chamber in steps of one order of magnitude, by feeding ~100, ~10, and ~1 mbar (limited by the pressure range of the manometer) of the calibration gas into the chamber, filling up with syngas to 1000 mbar, and recording chromatograms in the usual way. The fill-up gases H_2 and CO were passed through liquid N_2 cold traps to freeze out hydrocarbon contaminations, and CO was additionally passed through a hot trap to decompose carbonyls. A further dilution by one order of magnitude was prepared by pumping out ~90% of the last mixture (10 ppb) in the STM chamber, and filling up with syngas to 1000 mbar. For each dilution, five sequential chromatograms were taken; the results are shown in Table I.

The entered values are the respective averaged peak area/concentration ratios, normalized by the peak area/concentration ratios of the initial 10 ppm mixture of the calibration gas. One can see that the data of the individual hydrocarbons deviate from the ideal value of 1.00 by just a few percent, indicating good linearity between 10 ppm and 1 ppb, i.e., over four orders of magnitude.

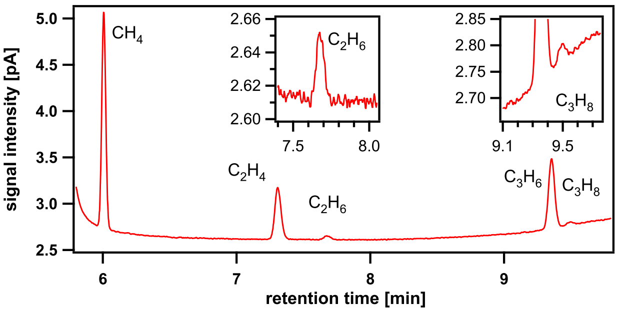

FIG. 4. Determination of the detection limit. The chromatogram was recorded on channel II after a 1 h Fischer–Tropsch experiment, showing peaks from C_2H_6 and C_3H_8 (magnified insets) close to the noise level of the base line. Conditions: H_2:CO = 2:1, total pressure 950 mbar, Co(0001) sample, and sample temperature 220 °C.

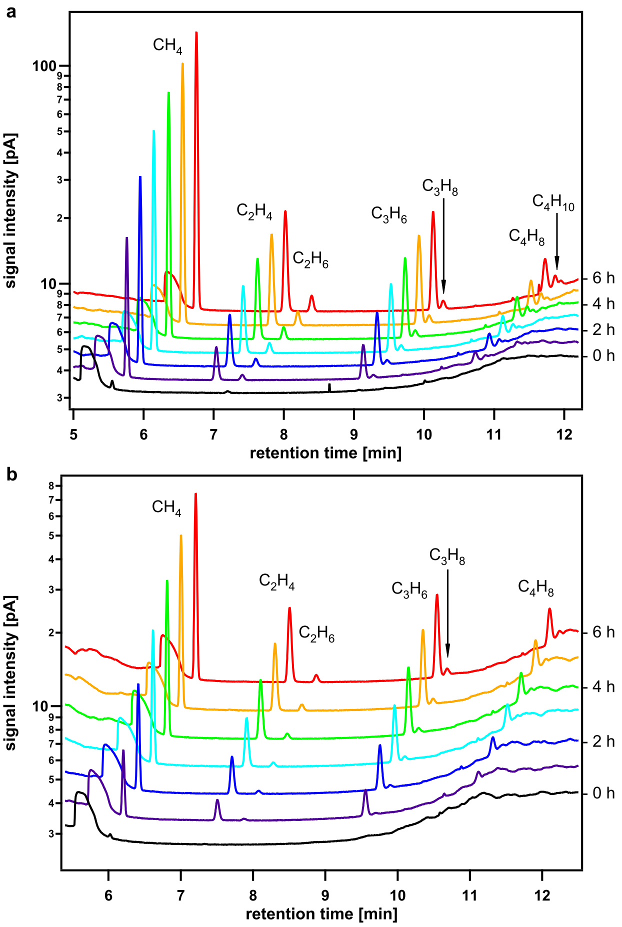

FIG. 5. Time series of chromatograms recorded on channel II during the Fischer–Tropsch synthesis. Conditions: H_2:CO = 2:1, total pressures 200 mbar (a) and 950 mbar (b), Co(0001) sample, and sample temperature 220 °C. The retention times and signal intensity axes refer to the chromatogram at $t = 0$ (black). The chromatograms taken at later reaction times are displaced by offsets along the x and y axes for better readability. The peak intensities in (b) are lower than in (a) because, at 950 mbar, proportionally less gas is extracted than at 200 mbar. This is partially compensated by the higher TON at the higher pressure, but the TON increases less than linearly with pressure.

TABLE II. TONs from the two experiments in Fig. 5, in units of product molecules per Co surface atom per second. Butane was at the detection limit and the marked value (*) only includes data points between 3 and 6 h. The CO consumption rate (last column) is evaluated by summing the TONs of the products after multiplying by the C numbers of the respective molecules.

p(mbar)	TON CH_4 (10^{-4} s^{-1})	TON C_2H_4 (10^{-4} s^{-1})	TON C_2H_6 (10^{-4} s^{-1})	TON C_3H_6 (10^{-4} s^{-1})	TON C_3H_8 (10^{-4} s^{-1})	TON C_4H_8 (10^{-4} s^{-1})	TON C_4H_{10} (10^{-4} s^{-1})	TON CO (10^{-4} s^{-1})
200	15.1	1.42	0.13	0.85	0.05	0.21	0.06	22.0
950	17.9	3.23	0.25	2.65	0.15	0.98	0.12*	37.6

One exception is the CH_4 signal at the highest dilution of 1 ppb, which is too high by a factor of 3. The source of this deviation was clarified by measurements with mixtures of (nominally) pure H_2 and CO. These mixtures, nevertheless, showed CH_4 signals between 0.3 and 3 ppb, indicating that the deviation of the methane signal is caused by methane traces in the syngas not completely removed by the liquid N_2 traps, rather than by non-linearities of the system. For the Fischer–Tropsch experiments, these traces are uncritical as the concentrations of CH_4 are higher.

The standard deviations of the linearity measurements (Table I) are low, demonstrating good reproducibility. We find that to obtain well reproducible results, sufficient time has to be given between measurements, which we attribute to the evacuation of the gas sampling and injection unit. This condition was fulfilled in the Fischer–Tropsch experiments where ~1 h was left between GC measurements.

Using the calibration, detection limits could be evaluated. Figure 4 shows a chromatogram from an experiment with very low signals from C_2H_6 and C_3H_8 (insets), close to the noise level of the baseline. The corresponding concentrations are 1.2 and 0.45 ppb, respectively. The signal to noise ratios, $S/N = 2\ H/h$,[40] where H is the peak height and h is the peak-to-peak noise level, are 8 and 4, respectively. When we apply the usual criterion for detection, $S/N \geq 3$, the detection limit of the system for hydrocarbons is 0.4 ppb. The limit for quantification, $S/N \geq 10$, is 1.3 ppb.

Figure 5 shows the application of the system in two Fischer–Tropsch experiments. In the examples, the sample temperature was 220 °C, the total pressures were 200 mbar [Fig. 5(a)] and 950 mbar [Fig. 5(b)], and batch conditions were applied. H_2:CO mixing ratios of 2:1 were used. The chromatograms show the typical product distributions obtained under these conditions, namely, C_1 to C_4 hydrocarbons in decreasing concentrations,[23,32] and higher fractions of unsaturated than of saturated hydrocarbons. The concentration of butane was just above the detection limit at the end of the experiments.

In these experiments, one chromatogram was recorded per hour over a time period of 6 h. As one can see, the peaks of all products steadily increase with time, as expected for a batch experiment with differential turnover. By contrast, the signals from the syngas matrix and the background at higher retention times remain constant. From the increments of the peaks per hour, and by using the STM chamber volume (1.8 l), the prepared surface area of the Co(0001) sample (19.6 mm^2), and the Co(0001) lattice constant (2.507 Å), the catalytic TONs of product molecules per surface atom and second are evaluated. Table II lists the time averages from the two experiments. Depending on the product molecule and the pressure, the data vary between $\sim 18 \times 10^{-4}\ s^{-1}$ and $\sim 0.1 \times 10^{-4}\ s^{-1}$. These extremely low values underline the contrast to the oxidation of CO with O_2 or NO, prototypical fast catalytic reactions, for which TONs between $10^{-1}\ s^{-1}$ and $10^3\ s^{-1}$ have been reported.[16,24] The GC system presented here thus provides access to the kinetics of reactions that are 4 to 8 orders of magnitude slower than the popular CO oxidation.

Finally, we point out that attaching the GC system to the STM chamber has not been connected with instrumental problems. Simultaneous measurements are possible, in principle, but we find them impractical. STM experiments in reactive gas atmospheres are considerably more difficult than in vacuum, mainly because of the lower stability of the tunneling tip and the enhanced thermal drift at the elevated temperatures, and permanent attention is required. Nevertheless, as the STM and GC measurements are performed with the same sample, under the same conditions, and in the same chamber, the term *in situ*/*operando* as used in the introduction is still appropriate. Moreover, both STM and GC experiments on the Fischer–Tropsch synthesis have been well reproducible so that the observed correlations between the TONs and the structure elements are valid. One such correlation, a linear scaling of the Fischer–Tropsch activity with the density of atomic steps on the Co surface, has led us to conclude that the steps are the active sites of this reaction.[23]

CONCLUSIONS

The automated GC system with its specially designed gas sampling and injection unit reaches the low detection limits we were aiming at. For the investigated example, hydrocarbon molecules produced by the Fischer–Tropsch synthesis on a Co(0001) model catalyst, detection and quantification limits of 0.4 and 1.3 ppb, respectively, have been determined. The high sensitivity does not compromise the quality of the chromatograms that display sharp, well-separated peaks of the various saturated and unsaturated hydrocarbon molecules formed by the reaction. TONs as low as $10^{-5}\ s^{-1}$ could be measured.

At the same time, the amount of extracted gas is kept small. Under the conditions of the experiments (200 and 950 mbar, chamber volume 1.8 l), the gas samples only correspond to molar fractions of 1.9 resp. 0.4% of the reaction gas so that the conditions are unchanged. The performance is a result of the compression of the gas samples before the injection and of the action of a cryo trap at one of the column heads. Together, both elements lead to strong concentration and focusing effects.

The GC system has been used in combination with STM, but it does not contain any features restricting it to STM studies. It could equally well be used for *in situ*/*operando* experiments with other enhanced-pressure techniques such as SFG, PM-RAIRS, NAP-XPS, and SXRD. The reactor chambers in such experiments are often smaller than the STM chamber used here so that the available gas samples are even smaller, which, of course, is compensated by higher product concentrations (given the same reaction). The use of a buffer volume would still make sense when operated at a lower filling pressure to keep the amount of extracted gas low. Experiments at higher pressures than 1 bar, already applied in an STM setup,[41] could be performed without modification. For lower pressures those that applied here—these are still required for most of the NAP-XPS systems—the filling pressure and the volume of the buffer loop could be adjusted. Of course, the system is not restricted to model systems but could also be used for "real" catalysis experiments utilizing powder samples at ambient pressure.

Finally, the system only contains few components that have specifically been employed for the Fischer–Tropsch experiments. The special detection problem—small amounts of hydrocarbons in a large syngas matrix—has determined the selection of the separation columns, the temperature of the cryo trap, and the type of detectors, but these are components and settings that could easily be changed for other, kinetically demanding reactions.

ACKNOWLEDGMENTS

This work was funded by the Deutsche Forschungsgemeinschaft (DFG, German Research Foundation)-WI 1003/8-1.

AUTHOR DECLARATIONS

Conflict of Interest

The authors have no conflicts to disclose.

Author Contributions

G.S. and J.S. designed and built the first version of the system, K.M.G. and B.B. modified the setup, K.M.G. tested the performance and wrote the manuscript, and J.W. wrote the manuscript and supervised the project.

DATA AVAILABILITY

The data that support the findings of this study are available from the corresponding author upon reasonable request.

REFERENCES

[1] H. Topsøe, "Developments in operando studies and in situ characterization of heterogeneous catalysts," J. Catal. **216**, 155–164 (2003).

[2] J. Dou, Z. Sun, A. A. Opalade, N. Wang, W. Fu, and F. Tao, "*Operando* chemistry of catalyst surfaces during catalysis," Chem. Soc. Rev. **46**, 2001–2027 (2017).

[3] F. C. Meunier, "The design and testing of kinetically-appropriate operando spectroscopic cells for investigating heterogeneous catalytic reactions," Chem. Soc. Rev. **39**, 4602–4614 (2010).

[4] S. W. Chee, T. Lunkenbein, R. Schlögl, and B. R. Cuenya, "*In situ* and *operando* electron microscopy in heterogeneous catalysis—Insights into multi-scale chemical dynamics," J. Phys.: Condens. Matter **33**, 153001 (2021).

[5] G. A. Somorjai and G. Rupprechter, "Molecular studies of catalytic reactions on crystal surfaces at high pressures and high temperatures by infrared–visible sum frequency generation (SFG) surface vibrational spectroscopy," J. Phys. Chem. B **103**, 1623–1638 (1999).

[6] K. Mudiyanselage and D. J. Stacchiola, "*In-situ* infrared spectroscopy on model catalysts," in *Characterization of Heterogeneous Catalysts*, edited by J. A. Rodriguez, J. C. Hanson, and P. J. Chupas (Wiley, 2013), pp. 209–239.

[7] F. Zaera, "New advances in the use of infrared absorption spectroscopy for the characterization of heterogeneous catalytic reactions," Chem. Soc. Rev. **43**, 7624–7663 (2014).

[8] H. Bluhm, M. Hävecker, A. Knop-Gericke, M. Kiskinova, R. Schlögl, and M. Salmeron, "*In situ* x-ray photoelectron spectroscopy studies of gas–solid interfaces at near-ambient conditions," MRS Bull. **32**, 1022–1030 (2007).

[9] D. E. Starr, Z. Liu, M. Hävecker, A. Knop-Gericke, and H. Bluhm, "Investigation of solid/vapor interfaces using ambient pressure x-ray photoelectron spectroscopy," Chem. Soc. Rev. **42**, 5833–5857 (2013).

[10] J. Schnadt, J. Knudsen, and N. Johansson, "Present and new frontiers in materials research by ambient pressure x-ray photoelectron spectroscopy," J. Phys.: Condens. Matter **32**, 413003 (2020).

[11] P. Bernard, K. Peters, J. Alvarez, and S. Ferrer, "Ultrahigh vacuum/high pressure chamber for surface x-ray diffraction experiments," Rev. Sci. Instrum. **70**, 1478–1480 (1999).

[12] B. L. M. Hendriksen, S. C. Bobaru, and J. W. M. Frenken, "Looking at heterogeneous catalysis at atmospheric pressure using tunnel vision," Top. Catal. **36**, 43–54 (2005).

[13] M. Salmeron and B. Eren, "High-pressure scanning tunneling microscopy," Chem. Rev. **121**, 962–1006 (2021).

[14] B. L. M. Hendriksen and J. W. M. Frenken, "CO oxidation on Pt(110): Scanning tunneling microscopy inside a high-pressure flow reactor," Phys. Rev. Lett. **89**, 046101 (2002).

[15] R. Blume, M. Hävecker, S. Zafeiratos, D. Teschner, E. Kleimenov, A. Knop-Gericke, R. Schlögl, A. Barinov, P. Dudin, and M. Kiskinova, "Catalytically active states of Ru(0001) catalyst in CO oxidation reaction," J. Catal. **239**, 354–361 (2006).

[16] A. Farkas, K. Zalewska-Wierzbicka, C. Bachmann, J. Goritzka, D. Langsdorf, O. Balmes, J. Janek, and H. Over, "High pressure carbon monoxide oxidation over platinum (111)," J. Phys. Chem. C **117**, 9932–9942 (2013).

[17] J. Knudsen, J. N. Andersen, and J. Schnadt, "A versatile instrument for ambient pressure x-ray photoelectron spectroscopy: The Lund cell approach," Surf. Sci. **646**, 160–169 (2016).

[18] M. Borasio, O. Rodríguez de la Fuente, G. Rupprechter, and H.-J. Freund, "In situ studies of methanol decomposition and oxidation on Pd(111) by PM-IRAS and XPS spectroscopy," J. Phys. Chem. B **109**, 17791–17794 (2005).

[19] S. Blomberg, J. Zetterberg, J. Gustafson, J. Zhou, C. Brackmann, and E. Lundgren, "Comparison of AP-XPS and PLIF measurements during CO oxidation over Pd single crystals," Top. Catal. **59**, 478–486 (2016).

[20] S. Böcklein, S. Günther, and J. Wintterlin, "High-pressure scanning tunneling microscopy of a silver surface during catalytic formation of ethylene oxide," Angew. Chem., Int. Ed. **52**, 5518–5521 (2013).

[21] M. Ehrensperger and J. Wintterlin, "*In situ* high-pressure high-temperature scanning tunneling microscopy of a Co(0001) Fischer–Tropsch model catalyst," J. Catal. **319**, 274–282 (2014).

[22] M. Ehrensperger and J. Wintterlin, "*In situ* scanning tunneling microscopy of the poisoning of a Co(0001) Fischer–Tropsch model catalyst by sulfur," J. Catal. **329**, 49–56 (2015).

[23] B. Böller, K. M. Durner, and J. Wintterlin, "The active sites of a working Fischer–Tropsch catalyst revealed by operando scanning tunnelling microscopy," Nat. Catal. **2**, 1027–1034 (2019).

[24] H. Permana, K. Y. Simon Ng, C. H. F. Peden, S. J. Schmieg, D. K. Lambert, and D. N. Belton, "Adsorbed species and reaction rates for NO–CO over Rh(111)," J. Catal. **164**, 194–206 (1996).

[25] J. P. Greenberg, B. Lee, D. Helmig, and P. R. Zimmerman, "Fully automated gas chromatograph-flame ionization detector system for the *in situ* determination of atmospheric nonmethane hydrocarbons at low parts per trillion concentration," J. Chromatogr. A **676**, 389–398 (1994).

[26] J. R. Hopkins, A. C. Lewis, and K. A. Read, "A two-column method for long-term monitoring of non-methane hydrocarbons (NMHCs) and oxygenated volatile organic compounds (o-VOCs)," J. Environ. Monit. **5**, 8–13 (2003).

[27] S. Saito, I. Nagao, and H. Kanzawa, "Characteristics of ambient C_2–C_{11} non-methane hydrocarbons in metropolitan Nagoya, Japan," Atmos. Environ. **43**, 4384–4395 (2009).

[28] A. K. Baker, F. Slemr, and C. A. M. Brenninkmeijer, "Analysis of non-methane hydrocarbons in air samples collected aboard the CARIBIC passenger aircraft," Atmos. Meas. Tech. **3**, 311–321 (2010).

[29] P. S. Cremer, X. Su, Y. R. Shen, and G. A. Somorjai, "Ethylene hydrogenation on Pt(111) monitored in situ at high pressures using sum frequency generation," J. Am. Chem. Soc. **118**, 2942–2949 (1996).

[30] M. Morkel, V. V. Kaichev, G. Rupprechter, H.-J. Freund, I. P. Prosvirin, and V. I. Bukhtiyarov, "Methanol dehydrogenation and formation of carbonaceous overlayers on Pd(111) studied by high-pressure SFG and XPS spectroscopy," J. Phys. Chem. B **108**, 12955–12961 (2004).

[31] M. Rößler, P. Geng, and J. Wintterlin, "A high-pressure scanning tunneling microscope for studying heterogeneous catalysis," Rev. Sci. Instrum. **76**, 023705 (2005).

[32] G. A. Beitel, C. P. M. de Groot, H. Oosterbeek, and J. H. Wilson, "A combined *in-situ* PM-RAIRS and kinetic study of single-crystal cobalt catalysts under synthesis gas at pressures up to 300 mbar," J. Phys. Chem. B **101**, 4035–4043 (1997).

[33] T. P. Wampler and E. J. Levy, "Cryogenic focusing of pyrolysis products for direct (splitless) capillary gas chromatography," J. Anal. Appl. Pyrolysis **8**, 65–71 (1985).

[34] B. Kolb, B. Liebhardt, and L. S. Ettre, "Cryofocusing in the combination of gas chromatography with equilibrium headspace sampling," Chromatographia **21**, 305–311 (1986).

[35] Z. Huang, J. Zhang, P. Zhang, H. Wang, Z. Pan, and L. Wang, "Analysis of volatile organic compounds in pleural effusions by headspace solid-phase microextraction coupled with cryotrap gas chromatography and mass spectrometry," J. Sep. Sci. **39**, 2544–2552 (2016).

[36] C. F. Poole, *The Essence of Chromatography* (Elsevier, 2003).

[37] T. Grobler, M. Claeys, E. van Steen, and M. J. Janse van Vuuren, "GC × GC: A novel technique for investigating selectivity in the Fischer–Tropsch synthesis," Catal. Commun. **10**, 1674–1680 (2009).

[38] K. Dettmer-Wilde and W. Engewald, *Practical Gas Chromatography* (Springer, Heidelberg, 2014).

[39] A. C. Frost and E. H. Amick, "Modified Stefan cell for gas diffusion measurements," Ind. Eng. Chem. Fundam. **12**, 129–133 (1973).

[40] The United States Pharmacopeial Convention, Rockville, MD, 2017.

[41] C. T. Herbschleb, P. C. van der Tuijn, S. B. Roobol, V. Navarro, J. W. Bakker, Q. Liu, D. Stoltz, M. E. Cañas-Ventura, G. Verdoes, M. A. van Spronsen, M. Bergman, L. Crama, I. Taminiau, A. Ofitserov, G. J. C. van Baarle, and J. W. M. Frenken, "The ReactorSTM: Atomically resolved scanning tunneling microscopy under high-pressure, high-temperature catalytic reaction conditions," Rev. Sci. Instrum. **85**, 083703 (2014).

CHAPTER 4

Experimental Results

Based on the above described setup and experimental preliminary work, *operando* STM studies of FT synthesis on cobalt single crystals were performed. This chapter presents two published studies. The first mainly covers the thesis by B. Böller, but it involves the application of the GC that was installed in the framework of the present thesis, as described above. The second was entirely performed in the framework of the present thesis. To identify the active sites of the FT reaction, the studies deal with the dependence of the catalytic activity on the density of steps on single crystal model catalysts.

To test the structure sensitivity of supported catalysts, the catalytic activity is usually measured as a function of the particle diameters of the catalysts. The analysis of such data is based on the assumption that the fraction of active sites varies with the diameter in a systematic way so that correlations provide indirect hints at the nature of these active sites.[122] One hypothesis states that specific ensembles of surface atoms are mainly responsible for the catalytic reactivity. As already mentioned in the introduction, for supported Co nanoparticles, the dependence of catalytic activity of FT reaction on the particle diameters is well known.[46,123–126] After a steep increase of the TOFs for small particles, the activity sharply bends over to a constant TOF for particles larger than 8 − 10 nm. A summary of several experimental studies is shown in Figure 4.1. Industrial FT catalysts have particle diameters in the range of the TOF plateau.[35] In accordance to this particle size dependence, simulations of the atomic structure of Co nanoparticles show an increasing concentration of step sites with growing particle diameters up to a saturation value at ~8 nm.[44]

These simulations are based on the fact that Co nanoparticles are to a considerable fraction fcc-packed. As mentioned above, fcc Co nanoparticles appear as rounded-off cubo-octahedra.[44,45] When these particles are very small, they do not display step sites but mainly corners and edge site. Step sites only form when the particles get bigger.[52] The step density-vs-particle size function quite closely follows the TOF-vs-particle size function of Figure 4.1. In general, curves as shown in Figure 4.1 are expected for

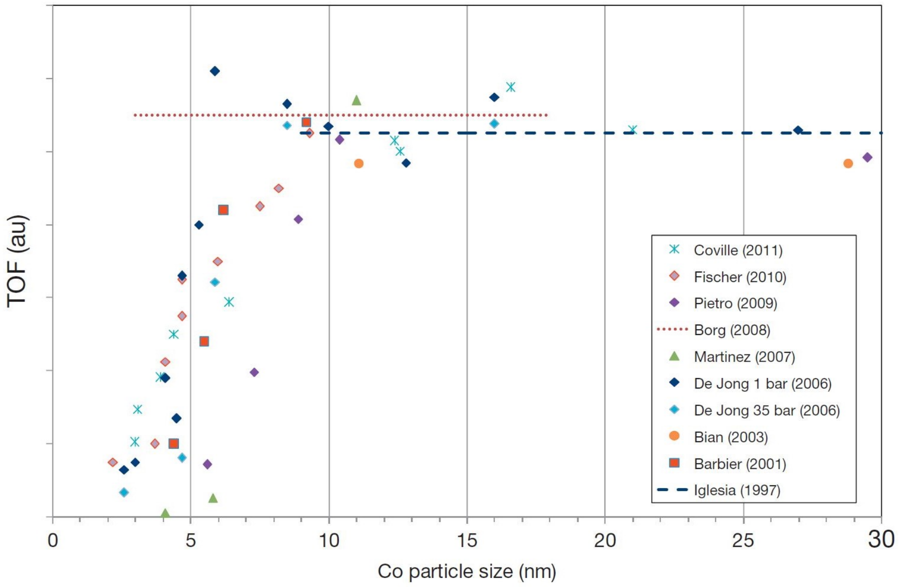

Figure 4.1: Overview of the catalytic activity (TOFs were rescaled) of Fischer-Tropsch synthesis on Co nanoparticles in dependence of the particle size. Reprinted from ref. [47], with permission from Elsevier.

reactions where the cleavage of a π bond of, e. g. CO, is necessary. For this reaction step, an active center with a unique configuration, consisting of neighboring highly- and low-coordinated metal atoms as it is the case at an atomic step, is required. This can explain the fact that the activity follows the probability of step sites.[52]

The structure-sensitivity of the Fischer-Tropsch reaction thus supports a reaction mechanism, in which step edge sites play a critical role. There are still several mechanisms that are discussed for the FTS, but the one mechanism that is structure-sensitive is the earliest and most popular carbide mechanism.[48,49] It assumes that the CO dissociation is the first, kinetically relevant reaction step, which is followed by a series of hydrogenation and polymerization steps which finally lead to hydrocarbons. DFT calculations in fact showed that the CO dissociation barrier is lower at step sites compared to terraces.[51,127–129]

Although this picture seems to be consistent, there has been no direct experimental proof that steps are actually the active sites in the FT synthesis. In order to probe the role of step edge sites in FTS, it was analyzed how the catalytic activity of Co single crystals depended on the surface structure by means of *operando* STM. The results are shown in the following sections in two published articles. Both studies deal with the variation of step densities. In the first study in section 4.1, the concentration of steps on the Co(0001) crystal was varied by Ar^+ sputtering. Literature data had indicated that sputtering increased the activity.[40] For the second study (section 4.2.1), a single crystal with a $(10\bar{1}15)$ orientation was used, which is vicinal to the (0001) surface.

The surface provides a high density of steps, which is in the range of step densities of nanoparticles. This study was designed to close the materials gap between surface science model systems and industrial catalysts.

All experiments were performed at the HP-STM setup under the same reaction conditions, namely an H_2:CO of 2:1, a total pressure of 950 mbar and a temperature of ~230 °C. Except for the total pressure, these parameters closely meet industrial conditions. Although GC and STM measurements can theoretically be performed in the same experiment, they were done separately for practical reasons. As in both cases the same conditions were used and the results were well reproducible, the studies can still be called *operando*. STM visualized the surface at an atomic scale under reaction conditions, and the catalytic activity was monitored by the new GC. Despite the pressure was one order of magnitude below industrial synthesis conditions, the experiments provide insights into a working catalyst.

4.1 *Operando* STM Study of Fischer-Tropsch Synthesis on a Co(0001) Catalyst

The article "The active sites of a working Fischer-Tropsch catalyst revealed by operando scanning tunnelling microscopy",[61] published in *Nature Catalysis*, presents the first experimental results achieved by the combined HP-STM/GC setup. The *operando* STM study on a Co(0001) single crystal deals with the question of how the catalytic activity depends on the surface structure. In order to vary the step density, the crystal was sputtered before some of the FT experiments. The step density was determined by STM, whereas the catalytic activity, expressed as TOFs, was evaluated from GC measurements. The key statements of the article are:

- The Co(0001) surface shows FT activity. Similar product distributions of C_1 to C_4 hydrocarbons[38,40] have been reported before for Co(0001). It can be concluded that data obtained with the modified setup are reliable.

- *Ex situ* XPS results neither show an oxidized nor a carbidic Co surface after the reactions. The Co surface must be largely metallic during the reaction and can only be covered by adsorbed species, which is in agreement with *in situ* spectroscopic work.[130–132]

- In contrast to the literature,[42] STM images do not show any roughening of the surface during the reaction or the dynamic formation of additional steps or cobalt islands. On the contrary, the roughened surface after sputtering became even smoother during the reactions. This flattening of the surface could also be detected in vacuum. These results disprove a widespread theory in the literature that additional active sites are formed under reaction conditions. The FT activity must be explained by pre-existing steps only. Furthermore, STM images show a fluctuation of steps, indicating that they remain active in the syngas environment and are not blocked by reaction intermediates.

- The catalytic activity scales with step density. This leads to the conclusion that the rate-limiting step requires steps as active sites. Because the dissociation barrier of CO is strongly reduced at step sites according to calculations, this observation is consistent with the carbide mechanism of the FTS. In this mechanism, the dissociation of CO is the first and rate-limiting reaction step.[48]

The following pages display the corresponding publication, ref. [61]: Böller, B., Durner, K. M. & Wintterlin, J. The active sites of a working Fischer–Tropsch catalyst revealed by operando scanning tunnelling microscopy. *Nat. Catal.* **2**, 1027-1034 (2019), Springer Nature Limited 2019. Reproduced with permission from Springer Nature.

The supporting information of this article is shown in Appendix E, beginning on page 107. The supplementary videos 1–4 are available on the website: `https://www.nature.com/articles/s41929-019-0360-1#Sec16`.

nature catalysis
ARTICLES
https://doi.org/10.1038/s41929-019-0360-1

The active sites of a working Fischer–Tropsch catalyst revealed by operando scanning tunnelling microscopy

Bernhard Böller, Katharina M. Durner and Joost Wintterlin*

Direct identification of the active sites of a working catalyst is still a major problem in heterogeneous catalysis. Here we present an operando scanning tunnelling microscopy study, in which insight into the nature of the active sites was obtained for the cobalt-catalysed Fischer–Tropsch synthesis. Experiments were performed on a Co(0001) sample under H_2/CO gas mixtures at pressures of up to 950 mbar and a temperature of ~500 K. On the same apparatus, turnover frequencies were measured with a customized gas chromatograph. The density of monoatomic steps of the sample was varied by sputtering. The Fischer–Tropsch activity scaled with step density, from which steps are identified as the active sites of this reaction. The long-standing idea that the activation of the Co catalyst is connected with a roughening of the surface is not confirmed. The known activity function can be explained by pre-existing steps without roughening.

Identifying the active sites on the surface of a working catalyst under industrial conditions is still a major scientific problem. (Here we use the term active site in Taylor's sense to denote a subgroup of atoms on the surface of a catalyst, usually a defect, at which a critical step of the reaction takes place[1].) The standard method for identifying active sites on a typical supported metal catalyst is to measure catalytic activity as a function of the diameter of the metal particles. Assuming that the edges and corners of the particles vary with diameter in a systematic way, correlations can be interpreted with respect to possible active sites[2]. However, microscopic information is lacking in these experiments and it is not clear whether the defects actually display the assumed structure and are accessible to the reaction, or are deactivated by reaction intermediates. The information is thus very indirect. Considerable progress has been made with in situ electron microscopy, but atomic resolution of individual active sites at pressures in the bar regime is still hard to reach.

Active sites have been identified directly by scanning tunnelling microscopy (STM) in surface science investigations. For example, NO molecules were observed to preferentially dissociate at atomic steps[3], but such experiments, performed under ultra-high vacuum (UHV), are obviously far from industrial conditions. Another approach has been to prepare high-index surfaces of single crystals, which have defined densities of step and kink sites, and then to perform activity measurements[4]. A possible problem here is that the morphology of a surface can considerably change when exposed to reactive gases, for example, by forming facets, and electron microscopy experiments on supported catalysts have indeed shown substantial morphology changes at elevated pressures[5–7].

In principle, STM should be able to provide information about active sites under reaction conditions, at least for single-crystal models. It has been shown that STM can work at gas pressures of ~1 bar, thus approaching the industrial regime[8–11], and in reaction gas mixtures surface phases related to activity have been resolved. For example, an oxidic state of a Pt surface could be connected with a high activity for the oxidation of CO[10]. STM can also work in liquids, and fluctuations of the tunnel current have been used to distinguish different sites for the hydrogen evolution reaction on metal electrodes[12]. However, identifying active sites by STM is still difficult. It not only requires stable atomic resolution under reaction conditions, but also the measurement of the formation rates of products under the same conditions, and the correlation of the structure elements that may represent active sites with activity. This has not been achieved so far.

An unusually complex reaction with respect to the nature of the active sites is the cobalt-catalysed Fischer–Tropsch (FT) synthesis. The reaction is an important industrial process used to produce liquid fuels, mainly in the form of linear hydrocarbons:

$$(2n+1)\mathrm{H}_2 + n\,\mathrm{CO} \rightarrow \mathrm{C}_n\mathrm{H}_{2n+2} + n\,\mathrm{H}_2\mathrm{O} \qquad (1)$$

The feedstock of reactant gases is synthesis gas (syngas), a ~2:1 mixture of H_2 and CO that, in modern low-temperature FT synthesis, reacts over oxide-supported Co catalysts at a temperature of ~500 K and at pressures of ~20–40 bar (ref. [13]). In the future, FT synthesis may also play a role in energy storage in so-called power-to-liquid processes in which the syngas is produced, for example, by reduction of CO_2 and electrolytic water splitting[14].

Information about the active sites has previously been obtained by the standard method, by measuring the activity of supported Co catalysts as a function of particle diameter[15]. The data showed an unusual pattern, a steeply increasing turnover frequency (TOF) with particle size for small particles up to a diameter of approximately 6 nm, and a sharp bend to a constant TOF for larger particles. The industrial Co catalyst is in the constant TOF regime[16]. The fact that the TOF was independent of particle size in the industrial regime would usually suggest a structure-insensitive reaction, but this conclusion disagrees with the classical reaction mechanism of FT synthesis[17]. According to this mechanism the rate-limiting step is the dissociation of the CO molecules, which should be strongly structure-sensitive.

This discrepancy seemed to be resolved by an early (ex situ) STM study[18], which showed that an originally flat Co(0001) sample had become completely rough after it was exposed to syngas, supposedly by the formation of small, monolayer-high cobalt islands.

Department Chemie, Ludwig-Maximilians-Universität München, Munich, Germany. *e-mail: wintterlin@cup.uni-muenchen.de

The island formation was suggested to be induced by the reactive syngas atmosphere, indicating that the active sites—steps or other defects—are somehow self-induced by the reaction. That a well-prepared Co(0001) surface was FT-active supported this model[19,20]. Another indication was the induction time known from supported FT catalysts that may be interpreted as a roughening period[21]. Recent density functional theory calculations explained the roughening as being caused by the spontaneous formation of monolayer cobalt islands that were stabilized by C atoms and CO molecules at the peripheral steps[22]. Another explanation, based on molecular dynamics simulations, was that carbon atoms penetrated into the first layer of the Co surface, displacing Co atoms that then condensed to form clusters[23]. This mechanism was shown to no longer work for Co particles below a critical size, so that the sharp activity drop towards smaller particles could also be explained. The roughening hypothesis provided a consistent explanation of most data, but it was entirely based on indirect experiments and modellings.

There have also been STM studies on the FT reaction at syngas pressures between 10 mbar and 3 bar (refs. [22,24–26]). Atomic resolution was accomplished, but results about the predicted roughening were contradictory. It has been argued that the roughening requires minimum pressures close to 1 bar (ref. [22]), but contaminants, in particular sulfur, may also play a role in morphology changes[25]. In none of these studies were correlations of possible active site features with activity determined.

Here we present an operando STM study, performed with a Co(0001) model catalyst at syngas pressures of up to 950 mbar and temperatures of ~500 K, where this has been achieved. The experiments were performed in a high-pressure reactor cell that houses the STM and is attached to a UHV chamber for sample preparation and post-reaction analysis[27]. The data show a clear correlation of the density of monoatomic steps with online-measured TOFs. However, the steps were not dynamically formed during the reaction, and an intentionally roughened surface even became smoother.

Results

Activity measurements. The present study was based on the ability to measure the FT activity of a Co single crystal in the STM cell and to perform these measurements with sufficient precision to discriminate between different states of the surface. Standard gas chromatography (GC) was not sensitive enough for the extremely low product concentrations. From the low ratio of sample surface (prepared area ~20 mm^2) to STM cell volume (~1.8 l), concentrations in the low ppm or even ppb regime were expected. To solve this problem, a specially configured GC was implemented (see Methods). Figure 1a shows gas chromatograms taken with this setup from a measurement with the well-prepared, annealed Co(0001) sample in 950 mbar syngas at a sample temperature of 493 K. Chromatograms were recorded every hour during a 5 h batch experiment. (All reaction experiments in this study were performed in batch mode, see Methods.) After the initial broad peak from the H_2/CO mixture, one can see sharp peaks from CH_4, C_2H_4, C_2H_6, C_3H_6, C_3H_8, C_4H_8 and, barely visible on this scale, C_4H_{10} on a sufficiently low background. Peaks from C_5 hydrocarbons were close to the detection limit of ~0.3 ppb and were not included in the analysis.

From the peak increments between the chromatograms TOFs of the individual hydrocarbons were calculated. The data (in units of product molecules per Co(0001) surface atom per second; Fig. 1b, blue dots) show the formation of hydrocarbons between C_1 and C_4 and a roughly linear decrease from C_1 to C_4 on the semi-logarithmic plot, except for a dip at the C_2 components. This distribution of C_1 to C_4 hydrocarbons is typical for Co(0001) under similar pressure and temperature conditions[19,20]; longer hydrocarbons would only form at the higher pressures used in the industrial process. Also, the slight deactivation on the time scale of several hours (here on average by 30% within 5 h) and, as seen in Fig. 1a, the higher selectivity for olefins than paraffins has been reported previously[19,20]. Even the absolute TOFs and the values of α, the chain growth probability, which was determined from the slope of the data in Fig. 1b, agree reasonably well with previously reported values[19,20,28]. We can therefore be sure that, despite the difficult geometry of the STM cell, valid activity data were measured, which is a precondition for the present operando study.

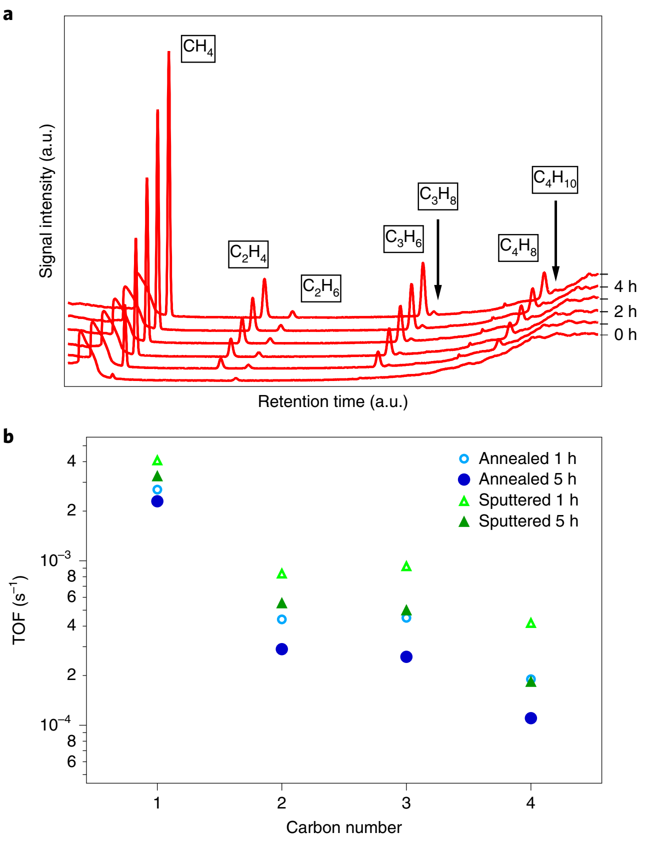

Fig. 1 | Catalytic activity of the Co(0001) sample measured in the STM cell. a, Gas chromatograms recorded during a reaction experiment in the STM cell with the annealed Co(0001) sample, in 950 mbar syngas, H_2:CO = 2:1, at 493 K, chromatograms taken every hour. a.u., arbitrary units. **b**, TOFs of the individual hydrocarbon products obtained with the annealed and the sputtered surface, from GCs recorded after 1 h and 5 h. The TOFs were evaluated with respect to the number of Co atoms on the polished and prepared part of the sample using the atom density of Co(0001) of 1.837×10^{19} m^{-2} and the area of the prepared surface of 19.6 mm^2; olefin and paraffin hydrocarbons with the same C numbers were combined (for the full data set see Supplementary Table 1). The chain growth probabilities, determined from the slopes, were, on the annealed sample, $\alpha = 0.46$ after 1 h and 0.39 after 5 h; on the sputtered sample $\alpha = 0.51$ after 1 h and 0.42 after 5 h.

In an attempt to enhance the density of active sites, the sample was Ar$^+$-sputtered after preparation. The TOFs measured thereafter (Fig. 1b, green triangles) show the same qualitative behaviour as the data from the well-prepared, annealed sample, but the values were all higher, by a factor of approximately 1.8. That the activity of a Co(0001) sample can be enhanced by sputtering has been reported before, without clarifying the nature of the created sites[20].

Chemical surface analysis. We also considered it important to obtain some knowledge about the chemical state of the surface. Using X-ray photoelectron spectroscopy (XPS) in the attached

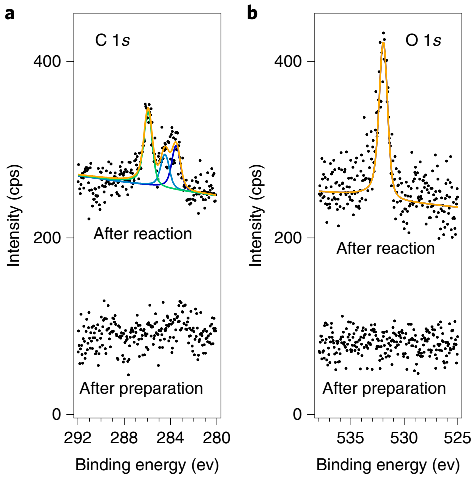

Fig. 2 | XPS spectra. a,**b**, The C 1s (**a**) and O 1s (**b**) regions. Bottom, spectra of the annealed sample after preparation in UHV; top, spectra after 6 h in syngas (950 mbar, H_2:CO = 2:1, 493 K). The low signal-to-noise ratios are explained by the beam sensitivity of the adsorption layer, so that the spectra had to be recorded relatively quickly. For survey spectra see Supplementary Fig. 1. cps, counts per second.

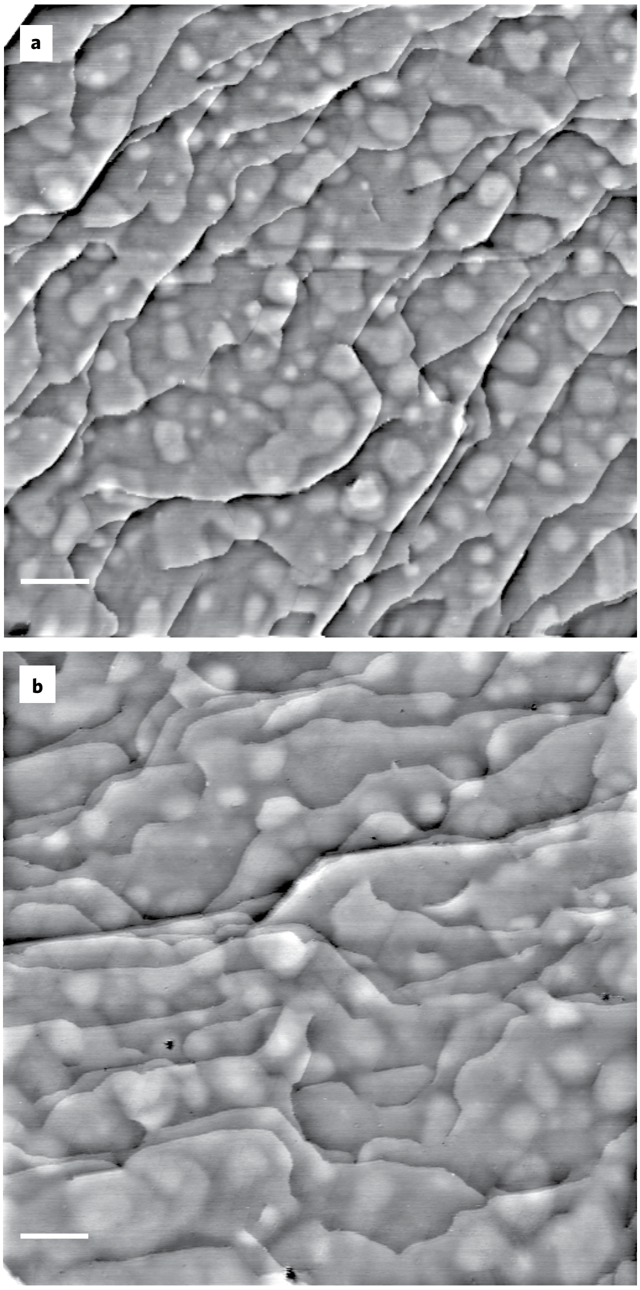

Fig. 3 | STM images of the Co(0001) sample in UHV and in 950 mbar syngas. a, The anealed Co(0001) sample in UHV at room temperature; 300 × 300 nm^2, tunnelling voltage $V_t = -1$ V tunnelling current $I_t = 0.7$ nA. Scale bar, 30 nm. **b**, The annealed Co(0001) sample in 950 mbar syngas, H_2:CO = 2:1, 493 K; image recorded 4.5 h after the start of the experiment (193 × 193 nm^2, $V_t = -0.05$ V; $I_t = 2.1$ nA). Scale bar, 20 nm.

UHV chamber this information was necessarily ex situ, but impurities from the reaction gases or major chemical changes of the surface, for example by an oxidation, might have been detected. S and Ni contaminants could be largely removed in this way (Methods). As expected, C and O compounds were regularly detected after reaction experiments (Fig. 2). The C 1*s* peak at 283.4 eV can be attributed to atomic carbon (0.16 of a monolayer, ML), the peak at 284.4 eV to adsorbed hydrocarbon moieties (0.10 ML), and the peak at 285.9 eV to adsorbed CO (0.25 ML). The O 1*s* peak at 532.1 eV is also mainly attributed to CO (0.26 ML), possibly including 0.01 or 0.02 ML of OH (averaged values; for variations see Supplementary Table 2). We assume that the amount of CO does not reflect the coverage during the reaction (close to 0.50 ML according to kinetics experiments[29]) but was changed during pumping down to UHV.

On the sputtered sample, the coverages after the 5 h reaction of 0.18 ML of atomic carbon, 0.14 ML of hydrocarbon moieties and 0.28 ML of CO (averaged values, for variations see Supplementary Table 2) were only marginally higher. There were also no distinct differences, for both types of samples, between reactions for 0.25 h, 4 h and 6 h (Supplementary Table 2). Whether this uniformity reflects immediately established steady-state coverages of reaction intermediates during reactions or similar processes during cooling and pumping after reactions we cannot determine. In any case, the coverages of the atomic C and hydrocarbon species were low and O species other than CO were almost completely absent. Massive carbide or oxide formation could therefore be ruled out. This was supported by the fact that, after the reaction experiments, almost as much CO was detected on the sample as on a clean Co(0001) surface in a room temperature UHV adsorption experiment (0.33 ML). The surface in the operando experiments must therefore be largely metallic Co. This finding agrees with most of the evidence from in situ spectroscopic work[30–32].

STM measurements. STM images of the prepared, annealed Co(0001) surface in UHV showed a characteristic morphology of mainly monoatomic steps, screw dislocations and flat hillocks (Fig. 3a). The hillocks are bulk defects caused by Ar atoms implanted into the crystal lattice during sputtering and not completely removed by annealing. The annealing temperature had to be kept at a low value (630 K) to avoid the hexagonal close-packed to face-centred cubic phase transition of Co at ~700 K (ref. [33]). Also the relatively high density of steps and screw dislocations is explained in this way. This morphology is typical for UHV-prepared Co(0001)[24,34].

Figure 3b shows an STM image recorded under 950 mbar syngas (H_2:CO = 2:1) at 493 K (not the same surface area). From the TOFs recorded in the same cell and under the same conditions (Fig. 1), the image shows an operating state of the sample that produces FT products. However, the general morphology of steps,

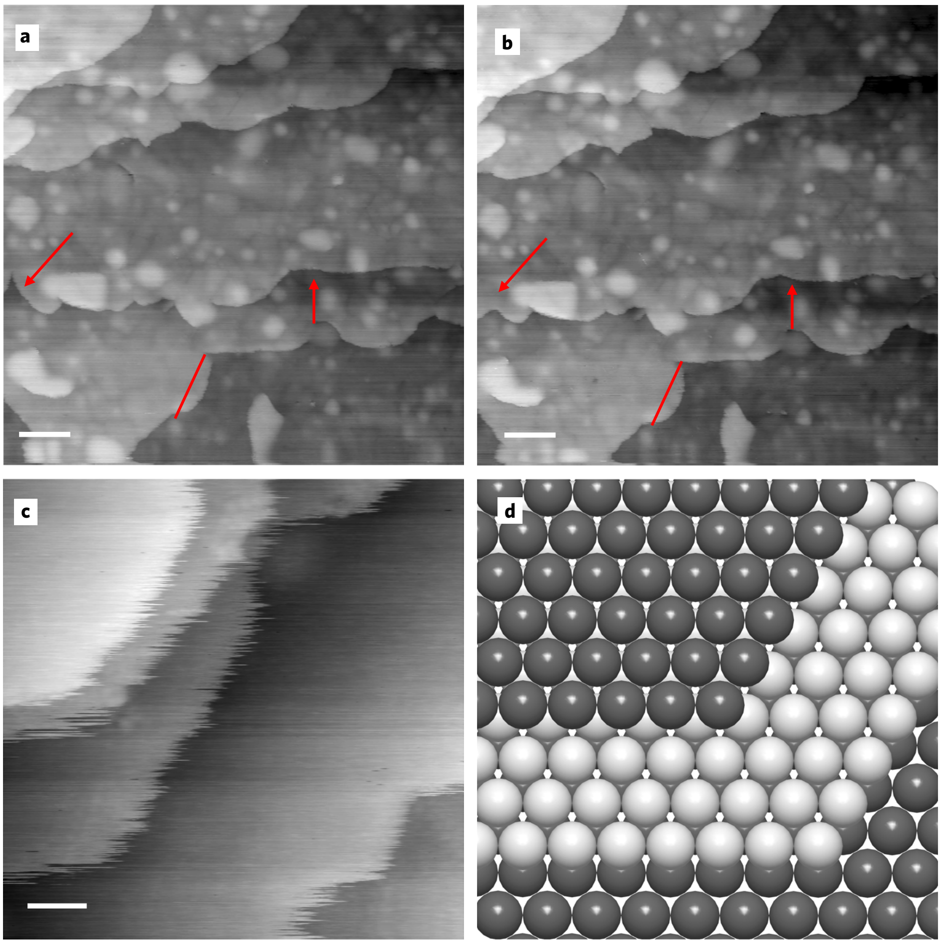

Fig. 4 | STM images of step fluctuations in syngas. a, The annealed Co(0001) sample in 200 mbar syngas, H_2:CO = 2:1, 493 K. **b**, The same surface area 20 min later. Arrows are drawn for better visualization of the step edge motions (200 × 200 nm^2, $V_t = -0.5$ V, $I_t = 0.7$ nA). Scale bars for **a**,**b**, 20 nm. **c**, Detail from the annealed Co(0001) sample in 950 mbar syngas, H_2:CO = 2:1, 493 K. The steps have the correct height of a monoatomic Co(0001) step, indicating that the fringes are caused by fast fluctuations of the step positions (20 × 20 nm^2, $V_t = +0.15$ V, $I_t = 2.1$ nA). Scale bar, 2 nm. **d**, A model of steps on Co(0001).

screw dislocations and hillocks appears unchanged from the surface in UHV (Fig. 3a). This finding was reproduced in all experiments at 950 mbar, and also under syngas pressures of 200 mbar. There were also no indications of the Co_2C phase, which forms a characteristic stripe structure[35,36], or of one of the structures induced by S contaminants[25], in agreement with the conclusions from XPS. In some data weak triangular structures were identified on the terraces that may be caused by low coverages of adsorbed C atoms (Supplementary Fig. 2). In none of the reaction experiments that lasted several hours were new cobalt islands observed to form.

On the other hand, the morphology was not static. Figure 4 shows two frames from an experiment in which the same surface area could be imaged over a time period of 80 min (for the full series see Supplementary Video 1). At the marked positions, the atomic steps changed, but these changes were fluctuations of already existing steps. That steps fluctuate at elevated temperatures is to be expected, and small-scale images showed typical fringes at the step edges (Fig. 4c; for a time series see Supplementary Video 2; note that we do not discriminate between the two types of steps on a Co(0001) surface, Fig. 4d). These fringes indicate Co atoms diffusing along the steps or detaching/reattaching to/from the terraces on a fast time scale with respect to the scanning frequency of the STM. That no new cobalt islands formed could therefore not be caused by a low mobility of Co atoms or by pinning of the step edges by adsorbates.

Sputtering led to a strongly modified morphology (Fig. 5). Directly after sputtering, with the sample still at room temperature but under 950 mbar syngas, the STM showed a pronounced hill-and-valley structure, but steps and terraces could still be identified on a small scale (Fig. 5a). When the temperature was raised to 493 K, after 30 min a clearer terrace/step morphology had evolved (Fig. 5b), with wider terraces and a lower average height difference between maxima and minima of the modulated topography. After 5 h the terraces had grown further and the height modulation had decreased further (Fig. 5c; note the different scale bars), although the changes happened more slowly than at the start. The highly stepped surface from the sputtering thus became smoother under the conditions of the reaction.

Figure 6 shows two images from a time series recorded after 80 min that indicates the mechanism of this smoothing (for the full series see Supplementary Video 3). One can see that at several locations the highest, mesa-like terraces were shrinking and finally dissolved, and at the same time the lowest cavities filled up and eventually disappeared. A quantitative analysis shows that the mass balance of Co atoms is closed (Supplementary Video 4 and Supplementary Fig. 3). There must be a flux of Co atoms

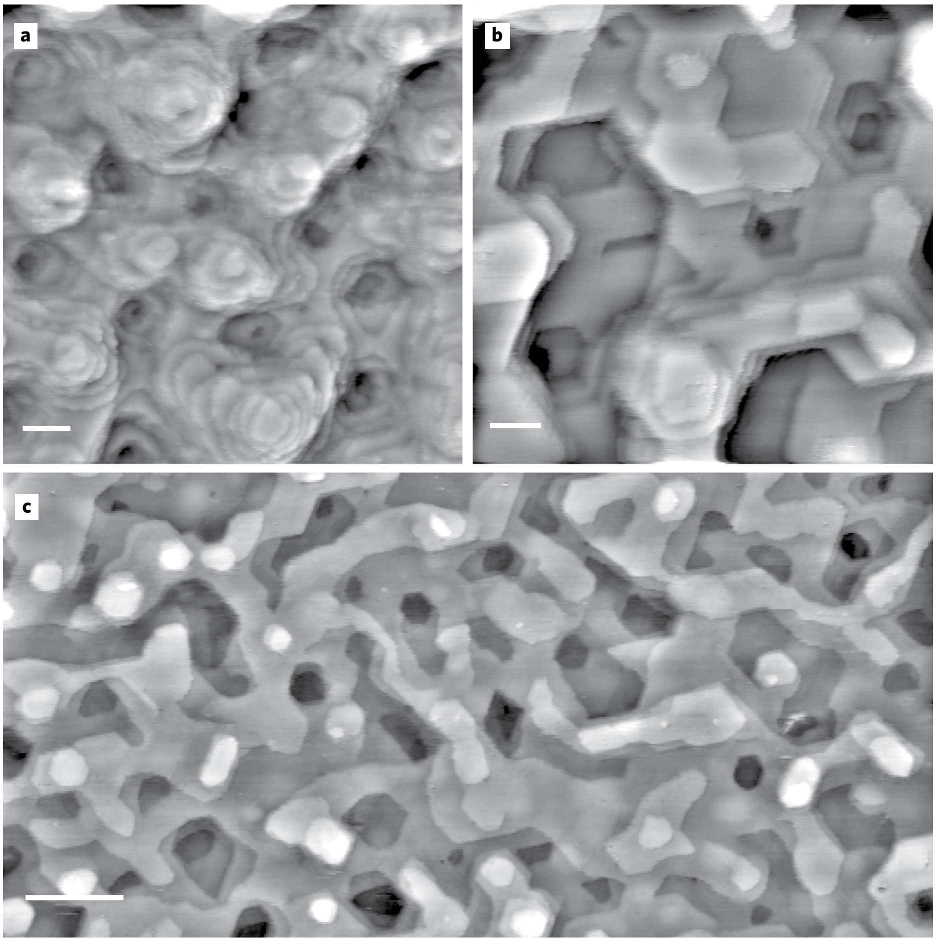

Fig. 5 | STM images of the Co(0001) sample in syngas after sputtering. a, At room temperature (43 × 43 nm^2, V_t = 0.3 V, I_t = 0.7 nA). Scale bar, 4 nm. **b**, 30 min after increasing the temperature to 493 K (50 × 50 nm^2, V_t = 0.05 V, I_t = 0.7 nA). Scale bar, 5 nm. **c**, 5 h after increasing the temperature to 493 K (200 × 100 nm^2, V_t = −0.3 V, I_t = 0.7 nA) Scale bar, 20 nm. All images were taken under 950 mbar syngas at H_2:CO = 2:1.

from the maxima to the minima of the topography across several steps, leading to a flatter surface. These effects confirm that the Co atoms are mobile under reaction conditions. Control experiments in UHV showed that the smoothing also happens in vacuum (Supplementary Fig. 4).

Correlation of activity and sites. What these data primarily show, in addition to the smoothing under reaction conditions, is that sputtering allowed us to vary the density of steps without inducing other defects. The sputtering initially may have created ill-defined atomic defects, but after 30 min under syngas at 493 K these had dissolved and only steps were detected. For a quantitative analysis the step lengths from several spatially uncorrelated scanning areas were evaluated for four states of the surface, the well-prepared annealed surface, the sputtered, highly-stepped surface after ~1 h, and the sputtered, partially smoothed surface after approximately 3 h and 5 h in syngas at 493 K. A plot of the TOF data from these four states (TOFs based on the consumption of CO) versus step density is shown in Fig. 7. Obviously, the activity of the sample scales with step density. That the linear regression function, even within the scatter of the data, does not intersect the origin can be explained by the blank activity of the Mo sample holder (0.5×10^{-3} s^{-1}) and an additional finite activity of the edges of the crystal.

As steps were the only varying features in these experiments, this correlation between TOF and step density is quite unambiguous. An obvious causal link is the dissociation of CO that is often assumed to be the rate-limiting step of the FT synthesis[17]. According to density functional theory calculations, the CO dissociation barrier is strongly lowered at step sites, to 1.61 eV (ref. [37]), from the very high values ranging from 2.28 to 3.80 eV on a terrace site[38]. The general reason for this is that the dissociation of molecules such as CO, NO and N_2, in which a π bond is cleaved, is favoured at steps because the transition state complex can bind to several metal atoms[39,40]. Alternatively, the dissociation of the H_2 molecules, which has been shown to be restricted on highly adsorbate-covered terraces, could be favoured at the steps[41]. It has also been suggested that the rate-limiting step is not the dissociation of CO at the steps but the subsequent hydrogenation of the CH_x moieties. Because the steps are still the source of the C atoms, also such complex explanations would be consistent with the correlation[42].

The fact that no surface roughening was observed but even a smoothing of the sputtered surface, disagrees with the hypothesis that under reaction conditions cobalt islands form, which is a process assumed to create additional active sites. We propose instead that the previous data can be explained without this effect, by pre-existing steps only. Actually, the initially described increasing TOF of the supported FT catalyst with particle size and the following saturation have been predicted for reactions involving the dissociation of molecules such as CO[40]. Highly coordinated sites, the active sites of these reactions, do not exist on the surfaces of very small

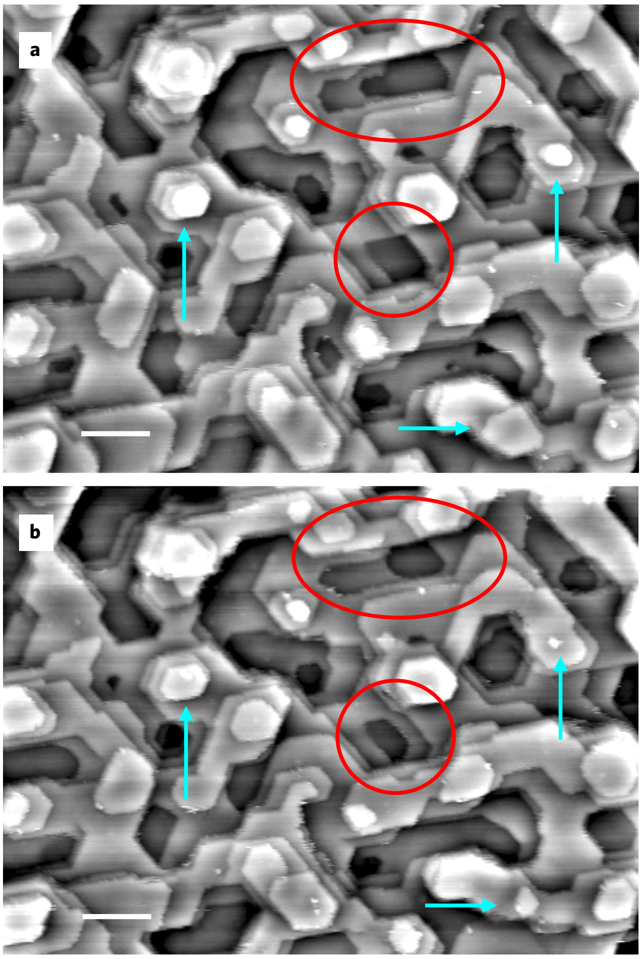

Fig. 6 | STM images of the smoothing of the sputtered Co(0001) sample in syngas. Images taken in 950 mbar syngas, H_2:CO = 2:1, 493 K. **a**, 1.5 h after increasing the temperature to 493 K. **b**, Image of the same area 1.5 h later. Areas where the topmost terraces partially dissolved and the low-lying cavities filled up are marked. Scale bars, 10 nm.

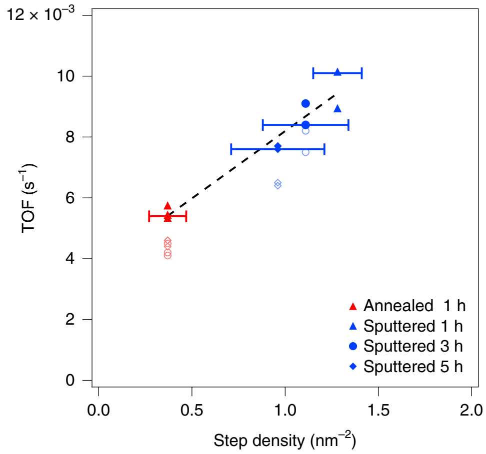

Fig. 7 | Plot of the CO-based TOFs versus step densities. CO-based TOFs were evaluated by multiplying the hydrocarbon-based TOFs by the number of C atoms of the individual products and adding up (Supplementary Table 1). The step densities were determined in STM experiments performed under exactly the same conditions as the TOFs. Data were taken from the annealed Co(0001) sample (first set), and the sputtered sample after 5 h (second set), 3 h (third set) and 1 h (fourth set). The density data, in units of Co step atoms per nm^2, are averages from 21, 12, 13 and 12 spatially uncorrelated images from the four sets, determined in three experiments with the annealed and two experiments with the sputtered surface; error bars depict s.d. The dashed line is a linear fit. TOFs from the sputtered surface have been corrected for a moderate deactivation observed for the annealed sample after 3 h and 5 h (open symbols) and are thus not related to structure changes. The open data points of the sputtered surface data are the corresponding uncorrected values, showing that the scaling persists even without the correction.

metal particles but they increasingly occur on larger particles until saturation is reached.

For Co particles the morphology has been modelled explicitly[43], using the observation that the Co particles of the FT catalyst are to a considerable fraction face-centred cubic rather than hexagonal close-packed[44], in contrast to bulk Co. In the model, face-centred cubic Co particles form cubo-octrahedrons with rounded edges (for illustrations see ref. [43]) that develop more steps and other highly coordinated sites with increasing size, until at some point the density of these sites saturates. In detail, the step density-versus-particle size function was not identical to the experimental TOF function (it saturated at smaller particle sizes and bent from an increasing to a constant value less abruptly) but qualitatively the behaviour was the same. From this model the atomic steps on the surfaces of the nanoparticles, which exist just as a result of their morphologies, could be sufficient to explain the TOF function, rendering an additional roughening unnecessary.

This idea could be quantitatively tested by means of the present data. For this purpose we extrapolated the regression line in Fig. 7 to the step densities evaluated by means of the cubo-octrahedron model. For ≥8 nm particles, for which most studies on supported Co catalysts have been performed, 17% of the surface atoms are step atoms (all step types combined) according to the model[43]. For a Co(0001) surface this fraction would correspond to a step density of 3.12 nm^{-2} for which the extrapolation from the data of Fig. 7 gives a CO-based TOF of $1.7 \times 10^{-2}\,s^{-1}$. Experimental TOFs, reported for supported Co catalysts for 1 bar and 493 K (refs. [15,45–47]), vary over a wide range, from $0.75 \times 10^{-2}\,s^{-1}$ to $6.3 \times 10^{-2}\,s^{-1}$, indicating that additional effects such as interactions of the Co particles with the support play a role. One should also keep in mind that in these studies the particles sizes were inferred ex situ and indirectly by chemisorption, X-ray diffraction and transmission electron microscopy, or combinations thereof. Nevertheless, the value extrapolated from the present data is within the order of magnitude of supported catalyst activities. The proposed model, where existing steps are the only active sites, can thus predict the activities of the supported catalyst within an order of magnitude.

Conclusions

In conclusion, atomic steps were identified as the active sites of the FT synthesis on a Co(0001) model catalyst. This was achieved in a direct way, by quantitatively correlating the density of steps determined by STM with catalytic activity measured by GC in the same apparatus and under the same conditions.

This finding has further implications for the understanding of the FT synthesis and possibly of other catalytic reactions. First, it shows that steps remain active under working conditions. One might have expected that the CO molecules and various reaction intermediates, that is, C, O and H atoms, and hydrocarbon moieties, which are present at the high pressure, preferentially bind to steps, thus self-poisoning these sites. However, no major deactivation with time was observed, and the STM did not show any formation of undefined structures at the steps. The reaction must be fast enough to keep the coverages of surface species, which may deactivate the steps, sufficiently low. Alternatively, stable adsorbate configurations at the steps may leave sufficient space to still enable dissociation processes[22].

Second, the result puts restrictions on reaction mechanisms. The sequence starting with the dissociation of CO followed by hydrogenation of C atoms and polymerization of CH_x species, although favoured by most researchers, is not undisputed, and other FT reaction mechanisms have been discussed. In an alternative, H-assisted mechanism the adsorbed CO first becomes partially hydrogenated and then the C–O bond is cleaved[48]. In this sequence the dissociation barrier is much lower, and the molecules could dissociate on the flat terraces. However, the present study shows that the rate-limiting step must be structure-sensitive.

Third, the result proves a long-standing idea in heterogeneous catalysis. That steps are active sites has been assumed for many reactions, and in particular it has been predicted by theory for reactions involving the cleavage of molecular π bonds. However, strictly speaking, there was no unique evidence for a working catalyst, and the available information from indirect experiments can be quite confusing, as was shown here for the FT synthesis. Here direct evidence was provided by analysis of atomic-scale data.

Methods

Chamber. The dual chamber apparatus consisting of an UHV chamber and the reactor cell with the STM has been described in detail previously[27]. The UHV chamber was equipped with a photoelectron spectrometer with a monochromatized Al Kα X-ray source and facilities for sample preparation. The reactor cell could be operated at pressures between UHV and 1 bar. During reaction experiments the sample was heated by means of an infrared laser coupled into the STM cell by a glass fibre. The FT products in the reactor cell were analysed online by means of a specially configured GC.

Gas purity. At the start of the project, after the Co sample had been in the reactor cell for several hours at ~500 K under syngas, Ni and S signals were detected by XPS. These contaminants had not been present in the previous experiments at 10 mbar (ref. [24]), but they were detected here in increasing amounts between 200 mbar and 950 mbar. The S contaminant was most probably caused by traces of sulfur compounds in the H_2 gas (99.9999%, AirLiquide) in concentrations below the detection limits of the quadrupole mass spectrometer. After implementing purifiers (MC1-904, MC50-403; SAES Pure Gas) and a liquid nitrogen cold trap in the H_2 line, S was no longer detected by XPS. The Ni contaminant was certainly caused by Ni carbonyl formed at Ni-containing components in the system and decomposed at the hot sample. To solve this problem, extensive efforts were made to remove all Ni-containing parts. Furthermore, the stainless steel reactor cell and almost all other stainless steel components of the reactor cell were coated with amorphous Si (SilcoGuard 1000, SilcoTek GmbH). To decompose carbonyls that may have already been contained in the gas bottle or formed in the gas line, the CO gas (99.997%, AirLiquide) was passed through a hot trap (a Cu pipe filled with molecular sieve at 300 °C) and then through a liquid nitrogen cold trap to freeze out residual carbonyls. With these measures, the Ni was reduced to the XPS detection limits in the 200 mbar experiments and to coverages between 0.01 and 0.10 of a ML in the 950 mbar experiments, after 6 h in syngas. The amounts of residual Ni were not correlated with activity, making any effects of the Ni traces on catalytic properties unlikely.

Sample preparation. The Co(0001) sample (5 mm diameter of the polished and prepared part) was mounted on a Mo holder. The temperature was measured with a type S thermocouple pressed against the rear side of the sample by means of a thin SiC disc. The SiC disc served as absorber of the infrared light from the heating laser. The sample was sputter-cleaned in the UHV chamber as previously described[24]. For the experiments with the sputtered surfaces, the sample was first prepared as usual and then Ar^+-sputtered (985 eV, ~3 μA) at temperatures below 373 K for 30 min without a final annealing step. Blank experiments were performed with Au(111) and Ag(111) samples mounted on the same type of holder as the Co sample.

Reaction experiments. After preparation in the UHV chamber, the sample was transferred to the reactor cell, H_2/CO gas mixtures were introduced and then the heating laser was turned on. All reaction experiments were performed in batch mode. We consider this uncritical for the evaluation of the TOF data because the CO conversions were only of the order of 10^{-6} per hour (Supplementary Table 1), which was a result of the small area of the prepared sample surface (19.6 mm^2) and the large reactor volume (1.8 l). The gas composition thus basically did not change during the experimental runs. Concentration gradients in the reactor could be neglected because of the low TOFs. At the end of an experiment, the laser heating was first turned off, so that the sample cooled down in syngas. In this way CO could remain adsorbed on the sample, which helped protect the surface from adsorption of hydrocarbons and water. When the temperature was below 70 °C the reactor cell was evacuated, and the sample was transferred to the preparation chamber. Usually this took 2 min. Finally, XPS spectra were taken.

Gas chromatography. The hydrocarbon products formed in the reactor cell were analysed with a GC (Trace 1310, ThermoFisher, using a 2 m HayeSep Q80/100 micropacked column, an additional 30 m TracePlot TG-BOND Q column and a flame ionization detector). The GC was customized for the special conditions of the STM experiments, namely pressures ≤1 bar and extremely low hydrocarbon concentrations from the FT synthesis. To meet these conditions, the GC was equipped with a special compression unit for gas sampling and a cryogenic, liquid nitrogen-cooled trap at the column (S + H Analytik GmbH). Minimum product concentrations of ~0.3 ppb could be measured in this way. In a typical 5 h or 6 h experiment, gas samples were taken every hour; pressure drops per GC measurement were approximately 6.5 mbar at a total pressure of 950 mbar, or 0.6%. Differential conditions were thus ensured.

STM. During experiments under syngas the scanning area was occasionally repositioned to exclude artefacts from the presence of the tip. STM images were processed using Igor Pro software (WaveMetrics) for plane and line noise correction and for contrast. The densities of step edge atoms were calculated from the total lengths of the step edges per surface area and using the Co–Co distance at a step along a close-packed direction (0.2507 nm). The total lengths of the step edges were measured manually; no automated analysis tools were applied. Of the steps, 5–10% were double steps (or closely spaced single steps); these were just counted twice, without considering possible special properties.

XPS. For coverage quantification by XPS, the peaks were fitted with Gaussians convoluted with Doniach–Šunjić functions after a linear background subtraction. C 1*s* and O 1*s* binding energies could be determined with a precision of approximately ±0.1 eV. The peak intensities were normalized by the respective cross-sections[49] and asymmetry parameters[50] at an angle of 66° between X-ray source and analyser. The transmission function of the analyser was roughly constant in the applied spectral range as determined with a clean Au(111) sample. The coverages of the adsorbates were calculated by normalizing the individual peak intensities by the Co $2p_{1/2}$ peak, which is proportional to the number of detected cobalt layers $\Lambda_{Co} = [1 - \exp(-d/\lambda)]^{-1}$; λ is the mean free path of the photoelectrons[51] and $d = 0.205$ nm is the layer distance of Co(0001). For simplicity, no damping of the Co $2p_{1/2}$ signal by the adsorbates was assumed at coverages well below one ML. Measurements of the saturation coverage of CO on the clean Co(0001) sample in UHV gave reproducible amounts of 0.30–0.33 ML CO, both from the C 1*s* and O 1s peaks, if the acquisition times were kept short (otherwise some CO desorption and decomposition could be observed when illuminating the sample with the X-ray source).

Data availability

The data that support the findings of this study are presented within the text and the supporting information or are available from the corresponding author upon reasonable request.

Received: 12 April 2019; Accepted: 28 August 2019;

References

1. Taylor, H. S. & Armstrong, E. S. A theory of the catalytic surface. *Proc. R. Soc. Lond.* **108**, 105–111 (1925).
2. Boudart, M. Catalysis by Supported Metals. *Adv. Catal.* **20**, 153–166 (1969).
3. Zambelli, T., Wintterlin, J., Trost, J. & Ertl, G. Identification of the 'active sites' of a surface-catalyzed reaction. *Science* **273**, 1688–1690 (1996).
4. Davis, S. M., Zaera, F. & Somorjai, G. A. Surface structure and temperature dependence of light-alkane skeletal rearrangement reactions catalyzed over platinum single-crystal surfaces. *J. Am. Chem. Soc.* **104**, 7453–7461 (1982).
5. Hansen, P. L. et al. Atom-resolved imaging of dynamic shape changes in supported copper nanocrystals. *Science* **295**, 2053–2055 (2002).
6. Vendelbo, S. B. et al. Visualization of oscillatory behaviour of Pt nanoparticles catalysing CO oxidation. *Nat. Mater.* **13**, 884 (2014).
7. Wang, Z. J., Farra, R., Cao, J., Schlögl, R. & Willinger, M. G. The dynamics of active metal catalysts revealed by in situ electron microscopy. *Microsc. Microanal.* **22**, 4–5 (2016).
8. Jensen, J. A., Rider, K. B., Salmeron, M. & Somorjai, G. A. High pressure adsorbate structures studied by scanning tunneling microscopy: CO on Pt(111) in equilibrium with the gas phase. *Phys. Rev. Lett.* **80**, 1228–1231 (1998).

9. Österlund, L. et al. Bridging the pressure gap in surface science at the atomic level: H/Cu(110). *Phys. Rev. Lett.* **86**, 460–463 (2001).
10. Hendriksen, B. L. M. & Frenken, J. W. M. CO oxidation on Pt(110): scanning tunneling microscopy inside a high-pressure flow reactor. *Phys. Rev. Lett.* **89**, 046101 (2002).
11. Böcklein, S., Günther, S. & Wintterlin, J. High-pressure scanning tunneling microscopy of a silver surface during catalytic formation of ethylene oxide. *Angew. Chem. Int. Ed.* **52**, 5518–5521 (2013).
12. Pfisterer, J. H. K., Liang, Y., Schneider, O. & Bandarenka, A. S. Direct instrumental identification of catalytically active surface sites. *Nature* **549**, 74–77 (2017).
13. Bartholomew, C. H. and Farrauto, R. J. *Fundamentals of Industrial Catalytic Processes* 2nd edn (Wiley-Interscience, 2006).
14. Kaiser, P., Pöhlmann, F. & Jess, A. Intrinsic and effective kinetics of cobalt-catalyzed fischer-tropsch synthesis in view of a power-to-liquid process based on renewable energy. *Chem. Eng. Technol.* **37**, 964–972 (2014).
15. den Breejen, J. P. et al. On the origin of the cobalt particle size effects in Fischer–Tropsch catalysis. *J. Am. Chem. Soc.* **131**, 7197–7203 (2009).
16. Oukaci, R., Singleton, A. H. & Goodwin, J. G. Comparison of patented Co F–T catalysts using fixed-bed and slurry bubble column reactors. *Appl. Catal. A* **186**, 129–144 (1999).
17. van Santen, R. A., Markvoort, A. J., Filot, I. A. W., Ghouri, M. M. & Hensen, E. J. M. Mechanism and microkinetics of the Fischer–Tropsch reaction. *Phys. Chem. Chem. Phys.* **15**, 17038–17063 (2013).
18. Wilson, J. & de Groot, C. Atomic-scale restructuring in high-pressure catalysis. *J. Phys. Chem.* **99**, 7860–7866 (1995).
19. Geerlings, J. J. C., Zonnevylle, M. C. & de Groot, C. P. M. Studies of the Fischer–Tropsch reaction on Co(0001). *Surf. Sci.* **241**, 302–314 (1991).
20. Beitel, G. A., de Groot, C. P. M., Oosterbeek, H. & Wilson, J. H. A combined in-situ PM-RAIRS and kinetic study of single-crystal cobalt catalysts under synthesis gas at pressures up to 300 mbar. *J. Phys. Chem. B* **101**, 4035–4043 (1997).
21. Schulz, H. Selforganization in Fischer–Tropsch synthesis with iron- and cobalt catalysts. *Catal. Today* **228**, 113–122 (2014).
22. Banerjee, A. et al. Shape and size of cobalt nanoislands formed spontaneously on cobalt terraces during Fischer–Tropsch synthesis. *J. Phys. Chem. Lett.* **7**, 1996–2001 (2016).
23. Zhang, X. Q., van Santen, R. A. & Hensen, E. J. M. Carbon-induced surface transformations of cobalt. *ACS Catal.* **5**, 596–601 (2015).
24. Ehrensperger, M. & Wintterlin, J. In situ high-pressure high-temperature scanning tunneling microscopy of a Co(0001) Fischer–Tropsch model catalyst. *J. Catal.* **319**, 274–282 (2014).
25. Ehrensperger, M. & Wintterlin, J. In situ scanning tunneling microscopy of the poisoning of a Co(0001) Fischer–Tropsch model catalyst by sulfur. *J. Catal.* **329**, 49–56 (2015).
26. Navarro, V., van Spronsen, M. A. & Frenken, J. W. M. In situ observation of self-assembled hydrocarbon Fischer–Tropsch products on a cobalt catalyst. *Nat. Chem.* **8**, 929–934 (2016).
27. Rößler, M., Geng, P. & Wintterlin, J. A high-pressure scanning tunneling microscope for studying heterogeneous catalysis. *Rev. Sci. Instrum.* **76**, 023705 (2005).
28. Oosterbeek, H. Bridging the pressure and material gap in heterogeneous catalysis: cobalt fischer–tropsch catalysts from surface science to industrial application. *Phys. Chem. Chem. Phys.* **9**, 3570–3576 (2007).
29. Yang, J. et al. Reaction mechanism of CO activation and methane formation on Co Fischer–Tropsch catalyst: a combined DFT, transient, and steady-state kinetic modeling. *J. Catal.* **308**, 37–49 (2013).
30. Huffman, G. P. et al. In-situ XAFS investigation of K-promoted Co catalysts. *J. Catal.* **151**, 17–25 (1995).
31. Ernst, B., Bensaddik, A., Hilaire, L., Chaumette, P. & Kiennemann, A. Study on a cobalt silica catalyst during reduction and Fischer–Tropsch reaction: in situ EXAFS compared to XPS and XRD. *Catal. Today* **39**, 329–341 (1998).
32. Cats, K. H. et al. X-ray nanoscopy of cobalt Fischer–Tropsch catalysts at work. *Chem. Commun.* **49**, 4622–4624 (2013).
33. Nishizawa, T. & Ishida, K. The Co (cobalt) system. *Bull. Alloy Phase Diagr.* **4**, 387–390 (1983).
34. Weststrate, C. J., van Helden, P., van de Loosdrecht, J. & Niemantsverdriet, J. W. Elementary steps in Fischer–Tropsch synthesis: CO bond scission, CO oxidation and surface carbiding on Co(0001). *Surf. Sci.* **648**, 60–66 (2016).
35. Böller, B., Ehrensperger, M. & Wintterlin, J. In situ scanning tunneling microscopy of the dissociation of CO on Co(0001). *ACS Catal.* **5**, 6802–6806 (2015).
36. Weststrate, C. J. et al. Atomic and polymeric carbon on Co(0001): surface reconstruction, graphene formation, and catalyst poisoning. *J. Phys. Chem. C.* **116**, 11575–11583 (2012).
37. Gong, X. Q., Raval, R. & Hu, P. CO dissociation and O removal on Co(0001): a density functional theory study. *Surf. Sci.* **562**, 247–256 (2004).
38. Qi, Y., Yang, J., Chen, D. & Holmen, A. Recent progresses in understanding of Co-based Fischer–Tropsch catalysis by means of transient kinetic studies and theoretical analysis. *Catal. Lett.* **145**, 145–161 (2015).
39. Hammer, B. & Nørskov, J. K. Theoretical surface science and catalysis—calculations and concepts. *Adv. Catal.* **45**, 71–129 (2000).
40. Van Santen, R. A. Complementary structure sensitive and insensitive catalytic relationships. *Acc. Chem. Res.* **42**, 57–66 (2009).
41. Weststrate, C. J. et al. Interaction of hydrogen with flat (0001) and corrugated (11–20) and (10–12) cobalt surfaces: insights from experiment and theory. *Catal. Today* https://doi.org/10.1016/j.cattod.2019.04.002 (2019).
42. Pestman, R., Chen, W. & Hensen, E. Insight into the rate-determining step and active sites in the Fischer–Tropsch reaction over cobalt catalysts. *ACS Catal.* **9**, 4189–4195 (2019).
43. van Helden, P., Ciobîcă, I. M. & Coetzer, R. L. J. The size-dependent site composition of FCC cobalt nanocrystals. *Catal. Today* **261**, 48–59 (2016).
44. Tsakoumis, N. E. et al. Fischer–Tropsch synthesis: an XAS/XRPD combined in situ study from catalyst activation to deactivation. *J. Catal.* **291**, 138–148 (2012).
45. Haddad, G. J., Chen, B. & Goodwin, J. J. G. Effect of La^{3+} promotion of Co/SiO$_2$ on CO hydrogenation. *J. Catal.* **161**, 274–281 (1996).
46. Ribeiro, F. H., Schach Von Wittenau, A. E., Bartholomew, C. H. & Somorjai, G. A. Reproducibility of turnover rates in heterogeneous metal catalysis: compilation of data and guidelines for data analysis. *Catal. Rev.* **39**, 49–76 (1997).
47. Bezemer, G. L. et al. Cobalt particle size effects in the Fischer–Tropsch reaction studied with carbon nanofiber supported catalysts. *J. Am. Chem. Soc.* **128**, 3956–3964 (2006).
48. Inderwildi, O. R., Jenkins, S. J. & King, D. A. Fischer–Tropsch mechanism revisited:alternative pathways for the production of higher hydrocarbons from synthesis gas. *J. Phys. Chem. C.* 1305–1307 (2008).
49. Yeh, J. J. & Lindau, I. Atomic subshell photoionization cross sections and asymmetry parameters: $1 \leqslant Z \leqslant 103$. *Data Nucl. Data Tables* **32**, 1–155 (1985).
50. Reilman, R. F., Msezane, A. & Manson, S. T. Relative intensities in photoelectron spectroscopy of atoms and molecules. *J. Electron. Spectrosc. Relat. Phenom.* **8**, 389–394 (1976).
51. Tanuma, S., Powell, C. J. & Penn, D. R. Calculations of electron inelastic mean free paths. V. Data for 14 organic compounds over the 50–2000 eV range. *Surf. Interface Anal.* **21**, 165–176 (1994).

Acknowledgements

We gratefully acknowledge financial support by the German Science Foundation (DFG) through grant no. WI 1003/8–1. We thank S. Günther, TU Munich, for help with the preparation of Supplementary Fig. 3 and Supplementary Video 4.

Author contributions

B.B. performed the STM, XPS and GC measurements and analysed the data. K.M.D. deployed and tested the GC. B.B. and J.W. wrote the manuscript. J.W. conceived and supervised the project.

Competing interests

The authors declare no competing interests.

Additional information

Supplementary information is available for this paper at https://doi.org/10.1038/s41929-019-0360-1.

Correspondence and requests for materials should be addressed to J.W.

Reprints and permissions information is available at www.nature.com/reprints.

4.2 FT Synthesis on a Co(10$\bar{1}$15) Crystal

Based on the evidence that steps are the active sites of the FT synthesis on the Co(0001) crystal, one can hypothesize that this is also the case for industrial FT catalysts. On the other hand, the surface structure of this single crystal is different from that of nanoparticles, and a Co(0001) single crystal can only be regarded as a model system. The aim of the study presented in this chapter is to bridge this materials gap between single crystals and nanoparticles.

In order to probe the effect of higher step densities than achieved with the sputtered Co(0001) surface, the catalytic activity of a Co(10$\bar{1}$15) single crystal was analyzed by *operando* FTS. The (10$\bar{1}$15) surface can be regarded as a 7.1° tilted surface of Co(0001) with a high density of straight atomic steps, where the terraces are alternating 7 and 9 atomic rows wide. This surface preserves the close-packed structure of the terraces of the Co(0001) surface, and only alters the step density. A model of the ideal Co(10$\bar{1}$15) surface is depicted in Figure 4.2.

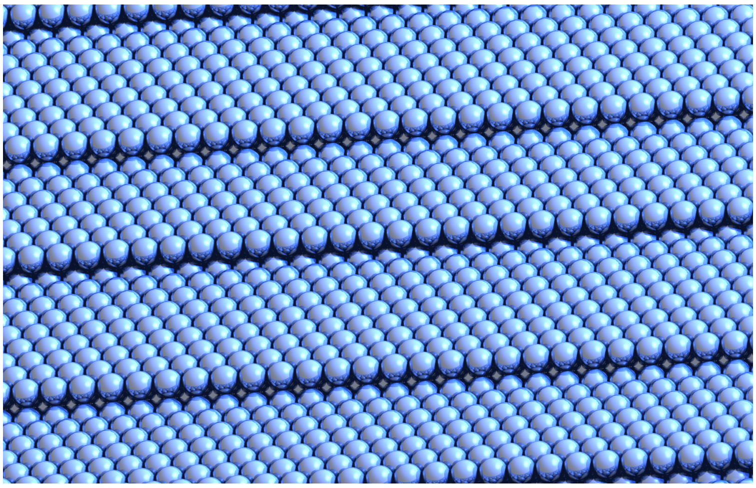

Figure 4.2: Model of the ideal Co(10$\bar{1}$15) surface. It can be regarded as a vicinal Co(0001) surface, containing 7 and 9 atomic rows wide terraces separated by straight steps.

As mentioned above, simulations of the morphology of fcc-packed Co nanoparticles showed that the step density levelled off at a particle diameter of ~8 nm. 17 % of the surface atoms of such particles are step (B_5-A, B_5-B) or kink (B_6) sites.[44] This is equal to a step density of ~3.0 nm^{-2} which is close to that of the ideal Co(10$\bar{1}$15) surface (2.44 nm^{-2}). With respect to the step density, the Co(10$\bar{1}$15) sample can thus be regarded as a single-crystal model for the nanoparticles of the supported FT catalyst.

In addition to the comparison with the Co(0001) crystal, the activity data of the Co(10$\bar{1}$15) model catalyst were used for a quantitative comparison to literature data from supported nanoparticles. For this analysis, one has to take into account that the activity of industrial catalysts may be affected by many factors. Besides the morphology, interactions with the supporting oxides as well as the presence of promotors can alter the behavior. Whether the activity of supported nanoparticles is determined by steps or overwhelmed by other effects was the second question to be answered by this study. Section 4.2.1 presents the results of the *operando* STM study on Co($10\bar{1}15$).

After publishing the article, it turned out that parts of the given temperatures were incorrect; a correction has been published (see section 4.2.2).

4.2.1 *Operando* STM Study to Bridge the Materials Gap between Single Crystals and Supported Catalysts

The article “*In Situ/Operando* STM of the Fischer-Tropsch Synthesis on a Co($10\bar{1}15$) Surface – A Study to Bridge the Materials Gap between Single-Crystal Models and Supported Catalysts”,[133] was published in *ACS Catalysis*. The key findings of the article are:

- The STM images show the expected highly stepped morphology. In detail, the surface topography differs from the ideal morphology of the Co($10\bar{1}15$) surface. While the ideal crystal would show hexagonally close-packed terraces with a width of 7 and 9 atomic rows, STM images reveal broader (0001) terraces separated by step bunches. In most cases, double steps could not be distinguished from closely spaced monoatomic steps. However, analysis of few high-resolution areas agrees with the theoretical step density of $2.44\,\mathrm{nm}^{-2}$.

- The surface morphology in the presence of the syngas is the same as in UHV, and it does not show any roughening during reaction. The same observation has been made before for the Co(0001) surface.[61] The hypothesis that the Co-based FT catalyst roughens under reaction conditions is therefore not confirmed. Furthermore, the surface stays metallic during the reaction, and *ex situ* XPS data show similar coverages of adsorbates as on the Co(0001) surface in the previous study.[61]

- Activity data from the annealed and sputtered Co(0001) surface were reproduced from ref. [61]. The product distributions of C_1 to C_4 hydrocarbons for the Co($10\bar{1}15$) single crystal are similar to those obtained from Co(0001). One can conclude that the reaction mechanisms on both crystals are the same and that the catalytic activity is only influenced by the steps.

- The range over which TOFs and step densities correlate was expanded by a factor of two compared to the previous study.[61] The fact that more olefins than paraffins of the C_2 to C_4 hydrocarbons are formed is in agreement with literature data from nanoparticles.[134] Also for this reason, on can conclude that the Co(10$\bar{1}$15) crystal is a valid model of industrial catalysts.

- The activity of the Co(10$\bar{1}$15) model system is in good agreement with the majority of reported values for Co nanoparticles. For this comparison, literature data were corrected for deviating temperatures and partial pressures. It can be concluded that the dominating factor for the activity is the step density also for supported catalysts.
- The materials gap between surface science models and industrial catalysts can be regarded as bridged for this system.

The article "*In Situ/Operando* STM of the Fischer-Tropsch Synthesis on a Co(10$\bar{1}$15) Surface – A Study to Bridge the Materials Gap between Single-Crystal Models and Supported Catalysts" published in *ACS catalysis* is reproduced with permission from *ACS Catal.* **2022**, *12*, 7199–7209. Copyright © 2022 The Authors. Published by American Chemical Society.

The supporting information of this article is presented in Appendix F, starting on page 117. The supporting video can be downloaded from the website: `https://pubs.acs.org/doi/10.1021/acscatal.2c00703`.

ACS Catalysis

pubs.acs.org/acscatalysis Research Article

In Situ/Operando STM of the Fischer–Tropsch Synthesis on a Co($10\bar{1}15$) Surface—A Study to Bridge the Materials Gap between Single-Crystal Models and Supported Catalysts

Katharina M. Golder and Joost Wintterlin*

Cite This: *ACS Catal.* 2022, 12, 7199–7209 **Read Online**

ACCESS | Metrics & More | Article Recommendations | Supporting Information

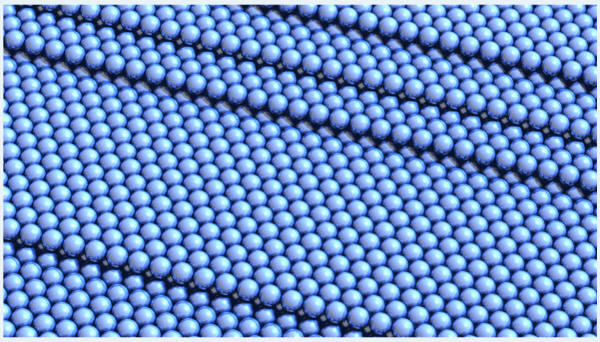

ABSTRACT: Co($10\bar{1}15$), a vicinal surface of the Co(0001) surface, has a similar density of steps as the supported Co catalysts used in the industrial Fischer–Tropsch synthesis. We have investigated whether this surface can serve as a model system to bridge the materials gap between single crystals and supported catalysts. Experiments on the Co($10\bar{1}15$) surface were performed by scanning tunneling microscopy (STM) under *in situ/operando* conditions and by gas chromatography (GC) with the same sample under the same conditions. X-ray photoelectron spectroscopy (XPS) was used for postreaction surface analysis. In the experiments, 2:1 mixtures of H_2 and CO (syngas) were applied at a total pressure of 950 mbar and at a sample temperature of 503 K. The morphology resolved by STM under these conditions showed long, narrow terraces as expected for the Co($10\bar{1}15$) surface but also step bunching. GC showed the formation of C_1 to C_4 hydrocarbons in considerably higher amounts compared to reference experiments with a Co(0001) sample. The activity of the Co($10\bar{1}15$) sample was higher than that of the Co(0001) sample by a factor approximately proportional to the density of atomic steps. It is concluded that atomic steps are the active sites on this highly stepped surface. An analysis of literature data of supported Co catalysts shows that the activities reported in the majority of these studies are comparable to those of the Co($10\bar{1}15$) sample.

KEYWORDS: *Fischer–Tropsch synthesis, turnover frequency, scanning tunneling microscopy, cobalt single crystal, structure sensitivity, in situ, operando, materials gap*

1. INTRODUCTION

We recently presented a study on the Fischer–Tropsch synthesis in which the surface of a Co(0001) single crystal has been imaged by scanning tunneling microscopy (STM) under *in situ/operando* conditions.[1] In the same apparatus, the catalytic activity has been measured by gas chromatography (GC). By combining these two techniques, it was shown that the catalytic turnover frequency (TOF), as determined by GC, scaled linearly with the density of monoatomic steps resolved by STM. This correlation was the clearest experimental evidence so far that the steps are the active sites of the Fischer–Tropsch synthesis on this model catalyst.

Here, we present an investigation that was performed to establish a closer link between model catalysts and the catalysts applied by industry. In the industrial Co-catalyzed Fischer–Tropsch synthesis, an approximate 2:1 mixture of H_2 and CO (syngas) reacts at total pressures of 20–40 bar and temperatures of ~500 K to give mainly linear, long-chain paraffins[2]

$$(2n + 1)H_2 + nCO \rightarrow C_nH_{2n+2} + nH_2O$$

The catalyst consists of metallic Co nanoparticles on an oxide support, e.g., on ZrO_2/SiO_2. A favorable fact for the analysis of this reaction is that it can also be performed under laboratory conditions, by applying syngas at ambient pressure. Under these conditions, the hydrocarbon molecules obtained as products are shorter,[3−6] but it can be assumed that essential aspects of the reaction mechanism are still captured. It is also possible to perform the reaction with Co single crystals instead of supported catalysts. Co(0001) and other crystal orientations have been found to be Fischer–Tropsch-active in 1 bar syngas and can therefore be regarded as model systems for the nanosized, metallic Co particles of the actual catalyst.[7−9] Using the result for Co(0001) that the steps are active, an obvious hypothesis is that atomic steps are also the active sites on the Co particles of the supported catalyst.

Received: February 9, 2022
Revised: May 4, 2022

The older view that the Fischer−Tropsch synthesis is a structure-insensitive reaction is in obvious contradiction to this hypothesis. However, in recent studies of supported catalysts, particle size effects were observed, which pointed to a pronounced structure sensitivity.[10−13] These studies showed that the activity of very small Co particles increased with increasing particle diameters until, at diameters between 6 and 10 nm, the activity leveled off, and then stayed constant over a wide range of particle sizes. The industrial catalysts are somewhat larger than the diameter beyond which the activity becomes constant.

Such activity-vs-particle size functions, which display an increase and then a leveling off, have actually been predicted for reactions in which a π bond of an adsorbed molecule is cleaved in a kinetically demanding reaction step.[14] In the present context, this would apply to CO. When a CO molecule dissociates at an atomic step, the transition state can simultaneously bind to the upper and lower edges of the step, which considerably lowers the activation energy.[15] That very small catalyst particles only show low activity can be explained by the fact that these particles only have edge and corner sites, i.e., low-coordinated atoms, but they do not have steps, i.e., sites consisting of neighboring low- and high-coordinated atoms. When the particles get bigger and develop larger facets, terraces form on these facets and, in this way, step sites are created. The density of step sites increases with diameter and reaches a maximum. Simulations of the atomic structure for the concrete case of Co nanoparticles in fact showed an increasing concentration of step sites with increasing diameter and then a saturation at approximately 8 nm.[16] This step density-vs-particle size function was in very good agreement with the initial activity-vs-particle size functions observed in the experiments.[10−13]

This correlation suggests a reaction mechanism in which the dissociation of CO plays a critical role. The earliest proposed and still most popular, so-called carbide mechanism of the Fischer−Tropsch synthesis fulfills this condition.[17,18] According to this mechanism, the first, kinetically relevant reaction step is the dissociation of adsorbed CO, which is followed by a series of hydrogenation and polymerization steps that finally lead to the hydrocarbon products. Atomic steps are required because, according to calculations, the barrier for the dissociation of CO on a close-packed Co surface is so high that this mechanism is practically excluded on a flat surface.[19−21] The fact that Co(0001) single crystals are Fischer−Tropsch-active is no contradiction because even Co single-crystal surfaces prepared in ultra-high vacuum (UHV) display appreciable concentrations of atomic steps.[1,22,23]

Taking these facts together, a consistent picture seems to emerge in which atomic steps are the active sites of the cobalt-catalyzed Fischer−Tropsch synthesis, and their main function is to facilitate the dissociation of the CO molecules. This does not exclude additional effects of steps, e.g., that H_2 preferentially dissociates at these sites when the surface is highly covered by adsorbates,[24] or that steps are preferred sites for the growth of the hydrocarbon chains.[25] It is also clear that the full mechanism of the Fischer−Tropsch synthesis is still far from being solved. However, with regard to its structure sensitivity, some qualitative understanding seems to have been reached.

On the other hand, there is still a massive materials gap between Co single-crystal models on the one hand and the industrial Fischer−Tropsch catalysts on the other. The morphologies are very different, and the presence of an oxide support and of possible promotors could strongly alter the behavior. Whether the activity of a supported catalyst is actually determined by atomic steps and not overwhelmed by other effects still needs to be shown. One possibility to achieve this is to show that the activity of Co particles can quantitatively be predicted from the activity of the step sites measured for a Co single crystal. In the previous *in situ*/*operando* STM study on Co(0001), we have extrapolated the data to the step densities of supported catalysts and obtained agreement of the activities within an order of magnitude, suggesting that this might indeed be possible.[1] However, a model that resembles the morphology of the Co particles more closely and gives a comparable activity would strongly support the hypothesis that atomic steps are also the active sites of the supported catalyst.

Here, we report about a study on the Co(10$\bar{1}$15) surface. It has a step density close to that of the Co particles at the onset of the constant plateau of the activity-vs-particle size function and thus models the narrow terraces and high step densities of the industrial supported catalyst. Experiments were performed by STM under *in situ*/*operando* conditions in combination with GC measurements. We have obtained images of the structure under reaction conditions and analyze whether the activity of this highly stepped surface is consistent with the activity of the step sites on the flat crystals. We then use these data to investigate how the activity relates to literature data of supported Fischer−Tropsch catalysts.

2. EXPERIMENTAL SECTION

The experiments were performed in an apparatus consisting of a reaction cell and a UHV chamber that has been described in detail previously.[26] In short, the employed UHV chamber was equipped with a spectrometer for X-ray photoelectron spectroscopy (XPS) using a monochromatic Al Kα source, an ion gun for sputtering, a quadrupole mass spectrometer, a low-energy electron diffraction (LEED) unit, and a sample manipulator. The UHV chamber was used for sample preparation before the reaction experiments and for surface analysis after the experiments in the reaction cell.

The reaction cell, a 1.8 l Si-coated stainless steel chamber, housed a home-built, beetle-type STM and was connected to the UHV chamber by a sample transfer system. A Pt/Ir tunneling tip was used for the present experiments. Pressures between UHV and 1 bar could be applied, and the STM could be operated at arbitrary pressures in this range (which makes use of the fact that STM is generally not restricted to UHV[27]). For pressure measurements in the bar range a diaphragm pressure gauge (CDG020D, Inficon) was used. In the reaction cell, the sample was heated by an infrared laser from the backside by means of a glass fiber that guided the laser light into the cell. For the syngas mixtures 99.9999% H_2 (AirLiquide) and 99.997% CO (AirLiquide) were used. Considerable efforts were made to additionally clean the gases before introducing them into the cell and to keep the formation of Ni carbonyl low. The measures taken, which included coating of all stainless steel parts of the reactor with amorphous Si, have been described before.[1] The STM itself, consisting of the scanning head, the sample mounting assembly, and the internal vibrational decoupling unit,[26] could not be coated. Reaction experiments were performed with the sample on the mounting assembly of the STM, and, for comparison of the activities, after de-installing the STM, with the sample held on a simplified mounting assembly in the reaction cell. Without installed STM, a residual amount of only 0.015 monolayers (ML) of Ni was detected by XPS after 1 h in syngas at the reaction temperature, and 0.12−0.17 ML after

6 h. (1 ML is defined here as one particle per Co surface atom.) With installed STM, the residual amount was 0.10 ML after 1 h and 0.62 ML after 6 h. The higher Ni amounts in the presence of the STM may be caused by the uncoated stainless steel parts of the STM or by traces of Ni on the walls of the STM components from previous experiments. However, the activities with and without installed STM were identical within the scatter of the data so that effects of Ni on the activities are unlikely. To safely exclude effects of Ni, most activity measurements were performed without installed STM.

The Co$(10\bar{1}15)$ sample (MaTeck GmbH) was a round, 5 mm wide disk with a 1 mm wide brim at which it was mounted to a Mo holder. The nominal residual surface roughness was less than 0.01 μm, the orientation was better than 0.1°. A SiC disc that served as absorber of the laser light was pressed to the backside of the crystal. The temperature was measured by means of a type S (PtRh/Pt) thermocouple clamped between the sample and the SiC disc (a type K thermocouple was excluded because it represents a source of Ni). The sample surface was prepared by repeated Ar^+ sputtering (1 keV, 10 min at room temperature, 5 min during heating up) and annealing to 623 K. Because of the hcp-to-fcc phase transition of Co at ~700 K, the sample temperature was kept below 630 K in all preparation steps. A consequence of this low preparation temperature was an imperfectly annealed surface topography, which is a general problem in experiments with Co single-crystal samples.

Blank TOFs measured with a Au(111) sample were ~1×10^{-4} s^{-1} for CH_4, 3×10^{-5} s^{-1} for ethylene, 8×10^{-6} s^{-1} for ethane, 1×10^{-5} s^{-1} for propylene, and 5×10^{-6} s^{-1} for propane. These values are more than an order of magnitude lower than the TOFs measured with the Co sample so that blank TOFs could be neglected in the quantitative analyses.

The Fischer−Tropsch products were analyzed by a specially designed GC system.[28] It was equipped with an automated gas sampling unit that extracted gas samples from the reaction cell at a pressure of 80 mbar, and then compressed the extracted volumes into the sample loops of the two channels of the GC. Concentration and peak focusing were achieved by means of a N_2-cooled cryo trap at one of the two separation columns. The GC system reached detection and quantification limits of 0.45 and 1.3 ppb (parts per billion), respectively (determined for propane). This high sensitivity was a precondition for analyzing the extremely low amounts of products formed on the single crystal in the relatively large reactor cell. Because of the low extracted gas volumes (0.4% of the reactor content per gas sample in the present experiments) and the low TOFs, the gas composition was unchanged during an experimental run and the reactions can be regarded as differential.

In a typical experiment, the sample was first prepared by sputtering and annealing in the UHV chamber until the C 1s signal was close to the detection limit of the XPS (~0.09 ML). Then, the sample was transferred to the reaction cell. After closing the valves to the UHV chamber and the vacuum pumps, the cell was filled with H_2 and CO at a mixing ratio of 2:1 and, in the present experiments, at a total pressure of 950 mbar. A first gas sample was extracted for GC analysis (0 h spectrum in the data shown below) after which the heating laser was turned on. The laser power was adjusted such that a constant sample temperature of ~503 K was held. Reaction experiments typically lasted several hours under batch conditions during which gas samples were taken every hour. Although possible in principle, GC measurements were usually not performed simultaneously with STM. However, the TOFs were measured with the same sample under the same T and p conditions so that the term *in situ*/*operando* still appears appropriate. After a reaction experiment, the heating laser was first turned off, and when the sample had cooled to a temperature below 70 °C the reaction cell was reevacuated. Finally, the sample was transferred to the UHV chamber and analyzed by XPS. Coverages of the surface species were determined by XPS from the cross sections of the elements as described before.[1]

For the purpose of comparison, TOFs were also measured with a Co(0001) sample, both after the same preparation procedure as applied for the Co$(10\bar{1}15)$ sample, and, to increase the step density of this flat surface, after additional sputtering for 10 min without final annealing. These experiments with Co(0001) were equivalent to those described in ref 1. They were repeated here because a new GC column had been mounted and we wanted to make sure that the TOFs from the Co$(10\bar{1}15)$ sample could quantitatively be compared to the TOFs from Co(0001). Unlike in the previous experiments, no normalization of the GC intensities was required. Also for reasons of quantitative comparison, the temperatures measured at the backsides of both samples were carefully calibrated with respect to a second pair of thermocouples directly welded to the front surfaces. We give the calibrated temperatures at the frontsides.

3. RESULTS

3.1. Structure Model of the Co$(10\bar{1}15)$ Surface. Figure 1 shows a structure model of the ideal Co$(10\bar{1}15)$ surface in a view from above [Figure 1a] and in a side view [Figure 1b]. We use the standard four Miller index nomenclature of hcp crystal surfaces, $(hk\overline{h+k}l)$, with $h = 1$, $k = 0$, $\overline{h+k} = \bar{1}$, and $l = 15$. Dark and bright atom layers mark the A and B planes of the hcp lattice of cobalt. The atomic steps run along a close-packed direction, and the hexagonally close-packed terraces between the steps are 7 and 9 atomic rows wide for the A and B planes, respectively. The ideal Co$(10\bar{1}15)$ surface can be regarded as a 7.1° tilted vicinal surface of Co(0001) with a high density of straight atomic steps. The density of step atoms is $\varrho_{\text{step atoms}} = 2/A$, where A, the area of a unit cell, is $A = (15/2)\sqrt{3}\,a^2$. With the

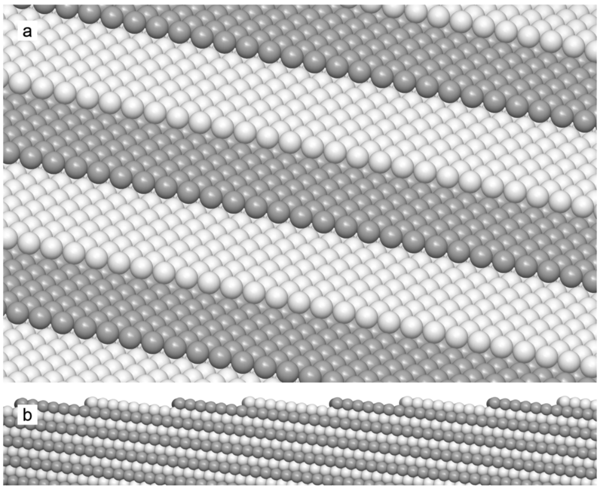

Figure 1. Structural model of the ideal Co$(10\bar{1}15)$ surface. (a) Top view and (b) side view. The atoms of the A and B layers of the hcp-stacked Co are shown as dark and light gray spheres, respectively.

lattice constant of Co of $a = 2.507$ Å, the step density of a perfect Co(10$\bar{1}$15) surface is 2.4 nm^{-2}. This value is comparable to the density of step sites of the 8 nm Co particles at the onset of the constant-activity plateau (see the Discussion section).

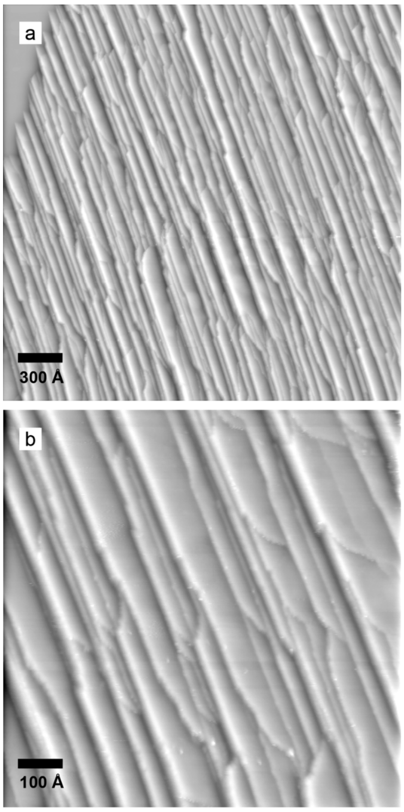

Figure 2. STM images of the Co(10$\bar{1}$15) surface in UHV at room temperature. (a) Large-scale image, tunneling voltage (V_t) = −0.2 V, tunneling current (I_t) = 0.7 nA. (b) Smaller-scale image, not from the same area, V_t = −0.2 V, I_t = 2.25 nA.

3.2. STM Experiments. Large-scale STM images of the Co(10$\bar{1}$15) surface, recorded in UHV at room temperature, show a pronounced stripe pattern [Figure 2a]. Smaller images [Figure 2b] show that the stripes consist of long, narrow, atomically flat terraces separated by linear steps, many of which are straight over several 100 Å. On a large scale, this morphology corresponds to expectations for the (10$\bar{1}$15) surface. Control experiments by LEED showed hexagonal diffraction spots, in agreement with the hexagonally close-packed terraces of the (10$\bar{1}$15) surface. The hexagonal diffraction pattern is tilted with respect to the surface normal of a Ag(111) reference sample, consistent with the tilting of the (10$\bar{1}$15) surface.

Upon closer inspection of the STM data, one can see that many of the terraces are significantly broader than the average width of 16.3 Å of the A and B terraces of the ideal surface, and at the same time, many steps are higher than a monoatomic step. The real (10$\bar{1}$15) surface shows significant step bunching.

In 950 mbar syngas (H_2/CO = 2:1), the STM images at room temperature [Figure 3a] and also at the reaction temperature of 503 K [Figure 3b] show, on a large scale, the same stripe pattern and step bunching as in UHV at room temperature [Figure 2a]. Also on a smaller scale (Figure 4), there are no obvious differences to the morphology of the surface in UHV. On this smaller scale, one can see that most of the step bunches actually consist of rows of parallel lower steps so that the actual step density is higher than apparent on the large-scale images. For example, along the line indicated in Figure 4a, one counts 43 steps, 29 of which are clearly resolved monoatomic steps [the profile is shown in Figure 4b] (an ideal (10$\bar{1}$15) surface would have 57 monosteps). On average over several images, 44% of the steps were resolved as monosteps and 10% as double steps; the rest are multiple steps.

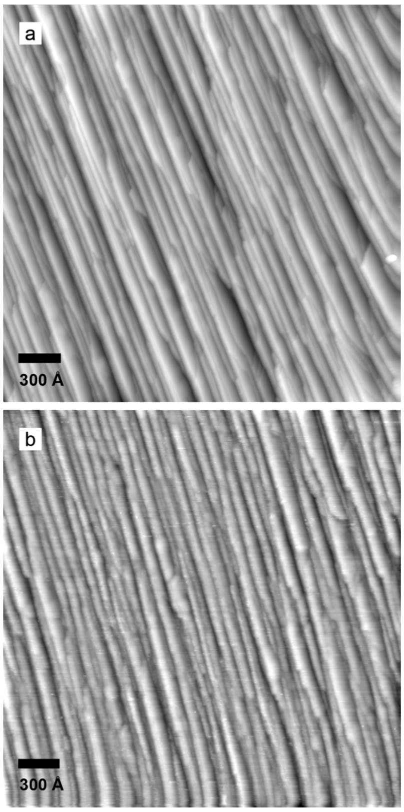

Figure 3. STM images of the Co(10$\bar{1}$15) surface in 950 mbar syngas at H_2/CO = 2:1: (a) at room temperature, V_t = −0.2 V, I_t = 0.7 nA; (b) at 503 K, 3.5 h after starting heating the sample to 503 K, V_t = −0.2 V, I_t = 0.7 nA.

Steps appearing two or more layers high are not necessarily actual double or multisteps but could be closely spaced, unresolved monosteps. The lateral resolution was high enough to image a long-wave moiré structure at room temperature in syngas [the hexagonal pattern on the terraces in Figure 4e], which is formed by a layer of CO molecules on the hexagonally close-packed terraces.[29] However, in the present experiments, two monosteps with a closer distance than ∼6 Å could not be resolved. The data do therefore not discriminate between actual double steps that represent small (10$\bar{1}$1) facets [Figure 5a,d] and two closely spaced monosteps that have one or two atomic rows in between [Figure 5b,c,e,f]. The same applies to higher steps. For this reason, the actual density of steps is probably higher than apparent on the large-scale images. The overall slope of the surface is in good agreement with the ideal value; the height difference of 118 Å across the 935 Å long profile [Figure 4b] corresponds to a tilt angle of 7.2°, quite exactly the value of the ideal (10$\bar{1}$15) surface of 7.1°.

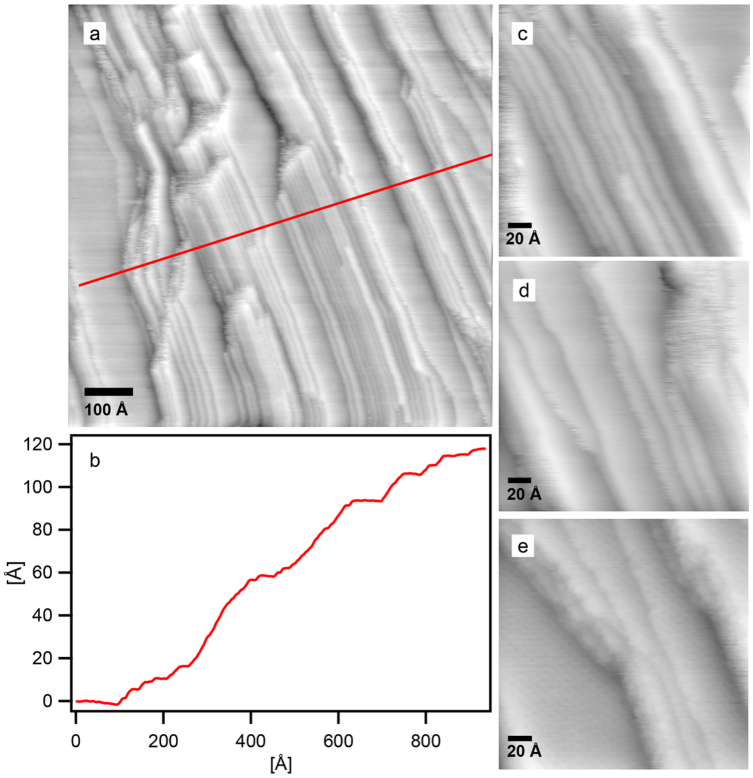

Figure 4. STM images of the Co(10$\bar{1}$15) surface taken in 950 mbar syngas at H_2/CO = 2:1. (a) Large-scale image, recorded 2.5 h after starting the experiment, 503 K, $V_t = -0.2$ V, $I_t = 0.7$ nA. (b) Line profile along the red line indicated in (a). (c) Small-scale image in syngas from a different position, 503 K, $V_t = -0.2$ V, $I_t = 0.7$ nA. (d) Small-scale image in syngas, 503 K, $V_t = -0.2$ V, It = 0.7 nA. (e) Small-scale image, recorded in syngas at room temperature, $V_t = -0.2$ V, $I_t = 0.7$ nA.

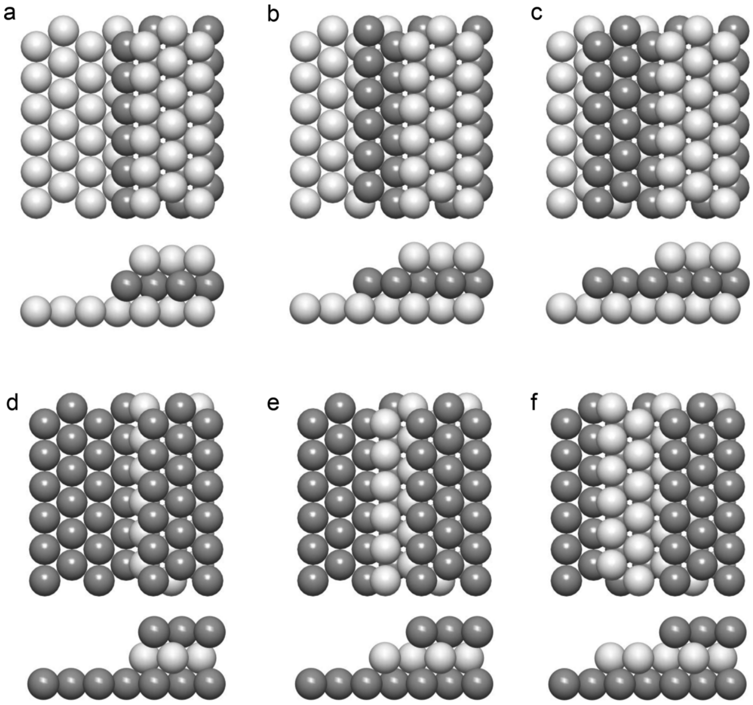

Figure 5. Structure models of double steps. (a) True double step between two B planes. (b, c) Two closely spaced monosteps between two B planes. (d) True double step between two A planes. (e, f) Two closely spaced monosteps between two A planes.

There were no indications that the step bunching was thermodynamically driven. We did not observe any systematic changes of the average morphology over several months of experiments, suggesting that there were no driving forces for the formation of certain facets. A more obvious reason for the step bunching is the restricted ordering kinetics at the relatively low annealing temperature during sample preparation. As mentioned in the Experimental Section, the incompletely annealed surface morphology is an inherent difficulty with Co single crystals. In order not to risk destroying the crystal, no attempts were made to anneal the sample at temperatures higher than ~700 K.

Despite this difficulty, a clear result is that the morphology under reaction conditions was unchanged with respect to the morphology in UHV at room temperature. Moreover, experiments under reaction conditions in which images could be recorded over longer time periods at the same position on the surface did not show any signs of roughening or formations of new terraces (Movie S1, recorded over a time period of 1.75 h). This fact also rules out effects of traces of sulfur that lead to pronounced morphology changes, as reported previously.[30] Sulfur poisoning would additionally have been connected with the formation of ordered structures that were not observed here, and no sulfur was detected by XPS after the experiments. The only structural effects observed here were the characteristic fringed steps in smaller-scale STM images [Figure 4c,d]. These fringes represent fast fluctuations on the time scale of the raster scanning which are caused by site exchanges of Co atoms at the steps edges, a known effect from metal surfaces and similarly observed in previous studies on Co(0001).[1,22] It indicates that the steps are dynamic and not blocked by reaction products.

3.3. GC Measurements. Figure 6a shows examples of gas chromatograms recorded during a reaction experiment under 950 mbar syngas and at a sample temperature of 503 K. The reaction ran for 6 h, a typical duration of the activity experiments, and gas samples were extracted every hour. The chromatograms show peaks from CH_4, C_2H_4, C_2H_6, C_3H_6, C_3H_8, C_4H_8, and C_4H_{10}, with decreasing concentrations from methane to the C_4 hydrocarbons. The fact that the concentrations of olefins are higher than those of the respective paraffins has similarly been reported before for the fraction of short hydrocarbons formed in the Fischer−Tropsch synthesis.[1,7−9,31] For the relatively low pressure applied here, this has been explained by the fact that the primarily formed olefins have to readsorb on the surface to become hydrogenated to give paraffins.[31] Because short hydrocarbons are only weakly held on the surface, their lifetime is too short for major hydrogenation.

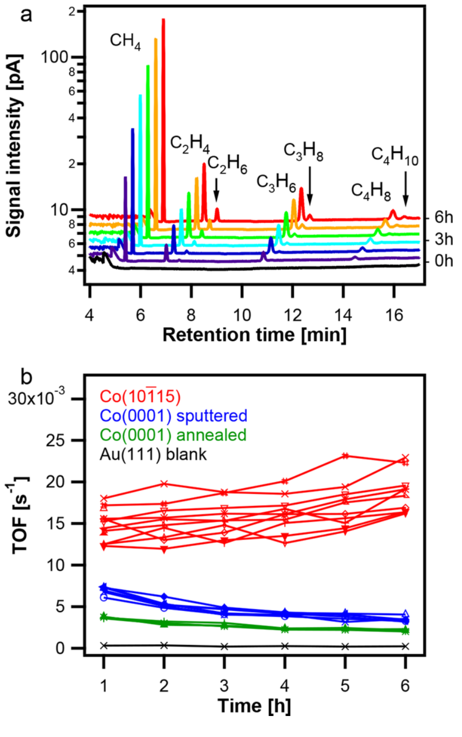

Figure 6. Activity measurements by GC. (a) Chromatograms taken every hour during a reaction experiment with the $\mathrm{Co}(10\bar{1}15)$ sample at a total syngas pressure of 950 mbar, $H_2/CO = 2:1$, 503 K. For clarity, the chromatograms are displaced with respect to each other along the x and y axes. (b) CO-based TOFs, plotted as functions of time, from 10 experiments with the $\mathrm{Co}(10\bar{1}15)$ sample (red), 6 experiments with the sputtered Co(0001) sample (blue), and 4 experiments with the annealed Co(0001) sample (green). The black data points are from a blank experiment with a Au(111) sample, performed at the same pressure and temperature.

The peaks in Figure 6a increase with time because of the batch conditions of the experiment. From the increases per hour and by utilizing the calibrated GC sensitivity together with the volume of the reaction chamber, the sample surface area, and the lattice constant of Co, TOFs of the individual hydrocarbon products per Co surface atom were evaluated.[28] These product-based TOFs were then multiplied by the respective numbers of C atoms and added up to give CO-conversion-based TOFs. The results from 10 such experiments, in units of converted CO molecules per Co surface atom per second, are plotted in Figure 6b as functions of time (red lines). One can see that the TOFs scatter around an initial average value of $15 \pm 1.8 \times 10^{-3}\ \mathrm{s}^{-1}$ and increase with time to a final average value of $19 \pm 2.3 \times 10^{-3}\ \mathrm{s}^{-1}$. The scatter of the data is most likely caused by small temperature variations, resulting from the fact that the thermal contact of the sample/sample holder unit to the mounting assembly varied somewhat between experiments (the sample had to be transferred from the preparation chamber to the reaction cell for each experiment). These variations in position were stronger for the $\mathrm{Co}(10\bar{1}15)$ than for the Co(0001) sample. Moreover, because an error in temperature leads to an error in the relative TOFs, the scatter of the data from the stepped surface, which has the highest TOFs, is more pronounced than that from the other sample.

The figure also shows the TOFs from four experiments with the Co(0001) sample in which the surface had been prepared by the standard method including a final annealing step (green), and six experiments in which the Co(0001) sample had been sputtered in a final step (blue). The sputtered Co(0001) sample was more active than the annealed surface, an effect we have analyzed before and which could be attributed to the higher density of steps created by the sputtering.[1] However, in all experiments and irrespective of the scatter of the data, the activity of the $(10\bar{1}15)$ sample significantly exceeded the activities of the annealed and of the sputtered Co(0001) sample.

The TOFs from the annealed Co(0001) surface [Figure 6b, green curves] slightly decreased with time, indicating some deactivation processes. The TOFs from the sputtered surface (blue curves) decreased more strongly which, as has been shown previously, was correlated with the time-dependent smoothing of the sputtered surface.[1] By contrast, the activity of the $(10\bar{1}15)$ sample (red curves) even showed a weak increase with time, reasons for which are unclear at present. As already mentioned, the STM did not show any systematic changes with time so that morphology effects are unlikely. The same holds for possible effects of Ni contaminants, as the TOFs were independent of the residual amount of Ni. One might speculate about a clean-up reaction that was removing carbon or oxygen contaminants deposited on the surface at the beginning of the experiments when the reaction cell was filled with syngas and the sample was still at room temperature.

From the GC data, an Anderson−Schulz−Flory (ASF) plot was prepared, the standard way of displaying product distributions in Fischer−Tropsch experiments (Figure 7).[32]

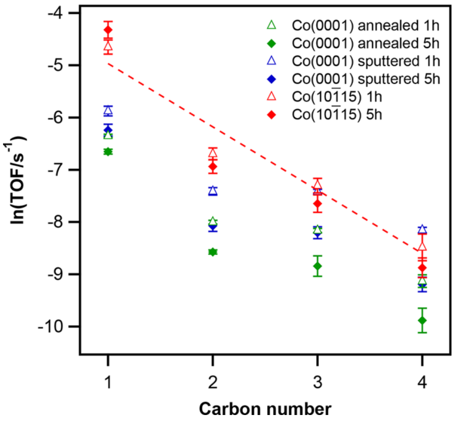

Figure 7. ASF plot of activity data from the Co single crystals. Data points are product-based TOFs from experiments with the Co(10$\bar{1}$15) sample and with the sputtered and annealed Co(0001) samples, respectively. Each data point is an average over 10, 6, and 4 measurements, respectively, and the TOFs of the olefinic and paraffinic hydrocarbons are added. The time instants at which the GCs were taken are indicated. A linear regression line that fits the Co(10$\bar{1}$15)/1 h data points is shown.

The plot shows the logarithmic, averaged TOFs of the individual hydrocarbons (olefins and paraffins added), and measured at two different time instants from the (10$\bar{1}$15) sample. It also includes the data from the annealed and from the sputtered Co(0001) sample. The dashed red line is a linear regression to the data from Co(10$\bar{1}$15) after 1 h. In all cases, the plots show a roughly linear decrease with chain length. However, as one can see for the Co(10$\bar{1}$15)/1 h data, the value for methane is higher than the linear regression line and the value for ethylene/ethane is lower. The other data show similar deviations. Such distributions, including the deviations of the C_1 and C_2 hydrocarbons, are characteristic for the Fischer−Tropsch synthesis under laboratory conditions.[1,7−9] The only systematic differences of the data from the (10$\bar{1}$15) sample with respect to those from the Co(0001) samples are shifts to higher values. However, the shifts of all products are similar (except for the C_4 hydrocarbons for which the absolute values are low), meaning that the product distributions were more or less the same for all samples. This result indicates that, qualitatively, the processes were the same on all investigated surfaces.

3.4. XPS Measurements. Examples of XP spectra, recorded before and after the reaction experiments, are shown in Figure 8. The extensively prepared (10$\bar{1}$15) sample did not show any intensity in the C 1s and O 1s spectral regions, indicating a clean surface. During series of reaction experiments, when the sample had undergone one preparation cycle, the XP spectra usually showed a small carbide signal, close to the XPS detection limit. After 6 h in syngas at 503 K, the C 1s region showed three peaks and the O 1s region one peak. The C 1s peak at 283.2 eV can be attributed to atomic carbon (0.14 ML), the peak at 284.3 eV to hydrocarbon moieties (0.32 ML), and the peak at 285.9 eV to adsorbed CO (0.27 ML). The O 1s peak at 531.9 eV can also mainly be attributed to adsorbed CO (0.29 ML). The spectra from the sputtered and the annealed Co(0001) surfaces showed similar C 1s peaks at 283.2 and 285.9 eV and an O 1s peak at 531.9 eV, whereas the 284.3 eV C 1 s peak was lower for the sputtered and yet lower for the annealed Co(0001) surface. Similar spectra were recorded after all reaction experiments. Spectra of the Co 2p region as well as survey spectra taken before and after a reaction experiment are shown in the Supporting Information (Figure S1).

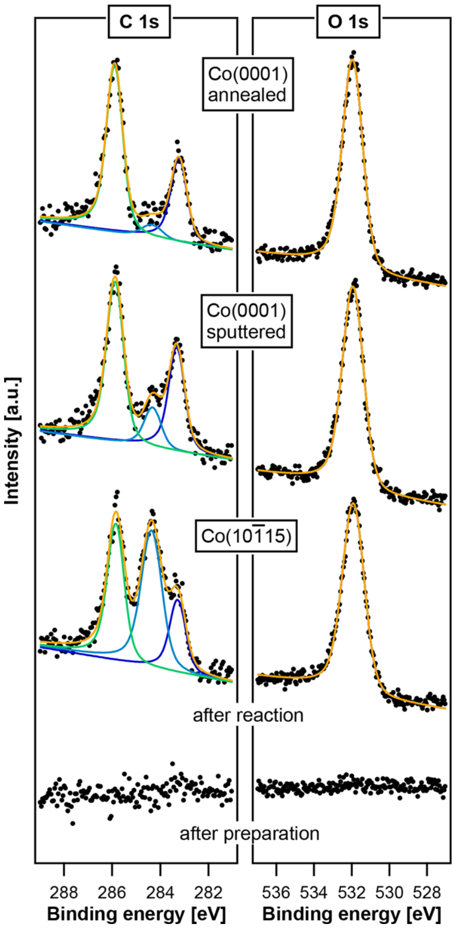

Figure 8. XP spectra of the C 1s and O 1s regions. The bottom spectra were recorded on the Co(10$\bar{1}$15) sample after preparation in UHV; the other spectra after 6 h reaction experiments in 950 mbar syngas, H_2/CO = 2:1, 503 K.

Because the XP spectra were recorded *ex situ*, their informative value about the composition of the surface layer during reaction is limited. The higher amounts of hydrocarbon moieties on the (10$\bar{1}$15) than on the Co(0001) sample may be caused by a higher coverage of intermediates during the reaction but may also result from readsorption of hydrocarbon molecules after the reaction when the sample cooled down in the reaction gas mixture.

However, a clear result is that even on the (10$\bar{1}$15) surface the coverages of the individual carbon and oxygen species were all lower than one ML. During reaction, the coverages of the atomic carbon and hydrocarbon species were probably even lower than measured by XPS because of the unavoidable readsorption processes at the end of the experiments. Only CO might have partially desorbed during sample transfer to the UHV chamber so that the measured CO coverages were probably lower than those in the syngas atmosphere. The Co $2p_{3/2}$ peak after reaction experiments was indistinguishable from the Co $2p_{3/2}$ peak of the UHV-cleaned metallic Co (Figure S1). It can be concluded that the surface during the reaction was not covered by a thick layer of Co carbide or oxide but remained metallic and was only covered by a sub-ML of adsorbed molecules. This fact is consistent with near-ambient pressure XPS data at similar temperatures.[33] It also agrees with the *in situ* STM data that showed an unchanged structure with respect to UHV. The fact that the adsorption layer was not resolved by STM results from the high mobility of the adsorbed particles at 503 K; we have not detected any structures similar to those in ref 34 that have been explained by a layer of adsorbed hydrocarbon molecules.

4. DISCUSSION

The data show a distinctly enhanced activity of the (10$\bar{1}$15) surface with respect to the Co(0001) surface but otherwise no obvious differences. Like in the case of the Co(0001) surface, the surface morphology in syngas remained the same as in UHV, the composition of the products was more or less the same, and the surface remained metallic. This indicates that the higher activity is primarily a consequence of a higher density of active sites.

To examine whether these active sites are formed by atomic steps, we constructed a plot of the CO-based TOF data as a function of the densities of step atoms (Figure 9). For the (10$\bar{1}$15) surface, we used the nominal density of step atoms of 2.4 nm^{-2} of the ideal Co(10$\bar{1}$15) surface (red data points). The step bunches in the STM images were thus counted as series of monosteps. For multistep geometries as those shown in Figure 5b,c,e,f, this can be justified by the local character of the dissociation of the CO molecules. It should not make a major difference whether the molecules dissociate at an ideal monostep with broad terraces on both sides, or at a monostep where one or both of the terraces are only one or two atoms wide. The same holds for other chemical processes at the steps. True multisteps [Figure 5a,d] may be different in this respect so that the concentration of these steps constitutes a residual uncertainty. For control, step lengths were determined in a few STM images that contained coherent areas with clearly resolved monosteps. With the Co lattice constant of 2.507 Å along the close-packed direction of the steps, a step atom density of 2.4 ± 0.2 nm^{-2}, was obtained, in agreement with the ideal value. The step atom densities of the annealed and of the sputtered Co(0001) surface, which we here used for comparison of the data, were adopted from ref 1 (green and blue data points). For the sputtered Co(0001) surface, three data points were available because the steps created by sputtering decreased by a measurable degree during an experimental run.[1]

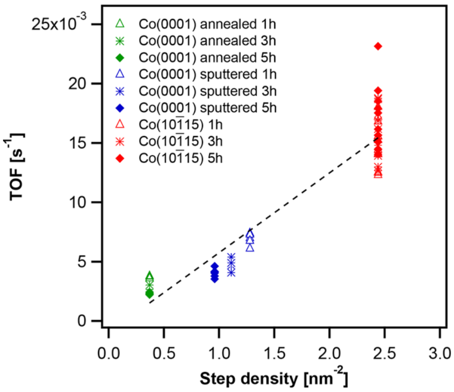

Figure 9. Plot of the CO-based TOFs vs step densities of the Co single crystals. Data from the annealed Co(0001) sample (green), from the sputtered Co(0001) sample (blue), and from the Co(10$\bar{1}$15) sample (red). The time instants are indicated.

Figure 9 shows that the activity scales with the density of step atoms, and a linear regression line (dashed) gives an acceptable fit. An approximately linear scaling has been observed before for the Co(0001) surface,[1] but with the data from the Co(10$\bar{1}$15) sample, the range where this correlation holds is expanded by a factor of 2. It can be concluded that steps are also the active sites on the Co(10$\bar{1}$15) surface.

Following an old claim how to report catalytic turnover frequencies,[35] these results can be used to evaluate TOFs in units of converted CO molecules per active site instead of the usual units of converted CO molecules per surface atom. With the step atom densities of the annealed Co(0001) surface, of the sputtered Co(0001) surface after 1, 3, and 5 h, and of the Co(10$\bar{1}$15) surface and the respective average TOFs, values of $1.4 \pm 0.3 \times 10^{-1}$, $1.00 \pm 0.06 \times 10^{-1}$, $0.73 \pm 0.06 \times 10^{-1}$, $0.73 \pm 0.07 \times 10^{-1}$, and $1.2 \pm 0.2 \times 10^{-1}\ \mathrm{s}^{-1}$, respectively, are obtained. The average is equal to 0.1 s^{-1}. The variations around this value reflect the same error as the deviations of the data points from the regression line in Figure 9. Considering the fact that different samples and sample states were analyzed, these variations are moderate so that the active site-referenced TOFs are comparable.

With the active sites identified for the Co(10$\bar{1}$15) sample, an attempt was made to relate the activity of this surface to literature data of supported Co catalysts. To obtain densities of step atoms for these systems, we used the fact that the Co nanoparticles of supported catalysts are to a considerable fraction fcc-packed, in contrast to the hcp-packing of bulk Co.[36] fcc-packed Co nanoparticles form relatively well-defined, rounded off cubo-octahedra that, according to recent *in situ* TEM experiments and calculations of the surface free energy, are stable in syngas at the reaction temperature.[37] The atomic structure of such particles has been investigated by simulations that also provided densities of step sites.[16] It was shown that the density first increases with particle size and then saturates at a particle diameter of ∼8 nm, as already mentioned in the Introduction section. The simulations discriminated between different local geometries of the step sites, namely, B_5-A sites with a local (100) configuration, B_5-B sites with a local (111) configuration, and kink sites.[16] For 8 nm particles, the obtained fractions with respect to all surface sites were 5.3% B_5-A sites, 6.7% B_5-B sites, and 5.0% kink sites; 65% of the surface sites were regular (111) sites, and 18% of the surface sites were regular (100) sites. From these percentages, we evaluated an area-based step density $\varrho_{\text{step atoms}}$

$$\varrho_{\text{step atoms}} = N_{\text{step atoms}}/A_{\text{surface}}$$

where $N_{\text{step atoms}} = N_{\text{B5-A}} + N_{\text{B5-B}} + N_{\text{kink}}$ is the total number of step sites. A_{surface} is the total surface area of a particle which is given by

$$A_{\text{surface}} = N_{(111)}A_{(111)} + N_{(100)}A_{(100)} + N_{\text{step atoms}}A_{\text{step site}}$$

$N_{(111)}$ and $N_{(100)}$ are the numbers of (111) and (100) unit cells, respectively; $A_{(111)}$ and $A_{(100)}$ are the respective unit cell areas; and $A_{\text{step site}}$ is the average area of a step site; $A_{(111)}$ and $A_{(100)}$ are crystallographically known, and we set $A_{\text{step site}}$ equal to $A_{(111)}$ for simplicity (the related error is low). Dividing all terms in the resulting expression by the total number of surface atoms, N_{surface}, and using the percentages from the simulations gives $\varrho_{\text{step atoms}} = 3.0\ \text{nm}^{-2}$, which is close to the step density of 2.4 nm^{-2} of the ideal $\mathrm{Co}(10\bar{1}15)$ sample. Because 3.0 nm^{-2} represented a saturation value, we can assume that this agreement remains valid also for somewhat larger particles.

It has also been mentioned in the Introduction section that several experimental studies showed that the activities of particles larger than 8 nm were constant, even up to 140 nm in one study.[10−13] For the analysis, we therefore included all investigations we could find that used particles with diameters between 8 and 140 nm and that report TOFs in units of converted CO molecules per surface atom per second. Most of these measurements were performed with particles smaller than 20 nm, namely, 44% with 8−13 nm, 21% with 13−18 nm particles. In cases where percent dispersions (%D) are given, we converted these into particle diameters (d) by the approximation $d = 97$ nm/%D for spherical Co particles (adapted from ref 38). TOFs measured at other temperatures and partial pressures than in our experiments we converted to our parameters [$T = 503$ K, $p(\mathrm{H_2}) = 0.63$ bar, $p(\mathrm{CO}) = 0.32$ bar] using the power law equation $\text{TOF} = kp(\mathrm{H_2})^{0.7}\ p(\mathrm{CO})^{-0.2}$, which has been shown to be a good description of the kinetics[39]

$$\text{TOF}_{\text{corr}} = \exp\left[-\frac{E_{\text{a}}}{R}\left(\frac{1}{503\ \text{K}} - \frac{1}{T}\right)\right]\left(\frac{0.63\ \text{bar}}{p(\mathrm{H_2})}\right)^{0.7}\left(\frac{0.32\ \text{bar}}{p(\mathrm{CO})}\right)^{-0.2}\text{TOF}$$

where E_{a} is the activation energy and R is the gas constant; for E_{a}, we used an average value of 100 kJ mol^{-1} from several published data.[39]

The statistics of the resulting TOF_{corr} values, extracted from 179 measurements in 49 studies is shown in Figure 10. A list of the values with the corresponding references is given in Table S1. As expected, the distribution has a considerable width. It is clear that there are several effects that influence the activity and are not included in the basic surface structure-based picture we use here. Effects leading to major deviations are probably the varying interactions of the Co particles with the different supports, the fact that certainly not all Co particles of a real catalyst are fcc-packed nanocrystals with an equilibrium shape, and that, at higher pressures, a liquid hydrocarbon film and restricted pore diffusion may slow down the kinetics. Furthermore, the methods to determine the surface areas of the particles (and thus the TOFs) have usually been relatively indirect, and the power law we have used to correct the temperatures and pressures is not precise over a wider parameter range.[40] Nevertheless, 70% of the reported TOF_{corr} values vary around a constricted range up to $32 \times 10^{-3}\ \text{s}^{-1}$.

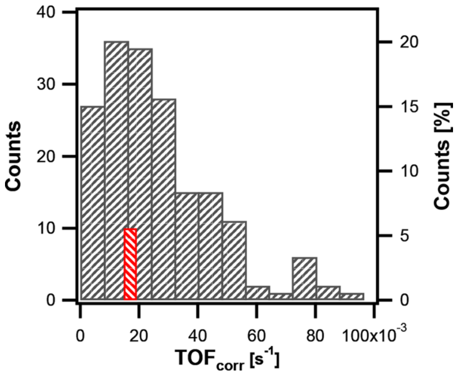

Figure 10. Statistics of Fischer−Tropsch activity data of supported Co catalysts from the literature and comparison with data from the $\mathrm{Co}(10\bar{1}15)$ sample. Gray bars indicate the numbers of measurements from the literature. Only those measurements were included in which the diameters of the Co particles were between 8 and 140 nm. The numbers of measurements are plotted vs the reported TOFs corrected for our temperature and pressure parameters. The TOF_{corr} step width of $8 \times 10^{-3}\ \text{s}^{-1}$ is arbitrary, but other reasonable widths give similar distributions. The red bar indicates the averaged TOFs measured with the $\mathrm{Co}(10\bar{1}15)$ sample; the width is given by the difference between the TOFs after 1 h and 6 h. For a list of all literature values used, see Table S1.

The average TOFs from the $(10\bar{1}15)$ surface, $15 \times 10^{-3}\ \text{s}^{-1}$ after 1 h and $19 \times 10^{-3}\ \text{s}^{-1}$ after 6 h, are in this range (Figure 10, red bar). It can be concluded that the $(10\bar{1}15)$ surface is, in fact, able to bridge the materials gap to the Co catalysts at the onset of the constant-activity plateau. The hypothesis that steps are the active sites also on the supported catalysts has thus been confirmed. On supported catalysts, additional effects do certainly play a role and may shift the activity to higher or lower values, but the dominating factor is the activity of the steps.

Why the activity of supported catalysts remains constant over such a large range of particle diameters beyond ∼8 nm is a more difficult question to answer. The maximum in the step site density-vs-particle diameter function might be broad but eventually the step density and consequently the TOF should decrease as the particles get larger.[14,41] To explain the constant activity, it has been suggested that Co surfaces roughen under reaction conditions so that the concentration of step sites on the particles remains constant.[42−44] However, this explanation is not confirmed by the present *in situ*/*operando* STM experiments at 950 mbar on the $(10\bar{1}15)$ surface. The data do not show any signs of roughening or of other structure changes under reaction conditions. Of course, we cannot exclude a roughening at higher syngas pressures. However, the constant-activity plateau of the supported catalysts reported in the literature was not restricted to higher pressures but was also observed at 1 bar.[10]

We propose instead that the constant activity is a result of the morphology of the particles. The mentioned atomic structure simulations showed that the surface morphology of Co particles up to a diameter of 8 nm is not given by the Wulff construction, a concept based on macroscopic surface energies. The particles are more compact, and their shapes are somewhere between actual spheres and the polyhedra predicted by the Wulff construction.[16] When such particles get larger but still follow this trend, an increase in particle size has to lead to additional terraces on the Wulff facets. In this way, additional steps are created. The number of step sites relative to the number of surface atoms and the density of active sites could therefore remain constant over a wider range of particle diameters.

5. CONCLUSIONS

In situ/operando STM experiments on the Fischer−Tropsch synthesis have been performed on a Co(10$\bar{1}$15) sample at a syngas pressure of 950 mbar and a temperature of 503 K. With the same sample and under the same conditions, the catalytic activity with respect to C_1 to C_4 hydrocarbons has been measured by GC, and reference experiments have been performed with a Co(0001) sample. Control experiments by XPS showed that the surfaces stay metallic under reaction conditions and are only covered by adsorbed atoms and molecules. Three main conclusions can be drawn from these combined experiments:

(i) The activity scales approximately linearly with the step density. This correlation remains valid over a considerably wider range than analyzed previously. The range has been extended by a factor of 2 with respect to the range of data from an annealed and a sputtered Co(0001) surface. This result strongly supports the hypothesis that atomic steps are the active sites for the Fischer−Tropsch synthesis on Co single-crystal model catalysts.

(ii) The TOFs on the Co(10$\bar{1}$15) surface agree relatively well with most of the TOF data from the literature on supported Co catalysts. The comparison is based on TOF data from supported Co catalysts with particle diameters between 8 and 140 nm and which were corrected for temperature and partial pressure differences. This agreement is consistent with a structure model of the Co nanoparticles of the catalyst according to which the particles form compact, fcc-packed cubo-octrahedra that have a similar density of atomic steps as the Co(10$\bar{1}$15) surface. The data from the Co(10$\bar{1}$15) model catalyst therefore confirm, in a quantitative way, the hypothesis that atomic steps are also the active sites on the Co particles of supported Fischer−Tropsch catalysts.

(iii) Like the Co(0001) surface in the previous study, the Co(10$\bar{1}$15) surface does not show any signs of roughening under the chosen conditions. The wide maximum in the activity of supported Fischer−Tropsch catalysts vs particle size is therefore most likely not caused by surface roughening. It is proposed instead that it is related to the compact shapes of the Co particles. The density of step sites on the surfaces of such particles and thus the density of active sites can thus be constant over a wide range of particle diameters.

■ ASSOCIATED CONTENT

Supporting Information

The Supporting Information is available free of charge at https://pubs.acs.org/doi/10.1021/acscatal.2c00703.

XP spectra of the Co 2p region and survey scans taken before and after a reaction and table of TOFs of supported Co catalysts from the literature (PDF)

STM images recorded over a time period of 1.75 h under reaction conditions (MOV)

■ AUTHOR INFORMATION

Corresponding Author

Joost Wintterlin − *Department of Chemistry, Ludwig-Maximilians-Universität München, 81377 Munich, Germany; Center for NanoScience, 80799 Munich, Germany;* orcid.org/0000-0002-0636-7538; Email: wintterlin@cup.uni-muenchen.de

Author

Katharina M. Golder − *Department of Chemistry, Ludwig-Maximilians-Universität München, 81377 Munich, Germany;* orcid.org/0000-0002-3100-8609

Complete contact information is available at: https://pubs.acs.org/10.1021/acscatal.2c00703

Author Contributions

K.M.G. performed the experiments and wrote the manuscript. J.W. supervised the project and wrote the manuscript.

Notes

The authors declare no competing financial interest.

■ ACKNOWLEDGMENTS

This study was funded by the Deutsche Forschungsgemeinschaft (DFG, German Research Foundation)—WI 1003/8-1.

■ REFERENCES

(1) Böller, B.; Durner, K. M.; Wintterlin, J. The active sites of a working Fischer−Tropsch catalyst revealed by operando scanning tunnelling microscopy. *Nat. Catal.* **2019**, *2*, 1027−1034.

(2) Bartholomew, C. H.; Farrauto, R. J. *Fundamentals of Industrial Catalytic Processes*, 2nd ed.; Wiley-Interscience: Hoboken, NJ, 2006; pp 398−486.

(3) Reuel, R. C.; Bartholomew, C. H. Effects of support and dispersion on the CO hydrogenation activity/selectivity properties of cobalt. *J. Catal.* **1984**, *85*, 78−88.

(4) Fu, L.; Bartholomew, C. H. Structure sensitivity and its effects on product distribution in CO hydrogenation on cobalt/alumina. *J. Catal.* **1985**, *92*, 376−387.

(5) Johnson, B. G.; Bartholomew, C. H.; Goodman, D. W. The role of surface structure and dispersion in CO hydrogenation on cobalt. *J. Catal.* **1991**, *128*, 231−247.

(6) Bezemer, G. L.; van Laak, A.; van Dillen, A. J.; de Jong, K. P. Cobalt Supported on Carbon Nanofibers—A Promising Novel Fischer-Tropsch Catalyst. In *Studies in Surface Science Catalysis*, Bao, X.; Xu, Y., Eds.; Elsevier, 2004; Vol. *147*, pp 259−264.

(7) Geerlings, J. J. C.; Zonnevylle, M. C.; de Groot, C. P. M. Studies of the Fischer-Tropsch reaction on Co(0001). *Surf. Sci.* **1991**, *241*, 302−314.

(8) Geerlings, J. J. C.; Zonnevylle, M. C.; de Groot, C. P. M. Structure sensitivity of the Fischer-Tropsch reaction on cobalt single crystals. *Surf. Sci.* **1991**, *241*, 315−324.

(9) Beitel, G. A.; de Groot, C. P. M.; Oosterbeek, H.; Wilson, J. H. A Combined in-Situ PM-RAIRS and Kinetic Study of Single-Crystal Cobalt Catalysts under Synthesis Gas at Pressures up to 300 mbar. *J. Phys. Chem. B* **1997**, *101*, 4035−4043.

(10) Bezemer, G. L.; Bitter, J. H.; Kuipers, H. P. C. E.; Oosterbeek, H.; Holewijn, J. E.; Xu, X.; Kapteijn, F.; van Dillen, A. J.; de Jong, K. P. Cobalt Particle Size Effects in the Fischer−Tropsch Reaction Studied with Carbon Nanofiber Supported Catalysts. *J. Am. Chem. Soc.* **2006**, *128*, 3956−3964.

(11) Prieto, G.; Martínez, A.; Concepción, P.; Moreno-Tost, R. Cobalt particle size effects in Fischer−Tropsch synthesis: structural and in situ spectroscopic characterisation on reverse micelle-synthesised Co/ITQ-2 model catalysts. *J. Catal.* **2009**, *266*, 129−144.

(12) den Breejen, J. P.; Radstake, P. B.; Bezemer, G. L.; Bitter, J. H.; Frøseth, V.; Holmen, A.; de Jong, K. P. On the Origin of the Cobalt Particle Size Effects in Fischer−Tropsch Catalysis. *J. Am. Chem. Soc.* **2009**, *131*, 7197−7203.

(13) Xiong, H.; Motchelaho, M. A. M.; Moyo, M.; Jewell, L. L.; Coville, N. J. Correlating the preparation and performance of cobalt catalysts supported on carbon nanotubes and carbon spheres in the Fischer−Tropsch synthesis. *J. Catal.* **2011**, *278*, 26−40.

(14) Van Santen, R. A. Complementary Structure Sensitive and Insensitive Catalytic Relationships. *Acc. Chem. Res.* **2009**, *42*, 57−66.

(15) Gong, X.-Q.; Raval, R.; Hu, P. CO dissociation and O removal on Co(0001): a density functional theory study. *Surf. Sci.* **2004**, *562*, 247−256.

(16) van Helden, P.; Ciobîcă, I. M.; Coetzer, R. L. J. The size-dependent site composition of FCC cobalt nanocrystals. *Catal. Today* **2016**, *261*, 48−59.

(17) Fischer, F.; Tropsch, H. Die Erdölsynthese bei gewöhnlichem Druck aus den Vergasungsprodukten der Kohlen. *Brennst. Chem.* **1926**, *7*, 97−104.

(18) van Santen, R. A.; Markvoort, A. J.; Filot, I. A. W.; Ghouri, M. M.; Hensen, E. J. M. Mechanism and microkinetics of the Fischer−Tropsch reaction. *Phys. Chem. Chem. Phys.* **2013**, *15*, 17038−17063.

(19) Qi, Y.; Yang, J.; Chen, D.; Holmen, A. Recent Progresses in Understanding of Co-Based Fischer−Tropsch Catalysis by Means of Transient Kinetic Studies and Theoretical Analysis. *Catal. Lett.* **2015**, *145*, 145−161.

(20) Liu, J.-X.; Su, H.-Y.; Sun, D.-P.; Zhang, B.-Y.; Li, W.-X. Crystallographic Dependence of CO Activation on Cobalt Catalysts: HCP versus FCC. *J. Am. Chem. Soc.* **2013**, *135*, 16284−16287.

(21) Petersen, M. A.; van den Berg, J.-A.; Ciobîcă, I. M.; van Helden, P. Revisiting CO Activation on Co Catalysts: Impact of Step and Kink Sites from DFT. *ACS Catal.* **2017**, *7*, 1984−1992.

(22) Ehrensperger, M.; Wintterlin, J. In situ high-pressure high-temperature scanning tunneling microscopy of a Co(0001) Fischer−Tropsch model catalyst. *J. Catal.* **2014**, *319*, 274−282.

(23) Weststrate, C. J.; van Helden, P.; van de Loosdrecht, J.; Niemantsverdriet, J. W. Elementary steps in Fischer−Tropsch synthesis: CO bond scission, CO oxidation and surface carbiding on Co(0001). *Surf. Sci.* **2016**, *648*, 60−66.

(24) Weststrate, C. J.; Mahmoodinia, M.; Farstad, M. H.; Svenum, I.-H.; Strømsheim, M. D.; Niemantsverdriet, J. W.; Venvik, H. J. Interaction of hydrogen with flat (0001) and corrugated (11−20) and (10−12) cobalt surfaces: Insights from experiment and theory. *Catal. Today* **2020**, *342*, 124−130.

(25) Zijlstra, B.; Broos, R. J. P.; Chen, W.; Bezemer, G. L.; Filot, I. A. W.; Hensen, E. J. M. The Vital Role of Step-Edge Sites for Both CO Activation and Chain Growth on Cobalt Fischer−Tropsch Catalysts Revealed through First-Principles-Based Microkinetic Modeling Including Lateral Interactions. *ACS Catal.* **2020**, *10*, 9376−9400.

(26) Rößler, M.; Geng, P.; Wintterlin, J. A high-pressure scanning tunneling microscope for studying heterogeneous catalysis. *Rev. Sci. Instrum.* **2005**, *76*, No. 023705.

(27) Salmeron, M.; Eren, B. High-Pressure Scanning Tunneling Microscopy. *Chem. Rev.* **2021**, *121*, 962−1006.

(28) Golder, K. M.; Böller, B.; Stienen, G.; Sickerling, J.; Wintterlin, J. A highly sensitive gas chromatograph for in situ and operando experiments on catalytic reactions. *Rev. Sci. Instrum.* **2021**, *92*, No. 124103.

(29) Böller, B.; Zeller, P.; Günther, S.; Wintterlin, J. High-Pressure CO Phases on Co(0001) and Their Possible Role in the Fischer−Tropsch Synthesis. *ACS Catal.* **2020**, *10*, 12156−12166.

(30) Ehrensperger, M.; Wintterlin, J. In situ scanning tunneling microscopy of the poisoning of a Co(0001) Fischer−Tropsch model catalyst by sulfur. *J. Catal.* **2015**, *329*, 49−56.

(31) Kuipers, E. W.; Vinkenburg, I. H.; Oosterbeek, H. Chain Length Dependence of α-Olefin Readsorption in Fischer-Tropsch Synthesis. *J. Catal.* **1995**, *152*, 137−146.

(32) Eilers, J.; Posthuma, S. A.; Sie, S. T. The shell middle distillate synthesis process (SMDS). *Catal. Lett.* **1990**, *7*, 253−269.

(33) Wu, C. H.; Eren, B.; Bluhm, H.; Salmeron, M. B. Ambient-Pressure X-ray Photoelectron Spectroscopy Study of Cobalt Foil Model Catalyst under CO, H2, and Their Mixtures. *ACS Catal.* **2017**, *7*, 1150−1157.

(34) Navarro, V.; van Spronsen, M. A.; Frenken, J. W. M. In situ observation of self-assembled hydrocarbon Fischer−Tropsch products on a cobalt catalyst. *Nat. Chem.* **2016**, *8*, 929−934.

(35) Boudart, M. Turnover rates in heterogeneous catalysis. *Chem. Rev.* **1995**, *95*, 661−666.

(36) Kitakami, O.; Sato, H.; Shimada, Y.; Sato, F.; Tanaka, M. Size effect on the crystal phase of cobalt fine particles. *Phys. Rev. B* **1997**, *56*, 13849−13854.

(37) De Vrieze, J. E.; Bremmer, G. M.; Aly, M.; Navarro, V.; Thybaut, J. W.; Kooyman, P. J.; Saeys, M. Shape of Cobalt and Platinum Nanoparticles Under a CO Atmosphere: A Combined In Situ TEM and Computational Catalysis Study. *ACS Catal.* **2019**, *9*, 7449−7456.

(38) Reuel, R. C.; Bartholomew, C. H. The stoichiometries of H2 and CO adsorptions on cobalt: Effects of support and preparation. *J. Catal.* **1984**, *85*, 63−77.

(39) Ribeiro, F. H.; Schach Von Wittenau, A. E.; Bartholomew, C. H.; Somorjai, G. A. Reproducibility of Turnover Rates in Heterogeneous Metal Catalysis: Compilation of Data and Guidelines for Data Analysis. *Cat. Rev.* **1997**, *39*, 49−76.

(40) Keyvanloo, K.; Lanham, S. J.; Hecker, W. C. Kinetics of Fischer-Tropsch synthesis on supported cobalt: Effect of temperature on CO and H2 partial pressure dependencies. *Catal. Today* **2016**, *270*, 9−18.

(41) Van Hardeveld, R.; Hartog, F. The statistics of surface atoms and surface sites on metal crystals. *Surf. Sci.* **1969**, *15*, 189−230.

(42) Wilson, J.; de Groot, C. Atomic-Scale Restructuring in High-Pressure Catalysis. *J. Phys. Chem. A* **1995**, *99*, 7860−7866.

(43) Zhang, X.-Q.; van Santen, R. A.; Hensen, E. J. M. Carbon-Induced Surface Transformations of Cobalt. *ACS Catal.* **2015**, *5*, 596−601.

(44) Banerjee, A.; Navarro, V.; Frenken, J. W. M.; van Bavel, A. P.; Kuipers, H. P. C. E.; Saeys, M. Shape and Size of Cobalt Nanoislands Formed Spontaneously on Cobalt Terraces during Fischer−Tropsch Synthesis. *J. Phys. Chem. Lett.* **2016**, *7*, 1996−2001.

4.2.2 Correction of Activity Data

Follow-up experiments showed that the published temperatures were partially incorrect. One error was caused by an erroneously corrected cross-fall between the two thermocouple inputs of the two-channel meter. A second error resulted from small variations in the glass fiber-to-sample distance when the simplified setup or the complete setup with the installed STM was used.

As a consequence, all temperatures of the Co(0001) sample, given in the *ACS Catalysis* article, and most temperatures of the Co($10\bar{1}15$) crystal were lower than given. For correction, the TOFs of the Co(0001) crystal were upscaled to compare them to those of the Co($10\bar{1}15$) crystal. A scaling factor was determined in reference experiments at higher temperatures. Additionally, only experiments performed with the simplified setup were included in the corrected version. The conclusion that the activity scales with the step density of the crystals and that, therefore, the steps must be the active sites remains unaffected.

In the following, the correction to the previous article "Correction to '*In Situ/Operando* STM of the Fischer-Tropsch Synthesis on a Co($10\bar{1}15$) Surface – A Study to Bridge the Materials Gap between Single-Crystal Models and Supported Catalysts'" published in *ACS catalysis* is reproduced with permission from *ACS Catal.* **2022**, *12*, 10560–10561. Copyright © 2022 The Authors. Published by American Chemical Society.

ACS Catalysis
pubs.acs.org/acscatalysis Correction

Correction to “*In Situ/Operando* STM of the Fischer–Tropsch Synthesis on a $Co(10\bar{1}15)$ Surface—A Study to Bridge the Materials Gap between Single-Crystal Models and Supported Catalysts”

Katharina M. Golder and Joost Wintterlin*

ACS Catal. **2022**, *12* (12), 7199–7209. DOI: 10.1021/acscatal.2c00703

Cite This: *ACS Catal.* 2022, 12, 10560−10561

In follow-up experiments we found that the temperatures in parts of the reaction experiments were lower than given in the publication. As described in the Experimental Section of the publication, temperatures were measured with thermocouple wires at the backsides of the samples. Temperature differences between the backsides and the polished and prepared frontsides were determined by calibration experiments using second pairs of thermocouple wires mounted to the frontsides. However, we found that the calibration factors were partially incorrect. Corrections are required that mainly affect the data of the Co(0001) sample used for reference purposes.

In the experiments with the $Co(10\bar{1}15)$ sample, the actual temperature was 501 K, ~2 K lower than given in the paper, which is within the error margins. However, for a subset of measurements, the precise calibration factors were uncertain. In the corrected Figures 6b and 9 (shown below) we therefore only include those measurements in which the calibration factor was certain (for both crystals). The time evolutions and distributions of the activities of the $Co(10\bar{1}15)$ sample are not significantly affected by this change (corrected Figures 6b and 9, red data points).

In the reference experiments with the Co(0001) sample, the actual temperature was 482 K, ~20 K lower than given in the paper, which is beyond the error margins. However, we can upscale the activities to 501 K, the temperature of the $Co(10\bar{1}15)$ experiments, by means of (shorter) measurements with the Co(0001) sample actually performed at 501 K within the same set of experiments. The resulting scaling factor is 1.59. A second set of experiments was performed after the setup of the Co(0001) sample had been changed. The scaling factor evaluated from those experiments (2.64) is therefore less reliable. However, we can use it to estimate error margins of the correction.

Figure 6b, which has been corrected by the scaling factor 1.59, shows upshifted activities of the sputtered and the annealed Co(0001) sample (blue and green data points, respectively). The time evolutions are unchanged. The corrected Figure 9 indicates the spreads from the two scaling factors as error bars on the data from the Co(0001) sample. Irrespective of these errors, the main result that the activity increases with the step density remains unaffected.

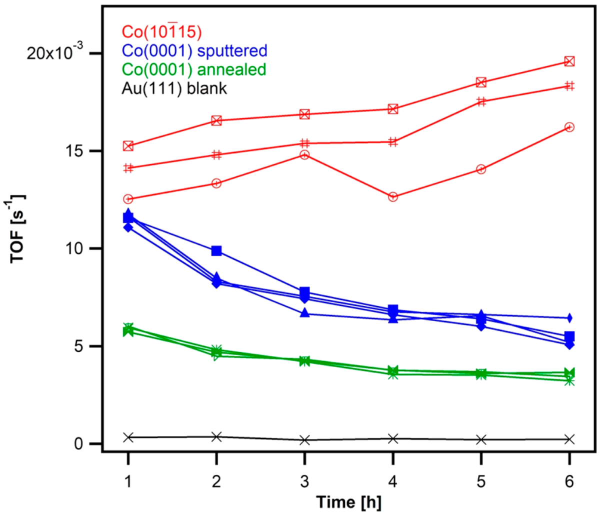

Figure 6b. CO-based TOFs as functions of time. Total pressure 950 mbar, $H_2/CO = 2:1$. Red: three experiments with the $Co(10\bar{1}15)$ sample at 501 K. Blue: four experiments with the sputtered Co(0001) sample at 482 K. Green: three experiments with the annealed Co(0001) sample at 482 K. The TOFs from the Co(0001) sample have been upscaled by a correction factor of 1.59 to make them comparable to the $Co(10\bar{1}15)$ data at 501 K. Black: blank experiment with a Au(111) sample, adopted from the original figure without change.

Two facts change. First, the linear regression line no longer intersects the origin (corrected Figure 9). Actually, this is not unexpected as a similar offset on the y axis has previously been seen in activity data of Co(0001) alone (ref 1 of the publication). It had been explained by a finite activity of the crystal rim, and we here explain it in the same way. Second, the activity of the sputtered Co(0001) sample after 1 h (corrected Figure 9, blue

https://doi.org/10.1021/acscatal.2c03712
ACS Catal. 2022, 12, 10560−10561

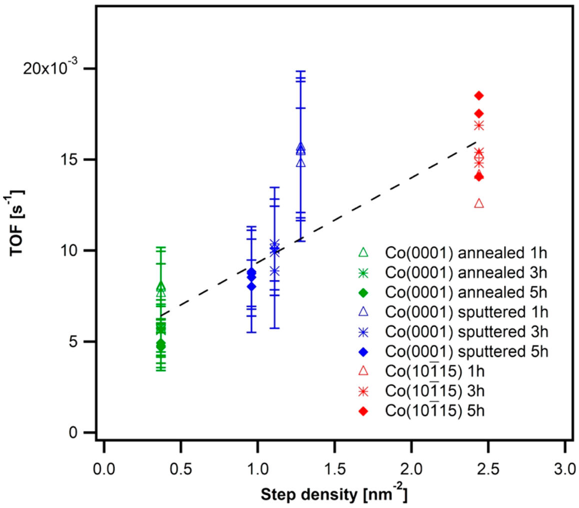

Figure 9. Plot of the CO-based TOFs vs step densities of the Co single crystals. The bars at the data from the Co(0001) sample indicate the spreads from the application of the two scaling factors. The linear regression line (black) was calculated from the activity values of the Co(0001) sample, obtained by applying the average of the two scaling factors (green and blue symbols), and from the activity values of the Co$(10\bar{1}15)$ sample (red symbols).

triangles) has shifted above the linear regression line. This fact indicates that, shortly after the sample has been sputtered, a further, nonstructural effect operates in addition to the steps. We speculate about adsorbed reaction intermediates and byproducts that increase with reaction time, partially deactivating the surface when steady-state conditions have been reached. The initial activity may therefore be higher. That the activity of the annealed Co(0001) sample decreases with time (corrected Figure 6b, green data points) also must have nonstructural reasons and is in line with this explanation.

The TOFs in units of converted CO molecules per active sites change by the correction. The corrected values for the annealed Co(0001) sample, for the sputtered Co(0001) sample after 1, 3, and 5 h (ranges from the application of the two scaling factors), and of the Co$(10\bar{1}15)$ sample are $(2.1-3.5) \times 10^{-1}$, $(1.7-2.7) \times 10^{-1}$, $(1.2-2.0) \times 10^{-1}$, $(1.2-2.0) \times 10^{-1}$, and 1.2×10^{-1} s^{-1}. The average value is 0.2 s^{-1}, compared to 0.1 s^{-1} before the correction.

The ASF plot (Figure 7) is only affected by constant shifts of the individual data sets along the *y* axis by applying the correction, whereas the variations within each data set remain unchanged. Figure 10 is not affected within the error margins.

The conclusions of the paper that the activity scales with the step density, that the TOFs on the Co$(10\bar{1}15)$ surface agree well with literature data of supported catalysts, and that the Co$(10\bar{1}15)$ surface does not roughen under reaction conditions remain unaffected.

CHAPTER 5

Summary and Outlook

Despite several decades of research on the Fischer-Tropsch reaction, many questions remained open, in particular about the nature of the active sites on the cobalt catalyst. This thesis revealed insights into the active sites of cobalt catalysts by means of *operando* STM FT studies on cobalt single-crystal models. The study is based on a new customized gas chromatograph that was attached to the existing HP-STM setup and on experiments with a stepped single crystal. Several experimental improvements were necessary to perform studies of the surface under FT reaction conditions.

After laying out the experimental setup and the applied analytical methods in chapter 2, chapter 3 described experimental improvements obtained during this work. To analyze the Ni contamination, a major problem in the previous work by B. Böller, efforts were spent to understand the source of the remaining Ni. In section 3.1, the configuration of a setup for Ni deposition tests as well as experimental test results were presented. It turned out that for a measurable transport of Ni to a heated sample by the Mond reaction, it was necessary to introduce a sheet of Ni as well as H_2S into the apparatus. After removing the Ni source, prolonged reactions in syngas were required to remove Ni in the following blank experiments. It was concluded that Ni was initially deposited in the setup an then had to be depleted by extensive reactions with CO. These results showed that not necessarily a new Ni source must be present, but that residual Ni from former experiments might cause the regularly detected amounts of Ni on the surface after a sample has been used for FTS in the STM chamber. A depletion is possible, but would take a long period of time.

A further problem were the glass fibers used for heating the samples during FT experiments which were damaged after a few reaction experiments. The analysis of damaged glass fibers in section 3.2 revealed that an enhanced temperature of the fiber tip and a changed topography of the front surface correlated. In order to reduce the glass fiber temperature, a new fiber type with aluminum cladding was tested. Its installation was the solution for a longer lifetime of the glass fibers.

One major challenge was the precise surface temperature measurement. In order to compare the catalytic activities of the Co(0001) and the new Co($10\bar{1}15$) crystals, temperature calibration measurements were performed directly at their surfaces. The results of these measurements (section 3.3) showed that the surface temperatures of the crystals are generally about 10 – 20 °C higher compared to the normally measured temperatures at the backsides of the crystals. It was also shown that aging of the used thermocouples played a role.

In order to analyze the catalytic activity of the single crystals within FT reaction, a customized GC was attached to the HP-STM (section 3.4). To analyze the low concentrations of hydrocarbons in the gas samples, the gas chromatograph was equipped with a special automated gas sampling and injection unit. It enabled the extraction of only small amounts of gas from the reaction cell below 1 bar and the compression of this gas to the injection pressure of 1000 mbar by means of the He carrier gas. To avoid peak broadening, a cryo trap was installed at the head of one column. With the chosen capillary and micropacked columns, short C_1 to C_4 olefins and paraffins could be separated in the range from ~1 – 10 000 ppb with a detection limit of 0.4 ppb.

This GC system facilitated *operando* measurements in combination with the HP-STM setup. The FT activity of the model catalysts could in this way be correlated with the morphology resolved by STM. The experimental results of two FT studies performed with H_2:CO mixtures of 2:1, at a total pressure of 950 mbar, and at a sample temperature of ~220 °C/230 °C were presented in chapter 4. The first study on a Co(0001) crystal (section 4.1) showed that the catalytic activity scaled with step density. By sputtering the step density of the surface could be enhanced, which led to an increased formation of products. Step edge sites were concluded to be the active sites of the FT synthesis. In a more general sense, the study proved a long-standing idea that steps are the active sites in heterogeneous catalysis by direct observation on the atomic scale. The hypothesis of a roughening of the surface during the reaction was disproved. The Co actually displayed a smoothing effect of the surface under reaction conditions.

The second *operando* study on the Co($10\bar{1}15$) crystal (section 4.2.1) aimed at bridging the materials gap between single crystals and supported nanoparticles. The Co($10\bar{1}15$) surface can be regarded as a vicinal (0001) surface with a step density in the range of industrially relevant nanoparticles. The TOFs from the Co($10\bar{1}15$) surface were higher than those of the annealed and sputtered Co(0001) surface. As the TOFs of the Co($10\bar{1}15$) crystal match those of supported catalysts reported in the literature, it was concluded that step edge sites are also the active sites on the supported catalysts. The materials gap for the Co-catalyzed FTS can be regarded as bridged.

Whether these results also apply for the higher pressures applied in the industrial process remains open. As already mentioned, a further increase in pressure by one order of magnitude is currently not possible. The maximum pressure is limited by the viewports and feedthroughs of the STM chamber that cannot sustain internal overpressures. The same holds for several valves at the STM cell. Another issue at higher pressures would be the limited gas diffusion. To conclude, for measurements at higher pressures, major modifications of the current setup would be needed.

APPENDIX A

List of Abbreviations

BtL	biomass to liquid
CtL	coal to liquid
DFT	density functional theory
EDX	energy dispersive X-ray spectroscopy
fcc	face-centered cubic
FID	flame ionization detector
FT	Fischer-Tropsch
FTS	Fischer-Tropsch synthesis
GC	gas chromatograph
GtL	gas to liquid
hcp	hexagonal close-packed
HP-STM	high-pressure scanning tunneling microscope
IMFP	inelastic mean free path
IR	infrared
LDOS	local density of states
LEED	low-energy electron diffraction
ML	monolayer
NV	needle valve
ppb	parts per billion
ppm	parts per million
ppt	parts per trillion
PtL	power to liquid

QMS	quadrupole mass spectrometry
RT	room temperature
SEM	scanning electron microscopy
STM	scanning tunneling microscopy
syngas	synthesis gas
TOF	turnover frequency
TON	turnover number, equal to TOF
UHV	ultra-high vacuum
V	(shut-off) valve
WGS	water-gas shift
XPS	X-ray photoelectron spectroscopy

APPENDIX B

XPS Analysis

Table B.1: Parameter values used for quantification of the surface composition at the HP-STM (see sections 4.1 and 4.2) by XPS. Al K_α-radiation ($h\nu = 1486.6\,\text{eV}$) was used.

	Co 2p	**O 1s**	**C 1s**	**S 2p**	**Ni 2p**
σ_X[68]	0.2591	0.040	0.013	0.022	0.2998
β_X[69]	1.446	2	2	1.149	1.434
$L_X(\gamma)^a$	1.182	1.252	1.252	1.145	1.181
E_B [eV]	778	530	285	165	853
E_{kin} [eV]	703.7	951.7	1196.7	1316.7	628.7
λ [nm] in Co[73,74]	1.196	1.490	1.769	1.902	1.103
$\Lambda_X{}^b$	6.494	7.961	9.354	10.019	6.030
$T(E_{kin})^c$	1	1	1	1	1

---

^{a}calculated by Equation 2.2.3, $\gamma = 66°$
^{b}calculated by Equation 2.2.6
^{c}calculated by Equation 2.2.4

Table B.2: Parameter values used for quantification of the surface composition at the XPS chamber (see section 3.1.4) by XPS. Mg K_α-radiation ($h\nu = 1253.6\,\text{eV}$) was used.

	Au 4f	**O 1s**	**C 1s**	**S 2p**	**Ni 2p**
σ_X[68]	0.4176	0.063	0.022	0.038	0.469
β_X[69]	1	2	2	1.149	1.434
$L_X(\gamma)^a$	1.200	1.400	1.400	1.230	1.287
E_B [eV]	84	530	285	165	853
E_{kin} [eV]	1164.1	718.1	963.1	1083.1	395.1
λ [nm] in Au[73,74]	0.654	1.213	1.471	1.640	1.640
$\Lambda_X{}^b$	3.501	5.181	6.228	6.727	3.731
$T(E_{kin})^c$	1.145	1.556	1.291	1.198	2.276

---

^{a}calculated by Equation 2.2.3, $\gamma = 75°$
^{b}calculated by Equation 2.2.6
^{c}calculated by Equation 2.2.4

APPENDIX C

GC Settings

C.2 Carrier Gas Supply

Table C.1: Standard settings for the carrier gas of the GC.

	AuxCarrier1	**AuxCarrier2**	**AuxCarrier3**
Current mode	Flow control	Flow control	Pressure control
Setpoint	$10.000\,\mathrm{mL\,min^{-1}}$	$5.000\,\mathrm{mL\,min^{-1}}$	50.00 kPa

C.3 Flame Ionization Detector

Table C.2: Standard FID settings for GC measurements.

Parameter	**Front Detector**	**Back Detector**
Temperature	250 °C	250 °C
Flame	on	on
Hydrogen	$35.0\,\mathrm{mL\,min^{-1}}$	$35.0\,\mathrm{mL\,min^{-1}}$
Air	$350.0\,\mathrm{mL\,min^{-1}}$	$350.0\,\mathrm{mL\,min^{-1}}$
Makeup gas	$35.0\,\mathrm{mL\,min^{-1}}$	$35.0\,\mathrm{mL\,min^{-1}}$

C.4 Oven Programs

Table C.3: Oven program 3 for GC measurements (ramped mode), used for the experiments in section 3.4 and 4.1.

Retention time [min]	Rate [°C min^{-1}]	Target value [°C]	Hold time [min]
0.000	Run		
4.500	0.00	35.0	4.5
12.100	25.00	200.0	1.0
	New Row		
13.250	Stop Run		

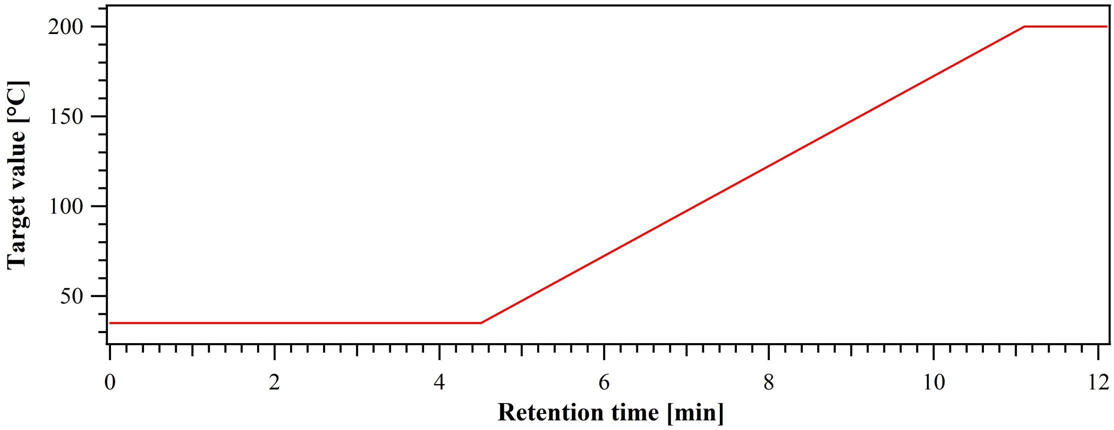

Figure C.1: Scheme of the original oven program 3. Details are listed in Table C.3.

Table C.4: Ofen program 13 for GC measurements (ramped mode), used for the experiments in section 4.2.

Retention time [min]	Rate [°C min^{-1}]	Target value [°C]	Hold time [min]
0	Run		
4.500	0	35.0	4.5
8.500	40	75.0	3.0
10.500	25	125.0	0.0
16.750	4	150.0	0.0
21.417	30	200.0	3.0
	New Row		
21.417	Stop Run		

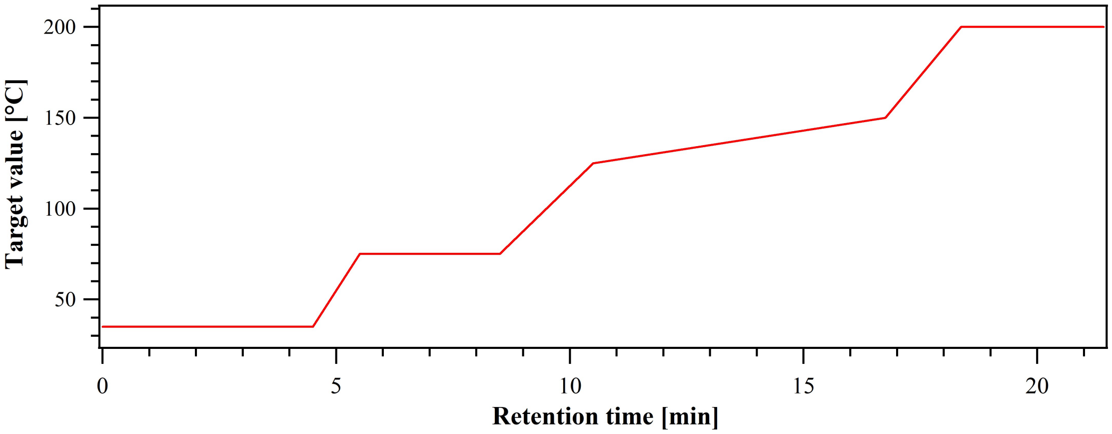

Figure C.2: Scheme of the new oven program 13. Details are listed in Table C.4.

C.5 Calibration Measurements

Calibration of the GC setup was performed by means of sequential dilutions of a custom-made calibration gas (Air Liquide, 150 bar). For this purpose, the calibration gas mixture, which contained ~10 ppm of methane, ethane, ethylene, propane, propylene, and butane in a syngas matrix,[2] was filled into the STM cell up pressures of 1[3], 10, and 100 mbar. By filling up with syngas, first with CO up to 320 mbar, then with H_2 to a total pressure of 950 mbar, final concentrations of the hydrocarbons ~10/100/1000 ppb were prepared. For the gas supply, the same pipes and gases as usually used for FT experiments were applied. Like in the FT experiments, both gases were led through cooling traps and CO additionally through a heating trap. For the dilution to 1 ppb hydrocarbons, the 10 ppb gas mixture (950 mbar calibration gas and syngas) was diluted a second time by a factor of $^{100}/_{950}$. For this purpose, the gas mixture in the STM cell was pumped out to a pressure of 100 mbar through the pump unit III after which the cell was refilled by CO and H_2 up to a pressure of 950 mbar. Before GC measurements, it was waited 1 h to allow the gas to mix properly and the pipe, connecting the STM cell and the GC, was evacuated two times to avoid concentration gradients. For the analysis of each dilution, five samples at a loop pressure of 80 mbar were taken from the mixture in the STM cell. It turned out that the interval between two GC measurements was important. As a result of the evacuation of the buffer loop, reproducible GC results were obtained, when the times between measurements were precisely the same. The theoretical mean values for each concentration used for calibration purpose are listed in Table C.5. Based on these values, the GC software

---

[2] As butylene was not included in the calibration gas mixture, it was calibrated separately (see ref. [63]).

[3] Although this pressure is below the pressure range specified by the manufacturer, it provided more reproducible results than further diluting a different gas mixture prepared before.

CHROMELEON 7.2 (Thermo Fisher) determines detailed values in ppb for each peak in a chromatogram. Details concerning the linearity of the calibration data are given in the publication "A highly sensitive gas chromatograph for *in situ* and *operando* experiments on catalytic reactions" starting on page 55. For more details of the data processing see section 2.4.

Table C.5: Calibration data for the GC. To achieve several concentration values for each component, the calibration gas was diluted with with syngas within the STM chamber. The Conc. Cal. Gas column shows the concentrations of the individual hydrocarbons in the calibration gas, as given by the manufacturer. The values in the four Dilution columns are the theoretical concentrations evaluated from the pressure ratios applied in the calibration measurements.

Hydro-carbons	**Ret. Time [min]**	**Conc. Cal. Gas**[b] **[ppb]**	**Dilution**[a] **1 ppm [ppb]**	**100 ppb [ppb]**	**10 ppb [ppb]**	**1 ppb [ppb]**
Methane	5.053	9670	1017.8947	101.7895	10.1789	1.0715
Ethylene	6.940	9580	1008.4211	100.8421	10.0842	1.0615
Ethane	7.525	9490	998.9474	99.8947	9.9895	1.0515
Propylene	11.197	9450	994.7368	99.4737	9.9474	1.0471
Propane	11.612	9600	1010.5263	101.0526	10.1053	1.0637
Butane	14.163	9500	1000.0000	100.0000	10.0000	1.0526

---

[a] Integrated into the Chromeleon software as *Levels 2–5*, used for the calibration plot.

[b] Integrated into the Chromeleon software as *Level 1* but excluded from the calibration plot.

APPENDIX D

Mass Spectra

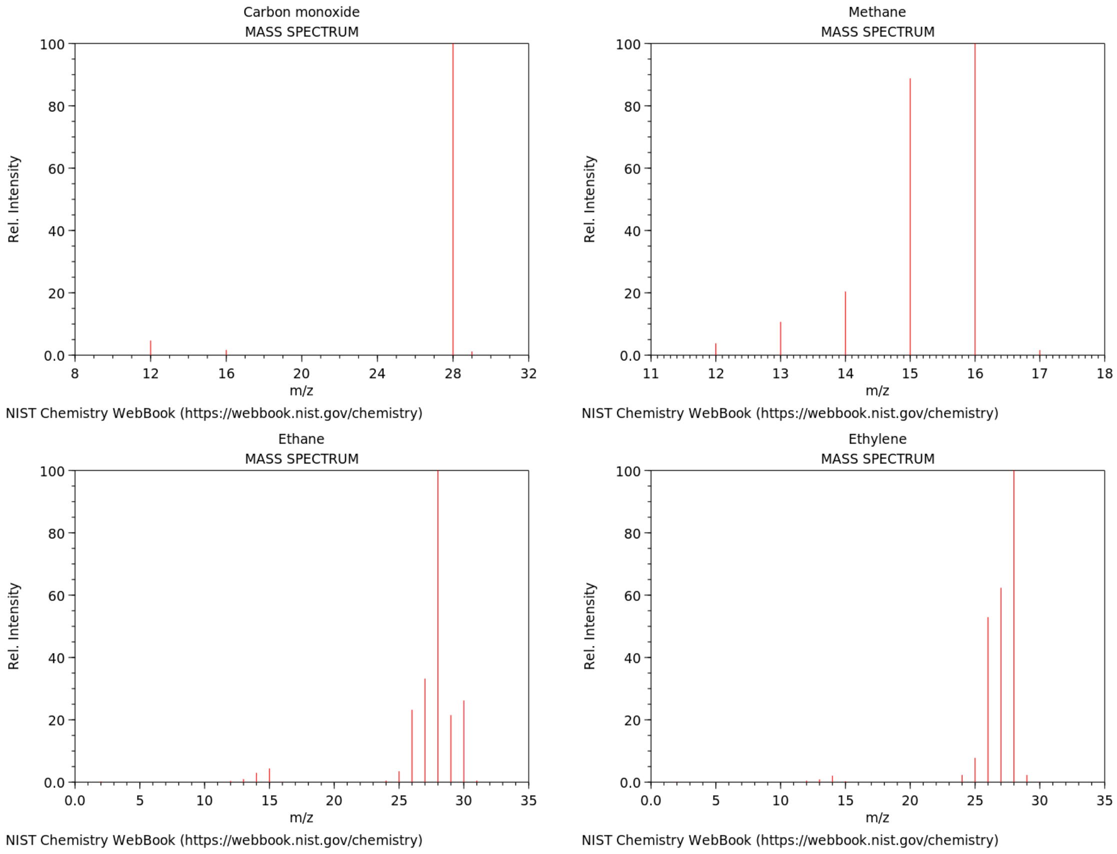
Carbon monoxide
MASS SPECTRUM

NIST Chemistry WebBook (https://webbook.nist.gov/chemistry)

Methane
MASS SPECTRUM

NIST Chemistry WebBook (https://webbook.nist.gov/chemistry)

Ethane
MASS SPECTRUM

NIST Chemistry WebBook (https://webbook.nist.gov/chemistry)

Ethylene
MASS SPECTRUM

NIST Chemistry WebBook (https://webbook.nist.gov/chemistry)

Figure D.1: Mass spectra of CO, methane, ethane, and ethylene from the NIST data base (ref. [120]).

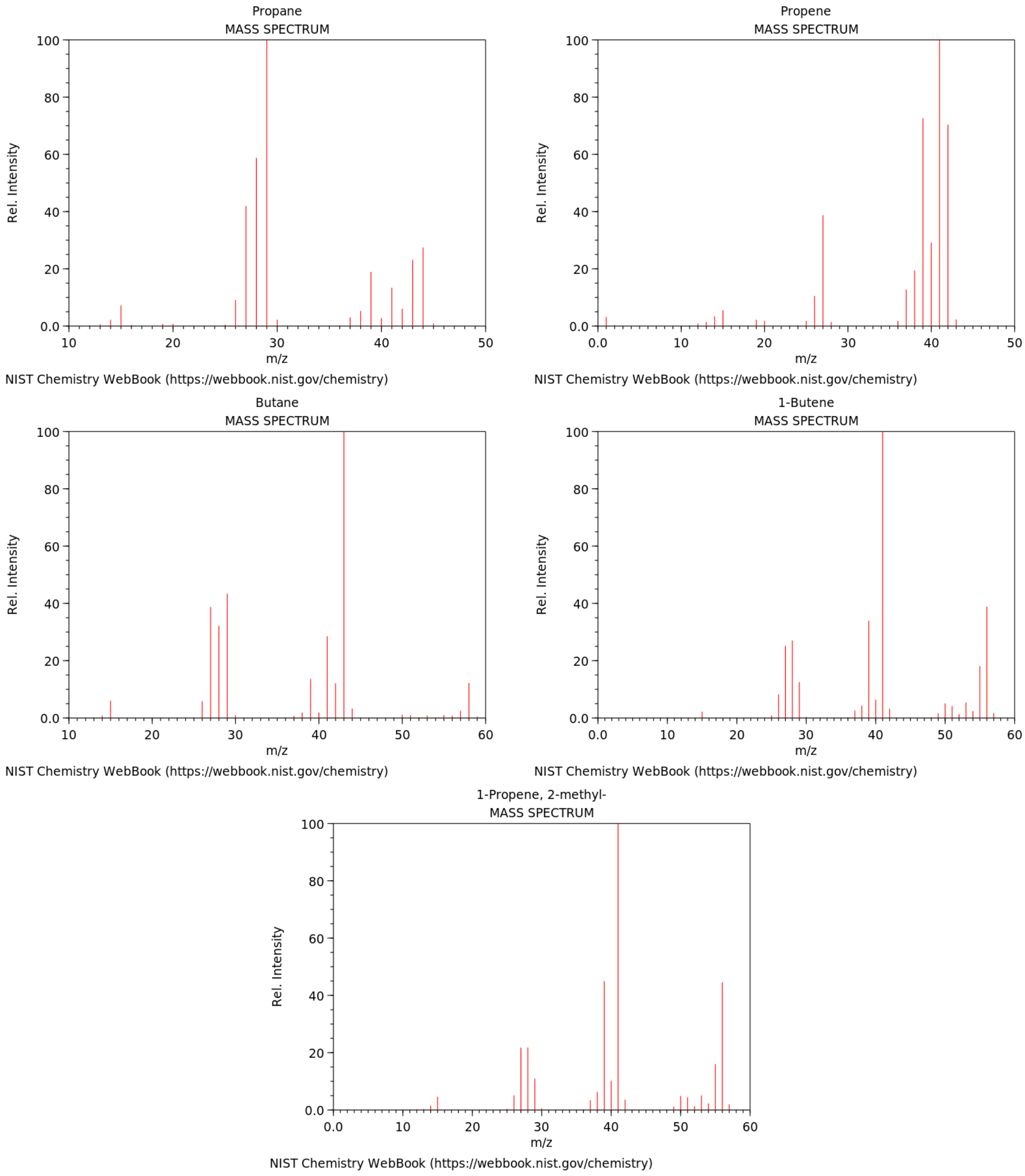

NIST Chemistry WebBook (https://webbook.nist.gov/chemistry)

NIST Chemistry WebBook (https://webbook.nist.gov/chemistry)

NIST Chemistry WebBook (https://webbook.nist.gov/chemistry)

NIST Chemistry WebBook (https://webbook.nist.gov/chemistry)

NIST Chemistry WebBook (https://webbook.nist.gov/chemistry)

Figure D.2: Mass spectra of propane, propylene, butane, α-butylene, and isobutylene from the NIST data base (ref. [120]).

APPENDIX E

Supporting Information for Chapter 4.1

In the following, the supporting information of the article “The active sites of a working Fischer-Tropsch catalyst revealed by operando scanning tunnelling microscopy” published in *Nature Catalysis* (see chapter 4.1) is reprinted with permission from *Nat. Catal.* **2**, 1027-1034 (2019), Springer Nature Limited 2019. It contains detailed TOFs and XPS data as well as STM images of possible carbon structures. In addition, it shows the evaluation of the mass transport of Co atoms that occured during the smoothing of the sputtered surface. The STM measurements shown in the Supplementary Figure 4 were performed in this work. The results are an important part of the publication, as they show that the smoothing of the Co(0001) surface also takes place in vacuum. It can be concluded that adsorbates do not play a role in the smoothing process of the sputtered surface which even takes place at the relatively low temperatures of the reactions. The smoothing (also shown in Supplementary Videos 3 and 4) is in contrast to the literature,[42] where a roughening process has been postulated.

The Supplementary Videos 1–4 show step fluctuations during the reactions as well as the smoothing of the sputtered Co(0001) surface. The videos are available on the website: `https://www.nature.com/articles/s41929-019-0360-1#Sec16`.

nature catalysis
SUPPLEMENTARY INFORMATION
https://doi.org/10.1038/s41929-019-0360-1

The active sites of a working Fischer–Tropsch catalyst revealed by operando scanning tunnelling microscopy

Bernhard Böller, Katharina M. Durner and Joost Wintterlin*

Department Chemie, Ludwig-Maximilians-Universität München, Munich, Germany. *e-mail: wintterlin@cup.uni-muenchen.de

The active sites of a working Fischer-Tropsch catalyst revealed by operando scanning tunnelling microscopy

Bernhard Böller, Katharina M. Durner, Joost Wintterlin

Department Chemie, Ludwig-Maximilians-Universität München, 81377 Munich, Germany

Content

Supplementary Tabels

Supplementary Table 1: Detailed TOFs of the formation of the individual hydrocarbon products (methane to butylene/butane) and of the consumption of CO from several experiments with the annealed and with the sputtered Co(0001) single crystal. The product-based TOFs of the individual hydrocarbons were calculated from the peak increments between GC spectra taken every hour. The CO-based TOFs were evaluated by multiplying the product-based TOFs by the number of carbon atoms in the individual hydrocarbon products and adding up. The values are given in units of product molecules per cobalt surface atom per second, using the atom density of Co(0001) of $1.837 \cdot 10^{19}$ m^{-2} and the area of the prepared surface of 19.6 mm^2.

The α values were obtained from plots of the logarithmic product-based TOFs vs. C numbers such as in fig. 1(b) of the main text.

Conversions *X* were calculated by dividing the numbers of consumed CO molecules by the initial numbers of CO molecules in the reactor. The numbers of consumed CO molecules were evaluated from the CO-based TOFs, the number of Co atoms on the sample surface, and the elapsed times (assuming negligible production of possible byproduct CO_2). The numbers of CO molecules in the reactor were calculated from the reactor volume (1.8 l) and the CO partial pressure of 317 mbar.

The data sets (a) and (b) were recorded with a time delay of one month and were normalized using the intensity of the combined H_2 and CO peak the chromatograms as internal standard. The first measurement with the annealed sample after 1 h was directly measured after calibration of the GC system with a calibration gas mixture and was therefore used as reference. The normalization corrected a continuous aging of the GC column mainly caused by the cryo trap. For comparison the uncorrected data are given in brackets.

Dataset (b) was used for figure 1(b) in the main text. All experiments were performed with 2:1 H_2:CO syngas mixtures at total pressures of 950 mbar and sample temperatures of 493 K.

(a)

	TOF (CH_4) [10^{-4} s^{-1}]	TOF (C_2H_4) [10^{-4} s^{-1}]	TOF (C_2H_6) [10^{-4} s^{-1}]	TOF (C_3H_6) [10^{-4} s^{-1}]	TOF (C_3H_8) [10^{-4} s^{-1}]	TOF (C_4H_8) [10^{-4} s^{-1}]	TOF (C_4H_{10}) [10^{-4} s^{-1}]	TOF (CO) [10^{-4} s^{-1}]	α	X [10^{-6}]
annealed										
1 h	29	2.9	0.57	3.4	0.26	1.7	--	54	0.43	0.5
3 h	28	2.4	0.45	2.4	0.25	1.2		46	0.38	1.5
	(26)	(2.2)	(0.41)	(2.2)	(0.22)	(1.1)		(42)		
5 h	27	2.0	0.42	1.9	0.09	1.1	--	42	0.38	2.5
	(24)	(1.7)	(0.37)	(1.6)	(0.07)	(1.0)		(37)		
sputtered										
1 h	52	7.2	0.77	6.8	0.34	1.5	--	89	0.34	0.8
	(46)	(6.4)	(0.68)	(6.0)	(0.30)	(1.3)		(79)		
3 h	47	5.1	0.70	5.2	0.26	0.96		75	0.31	2.5
	(40)	(4.3)	(0.6)	(4.5)	(0.22)	(0.8)		(64)		
5 h	42	4.6	0.62	3.9	0.18	1.0	--	64	0.31	4.2
	(35)	(3.8)	(0.52)	(3.2)	(0.15)	(0.08)		(53)		
annealed										
1 h	32	3.2	0.48	3.4	0.14	0.76	--	53	0.32	0.5
	(26)	(2.5)	(0.38)	(2.7)	(0.11)	(0.61)		(42)		
3 h	31	2.6	0.42	2.1	0.12	0.78		46	0.32	1.5
	(23)	(1.9)	(0.31)	(1.6)	(0.09)	(0.58)		(35)		
5 h	29	2.6	0.35	2.2	0.27	0.77		45	0.33	2.5
	(22)	(1.9)	(0.26)	(1.7)	(0.20)	(0.57)		(34)		

(b)

	TOF (CH_4) [10^{-4} s^{-1}]	TOF (C_2H_4) [10^{-4} s^{-1}]	TOF (C_2H_6) [10^{-4} s^{-1}]	TOF (C_3H_6) [10^{-4} s^{-1}]	TOF (C_3H_8) [10^{-4} s^{-1}]	TOF (C_4H_8) [10^{-4} s^{-1}]	TOF (C_4H_{10}) [10^{-4} s^{-1}]	TOF (CO) [10^{-4} s^{-1}]	α	X [10^{-6}]
annealed										
1 h	27	4.1	0.39	4.2	0.25	1.8	0.11	57	0.46	0.5
	(18)	(2.8)	(0.26)	(2.9)	(0.17)	(1.3)	(0.76)	(39)		
3 h	24	3.1	0.35	2.9	0.29	0.93	0.12	44	0.39	1.6
	(15)	(2.0)	(0.22)	(1.9)	(0.19)	(0.60)	(0.07)	(29)		
5 h	23	2.6	0.29	2.5	0.12	1.0	0.06	41	0.39	2.7
	(15)	(1.7)	(0.18)	(1.6)	(0.07)	(0.63)	(0.04)	(26)		
sputtered										
1 h	40	7.6	0.59	8.6	0.49	4.0	0.15	101	0.51	0.9
	(31)	(5.9)	(0.45)	(6.7)	(0.38)	(3.1)	(0.11)	(78)		
3 h	37	6.3	0.47	6.6	0.29	2.6	0.21	82	0.46	2.8
	(27)	(4.6)	(0.34)	(4.8)	(0.21)	(1.9)	(0.15)	(59)		
5 h	32	5.0	0.41	4.6	0.26	1.7	0.13	65	0.42	4.7
	(23)	(3.6)	(0.30)	(3.3)	(0.19)	(1.2)	(0.09)	(47)		

Supplementary Table 2: Carbon and oxygen coverages from XPS after reaction experiments. The data in (a) are from the annealed surface, the data in (b) from the sputtered surface. All experiments were performed at 950 mbar, H_2:CO = 2:1, 493 K. The XP spectra were recorded after the sample was kept at 493 K in the reaction gas atmosphere for the indicated reaction times. The various carbon species were identified by using their C 1s peaks, CO also by its O 1s peak, as described in the main text. The data show no obvious trends of the coverages with reaction times.

(a)

reaction time	atomic carbon	hydrocarbon moieties	CO (from C 1s)	CO (from O 1s)
0.25 h	0.16	0.07	0.32	0.32
2 h	0.14	0.02	0.24	0.21
2 h	0.15	0.18	0.33	0.30
4.5 h	0.16	0.05	0.25	0.25
6 h	0.16	0.14	0.22	0.19
6 h	0.14	0.10	0.21	0.17
6 h	0.23	0.19	0.23	0.34
6 h	0.14	0.06	0.24	0.28
6 h	0.14	0.12	0.19	0.29

(b)

reaction time	atomic carbon	hydrocarbon moieties	CO (from C 1s)	CO (from O 1s)
0.25 h	0.15	0.17	0.27	0.25
4 h	0.18	0.15	0.26	0.29
4.5 h	0.21	0.13	0.30	0.27
6 h	0.17	0.14	0.28	0.34
6 h	0.17	0.13	0.28	0.28

Supplementary Figures

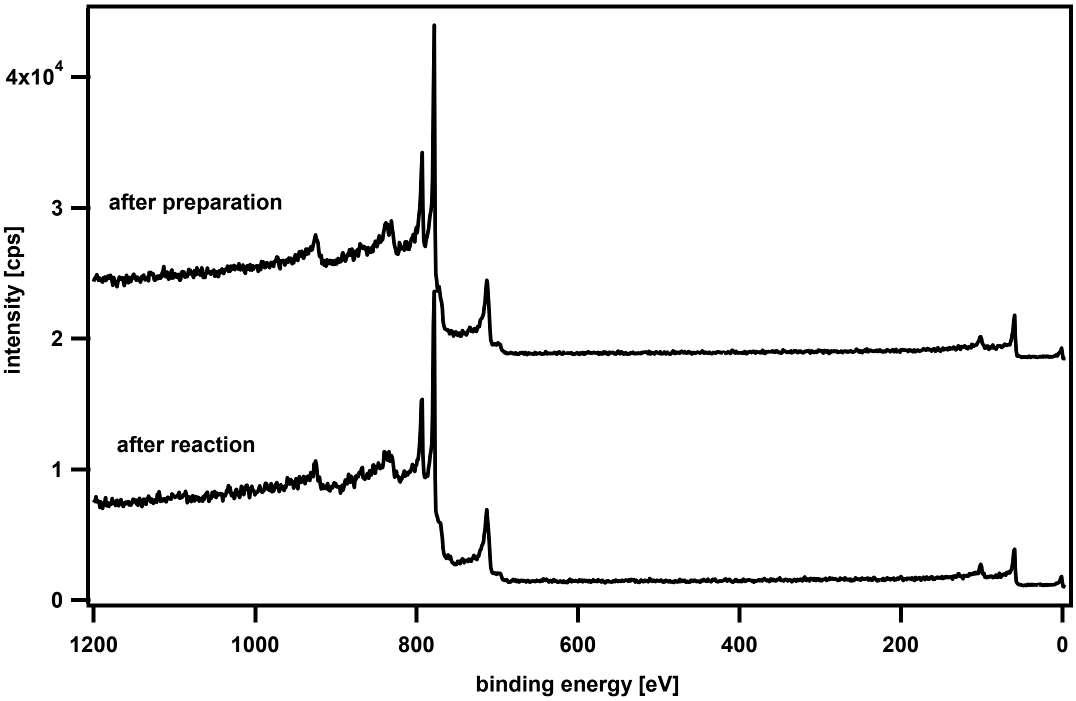

Supplementary Figure 1: XP survey spectra of the Co(0001) single crystal recorded after preparation in UHV and after 6 h of reaction in syngas (950 mbar, H_2:CO = 2:1, 493 K sample temperature), after sample transfer from the STM cell to the preparation chamber, i.e., *ex situ*. The spectra were measured using a monochromatized Al K_α X-ray source. As explained in the main text, *ex situ* XPS was used to ensure a clean sample after preparation, the absence of impurities after reaction experiments, and to quantify carbon and oxygen coverages. The survey spectra taken before and after reaction only show metallic Co and are almost identical, demonstrating that the reaction did not lead to significant adsorption of impurities or chemical changes of the surface. The low peaks in the C 1s and O 1s regions detected after the reaction (fig. 2 in the main text) are not visible on this scale.

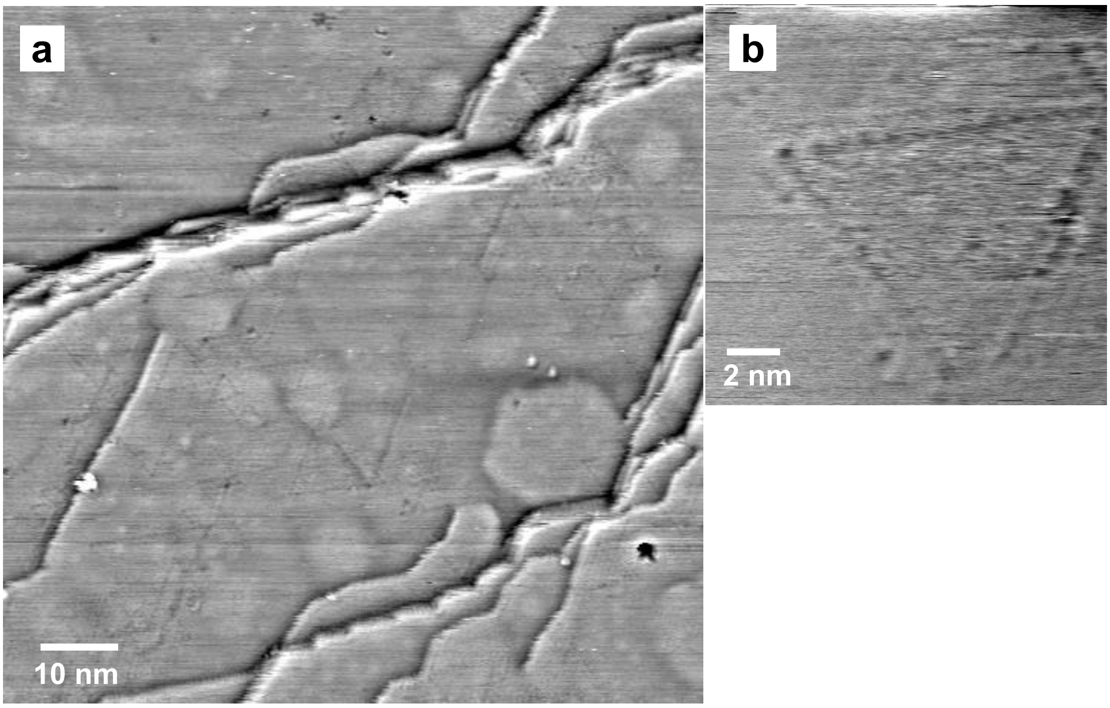

Supplementary Figure 2: STM images of a possible carbon structure on the annealed Co(0001) single crystal in 950 mbar syngas (H_2:CO = 2:1) at a sample temperature of 493 K. (a) STM image (90 nm x 90 nm, V_t = 0.05 V; I_t = 0.7 nA) recorded 1 h, (b) STM image (15 nm x 15 nm, V_t = 0.05 V; I_t = 0.7 nA) recorded 1.5 h after starting the sample heating to 493 K. The weak triangular structures on the terraces were similarly seen on the sputtered surface. They were only resolved under reaction conditions, never in UHV, and they appeared directly after heating the Co(0001) sample to 493 K in syngas and did not change in number and size during several hours of reaction. From their similarity to structures resolved in CO dissociation experiments on Co(0001) they may be interpreted as a reconstruction induced by C atoms[1]. A carbide phase has also been identified by *in situ* XPS, even though at a much lower syngas pressure[2]. The structure model proposed in ref. 1 was a local stacking fault - the top Co layer in the interior of a triangle is fcc-stacked - and the trench forming the dislocation between the hcp area outside and the fcc area inside was occupied by C atoms. Using this structure model to estimate the C coverage from the density of triangles gives considerably lower values than the approximately 0.16 ML measured by XPS. However, the reconstruction model has not been solved so far with respect to the arrangement and numbers of the C atoms along the dislocations. Moreover, as pointed out in the main text, a fraction of the carbon species measured *ex situ* by XPS may have formed during the cooling and pumping-down period after the syngas experiments. The C coverages during reactions may have been lower.

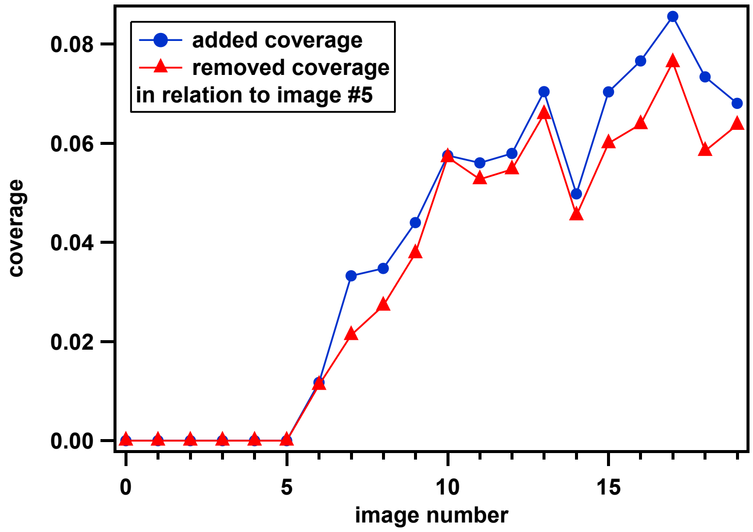

Supplementary Figure 3: Growth and shrinking of cobalt terraces quantified from movie 4. Blue dots represent incremental increases of the areas of the Co terraces, determined by integration of the bright areas in movie 4; red dots represent decreases, the integrated dark areas in movie 4. The two areas match very well, showing that the mass transport of Co atoms from high-lying to low-lying terraces is balanced. Image #5 served as reference image; images #1 to #4 were not included because the thermal drift was relatively strong in this phase and therefore the overlap with the rest of the series too low. In the time period of movie 4 of about 2.5 h the migration of the Co atoms led to a reduction of the step density of about 10 – 15 %.

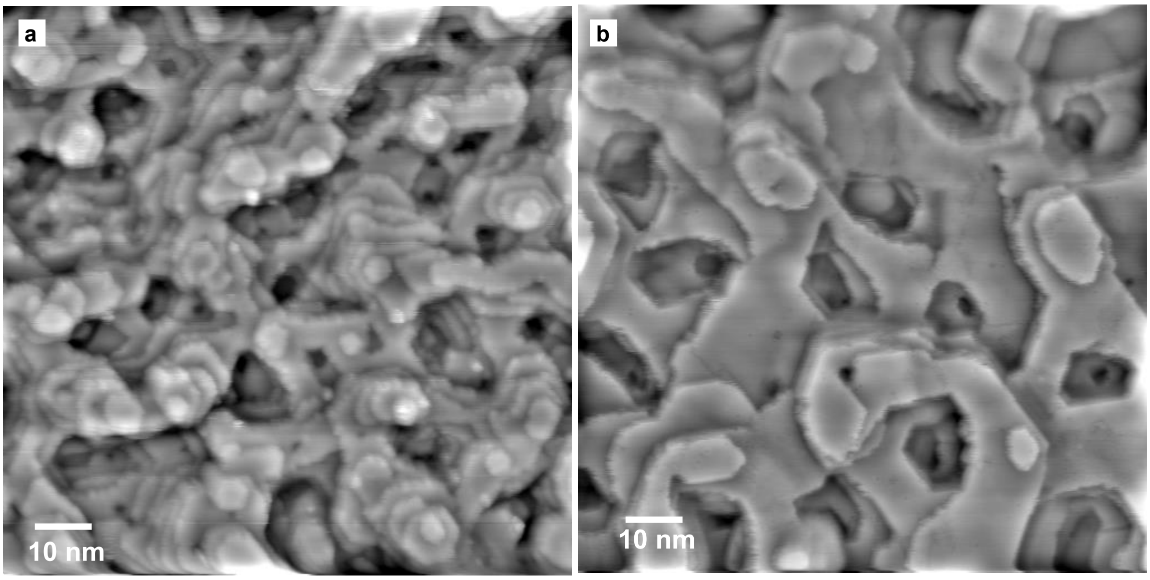

Supplementary Figure 4: STM images of the annealing of a sputtered surface in UHV. (a) At room temperature directly after sputtering (100 nm x 100 nm V_t = +1.0 V; I_t = 0.7 nA), (b) 2 h after raising the temperature to a constant value of 493 K (100 nm x 100 nm V_t = +0.5 V; I_t = 0.7 nA); the background pressure was approximately 3 x 10^{-9} mbar. The surface had been prepared and sputtered similarly as in the syngas experiments. The terraces similarly increase in UHV as under syngas, indicating that the same transport effects of Co atoms operate. The smoothing is therefore more an effect of temperature than of the adsorption layer of CO molecules, H atoms, and C_xH_y fragments present under FT conditions. After 3.5 h the experiment was terminated and XP spectra were taken. Coverages of 0.25 ML carbidic and 0.10 ML graphitic carbon and 0.06 ML of oxygen and minor amounts of adsorbed CO were detected. The formation of the C and O species can be explained by the adsorption and decomposition of residual gas components on the hot sample.

Supplementary References

1. Böller, B., Ehrensperger, M., Wintterlin, J. In Situ Scanning Tunneling Microscopy of the Dissociation of CO on Co(0001). *ACS Catal.*, **5**, 6802-6806, (2015).

2. Wu, C. H., Eren, B., Bluhm, H., Salmeron, M. B. Ambient-Pressure X-ray Photoelectron Spectroscopy Study of Cobalt Foil Model Catalyst under CO, H2, and Their Mixtures. *ACS Catal.* **7**, 1150-1157, (2017).

APPENDIX F

Supporting Information for Chapter 4.2.1

In the following, the supporting information of the article "*In Situ/Operando* STM of the Fischer-Tropsch Synthesis on a Co($10\bar{1}15$) Surface – A Study to Bridge the Materials Gap between Single-Crystal Models and Supported Catalysts" published in *ACS catalysis* (see chapter 4.2.1) is reproduced with permission from *ACS Catal.* **2022**, *12*, 7199–7209. Copyright © 2022 The Authors. Published by American Chemical Society. Herein, XP Co 2p detail spectra as well as survey scans of the Co($10\bar{1}15$) surface before and after an experiment are shown. Furthermore, the $\mathrm{TOF}_{\mathrm{corr}}$ values for supported Co catalysts are listed. These data were extracted from 179 measurements in 49 studies from the literature and converted to the respective experimental conditions as described in the article.

The supporting video shows a time lapse of STM images, recorded during a FT experiment; it and can be downloaded from the website: `https://pubs.acs.org/doi/10.1021/acscatal.2c00703`.

Supporting Information

In Situ/Operando STM of the Fischer–Tropsch Synthesis on a Co$(10\bar{1}15)$ Surface – A Study to Bridge the Materials Gap between Single-Crystal Models and Supported Catalysts

Katharina M. Golder[1] and Joost Wintterlin[1,2*]

[1]Dept. of Chemistry, Ludwig-Maximilians-Universität München
Butenandtstr. 5-13, 81377 Munich, Germany
[2]Center for NanoScience
Schellingstr. 4, 80799 Munich, Germany

*Corresponding Author; Email: wintterlin@cup.uni-muenchen.de

XP Spectra Recorded before and after a Reaction

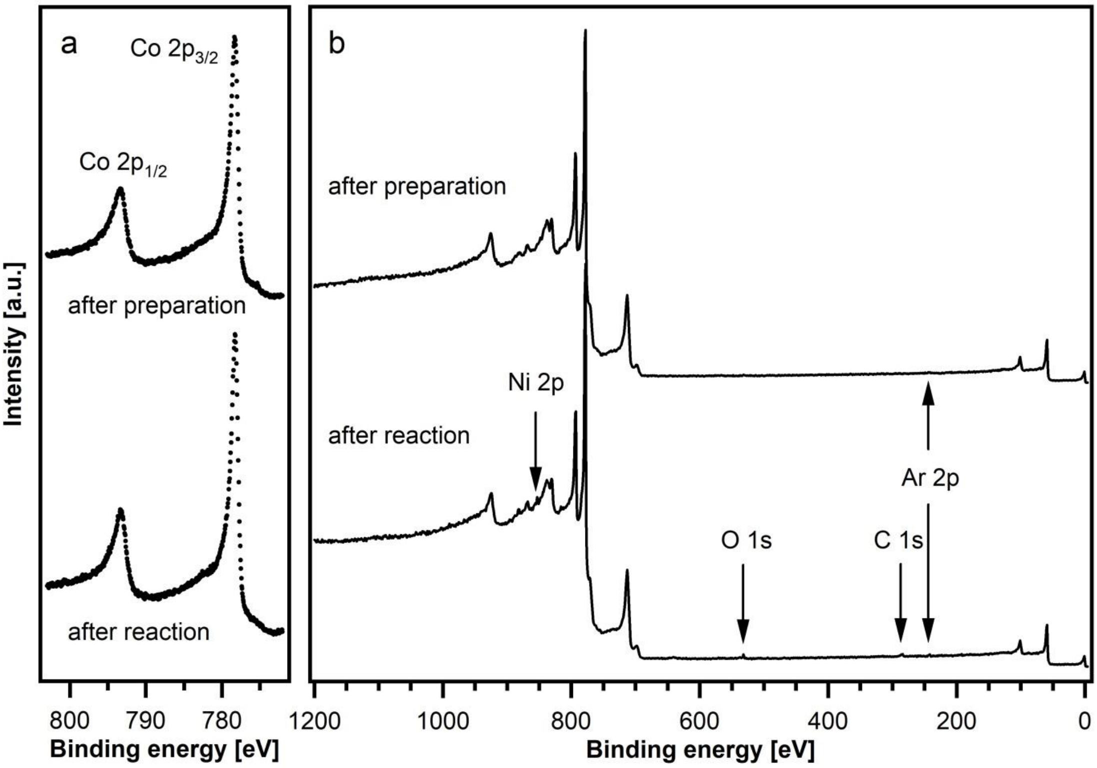

Figure S1. XP detail spectra of the Co 2p region (a) and survey scan (b) of the Co$(10\bar{1}15)$ sample after preparation in UHV and after a 6 h reaction experiment in syngas (950 mbar, H_2:CO = 2:1, sample temperature ~503 K). The Co $2p_{3/2}$ peaks in the spectra recorded before and after the experiment are basically identical [Figure S1a]; peak fitting yields binding energies of 778.25 eV and 778.23 eV, respectively. The unchanged Co peaks indicate that the surface stays metallic during the reaction. Weak signals of the species appearing after the reaction are visible in Figure S1b. The detail spectra of the O 1s and C 1s regions at higher magnification are shown in Figure 8 of the main text. The Ar signals detected before and after the reaction result from sputtering and are caused by Ar atoms in the Co bulk. Due to the low annealing temperature, Ar could not completely be removed after sputtering. Spectra from the Co(0001) sample are very similar.

Statistics of TOF Values of Supported Co Catalysts from the Literature

Table S1. $\mathrm{TOF_{corr}}$ values of supported Co catalysts used for Figure 10. Only data with particles ≥ 8nm are included. The original TOF values were extracted from the respective reference and converted to our experimental parameters [T = 503 K, $p(\mathrm{H_2})$ = 0.63 bar, $p(\mathrm{CO})$ = 0.32 bar] as described in the main text.

Ref.	Catalyst	particle diameter [nm]	$\mathrm{TOF_{corr}}$ [10^{-3} s^{-1}]
1	Co/SiO_2	9.2	18.9
2	Co/carbon	27	16.6
2	Co/carbon	12.8	15.2
2	Co/carbon	16	18.0
2	Co/carbon	8.5	17.7
2	Co/carbon	10	16.7
2	Co/carbon	16	10.0
2	Co/carbon	8.5	9.9
3	Co/carbon	12.4	21.9
3	Co/carbon	12.4	9.4
4	Co/carbon	13	21.3
5	Co/SiO_2	10.5	42.5
5	Co/SiO_2	29.4	42.5
5	Co/SiO_2	10.5	25.8
5	Co/SiO_2	29.4	38.4
5	Co/SiO_2	10.5	15.7
5	Co/SiO_2	29.4	22.4
6	Co/SiO_2	19	47.0
6	Co/SiO_2	19.9	48.6
6	Co/SiO_2	21.3	50.2
6	Co/SiO_2	23.5	51.7
6	Co/SiO_2	8.3	36.1
6	Co/SiO_2	9.9	43.4
6	Co/SiO_2	10.3	45.5
6	Co/SiO_2	13	46.5
7	Co/carbon	15	2.4
7	Co/carbon	15	2.1
8	Co/SiO_2	10.6	22.5
8	Co/SiO_2	8.9	17.3
8	Co/SiO_2	12.3	22.9
9	Co/carbon	16	23.9
9	Co/carbon	11	11.9
9	Co/carbon	8.5	11.9
10	Co/Al_2O_3	14	41.0
10	Co/Al_2O_3	35	41.0
11	Co/carbon	10.1	24.6
12	Co/SiO2	19.7	9.5
12	Co/ZrO_2/ SiO_2	18.6	13.4
12	Co/ZrO_2/ SiO_2	18	30.2
12	Co/ZrO_2/ SiO_2	9.2	68.5
12	Co/ZrO_2	11.3	28.8
13	Co/carbon	20.3	24.2
14	Co/Al_2O_3	11.1	40.0
14	Co/Al_2O_3	12.4	49.2
14	Co/Al_2O_3	14.5	74.2
15	Co/Al_2O_3	22	5.5
15	Co/Al_2O_3	13	6.2
15	Co/Al_2O_3	10	4.5
15	Co/Al_2O_3	10	5.2
15	Co/Al_2O_3	10	4.1
15	Co/Al_2O_3	10	5.2
16	Co/carbon (oxidized CNT)	10	5.9
16	Co/carbon (oxidized CNT)	9	2.1
16	Co/carbon (oxidized CNT)	10	0.5
17	Co/SiO_2	20.4	33.4
17	Co/SiO_2	26.9	32.4
18	Co/SiO_2	18	51.7
19	Co/SiO_2	10	1.6
19	Co/SiO_2	25	1.7
20	Co/SiO_2	9.9	48.4
20	Co/SiO_2	11	48.4
20	Co/SiO_2	12	48.4
20	Co/SiO_2	14.5	51.0
20	Co/SiO_2	14.7	45.9
20	Co/SiO_2	8	61.2
20	Co/SiO_2	8.8	56.1
21	Co/TiO_2	80.8	22.4
21	Co/TiO_2	44.1	22.0
21	Co/TiO_2	33.4	25.1
21	Co/TiO_2	18.3	20.9
21	Co/TiO_2	32.3	28.7
21	Co/TiO_2	14.9	22.8
21	Co/SiO_2	23.1	26.2
21	Co/SiO_2	30.3	20.2
21	Co/SiO_2	51.1	17.0

Ref.	Catalyst	particle diameter [nm]	TOF_{corr} [10^{-3} s^{-1}]
21	Co/SiO_2	19.4	25.3
21	Co/SiO_2	15.4	25.7
21	Co/SiO_2	16.2	23.8
21	Co/SiO_2	10.2	20.1
21	$Co/ZrO_2/SiO_2$	15.9	15.9
21	$Co/ZrTiO_2$	88.2	26.7
21	Co/Al_2O_3	26.9	18.6
21	Co/Al_2O_3	64.7	15.5
22	Co/TiO_2	44	17.3
23	Co/Al_2O_3	9.7	3.5
23	Co/Al_2O_3	16.2	10.1
24	Co/Al_2O_3	21	23.5
25	Co/Al_2O_3	12.8	3.4
25	Co/Al_2O_3	19	11.8
25	Co/Al_2O_3	24.9	20.3
25	Co/Al_2O_3	64.7	30.4
26	Co/TiO_2	11.6	13.5
26	$Co/C\text{-}TiO_2$	8.7	10.9
26	$Co/C\text{-}TiO_2$	28.8	9.6
26	$Co/C\text{-}TiO_2$	8.6	11.2
26	$Co/C\text{-}TiO_2$	12.3	11.0
27	Co/Al_2O_3	8.8	39.1
27	Co/Al_2O_3	13	25.3
27	Co/Al_2O_3	18	26.4
27	Co/Al_2O_3	22	29.9
27	Co/Al_2O_3	42	28.7
27	Co/TiO_2	21	46.0
27	Co/TiO_2	21	41.4
27	Co/TiO_2	24	41.9
27	Co/TiO_2	28	37.9
27	Co/TiO_2	32	39.1
27	Co/TiO_2	42	29.9
28	Co/SiO_2	15	45.8
29	Co/carbon	19.7	11.1
29	Co/carbon	21.1	7.7
29	Co/carbon	47.8	10.4
29	Co/carbon	51.5	9.9
29	Co/carbon	74.8	10.6
30	Co/ITQ2-zeolite	10.9	10.0
31	Co/SiO_2	8.6	35.6
31	Co/SiO_2	11	76.9
32	Co/carbon	10.8	31.5
32	Co/carbon	19.4	24.2
33	Co/ZnO	24.9	5.6
33	Co/ZnO	24.9	5.0
34	Co/Al_2O_3	9.3	42.3
34	Co/Al_2O_3	13	39.8
34	Co/Al_2O_3	17.5	34.8
35	Co/zeolite	136.6	3.0
35	Co/zeolite	10.1	3.2
35	Co/zeolite	8.7	2.5
36	Co/Al_2O_3	10.9	27.0
36	Co/Al_2O_3	10.7	15.5
36	Co/Al_2O_3	9.5	20.7
36	Co/Al_2O_3	10.7	19.0
36	Co/Al_2O_3	12.3	14.4
36	Co/Al_2O_3	13.7	17.2
36	Co/Al_2O_3	14.9	15.5
36	Co/Al_2O_3	16.7	12.6
37	Co/SiO_2	8.8	6.7
37	Co/SiO_2	9.7	9.2
37	Co/Al_2O_3	9.7	3.4
37	Co/Al_2O_3	9.8	14.7
37	Co/Al_2O_3	14.7	77.2
37	Co/TiO_2	21.6	46.6
37	Co/MgO	51.1	0.2
38	Co/carbon	11	9.7
39	Co/SiO_2	19.8	0.8
39	Co/SiO_2	10.6	0.4
40	Co/SiO_2	15	9.2
41	Co/Al_2O_3	15.2	29.9
41	Co/SiO_2	18.1	31.0
41	Co/TiO_2	41.7	30.4
42	Co/SiO_2	20.4	15.4
42	Co/SiO_2	12.2	13.7
42	Co/SiO_2	15.1	24.8
42	Co/SiO_2	17.9	16.4
42	Co/SiO_2	12.7	15.6
42	Co/SiO_2	12	17.8
43	Co/TiO_2	15	4.2
43	Co/TiO_2	11	23.2
43	Co/TiO_2	13	23.9
43	Co/TiO_2	14	23.9
43	Co/SiO_2	13	23.6
43	Co/SiO_2	9.6	37.3
44	Co/SiO_2	11.3	9.9
44	Co/SiO_2	11.3	12.3
44	$Co/TiSiO_2$	8.3	18.7
44	$Co/TiSiO_2$	9	22.2
45	Co/SiO_2	10.5	32.0
46	Co/carbon	12.4	74.1
46	Co/carbon	16.6	87.2

Ref.	Catalyst	particle diameter [nm]	TOF$_{corr}$ [10^{-3} s^{-1}]
46	Co/carbon	45	91.5
46	Co/carbon	12.6	74.1
46	Co/carbon	21	78.5
46	Co/carbon	14.2	82.8
47	Co/N-doped C	10.1	50.8
47	Co/N-doped C	12.1	53.2
48	Co/Al_2O_3	11.2	25.0
48	Co/Al_2O_3	15.1	30.6
49	Co/Al_2O_3	14	33.2
49	Co/Al_2O_3	35	35.5
49	Co/carbon	20	24.1
49	Co/carbon	10	25.8

Movie S1

Time lapse of 30 STM images recorded during a period of 1.75 h. Conditions were a total pressure of 950 mbar syngas of a H_2/CO = 2:1 mixture and a sample temperature of ~503 K. The first frame was taken 3.2 h after heating the sample to 503 K (500 x 500 Å, V_t = 0.5 V, I_t = 0.7 nA). The images were processed to correct plane and line noise, contrast, and thermal drift for better visibility of the steps.

References

(1) Barbier, A.; Tuel, A.; Arcon, I.; Kodre, A.; Martin, G. A. Characterization and Catalytic Behavior of Co/SiO2 Catalysts: Influence of Dispersion in the Fischer–Tropsch Reaction. *J. Catal.* **2001**, *200*, 106-116.

(2) Bezemer, G. L.; Bitter, J. H.; Kuipers, H. P. C. E.; Oosterbeek, H.; Holewijn, J. E.; Xu, X.; Kapteijn, F.; van Dillen, A. J.; de Jong, K. P. Cobalt Particle Size Effects in the Fischer−Tropsch Reaction Studied with Carbon Nanofiber Supported Catalysts. *J. Am. Chem. Soc.* **2006**, *128*, 3956-3964.

(3) Bezemer, G. L.; Radstake, P. B.; Falke, U.; Oosterbeek, H.; Kuipers, H. P. C. E.; van Dillen, A. J.; de Jong, K. P. Investigation of promoter effects of manganese oxide on carbon nanofiber-supported cobalt catalysts for Fischer–Tropsch synthesis. *J. Catal.* **2006**, *237*, 152-161.

(4) Bezemer, G. L.; van Laak, A.; van Dillen, A. J.; de Jong, K. P. Cobalt supported on carbon nanofibers- a promising novel Fischer-Tropsch catalyst. In *Studies in Surface Science and Catalysis*, Bao, X., Xu, Y. Eds.; Vol. 147; Elsevier, 2004; pp 259-264.

(5) Bian, G.-Z.; Fujishita, N.; Mochizuki, T.; Ning, W.-S.; Yamada, M. Investigations on the structural changes of two Co/SiO2 catalysts by performing Fischer–Tropsch synthesis. *Appl. Catal., A: General* **2003**, *252*, 251-260.

(6) Bian, G.; Mochizuki, T.; Fujishita, N.; Nomoto, H.; Yamada, M. Activation and Catalytic Behavior of Several Co/SiO2 Catalysts for Fischer−Tropsch Synthesis. *Energy Fuels* **2003**, *17*, 799-803.

(7) Chen, L.; Song, G.; Fu, Y.; Shen, J. The effects of promoters of K and Zr on the mesoporous carbon supported cobalt catalysts for Fischer–Tropsch synthesis. *J. Colloid Interface Sci.* **2012**, *368*, 456-461.

(8) Cheng, Q.; Tian, Y.; Lyu, S.; Zhao, N.; Ma, K.; Ding, T.; Jiang, Z.; Wang, L.; Zhang, J.; Zheng, L.; et al. Confined small-sized cobalt catalysts stimulate carbon-chain growth reversely by modifying ASF law of Fischer–Tropsch synthesis. *Nat. Commun.* **2018**, *9*, 3250.

(9) den Breejen, J. P.; Radstake, P. B.; Bezemer, G. L.; Bitter, J. H.; Frøseth, V.; Holmen, A.; de Jong, K. P. On the Origin of the Cobalt Particle Size Effects in Fischer−Tropsch Catalysis. *Journal of the American Chemical Society* **2009**, *131*, 7197-7203.

(10) Enger, B. C.; Fossan, Å.-L.; Borg, Ø.; Rytter, E.; Holmen, A. Modified alumina as catalyst support for cobalt in the Fischer–Tropsch synthesis. *J. Catal.* **2011**, *284*, 9-22.

(11) Eschemann, T. O.; Lamme, W. S.; Manchester, R. L.; Parmentier, T. E.; Cognigni, A.; Rønning, M.; de Jong, K. P. Effect of support surface treatment on the synthesis, structure, and performance of Co/CNT Fischer–Tropsch catalysts. *J. Catal.* **2015**, *328*, 130-138.

(12) Fang, X.; Liu, B.; Cao, K.; Yang, P.; Zhao, Q.; Jiang, F.; Xu, Y.; Chen, R.; Liu, X. Particle-Size-Dependent Methane Selectivity Evolution in Cobalt-Based Fischer–Tropsch Synthesis. *ACS Catal.* **2020**, *10*, 2799-2816.

(13) Fu, T.; Lv, J.; Li, Z. Effect of Carbon Porosity and Cobalt Particle Size on the Catalytic Performance of Carbon Supported Cobalt Fischer–Tropsch Catalysts. *Ind. Eng. Chem. Res.* **2014**, *53*, 1342-1350.

(14) Fu, L.; Bartholomew, C. H. Structure sensitivity and its effects on product distribution in CO hydrogenation on cobalt/alumina. *J. Catal.* **1985**, *92*, 376-387.

(15) Ghasvareh, P.; Smith, K. J. Effects of Co Particle Size on the Stability of Co/Al2O3 and Re–Co/Al2O3 Catalysts in a Slurry-Phase Fischer-Tropsch Reactor. *Energy Fuels* **2016**, *30*, 9721-9729.

(16) Ghogia, A. C.; Machado, B. F.; Cayez, S.; Nzihou, A.; Serp, P.; Soulantica, K.; Pham Minh, D. Beyond confinement effects in Fischer-Tropsch Co/CNT catalysts. *J. Catal.* **2021**, *397*, 156-171.

(17) Gnanamani, M. K.; Jacobs, G.; Shafer, W. D.; Davis, B. H. Fischer–Tropsch synthesis: Activity of metallic phases of cobalt supported on silica. *Catal. Today* **2013**, *215*, 13-17.

(18) Haddad, G. J.; Chen, B.; Goodwin, J. J. G. Effect of La3+Promotion of Co/SiO2on CO Hydrogenation. *J. Catal.* **1996**, *161*, 274-281.

(19) Herranz, T.; Deng, X.; Cabot, A.; Guo, J.; Salmeron, M. Influence of the Cobalt Particle Size in the CO Hydrogenation Reaction Studied by In Situ X-Ray Absorption Spectroscopy. *J. Phys. Chem. B* **2009**, *113*, 10721-10727.

(20) Ho, S. W.; Houalla, M.; Hercules, D. M. Effect of particle size on carbon monoxide hydrogenation activity of silica supported cobalt catalysts. *J. Phys. Chem.* **1990**, *94*, 6396-6399.

(21) Iglesia, E.; Soled, S. L.; Fiato, R. A. Fischer-Tropsch synthesis on cobalt and ruthenium. Metal dispersion and support effects on reaction rate and selectivity. *J. Catal.* **1992**, *137*, 212-224.

(22) Iglesia, E.; Soled, S. L.; Fiato, R. A.; Via, G. H. Dispersion, support, and bimetallic effects in Fischer-Tropsch synthesis on cobalt catalysts. In *Studies in Surface Science and Catalysis*, Curry-Hyde, H. E., Howe, R. F. Eds.; Vol. 81; Elsevier, 1994; pp 433-442.

(23) Johnson, B. G.; Bartholomew, C. H.; Goodman, D. W. The role of surface structure and dispersion in CO hydrogenation on cobalt. *J. Catal.* **1991**, *128*, 231-247.

(24) Kogelbauer, A.; Goodwin, J. J. G.; Oukaci, R. Ruthenium Promotion of Co/Al2O3Fischer–Tropsch Catalysts. *J. Catal.* **1996**, *160*, 125-133.

(25) Lee, J.-H.; Lee, D.-K.; Ihm, S.-K. Independent effect of particle size and reduction extent on CO hydrogenation over alumina-supported cobalt catalyst. *J. Catal.* **1988**, *113*, 544-548.

(26) Liu, C.; He, Y.; Wei, L.; Zhang, Y.; Zhao, Y.; Hong, J.; Chen, S.; Wang, L.; Li, J. Hydrothermal Carbon-Coated TiO2 as Support for Co-Based Catalyst in Fischer–Tropsch Synthesis. *ACS Catal.* **2018**, *8*, 1591-1600.

(27) Lögdberg, S.; Yang, J.; Lualdi, M.; Walmsley, J. C.; Järås, S.; Boutonnet, M.; Blekkan, E. A.; Rytter, E.; Holmen, A. Further insights into methane and higher hydrocarbons formation over cobalt-based catalysts with γ-Al2O3, α-Al2O3 and TiO2 as support materials. *J. Catal.* **2017**, *352*, 515-531.

(28) Lualdi, M.; Di Carlo, G.; Lögdberg, S.; Järås, S.; Boutonnet, M.; La Parola, V.; Liotta, L. F.; Ingo, G. M.; Venezia, A. M. Effect of Ti and Al addition via direct synthesis to SBA-15 as support for cobalt based Fischer-Tropsch catalysts. *Appl. Catal., A: General* **2012**, *443-444*, 76-86.

(29) Luo, Q.-X.; Guo, L.-P.; Yao, S.-Y.; Bao, J.; Liu, Z.-T.; Liu, Z.-W. Cobalt nanoparticles confined in carbon matrix for probing the size dependence in Fischer-Tropsch synthesis. *J. Catal.* **2019**, *369*, 143-156.

(30) Martínez, A.; Prieto, G. Breaking the dispersion-reducibility dependence in oxide-supported cobalt nanoparticles. *J. Catal.* **2007**, *245*, 470-476.

(31) Melaet, G.; Lindeman, A. E.; Somorjai, G. A. Cobalt Particle Size Effects in the Fischer–Tropsch Synthesis and in the Hydrogenation of CO2 Studied with Nanoparticle Model Catalysts on Silica. *Top. Catal.* **2014**, *57*, 500-507.

(32) Moreno-Castilla, C.; Carrasco-Marin, F. Cobalt catalysts supported on activated carbons: preparation and behaviour in the hydrogenation of carbon oxides. *J. Chem. Soc., Faraday Trans.* **1995**, *91*, 3519-3524, 10.1039/FT9959103519.

(33) Pan, Z.; Bukur, D. B. Fischer–Tropsch synthesis on Co/ZnO catalyst—Effect of pretreatment procedure. *Appl. Cat. A* **2011**, *404*, 74-80.

(34) Park, J.-Y.; Lee, Y.-J.; Karandikar, P. R.; Jun, K.-W.; Ha, K.-S.; Park, H.-G. Fischer–Tropsch catalysts deposited with size-controlled Co3O4 nanocrystals: Effect of Co particle size on catalytic activity and stability. *Appl. Catal., A: General* **2012**, *411-412*, 15-23.

(35) Prieto, G.; Martínez, A.; Concepción, P.; Moreno-Tost, R. Cobalt particle size effects in Fischer–Tropsch synthesis: structural and in situ spectroscopic characterisation on reverse micelle-synthesised Co/ITQ-2 model catalysts. *J. Catal.* **2009**, *266*, 129-144.

(36) Rane, S.; Borg, Ø.; Rytter, E.; Holmen, A. Relation between hydrocarbon selectivity and cobalt particle size for alumina supported cobalt Fischer–Tropsch catalysts. *Appl. Catal., A: General* **2012**, *437-438*, 10-17.

(37) Reuel, R. C.; Bartholomew, C. H. Effects of support and dispersion on the CO hydrogenation activity/selectivity properties of cobalt. *J. Catal.* **1984**, *85*, 78-88.

(38) Rivera-Torrente, M.; Hernández Mejía, C.; Hartman, T.; de Jong, K. P.; Weckhuysen, B. M. Impact of Niobium in the Metal–Organic Framework-Mediated Synthesis of Co-Based Catalysts for Synthesis Gas Conversion. *Catal. Lett.* **2019**, *149*, 3279-3286.

(39) Saib, A. M.; Claeys, M.; van Steen, E. Silica supported cobalt Fischer–Tropsch catalysts: effect of pore diameter of support. *Catal. Today* **2002**, *71*, 395-402.

(40) Smarzaro, J. L.; Baldanza, M. A. S.; de Almeida, A. J.; Caytuero, A.; Salim, V. M. M.; Passos, F. B.; Teixeira da Silva, V. Effect of Silica Encapsulation on Cobalt-Based Catalysts for Fischer–Tropsch Synthesis under Different Reaction Conditions. *Ind. Eng. Chem. Res.* **2021**, *60*, 11942-11953.

(41) Storsæter, S.; Borg, Ø.; Blekkan, E. A.; Holmen, A. Study of the effect of water on Fischer–Tropsch synthesis over supported cobalt catalysts. *J. Catal.* **2005**, *231*, 405-419.

(42) Sun, S.; Tsubaki, N.; Fujimoto, K. The reaction performances and characterization of Fischer–Tropsch synthesis Co/SiO2 catalysts prepared from mixed cobalt salts. *Appl. Catal., A: General* **2000**, *202*, 121-131.

(43) van Deelen, T. W.; Nijhuis, J. J.; Krans, N. A.; Zečević, J.; de Jong, K. P. Preparation of Cobalt Nanocrystals Supported on Metal Oxides To Study Particle Growth in Fischer–Tropsch Catalysts. *ACS Catal.* **2018**, *8*, 10581-10589.

(44) Venezia, A. M.; La Parola, V.; Liotta, L. F.; Pantaleo, G.; Lualdi, M.; Boutonnet, M.; Järås, S. Co/SiO2 catalysts for Fischer–Tropsch synthesis; effect of Co loading and support modification by TiO2. *Catal. Today* **2012**, *197*, 18-23.

(45) Wang, Z.-j.; Skiles, S.; Yang, F.; Yan, Z.; Goodman, D. W. Particle size effects in Fischer–Tropsch synthesis by cobalt. *Catal. Today* **2012**, *181*, 75-81.

(46) Xiong, H.; Motchelaho, M. A. M.; Moyo, M.; Jewell, L. L.; Coville, N. J. Correlating the preparation and performance of cobalt catalysts supported on carbon nanotubes and carbon spheres in the Fischer–Tropsch synthesis. *J. Catal.* **2011**, *278*, 26-40.

(47) Yang, Y.; Jia, L.; Hou, B.; Li, D.; Wang, J.; Sun, Y. The Correlation of Interfacial Interaction and Catalytic Performance of N-Doped Mesoporous Carbon Supported Cobalt Nanoparticles for Fischer–Tropsch Synthesis. *J. Phys. Chem. C* **2014**, *118*, 268-277.

(48) Yang, J.; Tveten, E. Z.; Chen, D.; Holmen, A. Understanding the Effect of Cobalt Particle Size on Fischer−Tropsch Synthesis: Surface Species and Mechanistic Studies by SSITKA and Kinetic Isotope Effect. *Langmuir* **2010**, *26*, 16558-16567.

(49) Yu, Z.; Borg, Ø.; Chen, D.; Enger, B. C.; Frøseth, V.; Rytter, E.; Wigum, H.; Holmen, A. Carbon Nanofiber Supported Cobalt Catalysts for Fischer–Tropsch Synthesis with High Activity and Selectivity. *Catal. Lett.* **2006**, *109*, 43-47.

References

[1] Rothenberg, G., Heterogeneous Catalysis In *Catalysis*; John Wiley and Sons, Ltd: **2008**; Chapter 4, 127–187.

[2] Schlögl, R. Heterogeneous Catalysis. *Angew. Chem. Int. Ed.* **2015**, *54*, 3465–3520.

[3] Nørskov, J. K.; Studt, F.; Abild-Pedersen, F.; Bligaard, T., Fundamental Concepts in Heterogeneous Catalysis; John Wiley and Sons, Incorporated: **2014**; Chapter 1, 1–5.

[4] Taylor, H. S.; Armstrong, E. F. A theory of the catalytic surface. *Proc. R. Soc., Lond., Ser. A* **1925**, *108*, 105–111.

[5] Topsøe, H. Developments in operando studies and in situ characterization of heterogeneous catalysts. *J. Catal.* **2003**, *216*, 155–164.

[6] Ertl, G.; Küppers, J., Low Energy Electrons and Surface Chemistry; Wiley-VCH: Weinheim, **1985**.

[7] Bartholomew, C. H.; Farrauto, R. J., Fundamentals of industrial catalytic processes, 2nd ed.; Wiley-Interscience: Hoboken, New Jersey, **2006**.

[8] Frenken, J. W. M.; Groot, I., Operando Research in Heterogeneous Catalysis; Springer Series in Chemical Physics; Springer International Publishing: **2017**.

[9] Salmeron, M.; Eren, B. High-Pressure Scanning Tunneling Microscopy. *Chem. Rev.* **2021**, *121*, 962–1006.

[10] Rasmussen, P. B.; Hendriksen, B. L. M.; Zeijlemaker, H.; Ficke, H. G.; Frenken, J. W. M. The „Reactor STM“: A scanning tunneling microscope for investigation of catalytic surfaces at semi-industrial reaction conditions. *Rev. Sci. Instrum.* **1998**, *69*, 3879–3884.

[11] McIntyre, B. J.; Salmeron, M.; Somorjai, G. A. A variable pressure/temperature scanning tunneling microscope for surface science and catalysis studies. *Rev. Sci. Instrum.* **1993**, *64*, 687–691.

[12] Tao, F.; Tang, D.; Salmeron, M.; Somorjai, G. A. A new scanning tunneling microscope reactor used for high-pressure and high-temperature catalysis studies. *Rev. Sci. Instrum.* **2008**, *79*, 084101.

[13] Laegsgaard, E.; Österlund, L.; Thostrup, P.; Rasmussen, P. B.; Stensgaard, I.; Besenbacher, F. A high-pressure scanning tunneling microscope. *Rev. Sci. Instrum.* **2001**, *72*, 3537–3542.

[14] Rößler, M.; Geng, P.; Wintterlin, J. A high-pressure scanning tunneling microscope for studying heterogeneous catalysis. *Rev. Sci. Instrum.* **2005**, *76*, 023705.

[15] Fischer, F.; Tropsch, H. Verfahren zur Gewinnung mehrgliedriger Paraffinkohlenwasserstoffe aus Kohlenoxyden und Wasserstoff auf katalytischem Wege, Patent, DRP 484337, **1925**.

[16] Khodakov, A. Y.; Chu, W.; Fongarland, P. Advances in the Development of Novel Cobalt Fischer–Tropsch Catalysts for Synthesis of Long-Chain Hydrocarbons and Clean Fuels. *Chem. Rev.* **2007**, *107*, 1692–1744.

[17] Dry, M. E. The Fischer–Tropsch process: 1950–2000. *Catal. Today* **2002**, *71*, 227–241.

[18] Davis, B. H. Fischer–Tropsch Synthesis: Comparison of Performances of Iron and Cobalt Catalysts. *Ind. Eng. Chem. Res.* **2007**, *46*, 8938–8945.

[19] Martinelli, M.; Gnanamani, M. K.; LeViness, S.; Jacobs, G.; Shafer, W. D. An overview of Fischer-Tropsch Synthesis: XtL processes, catalysts and reactors. *Appl. Catal., A: General* **2020**, *608*, 117740.

[20] Van der Laan, G. P.; Beenackers, A. A. C. M. Kinetics and Selectivity of the Fischer–Tropsch Synthesis: A Literature Review. *Cat. Rev. - Sci. Eng.* **1999**, *41*, 255–318.

[21] Schulz, H. Short history and present trends of Fischer–Tropsch synthesis. *Appl. Catal., A: General* **1999**, *186*, 3–12.

[22] Vogel, A. P.; van Dyk, B.; Saib, A. M. GTL using efficient cobalt Fischer-Tropsch catalysts. *Catal. Today* **2016**, *259, Part 2*, 323–330.

[23] Kaiser, P.; Pöhlmann, F.; Jess, A. Intrinsic and Effective Kinetics of Cobalt-Catalyzed Fischer-Tropsch Synthesis in View of a Power-to-Liquid Process Based on Renewable Energy. *Chem. Eng. Technol.* **2014**, *37*, 964–972.

[24] Swain, P. K.; Das, L. M.; Naik, S. N. Biomass to liquid: A prospective challenge to research and development in 21st century. *Renew. Sust. Energ. Rev.* **2011**, *15*, 4917–4933.

[25] Yang, L.; Ge, X.; Wan, C.; Yu, F.; Li, Y. Progress and perspectives in converting biogas to transportation fuels. *Renew. Sust. Energ. Rev.* **2014**, *40*, 1133–1152.

[26] Santos, R. G. d.; Alencar, A. C. Biomass-derived syngas production via gasification process and its catalytic conversion into fuels by Fischer Tropsch synthesis: A review. *Int. J. Hydrogen Energy* **2020**, *45*, 18114–18132.

[27] Sonal; Ahmad, E.; Upadhyayula, S.; Pant, K. K. Biomass-derived CO_2 rich syngas conversion to higher hydrocarbon via Fischer-Tropsch process over Fe–Co bimetallic catalyst. *Int. J. Hydrogen Energy* **2019**, *44*, 27741–27748.

[28] Müller, S.; Groß, P.; Rauch, R.; Zweiler, R.; Aichernig, C.; Fuchs, M.; Hofbauer, H. Production of diesel from biomass and wind power – Energy storage by the use of the Fischer-Tropsch process. *Biomass Conversion and Biorefinery* **2018**, *8*, 275–282.

[29] Gruber, H.; Groß, P.; Rauch, R.; Reichhold, A.; Zweiler, R.; Aichernig, C.; Müller, S.; Ataimisch, N.; Hofbauer, H. Fischer-Tropsch products from biomass-derived syngas and renewable hydrogen. *Biomass Conversion and Biorefinery* **2021**, *11*, 2281–2292.

[30] Davis, B. H. Fischer–Tropsch synthesis: Overview of reactor development and future potentialities. *Top. Catal.* **2005**, *32*, 143–168.

[31] Mahmoudi, H.; Mahmoudi, M.; Doustdar, O.; Jahangiri, H.; Tsolakis, A.; Gu, S.; Wyszynski, M. L. A review of Fischer Tropsch synthesis process, mechanism, surface chemistry and catalyst formulation. *Biofuels Engineering* **2017**, *2*, 11–31.

[32] Botes, F. G.; Niemantsverdriet, J. W.; van de Loosdrecht, J. A comparison of cobalt and iron based slurry phase Fischer–Tropsch synthesis. *Catal. Today* **2013**, *215*, 112–120.

[33] Vannice, M. A. The catalytic synthesis of hydrocarbons from H_2CO mixtures over the group VIII metals: I. The specific activities and product distributions of supported metals. *J. Catal.* **1975**, *37*, 449–461.

[34] Shimura, K.; Miyazawa, T.; Hanaoka, T.; Hirata, S. Factors influencing the activity of $Co/Ca/TiO_2$ catalyst for Fischer–Tropsch synthesis. *Catal. Today* **2014**, *232*, 2–10.

[35] Oukaci, R.; Singleton, A. H.; Goodwin, J. G. Comparison of patented Co F–T catalysts using fixed-bed and slurry bubble column reactors. *Appl. Catal., A: General* **1999**, *186*, 129–144.

[36] Ertl, G. Primary steps in catalytic synthesis of ammonia. *J. Vac. Sci. Technol. A* **1983**, *1*, 1247–1253.

[37] Somorjai, G. A.; Park, J. Y. Concepts, instruments, and model systems that enabled the rapid evolution of surface science. *Surf. Sci.* **2009**, *603*, 1293–1300.

[38] Geerlings, J. J. C.; Zonnevylle, M. C.; de Groot, C. P. M. Studies of the Fischer-Tropsch reaction on Co(0001). *Surf. Sci.* **1991**, *241*, 302–314.

[39] Geerlings, J. J. C.; Zonnevylle, M. C.; de Groot, C. P. M. Structure sensitivity of the Fischer-Tropsch reaction on cobalt single crystals. *Surf. Sci.* **1991**, *241*, 315–324.

[40] Beitel, G. A.; de Groot, C. P. M.; Oosterbeek, H.; Wilson, J. H. A Combined in-Situ PM-RAIRS and Kinetic Study of Single-Crystal Cobalt Catalysts under Synthesis Gas at Pressures up to 300 mbar. *J. Phys. Chem. B* **1997**, *101*, 4035–4043.

[41] Navarro, V.; van Spronsen, M. A.; Frenken, J. W. M. In situ observation of self-assembled hydrocarbon Fischer–Tropsch products on a cobalt catalyst. *Nat. Chem.* **2016**, *8*, 929–934.

[42] Wilson, J.; de Groot, C. Atomic-Scale Restructuring in High-Pressure Catalysis. *J. Phys. Chem.* **1995**, *99*, 7860–7866.

[43] Kitakami, O.; Sato, H.; Shimada, Y.; Sato, F.; Tanaka, M. Size effect on the crystal phase of cobalt fine particles. *Phys. Rev. B* **1997**, *56*, 13849–13854.

[44] Van Helden, P.; Ciobîcă, I. M.; Coetzer, R. L. J. The size-dependent site composition of FCC cobalt nanocrystals. *Catal. Today* **2016**, *261*, 48–59.

[45] Van Hardeveld, R.; Hartog, F. The statistics of surface atoms and surface sites on metal crystals. *Surf. Sci.* **1969**, *15*, 189–230.

[46] Bezemer, G. L.; Bitter, J. H.; Kuipers, H. P. C. E.; Oosterbeek, H.; Holewijn, J. E.; Xu, X.; Kapteijn, F.; van Dillen, A. J.; de Jong, K. P. Cobalt Particle Size Effects in the Fischer–Tropsch Reaction Studied with Carbon Nanofiber Supported Catalysts. *J. Am. Chem. Soc.* **2006**, *128*, 3956–3964.

[47] Van de Loosdrecht, J.; Botes, F. G.; Ciobica, I. M.; Ferreira, A.; Gibson, P.; Moodley, D. J.; Saib, A. M.; Visagie, J. L.; Weststrate, C. J.; Niemantsverdriet, J. W., 7.20 - Fischer–Tropsch Synthesis: Catalysts and Chemistry In *Comprehensive Inorganic Chemistry II (Second Edition)*, Reedijk, J., Poeppelmeier, K., Eds.; Elsevier: Amsterdam, **2013**, 525–557.

[48] Van Santen, R. A.; Markvoort, A. J.; Filot, I. A. W.; Ghouri, M. M.; Hensen, E. J. M. Mechanism and microkinetics of the Fischer-Tropsch reaction. *Phys. Chem. Chem. Phys.* **2013**, *15*, 17038–17063.

[49] Fischer, F.; Tropsch, H. Die Erdölsynthese bei gewöhnlichem Druck aus den Vergasungsprodukten der Kohlen. *Brennst.-Chem.* **1926**, *7*, 97–116.

[50] Pichler, H.; Schulz, H. Neuere Erkenntnisse auf dem Gebiet der Synthese von Kohlenwasserstoffen aus CO und H_2. *Chem. Ing. Tech.* **1970**, *42*, 1162–1174.

[51] Qi, Y.; Yang, J.; Chen, D.; Holmen, A. Recent Progresses in Understanding of Co-Based Fischer–Tropsch Catalysis by Means of Transient Kinetic Studies and Theoretical Analysis. *Catal. Lett.* **2015**, *145*, 145–161.

[52] Van Santen, R. A. Complementary Structure Sensitive and Insensitive Catalytic Relationships. *Acc. Chem. Res.* **2009**, *42*, 57–66.

[53] Banerjee, A.; van Bavel, A. P.; Kuipers, H. P. C. E.; Saeys, M. Origin of the Formation of Nanoislands on Cobalt Catalysts during Fischer–Tropsch Synthesis. *ACS Catal.* **2015**, *5*, 4756–4760.

[54] Ehrensperger, M.; Wintterlin, J. In situ high-pressure high-temperature scanning tunneling microscopy of a Co(0001) Fischer–Tropsch model catalyst. *J. Catal.* **2014**, *319*, 274–282.

[55] Ehrensperger, M.; Wintterlin, J. In situ scanning tunneling microscopy of the poisoning of a Co(0001) Fischer–Tropsch model catalyst by sulfur. *J. Catal.* **2015**, *329*, 49–56.

[56] Herbschleb, C. T. et al. The ReactorSTM: Atomically resolved scanning tunneling microscopy under high-pressure, high-temperature catalytic reaction conditions. *Rev. Sci. Instrum.* **2014**, *85*, 083703.

[57] Schulz, H. Major and Minor Reactions in Fischer–Tropsch Synthesis on Cobalt Catalysts. *Top. Catal.* **2003**, *26*, 73–85.

[58] Schulz, H. Selforganization in Fischer–Tropsch synthesis with iron- and cobalt catalysts. *Catal. Today* **2014**, *228*, 113–122.

[59] Banerjee, A.; Navarro, V.; Frenken, J. W. M.; van Bavel, A. P.; Kuipers, H. P. C. E.; Saeys, M. Shape and Size of Cobalt Nanoislands Formed Spontaneously on Cobalt Terraces during Fischer–Tropsch Synthesis. *J. Phys. Chem. Lett.* **2016**, *7*, 1996–2001.

[60] Zhang, X.-Q.; van Santen, R. A.; Hensen, E. J. M. Carbon-Induced Surface Transformations of Cobalt. *ACS Catal.* **2014**, 596–601.

[61] Böller, B.; Durner, K. M.; Wintterlin, J. The active sites of a working Fischer–Tropsch catalyst revealed by operando scanning tunnelling microscopy. *Nat. Catal.* **2019**, *2*, 1027–1034.

[62] Böcklein, S. Untersuchungen zur katalytischen Ethylenepoxidierung über Silber – Überbrückung des pressure gap-Problems, Dissertation, Ludwig-Maximilians-Universität München, **2013**.

[63] Böller, B. Die aktiven Zentren der Fischer-Tropsch-Synthese – Eine Studie mit dem operando-Rastertunnelmikroskop auf einem Co(0001)-Einkristall, Dissertation, Ludwig-Maximilians-Universität München, **2020**.

[64] Nishizawa, T.; Ishida, K. The Co (Cobalt) system. *J. Phase Equilib.* **1983**, *4*, 387–390.

[65] Schastlivtsev, V. M.; Khlebnikova, Y. V.; Tabatchikova, T. I.; Rodionov, D. P.; Sazonova, V. A. Formation of a structure in cobalt single crystals at the $\beta \longrightarrow \alpha$ transformation. *Dokl. Phys.* **2009**, *54*, 21–24.

[66] Hofmann, S., Auger- and X-Ray Photoelectron Spectroscopy in Materials Science: A User-Oriented Guide; Auger- and X-Ray Photoelectron Spectroscopy in Materials Science: A User-Oriented Guide; Springer-Verlag Berlin Heidelberg: **2013**.

[67] Moulder, J. F.; Stickle, W. F.; Sobol, P. E.; Bomben, K. D., Handbook of x-ray photoelectron spectroscopy; Perkin-Elmer Corporation: Eden Prairie, Minnesota, **1992**.

[68] Yeh, J. J.; Lindau, I. Atomic subshell photoionization cross sections and asymmetry parameters: $1 \leq Z \leq 103$. *Atom. Data and Nucl. Data* **1985**, *32*, 1–155.

[69] Reilman, R. F.; Msezane, A.; Manson, S. T. Relative intensities in photoelectron spectroscopy of atoms and molecules. *J. Electron. Spectrosc. Relat. Phenom.* **1976**, *8*, 389–394.

[70] Ehrensperger, M. Neue Einblicke in die Fischer-Tropsch-Synthese an Cobalt-Modellkatalysatoren: vom Ultrahochvakuum bis zur Hochdruck-Rastertunnelmikroskopie, Dissertation, Ludwig-Maximilians-Universität München, **2015**.

[71] Ganiek, M., Bachelorarbeit, Ludwig-Maximilians-Universität München, **2012**.

[72] Reichelt, R. Untersuchungen von Sauerstoffphasen auf der Silberoberfläche zum Verständnis der Ag-katalysierten Ethylenepoxidierung, Dissertation, Ludwig-Maximilians-Universität München, **2010**.

[73] NIST Electron Inelastic-Mean-Free-Path Database, Version 1.2, `https://www.nist.gov/srd/nist-standard-reference-database-71`.

[74] Tanuma, S.; Powell, C. J.; Penn, D. R. Calculations of electron inelastic mean free paths. V. Data for 14 organic compounds over the 50–2000 eV range. *Surf. Interface Anal.* **1994**, *21*, 165–176.

[75] Igor Pro – Version 6.3.7.2, WaveMetrics Inc., Lake Oswego, OR, USA, **2014**.

[76] Doniach, S.; Šunjić, M. Many-electron singularity in X-ray photoemission and X-ray line spectra from metals. *J. Phys. C: Solid State Phys.* **1970**, *3*, 285.

[77] Henzler, M.; Göpel, W., Oberflächenphysik des Festkörpers; Oberflächenphysik des Festkörpers; Vieweg+Teubner Verlag: Wiesbaden, **1991**, 1–643.

[78] Wiesendanger, R., Scanning Probe Microscopy and Spectroscopy – Methods and Applications; Cambridge University Press: Cambridge, **1994**.

[79] Tersoff, J.; Lang, N. D., 1. Theory of Scanning Tunneling Microscopy In *Methods in Experimental Physics*, Stroscio, J. A., Kaiser, W. J., Eds.; Academic Press: **1993**, 1–29.

[80] Boudart, M. Turnover Rates in Heterogeneous Catalysis. *Chem. Rev.* **1995**, *95*, 661–666.

[81] Mond, L.; Langer, C.; Quincke, F. L.—Action of carbon monoxide on nickel. *J. Chem. Soc., Trans.* **1890**, *57*, 749–753.

[82] Kerfoot, D. G. E., Nickel In *Ullmann's Encyclopedia of Industrial Chemistry*; Wiley-VCH Verlag: **2000**, 37–101.

[83] Goldberger, W. M.; Othmer, D. F. Kinetics of Nickel Carbonyl Formation. *Ind. Eng. CHem. Process Des. Dev.* **1963**, *2*, 202–209.

[84] De Groot, P.; Coulon, M.; Dransfeld, K. $Ni(CO)_4$ formation on single Ni crystals: Reaction kinetics and observation of surface facetting induced by the reaction. *Surf. Sci.* **1980**, *94*, 204–220.

[85] Pichler, H.; Walenda, H. Über die Bildung von Eisencarbonyl bei der Einwirkung von Kohlenoxyd auf Stahl. *Brennst.-Chem.* **1940**, *21*, 133–144.

[86] Ludlum, K. H.; Eischens, R. P. Carbonyl formation in stainless steel infrared cells. *Surf. Sci.* **1973**, *40*, 397–398.

[87] Inouye, H.; DeVan, J. H. Formation of iron carbonyl between a 1/2 pct Mo steel and high-pressure gases containing carbon monoxide. *JMES* **1979**, *1*, 52–60.

[88] Heinicke, G.; Harenz, H. Chemische Beeinflussung mechanisch aktivierter Reaktionen. II. Chemische Aktivierung der mechanisch angeregten Nickel- und Eisencarbonylbildung. *Z. Anorg. Allg. Chem.* **1963**, *324*, 185–196.

[89] Mittasch, A. Über die chemische Dynamik des Nickelkohlenoxyds. *Z. Phys. Chem.* **1902**, *40*, 1–83.

[90] Greiner, G.; Menzel, D. Promotion and inhibition of Ni(CO)$_4$ formation on Ni(100): A kinetic investigation coupled with ESCA measurements. *J. Catal.* **1982**, *77*, 382–396.

[91] Zeller, P.; Henß, A.-K.; Weinl, M.; Diehl, L.; Keefer, D.; Lippmann, J.; Schulz, A.; Kraus, J.; Schreck, M.; Wintterlin, J. Detachment of CVD-grown graphene from single crystalline Ni films by a pure gas phase reaction. *Surf. Sci.* **2016**, *653*, 143–152.

[92] Sandvik Sandvik 5R75 Datasheet, (cited 22.10.2021), available from: `https://www.materials.sandvik/en/materials-center/material-datasheets/tube-and-pipe-seamless/sandvik-5r75/`.

[93] Johansson, G.; Hedman, J.; Berndtsson, A.; Klasson, M.; Nilsson, R. Calibration of electron spectra. *J. Electron. Spectrosc. Relat. Phenom.* **1973**, *2*, 295–317.

[94] Gelius, U.; Hedén, P. F.; Hedman, J.; Lindberg, B. J.; Manne, R.; Nordberg, R.; Nordling, C.; Siegbahn, K. Molecular Spectroscopy by Means of ESCA III.Carbon compounds. *Phys. Scr.* **1970**, *2*, 70–80.

[95] Estrade-Szwarckopf, H.; Rousseau, B. U.P.S. and X.P.S. studies of alkali-graphite intercalation compounds. *Synth. Met.* **1988**, *23*, 191–198.

[96] Dodero, G.; De Michieli, L.; Cavalleri, O.; Rolandi, R.; Oliveri, L.; Daccà, A.; Parodi, R. l-Cysteine chemisorption on gold: an XPS and STM study. *Colloids Surf., A: Physicochem. Eng. Aspects* **2000**, *175*, 121–128.

[97] Illing, G.; Heskett, D.; Plummer, E. W.; Freund, H. J.; Somers, J.; Lindner, T.; Bradshaw, A. M.; Buskotte, U.; Neumann, M.; Starke, U.; Heinz, K.; De Andres, P. L.; Saldin, D.; Pendry, J. B. Adsorption and reaction of CO$_2$ on Ni{110}: X-ray photoemission, near-edge X-ray absorption fine-structure and diffuse leed studies. *Surf. Sci.* **1988**, *206*, 1–19.

[98] Dickinson, T.; Povey, A. F.; Sherwood, P. M. A. Dissolution and passivation of nickel. An X-ray photoelectron spectroscopic study. *J. Chem. Soc., Faraday Transactions 1: Physical Chemistry in Condensed Phases* **1977**, *73*, 327–343.

[99] Brundle, C. R.; Chuang, T. J.; Rice, D. W. X-ray photoemission study of the interaction of oxygen and air with clean cobalt surfaces. *Surf. Sci.* **1976**, *60*, 286–300.

[100] Wagner, C. D.; Zatko, D. A.; Raymond, R. H. Use of the oxygen KLL Auger lines in identification of surface chemical states by electron spectroscopy for chemical analysis. *Anal. Chem.* **1980**, *52*, 1445–1451.

[101] Wagner, C. D.; Passoja, D. E.; Hillery, H. F.; Kinisky, T. G.; Six, H. A.; Jansen, W. T.; Taylor, J. A. Auger and photoelectron line energy relationships in aluminum–oxygen and silicon–oxygen compounds. *J. Vac. Sci. Technol.* **1982**, *21*, 933–944.

[102] Olefjord, I.; Mathieu, H. J.; Marcus, P. Intercomparison of surface analysis of thin aluminium oxide films. *Surf. Interface Anal.* **1990**, *15*, 681–692.

[103] Biesinger, M. C.; Payne, B. P.; Grosvenor, A. P.; Lau, L. W. M.; Gerson, A. R.; Smart, R. S. C. Resolving surface chemical states in XPS analysis of first row transition metals, oxides and hydroxides: Cr, Mn, Fe, Co and Ni. *Appl. Surf. Sci.* **2011**, *257*, 2717–2730.

[104] Heinicke, G. Chemische Beeinflussung mechanisch aktivierter Reaktionen. I. Der Einfluß von Inhibitoren auf die mechanisch angeregte Bildung von Nickelcarbonyl. *Z. Anorg. Allg. Chem.* **1963**, *324*, 173–184.

[105] Shalvoy, R. B.; Reucroft, P. J. Characterization of a sulfur-resistant methanation catalyst by XPS. *J. Vac. Sci. Technol.* **1979**, *16*, 567–569.

[106] Rohani, V.; Iwarere, S.; Fabry, F.; Mourard, D.; Izquierdo, E.; Ramjugernath, D.; Fulcheri, L. Experimental Study of Hydrocarbons Synthesis from Syngas by a Tip–Tip Electrical Discharge at Very High Pressure. *Plasma Chem. Plasma Process.* **2011**, *31*, 663.

[107] Iwarere, S.; Rohani, V.; Ramjugernath, D.; Fabry, F.; Fulcheri, L. Hydrocarbons synthesis from syngas by very high pressure plasma. *Chem. Eng. J.* **2014**, *241*, 1–8.

[108] Matar, S.; Hatch, L. F., Chapter Three – Crude Oil Processing and Production of Hydrocarbon Intermediates In *Chemistry of Petrochemical Processes (Second Edition)*, Matar, S., Hatch, L. F., Eds.; Gulf Professional Publishing: Woburn, **2001**, 49–110.

[109] Hollemann, A.; Wiberg, N., Lehrbuch der Anorganischen Chemie, 102nd ed.; de Gruyter: Berlin, **2008**.

[110] Subramani, V.; Sharma, P.; Zhang, L.; Liu, K., Catalytic Steam Reforming Technology for the Production of Hydrogen and Syngas In *Hydrogen and Syngas Production and Purification Technologies*, **2009**, 14–126.

[111] Atkins, P.; de Paula, J., Physikalische Chemie, 4th ed.; Wiley-VCH: Weinheim, **2006**.

[112] Ahmed, S.; Aitani, A.; Rahman, F.; Al-Dawood, A.; Al-Muhaish, F. Decomposition of hydrocarbons to hydrogen and carbon. *Appl. Catal., A* **2009**, *359*, 1–24.

[113] Bennett, H. E. The Contamination of Platinum Metal Thermocouples. *Platinum Met. Rev.* **1961**, *5*, 132–133.

[114] Pollock, D. D. Thermocouples in High-Temperature Reactive Atmospheres. *Combust. Sci. Technol.* **1984**, *42*, 111–113.

[115] Bentley, R., Handbook of Temperature Measurement Vol. 3: The Theory and Practice of Thermoelectric Thermometry; Handbook of Temperature Measurement; Springer Singapore: **1998**.

[116] Ocken, H.; Van Vucht, J. H. N. Phase equilibria and superconductivity in the molybdenum-platinum system. *J. Less-common Met.* **1968**, *15*, 193–199.

[117] Kim, J.-S.; Seol, D.; Ji, J.; Jang, H.-S.; Kim, Y.; Lee, B.-J. Second nearest-neighbor modified embedded-atom method interatomic potentials for the Pt-M (M = Al, Co, Cu, Mo, Ni, Ti, V) binary systems. *Calphad* **2017**, *59*, 131–141.

[118] Rooksby, H. P.; Lewis, B. Relations between the structures of phases in the system platinum-molybdenum. *J. Less-common Met.* **1964**, *6*, 451–460.

[119] Selman, G. L. The Platinum-Molybdenum System – The formation of intermediate phases. *Platinum Met. Rev.* **1967**, *11*, 132–137.

[120] NIST Chemistry WebBook, `https://webbook.nist.gov/chemistry/`.

[121] Golder, K. M.; Böller, B.; Stienen, G.; Sickerling, J.; Wintterlin, J. A highly sensitive gas chromatograph for in situ and operando experiments on catalytic reactions. *Rev. Sci. Instrum.* **2021**, *92*, 124103.

[122] Boudart, M., Catalysis by Supported Metals In Eley, D., Pines, H., Weisz, P. B., Eds.; Adv. Catal. *20*; Academic Press: **1969**, 153–166.

[123] Den Breejen, J. P.; Radstake, P. B.; Bezemer, G. L.; Bitter, J. H.; Frøseth, V.; Holmen, A.; Jong, K. P. d. On the Origin of the Cobalt Particle Size Effects in Fischer–Tropsch Catalysis. *J. Am. Chem. Soc.* **2009**, *131*, 7197–7203.

[124] Wang, Z.-j.; Skiles, S.; Yang, F.; Yan, Z.; Goodman, D. W. Particle size effects in Fischer–Tropsch synthesis by cobalt. *Catal. Today* **2012**, *181*, 75–81.

[125] Prieto, G.; Martínez, A.; Concepción, P.; Moreno-Tost, R. Cobalt particle size effects in Fischer-Tropsch synthesis: structural and in situ spectroscopic characterisation on reverse micelle-synthesised Co/ITQ-2 model catalysts. *J. Catal.* **2009**, *266*, 129–144.

[126] Xiong, H.; Motchelaho, M. A. M.; Moyo, M.; Jewell, L. L.; Coville, N. J. Correlating the preparation and performance of cobalt catalysts supported on carbon nanotubes and carbon spheres in the Fischer–Tropsch synthesis. *J. Catal.* **2011**, *278*, 26–40.

[127] Gong, X.-Q.; Raval, R.; Hu, P. CO dissociation and O removal on Co(0001): a density functional theory study. *Surf. Sci.* **2004**, *562*, 247–256.

[128] Liu, J.-X.; Su, H.-Y.; Sun, D.-P.; Zhang, B.-Y.; Li, W.-X. Crystallographic Dependence of CO Activation on Cobalt Catalysts: HCP versus FCC. *J. Am. Chem. Soc.* **2013**, *135*, 16284–16287.

[129] Petersen, M. A.; Van Den Berg, J.-A.; Ciobîcă, I. M.; van Helden, P. Revisiting CO Activation on Co Catalysts: Impact of Step and Kink Sites from DFT. *ACS Catal.* **2017**, *7*, 1984–1992.

[130] Huffman, G. P.; Shah, N.; Zhao, J. M.; Huggins, F. E.; Hoost, T. E.; Halvorsen, S.; Goodwin, J. G. In-Situ XAFS Investigation of K-Promoted Co Catalysts. *J. Catal.* **1995**, *151*, 17–25.

[131] Ernst, B.; Bensaddik, A.; Hilaire, L.; Chaumette, P.; Kiennemann, A. Study on a cobalt silica catalyst during reduction and Fischer–Tropsch reaction: In situ EXAFS compared to XPS and XRD. *Catal. Today* **1998**, *39*, 329–341.

[132] Cats, K. H.; Gonzalez-Jimenez, I. D.; Liu, Y.; Nelson, J.; van Campen, D.; Meirer, F.; van der Eerden, A. M. J.; de Groot, F. M. F.; Andrews, J. C.; Weckhuysen, B. M. X-ray nanoscopy of cobalt Fischer-Tropsch catalysts at work. *Chem. Commun.* **2013**, *49*, 4622–4624.

[133] Golder, K. M.; Wintterlin, J. In Situ/Operando STM of the Fischer–Tropsch Synthesis on a Co($10\bar{1}15$) Surface – A Study to Bridge the Materials Gap between Single-Crystal Models and Supported Catalysts. *ACS Catal.* **2022**, *12*, 7199–7209.

[134] Lyu, S.; Wang, L.; Zhang, J.; Liu, C.; Sun, J.; Peng, B.; Wang, Y.; Rappé, K. G.; Zhang, Y.; Li, J.; Nie, L. Role of Active Phase in Fischer–Tropsch Synthesis: Experimental Evidence of CO Activation over Single-Phase Cobalt Catalysts. *ACS Catal.* **2018**, *8*, 7787–7798.

Danksagung

Zum Schluss möchte ich allen herzlich danken, die in den letzten Jahren durch Diskussionen, Ideen oder tatkräftige Unterstützung im Labor dafür gesorgt haben, dass meine Motivation aufrecht erhalten bleibt und somit zum Gelingen dieser Arbeit beigetragen haben. Mein besonderer Dank gilt:

- **Prof. Dr. Joost Wintterlin** für die Möglichkeit meine Doktorarbeit in seinem Arbeitskreis durchführen zu können, für das entgegengebrachte Vertrauen, das stets offene Ohr und die tatkräftige Unterstützung bei der Klärung immer wieder neu aufgetretenen experimentellen Herausforderungen, die es zu lösen galt.

- **Prof. Dr. Sebastian Günther** für die Übernahme des Zweitgutachtens und für anregenden Diskussionen und Ideen, die zur Überwindung mancher experimenteller Schwierigkeiten beigetragen haben.

- **Dr. Bernhard Böller** für die exzellente Betreuung während meiner Masterarbeit und die geduldige Einarbeitung an der HP-STM Apparatur und am Reaktor, die zahlreichen Tricks, Ideen und Hilfestellungen beim Lösen von schier unlösbar erscheinenden Problemen und der Vermittlung zahlloser handwerklicher Fertigkeiten, ohne die einige Apparaturen nicht existieren würden.

- Meinen aktuellen und ehemaligen Arbeitskollegen und -kolleginnen **Hannah Illner**, **Dr. Paul Leidinger**, **Dr. Ann-Kathrin Henß**, **Dr. Regina Wyrwich** und **Dr. Jürgen Kraus** für die freundliche und hilfsbereite Arbeitsatmosphäre, die gegenseitige tatkräftige Unterstützung und die heiteren Eis- und Kuchenpausen.

- Den Feinmechanikern **Ralf Hiermaier**, **Tomas Gisicius** und **Fabian Kreuzer** für ihre kompetente, schnelle Hilfe und akkurate Umsetzung bei der Anfertigung zahlreicher Sonderanfertigungen für die HP-STM Apparatur.

- Den Elektronikern **Axel Gersdorf** und **Herbert Bachmeier** für die zahllosen Reparaturen unserer in die Jahre gekommenen elektronischen Bauteilen sowie der kompetenten Beratung hinsichtlich so mancher Fehlersuche.

- **Dr. Steffen Schmidt** aus dem Arbeitskreis Prof. Thomas Bein für die kompetente Durchführung der SEM- und EDX-Messungen von teilweise sehr schwierig zu handhabenden Proben sowie der Hilfestellung bei der Interpretation der Ergebnisse.
- **Rita Römling-Engl**, **Regina Huber**, **Uta Le Guay** und **Elisabeth Wutz** für die zuverlässige Unterstützung bei der Bewältigung aller bürokratischen Hürden.
- Meinen Praktikanten **Yannick Kunzelmann** und **Melanie Burkhard** für ihre Unterstützung beim Nickelnachweis Projekt. Durch ihren unermüdlichen Fleiß und ihre Neugierde konnten wir Licht in die Nickel-Problematik bringen.
- **Sebastian Daszko** für die engagierte Fortführung meines Projekts während seiner Masterarbeit.
- Meinen **Chemikern**, ohne deren Zusammenarbeit bei Klausurvorbereitungen, Übungszetteln oder Protokollen die lange Zeit des Studiums um einiges kräftezehrender und weniger witzig gewesen wäre. Danke für unsere Corona-Calls, das Mitleiden, das Mitfreuen und die vielen schönen (Spiele-)abende.

LAST BUT NOT LEAST! möchte ich mich ganz herzlich bei meiner Familie und meinem Mann Max für ihre Unterstützung, ihr Verständnis und ihre Geduld bedanken. Ohne euch wäre ich sicher nicht so weit gekommen. Danke für die sehr wertvolle Gewissheit, dass ich immer auf eure Unterstützung zählen kann.